Global Modelling of Atmospheric Halogen Chemistry in the Marine Boundary Layer

Dissertation

zur Erlangung des Doktorgrades (Dr. rer. nat.)
der Mathematisch-Naturwissenschaftlichen Fakultät
der Rheinischen Friedrich-Wilhelms-Universität Bonn

vorgelegt von
Astrid Kerkweg
aus Essen

Bonn, 7. Juli 2005

Angefertigt mit Genehmigung der Mathematisch-Naturwissenschaftlichen Fakultät der Rheinischen Friedrich-Wilhelms-Universität Bonn

1. Gutachter: Prof. Dr. Jos Lelieveld
2. Gutachter: Prof. Dr. Andreas Bott

Tag der Promotion: 18.10.2005

Diese Dissertation ist auf dem Hochschulschriftenserver der ULB Bonn
http://hss.ulb.uni-bonn.de/diss_online elektronisch publiziert.

Erscheinungsjahr: 2005

Abstract

The importance of reactive halogen chemistry in our atmosphere has become evident throughout the last decades. The discovery of the chemical reactions leading to the stratospheric ozone hole over the South Pole in spring was followed by the exploration of the Arctic tropospheric ozone holes developing in early spring. The effects of halogen chemistry are not limited to polar regions. The largest chlorine and bromine source to the atmosphere is the sea through sea salt aerosol, thus reactive halogen chemistry is expected to have an influence on global tropospheric chemistry, too. Bromine can react through two major pathways, both leading to ozone loss: firstly, one cycle of bromine release from the aerosol is an autocatalytic ozone destruction cycle producing two Br radicals while destroying one ozone molecule and losing one Br radical. Secondly, in a gas phase cycle BrO, formed by reaction of Br with O_3, reacts with HO_2 leading to HOBr, which is photolysed back into OH and Br and restarts the ozone destruction cycle. The latter pathway does not only reduce ozone but also influences the oxidising capacity of the atmosphere by transferring HO_2 back to OH. In addition, bromine chemistry enhances the loss of nitrogen oxides to the aerosol by formation of $BrNO_3$.

For the first time a global model study of halogen chemistry in the marine boundary layer was accomplished, using a prognostically calculated aerosol distribution as well as calculating explicitly halogen release from the aerosol. The general circulation model ECHAM5 is used, linked to the Modular Earth Submodel SYstem (MESSy). The halogen chemistry mechanism including gas and aerosol phase reactions was developed within this thesis work and implemented as a submodel of MESSy. The MESSy submodel M7 - a seven modal aerosol representation - provides the prognostically calculated aerosol distribution.

First results show pronounced maxima of reactive halogen species (RHS) in the mid-latitude marine boundary layer in the northern hemisphere, reaching more than 1 pmol/mol BrO during daytime. Two prerequisites must be fulfilled to achieve these high maxima: firstly, sea salt emissions need to be relatively strong to provide an extensive bromide source and secondly, the acid supply needs to be sufficiently high to continuously acidify the aerosol, reaching pH values of approximately 4-5. By comparing the model results to -very scarce- measurements, however, it appears that the peak BrO mixing ratios are somewhat overestimated in the northern hemisphere, whereas simulated BrO concentrations in the southern hemisphere are lower than expected. Possible reasons, why modelled BrO mixing ratios are overestimated in the northern hemisphere and underpredicted in the southern hemisphere, are discussed. The simulated meteorology strongly influences the amount of RHS, since the surface wind speed drives the amount of sea salt emitted, being a prerequisite for RHS chemistry. This is illustrated by comparison of a climatological simulation to one, in which actual meteorological conditions are simulated through data assimilation (nudging). The differences between these simulations are addressed in more detail and suggestions for further improvements are presented.

Contents

Abstract **iii**

1 Introduction **1**

2 Halogen Chemistry - An Overview **5**
2.0.1 Aerosols . . . 7
2.0.2 Chlorine and Bromine Chemistry . . . 8
2.0.3 Iodine Chemistry . . . 17
2.0.4 Halogens in the Free Troposphere . . . 22

3 Model Descriptions **25**
3.1 ECHAM5 - A Model Description . . . 25
3.1.1 Data Assimilation . . . 26
3.2 MESSy . . . 26
3.2.1 MECCA - A Gas Phase Chemistry Mechanism . . . 28
3.2.2 MECCA-MBL . . . 29
3.2.3 Photolysis . . . 31
3.2.4 The Aerosol Module M7 . . . 32
3.2.5 Sedimentation . . . 33
3.2.6 Scavenging and Wet Deposition . . . 34
3.2.7 Emissions . . . 34
3.2.8 Dry Deposition . . . 36
3.2.9 Clouds and Convective Transport Processes . . . 38
3.2.10 Diagnostic Tools . . . 38

4 Results **39**
4.1 Simulation Setup . . . 39
4.2 Atmospheric Sea Salt Distributions . . . 40
4.3 Aerosol pH . . . 56
4.4 Reactive Halogen Chemistry . . . 60
4.5 Influences on Other Trace Gases . . . 66
4.6 Short-term Chemical Cycles . . . 74

5 Discussion **91**
5.1 Numerical Stiffness of the Chemical Solver . . . 92
5.2 Uncertainties Influencing the Emission Fluxes . . . 93
5.2.1 Dynamics . . . 93
5.2.2 Process Splitting of Emission and Deposition Calculations . . . 95

5.3 Interactions between Chemical and Physical Processes 96
5.4 Impact of RHS chemistry 96
5.4.1 ... on Ozone 96
5.4.2 ... on DMS and DMSO 96
5.4.3 ... on HCHO 97
5.4.4 ... on Uptake of Nitrogen Oxides and Nitric Acid 97

6 Conclusions **99**

A Abbreviations **101**

B Variable Definitions **103**

C MECCA Reaction Tables **105**

D SCAV Reaction Tables **117**

List of Tables **123**

Bibliography **125**

Acknowledgements **141**

Curriculum Vitae **143**

Chapter 1

Introduction

The onset of science in atmospheric chemistry was the discovery that not an ominous 'aether' is surrounding us but a mixture of gas molecules. In the 19th century the major composition of the atmosphere was successfully investigated, revealing that air is mainly composed of N_2, O_2, water vapour and CO_2 and additional -but minor- noble gases. Subsequently, the interest was shifted from these major components to trace gases present at mixing ratios of orders 10^{-6}, 10^{-9} or even less. Despite their low concentrations they determine the chemistry and the radiative properties of the atmosphere, thus controlling climate. The fact that mankind substantially influences atmospheric chemistry and thus climate enhances the relevance of atmospheric science. Greenhouse gases such as carbon dioxide (CO_2) and methane (CH_4) heat the atmosphere by absorbing infrared radiation emitted by the earth and reemitting it in all directions, thus trapping heat within the atmosphere.

Ozone is another trace gas known to influence climate as well as human health. Abundant in high concentrations in the stratosphere it absorbs incoming short wave (solar) radiation, heating the stratosphere and protecting life on earth by preventing the deeper penetration of harmful ultraviolet (UV) radiation. Radiation of UV wavelengths can strongly affect life on earth. In the troposphere ozone is harmful for humans and ecosystems if present in high concentrations. The so-called 'summer-smog' has recently provoked political consequences in some countries.

Since most gases can interact, a change in the concentration of one trace gas can lead to changes in the concentrations of other species, showing an effect on climate that is not directly predictable from the initial concentration change. An important goal of atmospheric science is to understand these interactions and feedback mechanisms to be able to assess the impact of changes in atmospheric composition on the weather and climate, e.g., caused by anthropogenic emissions, volcanic eruptions and desert storms. Recently atmospheric science has reached a dimension of societal importance, and the control of emission of specific gases requires international agreements, as was accomplished in banning the chlorofluorocarbons (CFCs).

In addition to trace gases, aerosols, microscopic, air-borne and sometimes humidified particles such as pollen, sea salt or sulphate particles, are also known to influence climate. They scatter the incoming and outgoing radiation, affecting the energy budget of the atmosphere. Furthermore, they take up and release atmospheric gases. Aerosols act as cloud condensation nuclei (CCN) and without them cloud formation could not take place. The number of CCN determines the formation, microphysics and chemical composition of a cloud, which in turn influences the radiation budget (by scattering and reflection) and

the chemical composition of the atmosphere (e.g. by scavenging of trace gases into the droplets).

In this study one special part of the complex atmospheric system dealing with gas and aerosol interactions is addressed: sea salt aerosol emitted from the sea is a source of reactive halogen species (e.g. Br_2 and BrCl). Their release from the aerosol and subsequent photolysis enhances the oxidising capacity of the atmosphere. Furthermore the bromine radicals efficiently destroy ozone, impacting the ozone chemistry in the troposphere to a significant degree.

In this work the first study is presented, in which halogen chemistry in the marine boundary layer (MBL) is evaluated with a fully prognostic global model. The prognostic calculation is twofold. Firstly, the release of halogens from the aerosol and their recycling is explicitly simulated by an aerosol phase chemistry mechanism. Secondly, the aerosol distribution as prerequisite for the aerosol phase chemistry is prognostically calculated by an aerosol model. Until now, only one of these two key aspects of MBL chemistry has been addressed within one model. On the one hand some box and column model studies have been performed with a very detailed gas and aerosol halogen chemistry mechanism. On the other hand, only a few global studies of halogen chemistry have been carried out so far, all of them using coarse parameterisations of the halogen release process.

Some box models include very detailed aerosol chemistry. They have been widely used to study halogen chemistry and its influence on other species in many different situations. The work of Sander and Crutzen (1996) was the first of a series of studies using the box Model Of Chemistry Considering Aerosols (MOCCA[1]). They examined the importance of chlorine and bromine chemistry in polluted air masses and found that the aerosol is a significant sink for NO_3 and N_2O_5. Furthermore they pointed out the importance of a catalytic Br chain reaction leading to significant ozone loss and to the pH dependency of the bromine activation reactions (for more details about the chemistry reactions see Chapter 2). In another box model study Sander et al. (1999) evaluated the importance of heterogeneous reactions of $BrNO_3$ for marine tropospheric chemistry. They found that the influence of $BrNO_3$ is fourfold. Firstly, the transfer of NO_x (= NO + NO_2) to the aerosol is accelerated. Secondly, the bromide and chloride loss from the sea salt aerosol is enhanced. This dehalogenation takes place without the consumption of acidity of the aerosol. Thirdly, the enhanced uptake of NO_x and the increase in gas phase bromine species lead to additional ozone destruction and fourthly, the increase of reactive chlorine affects the gas phase hydrocarbons as well as the S(IV) oxidation by HOCl in the sea salt aerosol.

Vogt et al. (1996) were the first to propose the autocatalytic mechanism for halogen release from sea salt aerosol in clean air masses at mid-latitudes. This is coupled to enhanced S(IV) oxidation within the aerosol and significant gas phase ozone loss. Vogt et al. (1999) published a box model study mostly dealing with iodine chemistry. For this they extended the MOCCA box model by the most important iodine reactions. They emphasised the possibility that sea salt aerosol is not necessarily a permanent sink for iodine compounds by scavenging the highly soluble gases HOI, HI, INO_2 and INO_3. Iodine can be released back to the gas phase by the formation of relatively insoluble species such as IBr, ICl and I_2. In their study most of the particulate iodine was in the form of iodate (IO_3^-). In addition, some further model studies on the importance of iodine have been performed (Chameides and Davis, 1980; Jenkin et al., 1985; Chatfield and Crutzen,

[1] by R. Sander, see *http://www.mpch-mainz.mpg.de/~sander/mocca*

1990; Solomon et al., 1994; Davis et al., 1996). These are not be reviewed in more detail, because the present study focuses on bromine and chlorine chemistry. Toyota et al. (2001) presented a study with the box model SEAMAC (size-SEgregated Aerosol model of the Marine Air Chemistry). In addition to a chemistry mechanism similar to MOCCA, SEAMAC includes a size-segregated (eight bin) description of the aerosol distribution. Toyota et al. (2001) compared this size dependent approach to a bulk approach and found that the chemistry simulated by the bulk model overestimates the gas phase bromine mixing ratios, because it does not capture the decreased volatilisation rates of bromine from the small particles caused by the rapid depletion of bromide. The SEAMAC model was also used to investigate the interactions between VOCs (Volatile Organic Compounds) and reactive halogen species in the MBL (Toyota et al., 2004). It was shown that CH_3CHO and alkenes of oceanic origin strongly impede the autocatalytic halogen release from sea salt aerosol to the remote MBL. Mixing ratios of brominated compounds, which were produced in this way, are likely to reach 10-20% or more of the inorganic bromine species over wide regions over the ocean.

The box model studies mentioned above were not linked to measured data. Nevertheless, box models are also used to simulate and explain data obtained at measurement campaigns. For instance Wagner et al. (2002) investigated the formaldehyde budget during the INDian Ocean EXperiment (INDOEX) campaign 1999. To evaluate the contributions of methane and non-methane volatile organic compounds, they applied the MOCCA box model. In a sensitivity study they prescribed different gas phase concentrations of BrO and Cl radicals to evaluate the impact of halogens on the formaldehyde budget. They found that a change in BrO mixing ratios does not influence the HCHO budget at all. An increase in the Cl radical concentrations to more than 10^5 atoms/cm^3 leads to an increase in the formaldehyde mixing ratios. Pszenny et al. (2004) used the box model MOCCA to simulate a more detailed chemistry for their measured data at Oahu, Hawaii 1999. Because some of the methods applied do not measure each single species but groups as total inorganic bromine, or HCl^* (primary HCl) and Cl^* (including Cl_2 and HOCl), the model was applied to help analysing the measurements. For example for Cl^* no diurnal cycle was measured. The model study showed diurnal cycles of individual components, but no diurnal cycle for the sum of these components, in agreement with the measurements.

Von Glasow et al. (2002) expanded the halogen chemistry calculations by one dimension to resolve halogen chemistry throughout the MBL height, by extending the microphysical column model MISTRA (Bott et al., 1996; Bott, 1997) by the chemistry scheme of MOCCA. Von Glasow et al. (2002) showed in their study many interactions between halogens and other species, which could have been modelled also in a box model. In addition they evaluated the vertical profiles of the species within the inversion topped boundary layer. For example, they found that the BrO mixing ratio increases from the ocean's surface up to the boundary layer top and rapidly vanishes aloft. The BrO profile is directly coupled to the aerosol pH, which is decreasing and thus accelerating bromine release with height.

Box models as well as column models are always restricted to more or less 'ideal conditions'. Here 'ideal' refers to the fact that many interactions occurring in reality can not be modelled with a box or column model due to the limited domain. For example, horizontal transport is neglected in box and column models. The vertical transport can not be calculated within a box model and in a cloumn model only up to the height covered by the model, which is often below the top of the atmosphere or even below the tropopause. Thus variation of the incoming radiation due to clouds above the model

domain as well as the impact of cloud chemistry in a higher part of the atmosphere can not be modelled in models with such limited domains. Thus the desire has grown to model halogen chemistry in global models which cover much larger domains. As halogen chemistry mechanisms as well as global models are computationally expensive, it was not possible to perform such simulations for a period of a year or more. Along with the increasing computer power, two simplified global halogen chemistry model studies have been performed recently. First, to investigate the influence of bromine chemistry on ozone in the free troposphere, von Glasow et al. (2004) carried out a global model study with the chemistry transport model (CTM) MATCH (Model of Atmospheric Transport and CHemistry). To reduce computational costs, they applied a very coarse resolution (T10) and omitted the aerosol phase chemistry and the bromine release mechanism. Instead they prescribed fluxes of organic or inorganic bromine being transported upward from the boundary layer or descending from the stratosphere, respectively. These fluxes have been chosen in a way that BrO mixing ratios are abundant in the free troposphere from a few tenths to 2 pmol/mol. Von Glasow et al. (2004) found large influence even for small BrO mixing ratios on ozone, up to 18% less O_3 in widespread areas and locally even up to 40%.

The second global model study was performed by Xin Yang (pers. comm., University of Cambridge), with the CTM TOMCAT[2]. He also did not simulate the aerosol phase chemistry explicitly. But as an improvement in comparison to the study of von Glasow et al. (2004), he determined the source of bromine to the gas phase in a 'semi-prognostically' way. The sea salt emission flux is prognostically calculated (Monahan, 1986) and the source of bromine to the gas phase is determined by a rough parameterisation of the bromine release from the aerosol. For this he prescribes an enrichment factor to all freshly emitted sea salt, i.e. he assumes that some of the bromine abundant in the freshly emitted aerosol is instantaneously released to the gas phase. This is a very coarse parameterisation as the enrichment factor depends on many environmental conditions (e.g. acid supply or cloud evaporation). He justifies this approach based on the review of Sander et al. (2003a), who stated that the global average enrichment factor of bromide derived from available measurements is about 0.5. These are the only global model studies performed so far. As explained above, they are both dealing with more or less simplified parameterisations to model the gas phase source of bromine. Thus until now no study with an explicit calculation of the halogen release to the gas phase has been carried out.

In this study results are presented of the first attempt to model this process explicitly in a global model. For this the halogen gas and aerosol phase chemistry mechanism as used by von Glasow et al. (2002) was adopted for three dimensional simulations. An additional improvement to both of the aforementioned global models is that in this study a general circulation model (GCM) is applied, instead of CTMs as in the other two evaluations. The advantage is that with GCMs the meteorological processes are explicitly simulated at relatively high time resolution, whereas CTMs adopt offline calculated meteorological data to simulate transport based on 6-hourly averages.

In the next chapter an overview of the current knowledge of halogen chemistry is given. Chapter 3 introduces the models applied in this study. The results of the simulations are shown and discussed in Chapter 4 and Chapter 5, respectively. Chapter 6 summarises the conclusions. The meanings of acronyms are listed in Appendix A. Appendix B shows the variables used in the formulas and their units.

[2] *http://www.env.leeds.ac.uk/~martyn/slimcat.html*

Chapter 2

Halogen Chemistry - An Overview

Throughout the past decades evidence has accumulated that halogen chemistry can significantly influence atmospheric chemistry. The first time that processes related to halogens reached international attention was the discovery of chemical reactions which cause stratospheric ozone destruction. Molina and Rowland (1974) were the first who pointed out the impact of chlorofluorocarbons (CFC) within this process.

The production of chlorine radicals via the photolysis of chlorofluorocarbons

$$\mathrm{CFC} + h\nu \quad \rightarrow \quad \mathrm{Cl}\cdot + \mathrm{CFC}\cdot$$

leads to the initiation of a catalytic ozone destruction cycle (Solomon, 1990):

$$\begin{aligned} 2\ (\mathrm{Cl} + \mathrm{O_3}) &\rightarrow 2(\mathrm{ClO} + \mathrm{O_2}) \\ \mathrm{ClO} + \mathrm{ClO} + \mathrm{M} &\rightarrow \mathrm{Cl_2O_2} + \mathrm{M} \\ \mathrm{Cl_2O_2} + h\nu &\rightarrow \mathrm{Cl} + \mathrm{ClO_2} \\ \mathrm{ClO_2} + \mathrm{M} &\rightarrow \mathrm{Cl} + \mathrm{O_2} \\ \hline \textbf{Cycle I}\ \text{net} : 2\mathrm{O_3} + h\nu &\rightarrow 3\mathrm{O_2} \quad . \end{aligned}$$

The Cl radicals react with ozone to yield chlorine oxide and oxygen. In a self-reaction the dimer Cl_2O_2 is formed, which is subsequently broken down by photolysis and collision with air molecules (M) to yield back the two chlorine radicals. Thus within one cycle two ozone molecules are destroyed. Bromine is also able to contribute to ozone destruction. In this case no ClO dimer has to be formed which is the rate limiting step in Cycle I.

$$\begin{aligned} \mathrm{Cl} + \mathrm{O_3} &\rightarrow \mathrm{ClO} + \mathrm{O_2} \\ \mathrm{Br} + \mathrm{O_3} &\rightarrow \mathrm{BrO} + \mathrm{O_2} \\ \mathrm{ClO} + \mathrm{BrO} + \mathrm{M} &\rightarrow \mathrm{Br} + \mathrm{ClO_2} \\ \mathrm{ClO_2} + \mathrm{M} &\rightarrow \mathrm{Cl} + \mathrm{O_2} \\ \hline \textbf{Cycle II}\ \text{net} : 2\mathrm{O_3} + \mathrm{M} &\rightarrow 3\mathrm{O_2} \quad . \end{aligned}$$

All these halogen species taking part in the rapid ozone destruction cycles are generally referred to as the group of reactive halogen species (RHS). This group includes X, X_2, XY, XO, OXO, HOX, XNO_2 and XNO_3, where X, Y denote Cl and Br (and possibly I).

After the destruction of ozone by halogen oxides in the stratosphere was internationally recognised, other researchers found an almost complete depletion of ozone in the Arctic troposphere in early spring (Barrie et al., 1988; Solberg et al., 1996; McElroy et al., 1999; Hönninger and Platt, 2002; Platt and Hönninger, 2003). These events are similar to the stratospheric ozone hole, initiated by photolysis of halogen species by the first light in spring. However, the subsequent ozone destruction cycles differ considerably. The ozone depletion events in the polar troposphere usually last for a few days, during which the ozone is completely destroyed within a layer of a few hundred meters depth over areas of several million square meters. A positive correlation of high BrO mixing ratios (around 30 pmol/mol) and total ozone destruction (about 30-40 nmol/mol ozone within one or two days) has been observed during these events (Wagner and Platt, 1998; Hönninger and Platt, 2002; Platt and Hönninger, 2003). These Arctic events have been the first hint that halogen chemistry is of some importance also in the lowest part of the atmosphere.

Nagao et al. (1999) reported the observation of two different ozone depletion events in the sub-tropical marine boundary layer (MBL) over the North Pacific. In addition to the DOD (Daytime Ozone Destruction) event associated with UV photolysis and subsequent HO_x reactions, a Sunrise Ozone Destruction (SOD) was observed. They were the first who associated observed ozone destruction with bromine chemistry, so far only known to be relevant in the Arctic or proposed to be important in the mid-latitudes based on model studies. Nagao et al. (1999) assumed that the observed SOD is likely to take place via

$$\mathrm{Br} + \mathrm{O_3} \quad \rightarrow \quad \mathrm{BrO} + \mathrm{O_2} \quad ,$$

because Br containing gases, which escape from sea salt aerosol, accumulate during night and are rapidly photolysed to Br radicals after sunrise. This was one of the first observations that seemed to manifest the importance of bromine chemistry in the MBL. The main source of halogens in the troposphere is the release from sea salt aerosol. Therefore halogen chemistry should be most active over the open ocean and globally impact chemistry and climate because the oceans cover more than 70% of the earth's surface. A second important source over the oceans is the degradation of halocarbons by photolysis. Their largest natural source is the production by algae and phytoplankton. Additional (local and thus minor) sources of halogens in the troposphere do exist: BrO was detected in volcanic plumes by Bobrowski et al. (2003). Other natural sources are biomass burning, degradation of organic matter and some biological processes involving fungi. Anthropogenic sources include fossil fuel combustion, where leaded petrol is a major source of brominated compounds, and the use of CFCs. Their replacements, the hydrochlorofluorocarbons (HCFC) are less photostable and therefore potentially larger halogen sources for the troposphere as the CFCs. Because halogen chemistry often competes with other (in atmospheric research well established) reaction pathways, accounting for halogen chemistry may lead to a new understanding of the importance of specific reactions. A short review of the current knowledge of processes and reactions related to halogen chemistry is given in this chapter. Only processes involving the halogens chlorine, bromine and iodine are addressed, because the very unreactive HF is efficiently formed in the troposphere via

$$\mathrm{F} + \mathrm{H_2O} \quad \rightarrow \quad \mathrm{HF} + \mathrm{OH} \quad ,$$

thus making fluorine chemistry unimportant for detailed tropospheric chemistry investigations. Of course HF is a powerful greenhouse gas and may therefore be relevant for climate change studies, but it has no effect on the reaction mechanisms described here. Thus fluorine is neglected in the following.

2.0.1 Aerosols

The investigation of halogen chemistry in the mid-latitude and tropical MBL is not possible without the consideration of aerosols. Firstly, sea salt aerosol is the main source of chlorine and bromine over the ocean and secondly, the aerosol particles themselves provide a surface for additional halogen recycling as is pointed out in detail later. Thus aerosols may be called 'the driving force' of halogen chemistry in the MBL. Because of their importance for the processes involved a short overview of aerosol distributions and compositions in the MBL is given here.

Usually the aerosol spectrum is divided into three or four size ranges, i.e. modes. The smallest one, the nucleation mode, includes particles smaller than 5 nm. They consist mainly of sulphate as they are freshly nucleated and the main precursor gas for particle nucleation is sulphuric acid. Particles larger than 5 nm but smaller than approximately 50 nm are called 'Aitken mode' particles. They consist mostly of sulphate as well as organic and black carbon. This and the next larger mode (the so-called 'accumulation mode', that includes particles up to a radius of 500 nm) are often treated as one mode. The largest particles are contained in the 'coarse mode', which includes all particles larger than 500 nm and is mainly composed of sea salt and mineral dust.

For halogen chemistry over the remote ocean, which is the focus of this study, the accumulation mode and the coarse mode are of main interest. Over the ocean the accumulation mode mainly consists of sulphur species, apart from some organic matter which originates from algae and phytoplankton. Therefore this mode is henceforth referred to as 'sulphate aerosol'. The coarse mode comprises mainly sea salt, which is the dominant source of halogens over the remote ocean. This mode is called 'sea salt aerosol'. The two modes are of different origin and because of their distinct chemical composition their chemical behaviour also differs. Both are described in the following subsections.

Sulphate Aerosol

The sulphate aerosol is dominant by number over the remote ocean. The origin of sulphate aerosol is basically nucleation of sulphuric acid to new particles and subsequent growth by condensation of SO_2, H_2SO_4, and (in polluted regions) HNO_3 on existing particles. The major source of sulphur in the gas phase of the MBL is dimethyl sulphide (DMS) production by phytoplankton in the ocean, subsequently released to the atmosphere. DMS is oxidised by OH, NO_3 and Cl to form mostly SO_2, which is directly taken up by existing particles or oxidised by OH to form H_2SO_4 which is taken up by particles or produces new particles via nucleation. In air masses of continental and/or anthropogenic origin additional sources of sulphur are dominant. Advection of sulphur dioxide containing plumes originating from e.g. biomass burning or urban and industrial outflow may also contribute to the formation of new and the growth of existing particles. Submicron marine aerosol typically consists of an internal mixture of NH_4HSO_4, $(NH_4)_2SO_4$ and H_2SO_4. In polluted areas NH_4NO_3 is also part of this mixture.

Sulphate aerosol has an atmospheric lifetime of approximately one week, which is relatively long in comparison to the other aerosol size classes. Smaller aerosols are often scavenged by larger aerosols, called coagulation, and they grow rapidly and enter the accumulation mode size range. Larger aerosols are more rapidly deposited or sedimented because of their larger mass. Due to its relatively long lifetime sulphate aerosol accumulates in the boundary layer and thus dominates the overall aerosol distribution by number.

Sea Salt Aerosol

In contrast to sulphate aerosol, sea salt aerosol dominates the aerosol distribution by mass. As stated above, the lifetime of sea salt aerosol is mainly determined by its size. The removal processes like sedimentation, dry deposition and wet deposition are much more efficient for sea salt than for sulphate aerosol, limiting the lifetime of sea salt aerosol to approximately two days (Sander and Crutzen, 1996).

The only source of sea salt aerosol is the ocean. Due to wave action caused by surface winds, droplets of ocean water become air-borne. Two mechanisms of sea salt production prevail. Firstly, air bubbles that have been entrained from the atmosphere into the wave crest burst, producing small droplets from the water film (that has been between the air bubble and the atmosphere). Secondly, larger droplets are produced if stronger winds blow over the wave crest producing the so-called 'sea spray'. For more details see Pruppacher and Klett (1997).

The largest droplets usually quickly sediment back to the ocean whereas the smaller particles remain and equilibrate with the environmental air. The sea water pH is around 8 (Keene et al., 1998). The aerosols equilibrate rapidly with the ambient moisture, thus the ionic strength increases with decreasing radius. This leads to a slight increase in pH. Condensation of gaseous acids (e.g. H_2SO_4 or HNO_3) onto the aerosol reduces the pH. The number concentration of air-borne sea salt particles depends on the wind speed. The higher the wind speed, the higher the aerosol production, yielding more and larger air-borne particles. The concentrations of the components of freshly emitted sea salt aerosol particles are most probably the same as in sea water. Sea salt approximately contains by weight 55.7% Cl, 0.19% Br and 0.00002% I (Platt and Janssen, 1995). Although lower in abundance, bromine is a much more reactive species in the troposphere than chlorine, e.g. in catalysing the ozone destruction.

2.0.2 Chlorine and Bromine Chemistry

The dominant source of chlorine and bromine in the MBL is sea salt aerosol. But apart from having the same source, the release mechanisms differ for these two species.

Acid displacement is the major process leading to chlorine release from aerosol into the gas phase. Strong acids like H_2SO_4 are scavenged by the aerosol. In the humidified aerosol at low pH the acid reacts with sodium chloride to produce hydrochloric acid which is released to the gas phase because of its low solubility:

$$\begin{aligned} H_2SO_4(g) &\rightarrow H_2SO_4(aq) \\ H_2SO_4 + 2NaCl &\rightarrow 2HCl + Na_2SO_4 \\ 2HCl(aq) &\rightarrow 2HCl(g) \\ \hline \text{net} : H_2SO_4(g) + 2NaCl(aq) &\rightarrow 2HCl(g) + Na_2SO_4(aq)\ . \end{aligned} \tag{2.1}$$

HNO_3 and methanesulphonic acid (MSA) can also react with NaCl, similar as H_2SO_4 in Reactions 2.1. One special aspect of acid displacement is, that the uptake of one molecule of diprotonated acid (H_2SO_4) is followed by the release of two molecules of monoprotonated acids (HCl). Thus the occurrence of Cl^- in the aerosol buffers the aerosol pH to a significant degree.

HBr is much more soluble than HCl. Therefore the mechanism of bromine release is different: HOBr is scavenged from the gas phase. It reacts in the aqueous phase with H^+

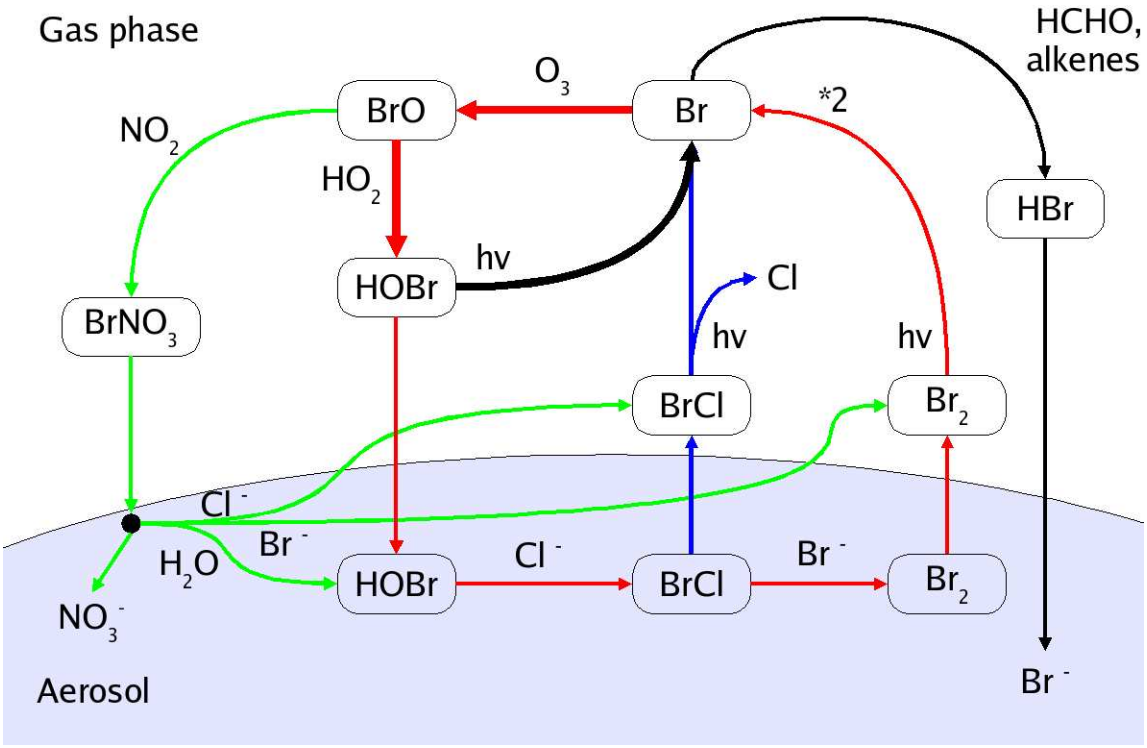

Figure 2.1: The most important bromine reactions in the gas and aerosol phase (from Sander et al., 2003a). Bold arrows denote the ozone destruction cycle, red arrows the autocatalytic bromine release cycle, blue ones the branch setting free Cl atoms and green arrows the NO_x chemistry important in polluted areas.

and a bromide ion to produce water and Br_2. This is only slightly soluble and promptly degases. During daytime Br_2 is rapidly photolysed into bromine radicals which react with ozone to yield BrO and oxygen. BrO further reacts with HO_2 to produce HOBr being highly soluble and entering the aerosol phase to continue the cycle:

$$\begin{aligned}
\mathrm{HOBr(g)} &\rightarrow \mathrm{HOBr(aq)} \\
\mathrm{HOBr(aq) + H^+ + Br^-} &\rightarrow \mathrm{H_2O + Br_2} \qquad (2.2)\\
\mathrm{Br_2(aq)} &\rightarrow \mathrm{Br_2(g)} \\
\mathrm{Br_2 + } h\nu &\rightarrow \mathrm{Br + Br} \\
\mathrm{Br + O_3} &\rightarrow \mathrm{BrO + O_2} \\
\mathrm{BrO + HO_2} &\rightarrow \mathrm{HOBr + O_2}
\end{aligned}$$

$$\textbf{Cycle III net}: \mathrm{O_3 + HO_2 + H^+ + Br^-} \rightarrow \mathrm{Br + 2\ O_2 + H_2O}\ .$$

For every bromine radical reacting with ozone two new bromine radicals are produced by release from the aerosol phase and subsequent photolysis. This gives rise to a rapidly ozone destroying autocatalytic bromine release cycle. This mechanism can actually lead to a 'bromine explosion'. The importance of this reaction chain is limited to acidified aerosol (pH < 6.5). Cycle III is acid-catalysed (Reaction 2.2), but this dependence is weaker than that of chlorine release via acid displacement, requiring pH values lower than

5. Figure 2.1 shows the main reaction paths of bromine in the gas and aerosol phase. Cycle III is indicated with red arrows. The major differences between the chlorine and the bromine release mechanisms are the products released to the gas phase. HCl is a relatively unreactive species in comparison to Br_2 (a RHS). HCl reacts mainly with hydrocarbons and is efficiently removed by deposition processes, whereas Br_2 is rapidly photochemically transformed to highly reactive Br radicals leading to many subsequent reactions.

Sulphate and sea salt aerosol are different types of sources for reactive bromine and chlorine. Due to its composition sea salt aerosol is a primary source of chlorine and bromine, whereas sulphate aerosol takes up halogens from the gas phase, which are subsequently processed by the above described mechanism and released back into the gas phase, triggered by the low pH of the sulphate aerosol. Thus sulphate aerosol plays an important role as a recycling surface area for halogen chemistry and accelerates the catalytic cycles once halogen containing species are condensed onto the sulphate aerosol. Vogt et al. (1996) showed that the magnitude of bromine recycling is higher if sulphate aerosol is considered.

Bromine as well as chlorine degassing leads to a deficit of the respective halogen in the aerosol phase in comparison to fresh sea salt. A dimensionless measure for the effectiveness of this process is given by the enrichment factor of $EF(X^-)$, with X^- =[Cl^-, Br^-], defined as follows:

$$EF(X^-) \quad = \quad \frac{[X^-]}{[Na^+]} \Big/ \frac{[X^-]_{sea}}{[Na^+]_{sea}} \quad . \tag{2.3}$$

$[X^-]$ is the concentration of X^-, the subscript 'sea' denotes the concentrations in sea water. The enrichment factor equals 1 if the concentration of the respective halide is the same as in sea water. It is larger than one if chloride or bromide are enriched in the aerosol and smaller than one if they are depleted. In the literature often *depletions* and not enrichment factors are reported. The simple relationship is

$$depletion \quad = \quad 1 - EF \quad . \tag{2.4}$$

The degree of depletion in chlorine depends very strongly on the acidity of the aerosol. Above a pH of 3 to 4 no depletions are detectable. The more the pH decreases the more outgassing of HCl takes place. Vogt et al. (1996) found in a box model study that for clean air after 2 days only 1% of the chlorine was depleted. The deficits depend very strongly on the amount of acids available to condense on the particles. Sander and Crutzen (1996) found in a box model study for polluted air conditions depletions of up to 75%. These are confirmed by Erickson III et al. (1999) who reported a similar value in pristine environment for a global model study. They found that the deficits are largest in the submicrometer aerosol. Their small surface-to-volume ratio allows small aerosol particles to be acidified more rapidly because the transferred amount of condensing gases into a distinct volume is faster than for sea salt aerosols.

The aerosol is much more rapidly depleted in bromine than in chlorine, because the bromine release cycle does not depend as much on acidity as chlorine release and many reactions are faster for bromine than for chlorine. Vogt et al. (1996) found in their model study a bromine depletion of about 90%. Keene et al. (1998) investigated in a model study the dependence of depletion on aerosol pH. They found for pH values of 3, 5.5 and 8 deficits of about $> 99\%$, 98% and only 6%, respectively. Ayers et al. (1999) observed similar deficits. Sander et al. (2003a) reviewed measurements of bromine depletions and found a strong particle radius dependence. Particles in the medium size range of a few

μm are usually depleted in bromine as the bromine activation cycle is dominant for these particles. For very small particles an enrichment in bromine was found which is not yet explained. Because of their short lifetime (due to sedimentation) very large particles are almost around $EF(Br^-) = 1$, as on this short time scale the depletion mechanism is not efficient.

The different activation mechanisms are responsible for the fact that bromine is released more easily into the atmosphere than chlorine. This is notable, particularly since in fresh aerosol the Br:Cl molar ratio is only 1:650.

Cycle III gives only the overall effect of bromine cycling. Because chloride is much more abundant in the aerosol, Reaction 2.2 is likely to proceed in more steps:

$$\begin{aligned} HOBr(aq) + H^+ + Cl^- &\rightarrow H_2O + BrCl \\ BrCl + Br^- &\rightleftharpoons Br_2Cl^- \\ Br_2Cl^- &\rightarrow Br_2 + Cl^- \quad . \end{aligned}$$

Only after bromine is already strongly depleted, BrCl can significantly degas from the aerosol phase (see blue arrows in Figure 2.1):

$$BrCl(aq) \rightarrow BrCl(g) \tag{2.5}$$

$$BrCl + h\nu \rightarrow Br + Cl \quad . \tag{2.6}$$

It should be stressed that in this case chlorine is also released in form of RHS. But atomic Cl in the MBL reacts mostly with hydrocarbons to yield the relatively inert HCl (Keene et al., 1998). The corresponding reaction of Br radicals with alkanes (see black arrows in Figure 2.1) is much slower than for Cl radicals. The HBr produced is much more soluble than HCl, thus Reactions 2.5 and 2.6 are a source of gaseous HCl but not of HBr. The main effect of reactive chlorine in the MBL is the breakdown of hydrocarbons, whereas that of reactive bromine is mainly ozone destruction. In both cases this impacts the oxidising capacity of the atmosphere. Additionally, von Glasow et al. (2002) showed in their model simulation that significant chlorine activation is dependent on interaction with bromine. Their simulation without bromine chemistry but with chlorine chemistry gave the same results as the simulation without halogens.

As shown in the introduction of this chapter, halogen chemistry arouses scientific interest because of interaction of halogens with other atmospheric chemistry cycles that are often thought to be well understood without the accounting for halogen chemistry. In the following the effects of halogen chemistry on ozone and on sulphur cycles are briefly reviewed.

The two main ozone loss processes discussed in the literature are firstly ozone destruction via photolysis and subsequent reaction with water vapour

$$\begin{aligned} O_3 + h\nu &\rightarrow O(^1D) + O_2 \\ O(^1D) + H_2O &\rightarrow 2OH \end{aligned}$$

and secondly via reaction of ozone with HO_2

$$O_3 + HO_2 \rightarrow OH + 2O_2 \quad .$$

These are not the only efficient mechanisms as investigated by recent model studies (Sander and Crutzen, 1996; Vogt et al., 1999; von Glasow et al., 2002). Each cycle of bromine

activation destroys one ozone molecule (Cycle III), as every iteration of the cycle produces two Br radicals while only one Br radical is consumed, obviously forming an autocatalytic ozone destruction cycle.

There are two additional cycles destroying ozone which, in contrast to Cycle III, proceed in the gas phase only. At low BrO concentrations the reaction of BrO with HO_2 is the faster propagating step resulting in Cycle IV (see bold arrows in Figure 2.1):

$$\begin{aligned} \mathrm{Br} + \mathrm{O_3} &\rightarrow \mathrm{BrO} + \mathrm{O_2} \\ \mathrm{BrO} + \mathrm{HO_2} &\rightarrow \mathrm{HOBr} + \mathrm{O_2} \\ \mathrm{HOBr} + h\nu &\rightarrow \mathrm{Br} + \mathrm{OH} \\ \mathrm{OH} + \mathrm{CO}(+\mathrm{O_2}) &\rightarrow \mathrm{HO_2} + \mathrm{CO_2} \\ \hline \textbf{Cycle IV}\ \text{net}: \mathrm{O_3} + \mathrm{CO} &\rightarrow \mathrm{O_2} + \mathrm{CO_2}\ , \end{aligned}$$

whereas at high BrO mixing ratios the self-reaction of BrO becomes relevant:

$$\begin{aligned} 2\,\mathrm{Br} + 2\,\mathrm{O_3} &\rightarrow 2\,\mathrm{BrO} + 2\,\mathrm{O_2} \\ \mathrm{BrO} + \mathrm{BrO} &\rightarrow 2\,\mathrm{Br} + \mathrm{O_2} \\ \hline \textbf{Cycle V}\ \text{net}: 2\,\mathrm{O_3} &\rightarrow 3\,\mathrm{O_2}\ . \end{aligned}$$

The reaction of BrO with ClO is four times faster than the BrO self-reaction, accelerating the ozone destruction if both halogen oxides are present in significant amounts. Arctic tropospheric ozone depletion events show how efficient this process can be (Hönninger and Platt, 2002; Platt and Hönninger, 2003). The autocatalytic process is not interrupted until all ozone is destroyed. These extreme events only happen at specific meteorological conditions during which exchange with the environment is suppressed. In the Arctic polar night bromine and chlorine containing gases are deposited on the ice shields. They are photolysed rapidly by the first sunlight in spring. This leads to very high concentrations of halogen radicals which destroy the ozone very efficiently. These high concentrations do normally not occur in the troposphere outside the polar regions, but the potential of this process is high enough to cause considerable ozone loss even in the mid-latitudes. This is underscored by two model studies which show the strong influence of halogens on ozone concentrations. In the first study A. Cox et al. (pers. comm.) modelled BrO chemistry with a very simplified approach, i.e. a parameterisation of the bromine chemistry in the aerosol. Their simulation indicates very high BrO mixing ratios and an ozone loss up to 40% (in the free troposphere) in comparison to the simulation without halogen chemistry. Von Glasow et al. (2004) performed a model study with the MATCH model (Model of Atmospheric Transport and CHemistry) utilising a prescribed aerosol distribution and found much higher ozone destruction in the simulation including halogens than without, even for small BrO mixing ratios. If these model results can be confirmed by further model studies and measurements, a 'new' (until now disregarded) ozone source for the troposphere may have to be found to explain the measured ozone mixing ratios.

Another area with similar importance for atmospheric chemistry and climate is the sulphur cycle. DMS (DiMethyl Sulphide), oxidation to SO_2 is the main precursor for sulphate aerosol over the oceans. The pathways of the oxidation mechanism determine the properties of the sulphate aerosol produced. Because sulphate aerosol acts as cloud condensation nuclei (CCN), it can influence the number and size of droplets forming clouds and therefore affect the cloud albedo and thus climate.

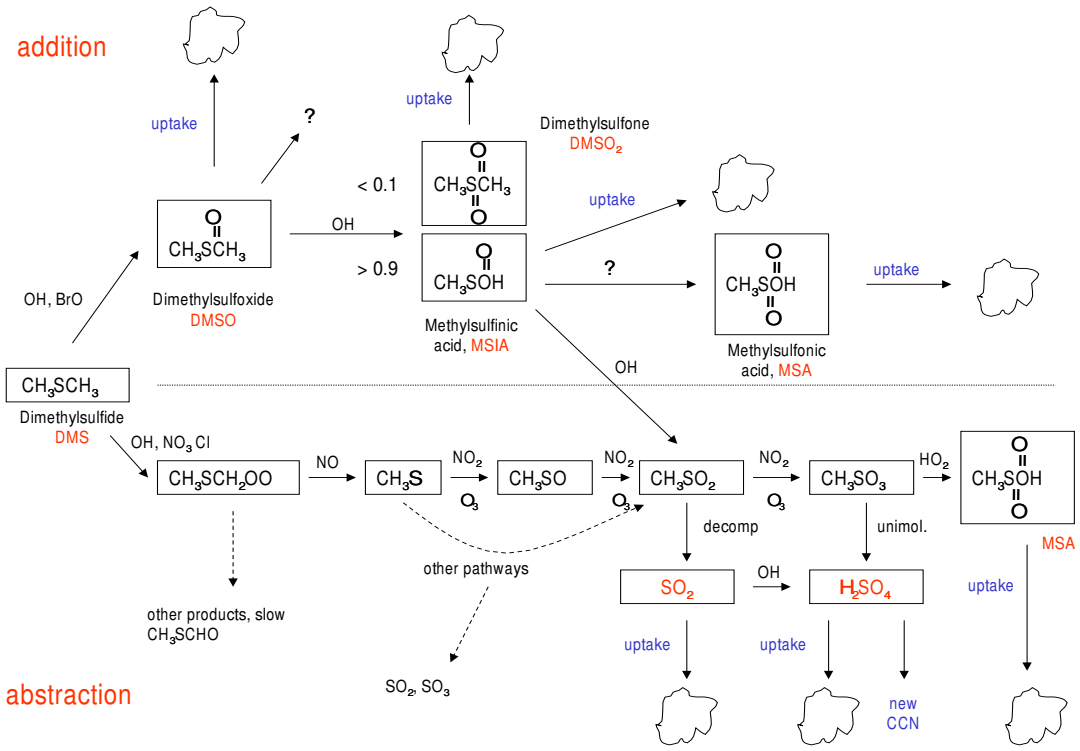

Figure 2.2: DMS oxidation scheme (von Glasow and Crutzen, 2004).

An evaluation of the impact of halogens on DMS oxidation was attempted by von Glasow and Crutzen (2004). They found that even at BrO mixing ratios lower than 0.5 pmol/mol the importance of the addition pathway (see Figure 2.2) strongly increases. It is uncertain how much this influences the particle formation, because the production yield of the reaction MSIA + OH (MSIA = Methyl SulphInic Acid) is still unknown. If only 5% would yield MSA (Methyl Sulphonic Acid), the gas phase production pathway would be dominant for MSA, implying that less SO_2 will be formed. Thus the condensation of sulphur species (in the form of MSA) on existing particles and therefore the growth of existing particles is favoured by this process instead of the nucleation of new sulphate aerosol particles. In the end this process counteracts the often discussed 'first anthropogenic indirect aerosol effect' (changing cloud albedo). In contrast to the anthropogenic effect, the enhanced uptake of sulphur on existing particles leads to a smaller number of relatively large CCN instead of the formation of new particles, which may cause a reduction in cloud albedo. During cloud formation this smaller number of large CCN results in larger droplets undergoing much more efficiently collision-coalescence und thus promoting a more efficient washout of particles, which reduces the lifetime of the cloud and thus again the global cloud albedo ('second indirect aerosol effect'). To summarise, the inclusion of halogen chemistry increases the rate of DMS oxidation, reduces the DMS to SO_2 conversion efficiency and favours the formation of additional particulate sulphate. In turn, this can counteract the often discussed 'first anthropogenic indirect aerosol effect'.

Halogen chemistry does not only influence the gas phase as well as the nucleation and growth of aerosol. The chemical reactions in the aerosol phase are also affected. Keene et al. (1998) studied the impact of the aerosol pH on S(IV) oxidation and found that

at a pH of 5.5 (which is a typical value in clean marine air masses) oxidation by HOCl dominates the S(VI) production in the aerosol phase. At a pH of 8 S(IV) + O_3 is the major sulphur oxidation pathway. At low pH values (smaller than 3) the S(VI) production slows down significantly because of the decreased solubility of SO_2. Keene et al. (1998) reported only the effect of HOCl on S(IV) oxidation without quantifying the relative importance of HOBr, even though they included HOBr into their study. Vogt et al. (1996) found the reactions

$$\begin{aligned} HOBr + SO_3^{2-} &\rightarrow HBr + SO_4^{2-} \\ HOBr + HSO_3^- &\rightarrow HBr + HSO_4^- \end{aligned}$$

to contribute 20% to the S(IV) oxidation.

The processes and their impact on other atmospheric chemistry cycles have been discussed only for clean marine air so far. In polluted air the NO_x chemistry[1] plays a dominant role. The heterogeneous reaction of gaseous N_2O_5 with the dissolved aerosol compounds sodium chloride or sodium bromide is of prime importance (Behnke et al., 1997; Schweitzer et al., 1998):

$$\begin{aligned} N_2O_5(g) + NaX(aq) &\rightarrow XNO_2(g) + NaNO_3 \\ XNO_2 + h\nu &\rightarrow X + NO_2 \end{aligned}$$

(with X = Cl, Br). In this reaction a nitryl halide is produced, which rapidly photolyses during daylight to yield an atomic halogen radical. This is the main path for halogen activation in polluted air masses. Additionally, it leads to dehalogenation of the aerosol without consuming acidity and may thus be able to deplete alkaline aerosol particles.

The halogen radical X usually reacts with ozone to halogen oxides, which in NO_x rich air are likely to react with NO_2 to form halogen nitrates:

$$XO + NO_2 \rightarrow XNO_3 \quad .$$

The main sink for halogen nitrates in the gas phase is photolysis or scavenging by aerosol particles (see green arrows in Figure 2.1). Thus halogen nitrates contribute to the denoxification of the gas phase, with $BrNO_3$ having the major effect, whereas the $ClNO_3$ has a negligible impact (Sander et al., 1999). The abundance of HNO_3 in the gas phase is an additional source of acidity for the aerosol phase (Keene et al., 1998):

$$HNO_3(g) \rightarrow H^+ + NO_3^- \quad . \tag{2.7}$$

However, the uptake of XNO_3

$$XNO_3(g) + H_2O \rightarrow HOX(aq) + H^+ + NO_3^- \tag{2.8}$$

does not lead to an acidification of sea salt aerosol because this reaction is immediately followed by

$$HOX + Y^- + H^+ \rightarrow XY + H_2O \quad , \tag{2.9}$$

[1] NO_x is the sum of the nitrogen oxides NO and NO_2

which consumes the H^+ provided by Reaction 2.8. Thus by Reactions 2.8 and 2.9 halides are substituted by nitrates. In the MBL Reaction 2.7 should be dominant in air masses containing photochemically aged pollutants (Keene et al., 1998). However by incorporation of nitrate into the aerosol with the help of halogens, an important additional removal mechanism for NO_x in moderately polluted air masses is found by the deposition and sedimentation of aerosol.

Photolysis is the dominant process driving the gas phase chemistry of reactive halogen species. Thus the concentrations of the different halogen species vary diurnally. X_2 and XY (with X,Y = Cl, Br or I) accumulate during the night in the gas phase. After sunrise they are photochemically destroyed and the autocatalytic destruction resumes. Br and BrO are detected in significant amounts during daytime with maxima at noon for Br and at sunrise and dawn for BrO. This behaviour is confirmed by the model study of von Glasow et al. (2002). The nighttime reservoir species reach maximum concentrations in the early morning hours before sunrise. The diurnal variation of BrO was measured amongst others by Matveev et al. (2001). However, according to the review of Sander et al. (2003a) the measurements reported so far show no consistent picture for bromine species. In some experiments there are diurnal variations whereas others show none. Thus no final statement can be given about diurnal variations.

The results of a 1D model study of von Glasow et al. (2002) predict maxima of BrO and acidity at the top of the boundary layer. To the authors knowledge there are no measurements available which could confirm this prediction about the vertical distribution of aerosol acidity and BrO.

The only marine bromine source mentioned so far is sea salt aerosol. However, there are additional sources in marine areas. Bromine is emitted in the form of bromocarbons by algae and phytoplankton. Measurements of significant concentrations of organo-bromines are reported in the literature (Matveev et al., 2001; Carpenter et al., 1999). The bromocarbons are relatively photostable (the photolytical lifetime of CH_3Br is of the order of one year (Yvon and Butler, 1996)) and their reaction with the hydroxyl radical is rather slow. The effective source strength of bromine in the MBL given by bromocarbons is negligibly small in comparison to sea salt, even if the absolute concentrations of bromocarbons are relatively high. The importance of bromocarbons increases with altitude. Due to the lower abundance or even absence of sea salt in the upper troposphere and stratosphere, respectively, the bromocarbons are the dominating source of bromine in these parts of the atmosphere.

Based on the conclusion that halogen chemistry can significantly influence tropospheric chemistry, widespread measurements of halogen containing compounds would be desirable. However, only little data of halogens measured in the gas phase are available, which is partly because of difficulties in finding an appropriate measurement technique. Due to the low concentrations measurements are rather difficult. Thus sometimes concentrations of groups of species are reported. Pszenny et al. (1993) and Pszenny et al. (2004) measured such group concentrations by mist chambers. They found for a group $HCl^\star$ (i.e. primary HCl and $ClNO_3$, $ClNO_2$ and NOCl) mixing ratios in the range of 30 to 250 pmol/mol and for $Cl^\star$ (Cl radicals, Cl_2 and any HOCl not trapped in an acidic mist chamber) between 6 and 38 pmol(Cl)/mol during a campaign at Hawaii, USA (Pszenny et al., 2004). At a measuring site at Virginia Key, Florida, USA the mixing ratios were 40 to 268 pmol/mol for the $HCl^\star$ group and $<$ 26 to 254 pmol(Cl)/mol for $Cl^\star$. Platt and Janssen (1995) reviewed hydrogen chlorine measurements, ranging from 0.1 up to 250 pmol/mol in the MBL (see references therein). ClO was measured by Stutz et al. (2002) at mixing ratios

of 15 pmol/mol at the Great Salt Lake, Utah, USA. Spicer et al. (1998) measured Cl_2 with an atmospheric pressure chemical ionisation tandem mass spectrometer at the coast of Long Island, New York, USA. The mixing ratios ranged from $<$ 10 to 150 pmol/mol. This is more than predicted by a model study of Vogt et al. (1996), who simulated steady state mixing ratios of 0.4 to 1.5 pmol/mol Cl_2. Spicer et al. (1998) observed a nighttime accumulation of Cl_2 (where mixing ratios of 40 to 150 pmol/mol were reached), which ceased after sunrise and dropped to values smaller than 15 pmol/mol. This agrees very well with the observations by Pszenny et al. (1993).

The most common method used for measurements of halogen oxides is DOAS (Differential Optical Absorption Spectroscopy). For a description of the DOAS instrument see Platt et al. (1979) and Carslaw et al. (1997a,b). But even for the DOAS instrument most of the ambient gas phase concentrations are below the detection limit. Sander et al. (2003a) listed measurements of BrO reported in the literature so far (see their Table 5). Mostly mixing ratios were below the detection limit. Some mixing ratios near the detection limit were reported by Allan (1998) and James et al. (2000) for a site at Mace Head, Ireland. They range between 0.3 and 2.5 pmol/mol. Leser et al. (2003) reported measurements of typical levels for the MBL of around 1.0 to 3.6 pmol/mol for a ship cruise from Bremerhaven, Germany to Cape Town, South Africa. A higher value of up to 6 pmol/mol was found by Stutz et al. (2002) over the Great Salt Lake, Utah, USA. Hebestreit et al. (1999) reported daily maxima of around 80 pmol/mol over the Dead Sea. For the same site Matveev et al. (2001) mentioned the highest mixing ratio ever measured in the troposphere so far of about 176 pmol/mol. It has to be kept in mind that the measurements at the salt lakes and the Dead Sea are not representative for the MBL. In summary, there are insufficient reliable measurements of individual bromine species for the MBL. Total gaseous bromine has been measured at different locations and typically reaches a few pmol/mol (Sander et al., 2003a).

Even though most of the attempts to measure reactive halogen species failed (because the detection limits of the instruments so far available are too high), one has to keep in mind that the upper limit given by the detection limit is in full agreement with model studies (von Glasow et al., 2002). As predicted by models, such concentrations are high enough to influence atmospheric chemistry (e.g. the ozone budget). Thus it is desirable to try to lower the detection limits of current instruments.

The measurements of concentrations within the aerosol phase are equally scarce. Ayers et al. (1999) found from measurements at Cape Grim and Macquarie Island, Australia very small Cl^- depletions, whereas the average enrichment factors (EF) for bromine ranged between 0.7 and 0.5 (Ayers et al. (1999) reported depletions of 30% to 50%), with a seasonality of high EFs in winter (approx. 0.9 (10%)) and small ones in sommer ($<$ 0.2 (80%)). Measurements of aerosol components are usually performed by cascade impactors as reported by Pszenny et al. (2004). Sievering et al. (1990) found for measurements at the U.S. east coast and at Bermuda, that in submicrometer aerosol the main displacing species of Cl^- is SO_4^{2-}, whereas for large aerosol NO_3^- contributes also a significant amount. Huebert et al. (1996) measured aerosol phase mixing ratios during the ASTEX/MAGE (Atlantic Stratocumulus Transition EXperiment/Marine Aerosol and Gas Exchange) experiment at Santa Maria, Azores, Portugal. They reported the following average aerosol phase mixing ratios for clean marine (and continental polluted) air masses in the boundary layer: MSA: 27 pmol/mol (36 pmol/mol), NO_3^-: 240 pmol/mol (1200 pmol/mol) , non-sea salt sulphate: 370 pmol/mol (1800 pmol/mol), and NH_4^+: 315 pmol/mol (2300 pmol/mol). Additionally, they confirmed that most ammonia and non-sea salt sulphate

was contained in submicrometer particles, whereas Na^+, Cl^- and NO_3^- are dominant in supermicrometer aerosol. Gabriel et al. (2002) found very high chlorine and bromine deficits in heavily polluted air masses during the INDOEX (INDian Ocean EXperiment) campaign. Whereas chlorine was depleted in all samples, for bromine some enrichments were found near the Indian coast. This effect is explained by the abundance of the fuel additive 1,2-dibromoethane in air masses containing automobile exhaust of cities like Bombay and Calcutta.

As mentioned above, many reactions in the aerosol phase depend on the aerosol pH (e.g. recycling of bromine via Equation 2.2 or S(IV) oxidation (Keene et al., 1998)). Thus the direct investigation of the aerosol pH is of great interest. As sea water has a pH of 8, sea salt is a source of alkalinity to the atmosphere. Fresh air-borne sea salt aerosol that evaporates to equilibrate with the surrounding air could reach a pH of around 10.5, if no simultaneous uptake of acids takes place. Normally, the particles are rapidly acidified by condensation of gaseous acids available in the atmosphere. The acidification is buffered by two mechanisms: firstly, fresh alkaline sea salt aerosol is buffered by HCO_3^- and secondly, in aged sea salt aerosol the acid displacement reaction of HCl provides a mechanism of pH buffering. Erickson III et al. (1999) found in a model study that sea salt particles of different sizes all equilibrated at the same pH, because the smallest particles were degassing HCl and thus maintaining constant pH, whereas the larger ones become acidified by scavenging HCl. Keene and Savoie (1998) observed the same behaviour during a field campaign at Bermuda during spring. Because bromine and chlorine activation is acid-catalysed, it is very important to know the pH of the aerosol. Thus investigation of aerosol pH is a very interesting aspect of research. But the aerosol pH is seldom determined directly. Pszenny et al. (2004) deduced it by means of thermodynamic data and measured HCl and Cl^- mixing ratios. They report a median pH of 5.1 for supermicrometer aerosol. This method is explained in detail by Keene and Savoie (1998), who found sea salt aerosol pH values ranging between 2 and 4 for moderately polluted air at Bermuda. Another technique is supported by modelling (Keene et al., 1998). Keene et al. (2002) measured pH directly with a modified Graseby-Anderson cascade impactor. These measurements took place in moderately polluted air at Bermuda during spring. They found that most of the acidity was provided by bisulphate in all aerosol size classes, and not only in the submicrometer aerosol. The smaller the aerosol the higher is the acidity. Thus submicrometer aerosol in moderately polluted air has a pH in the range of 1 to 3, whereas the sea salt pH ranges between 3 and > 5.3 (this was the upper limit for pH measurements with this instrument). Radius dependencies of pH were also found by Winkler (1980, 1986). He reports for the clean marine air over the North and South Atlantic pH values of 1 to 3 for submicrometer and of 7 to 8.7 for sea salt aerosol. Thus here the sea salt aerosol is alkaline in contrast to the measurements of Keene et al. (2002) where it was acidic, too. Thus the acidifying effect of polluted air on sea salt becomes obvious.

As stated by Keene et al. (1998), it is still an open question whether aged sea salt aerosol over the remote open ocean is still alkaline, neutral or acidic. Thus a lot of theories about the importance of chlorine and bromine chemistry have been developed on the basis of model studies which still lack the confirmation by measurements.

2.0.3 Iodine Chemistry

The most striking difference between chlorine and bromine chemistry on the one hand and iodine chemistry on the other hand is the source of the respective halogens. Whereas

Table 2.1: Measurements of iodocarbons. Note: Schwarz (2003) reports measurements at different sites near Dagebüll, Germany. The locations differ significantly as a function of the type of algae.

Compound	Region	Mixing Ratios [pmol/mol]		Reference
		mean	range	
CH_3I	Rishiri Island		0.6-2.3	Kanaya et al. (2002)
	Mace Head, Ireland	0.43	0.12-1.47	Carpenter et al. (1999)
	Spitzbergen	1.04	< 0.004-2.12	Schall and Heumann (1993)
	Dagebüll 2001	4.92	2.1-11.2	Schwarz (2003)
	Dagebüll 2002/1	12.95	4.7-23.5	Schwarz (2003)
	Dagebüll 2002/2	16.76	9.0-40.8	Schwarz (2003)
CH_2I_2	Rishiri Island		< 0.3	Kanaya et al. (2002)
	Mace Head, Ireland	0.05	< 0.02-0.36	Carpenter et al. (1999)
	Spitzbergen	0.46	< 0.08-1.02	Schall and Heumann (1993)
	Dagebüll 2001	0.18	0.04-0.6	Schwarz (2003)
	Dagebüll 2002/1	1.03	0.3-3.1	Schwarz (2003)
	Dagebüll 2002/2	2.75	1.6-8.9	Schwarz (2003)
CH_2ICl	Rishiri Island		0.1-0.8	Kanaya et al. (2002)
	Mace Head, Ireland	0.11	< 0.02-0.21	Carpenter et al. (1999)
	Spitzbergen	0.07	< 0.004-0.18	Schall and Heumann (1993)
	Dagebüll 2001	0.23	0.1-0.4	Schwarz (2003)
	Dagebüll 2002/1	0.20	0.1-0.3	Schwarz (2003)
	Dagebüll 2002/2	0.68	0.7-2.2	Schwarz (2003)
CH_2IBr	Mace Head, Ireland	0.08	< 0.02-0.32	Carpenter et al. (1999)
	Dagebüll 2001	0.09	0.02-0.2	Schwarz (2003)
	Dagebüll 2002/1	0.17	0.01-0.5	Schwarz (2003)
	Dagebüll 2002/2	0.37	0.4-0.9	Schwarz (2003)
C_2H_5I	Rishiri Island		0.2-1.4	Kanaya et al. (2002)
	Mace Head, Ireland	0.06	< 0.02-0.21	Carpenter et al. (1999)
	Dagebüll 2001	0.47	0.1-1.1	Schwarz (2003)
	Dagebüll 2002/1	0.42	0.3-0.7	Schwarz (2003)
	Dagebüll 2002/2	1.04	0.8-2.3	Schwarz (2003)

sea salt is the dominant source of chlorine and bromine over the remote ocean, the main source of iodine is the biological activity of algae. Various iodocarbons are emitted by different kinds of macroalgae and phytoplankton, often supersaturating the ocean water with respect to iodocarbons (the exact release mechanism is still unkown), causing a flux of iodocarbons from the ocean's surface to the atmosphere. The most important iodocarbons are CH_3I, CH_2I_2, CH_2ClI, C_3H_7I and C_2H_5I (Kanaya et al., 2002; Vogt et al., 1999; Carpenter et al., 1999). Measurements of these species are very sparse and the concentrations are often below the detection limit. Most data are available for methyl iodide. Its estimated global annual release is 1-2 Tg/yr (Davis et al., 1996; Vogt et al., 1999; Zafiriou, 1974), whereas an early estimate of Lovelock et al. (1973) was 40 Tg/yr. A recent calculation with a coupled atmosphere-ocean model by Bell et al. (2002) yields a much smaller global CH_3I release of 214 Gg/yr. Measured methyl iodide mixing ratios in

the MBL range from background concentrations of 1-3 pmol/mol (Lovelock et al., 1973; Cicerone, 1981; Singh et al., 1983; Rasmussen et al., 1982; Reifenhäuser and Heumann, 1992; Schall and Heumann, 1993) to values of 10-20 pmol/mol in areas of high biological activity (Davis et al., 1996; Rasmussen et al., 1982) with a maximum of 43 pmol/mol reported by Oram and Penkett (1994). Most of the iodocarbon mixing ratios measured so far are listed in Table 2.1. Their source strength is largely unkown because measurements are too sparse to extrapolate to a global scale (see also Carpenter et al., 1999; Davis et al., 1996). It is difficult to extrapolate the source strength of iodocarbons to longer time scales and larger regions due to their high variability in space and time. Additionally, a high dependence of the emission fluxes on tides is reported (Carpenter et al., 1999 and J. Plane, pers. comm.). Maximum emissions are always found during low tide when algae in coastal regions are exposed to air, triggering the algae to produce more halocarbons. During the AFOHAL campaign 2003 near Brest very high concentrations have been found, where large algae fields fall dry during low tide (A. Schwarz, pers. comm., 2003). Because these conditions prevail in coastal regions only, such high emission events seem to be restricted to these ecosystems.

Iodine gas phase chemistry is triggered by daylight. Iodocarbons emitted from the sea accumulate in the boundary layer during night. During daytime iodocarbons are rapidly photolysed to produce iodine radicals:

$$\mathrm{RI} + h\nu \quad \rightarrow \quad \mathrm{I} + \mathrm{R} \quad ,$$

where R denotes the alkyl part of the respective iodocarbon. Iodine radicals are very reactive and thus participate in many reaction cycles similar to those of bromine (but with different reaction rates). Iodine radicals take part in ozone destruction cycles (see e.g. Vogt et al., 1999; Carpenter et al., 1999):

$$\begin{aligned} \mathrm{I} + \mathrm{O_3} &\rightarrow \mathrm{IO} + \mathrm{O_2} && (2.10)\\ \mathrm{IO} + \mathrm{HO_2} &\rightarrow \mathrm{HOI} + \mathrm{O_2} && (2.11)\\ \mathrm{HOI} + h\nu &\rightarrow \mathrm{OH} + \mathrm{I} \end{aligned}$$

$$\textbf{Cycle VI} \text{ net}: \quad \mathrm{O_3} + \mathrm{HO_2} \rightarrow \mathrm{OH} + 2\mathrm{O_2} \quad ,$$

$$\begin{aligned} 2(\mathrm{I} + \mathrm{O_3}) &\rightarrow 2(\mathrm{IO} + \mathrm{O_2})\\ \mathrm{IO} + \mathrm{IO} + \mathrm{M} &\rightarrow \mathrm{I_2O_2} + \mathrm{M} && (2.12)\\ \mathrm{I_2O_2} + h\nu &\rightarrow 2\mathrm{I} + \mathrm{O_2} && (2.13) \end{aligned}$$

$$\textbf{Cycle VII} \text{ net}: \quad 2\mathrm{O_3} \rightarrow 3\mathrm{O_2} \quad .$$

For Equation 2.12 and 2.13 the alternative pathway

$$\mathrm{IO} + \mathrm{IO} \quad \rightarrow \quad 2\mathrm{I} + \mathrm{O_2}$$

may also be of importance. Cycle VII usually dominates the ozone destruction when iodine concentrations are high, whereas Cycle VI dominates at low iodine concentrations. Depending on the BrO concentration an additional cycle may influence the ozone destruction (Vogt et al., 1999):

$$\begin{aligned} \mathrm{I} + \mathrm{O_3} &\rightarrow \mathrm{IO} + \mathrm{O_2} \\ \mathrm{Br} + \mathrm{O_3} &\rightarrow \mathrm{BrO} + \mathrm{O_2} \\ \mathrm{IO} + \mathrm{BrO} &\rightarrow \mathrm{IBr} + \mathrm{O_2} \\ \hline \textbf{Cycle VIII} \text{ net}: \quad \mathrm{I} + \mathrm{Br} + 2\mathrm{O_3} &\rightarrow \mathrm{IBr} + 3\mathrm{O_2} \quad . \end{aligned}$$

The corresponding reaction with ClO + IO is of minor importance because of the lower concentration of ClO and the smaller rate coefficient for this reaction. An additional contribution to ozone destruction is a second path of the reaction of IO with another halogen oxide.

$$\mathrm{XO} + \mathrm{YO} \rightarrow \mathrm{OXO} + \mathrm{Y} \quad ,$$

where X and Y are Cl, Br or I. Usually the OXO is destroyed photochemically to yield XO and O and therefore does not contribute anything to ozone destruction. But OIO photolysis can result in the production of oxygen and an iodine radical and thus contribute to ozone destruction as shown by Ashworth et al. (2002):

$$\mathrm{OIO} + h\nu \rightarrow \mathrm{I} + \mathrm{O_2} \quad .$$

However, this has been challenged by Misra and Marshall (1998), Cox et al. (1999), Allan et al. (2001) and Bloss et al. (2001) who suggest that OIO is photostable. Even though most of the IO produced by Reaction 2.10 is photolysed back into I and O radicals, ozone destruction increases in the presence of iodine.

There is an indirect effect in addition to the direct ozone destruction by iodine. Hypoiodous acid (HOI) from Reaction 2.11 is taken up by the aerosol. This reaction -promoted by acidity- leads to the formation of ICl and IBr, which subsequently escape to the gas phase because of their low solubility:

$$\begin{aligned} \mathrm{HOI} + \mathrm{Cl^-} + \mathrm{H^+} &\rightarrow \mathrm{ICl} + \mathrm{H_2O} \\ \mathrm{HOI} + \mathrm{Br^-} + \mathrm{H^+} &\rightarrow \mathrm{IBr} + \mathrm{H_2O} \quad . \end{aligned}$$

Therefore iodine provides a mechanism of chlorine and bromine release and enhances ozone destruction by other halogens. The DMS oxidation by IO is much slower than by BrO, hence the influence of IO on DMS oxidation is rather small. The iodine radicals and the iodine monoxide also react with other trace gases to form some soluble gases:

$$\begin{aligned} \mathrm{IO} + \mathrm{HO_2} &\rightarrow \mathrm{HOI} + \mathrm{O_2} \\ \mathrm{I} + \mathrm{HO_2} &\rightarrow \mathrm{HI} + \mathrm{O_2} \\ \mathrm{IO} + \mathrm{NO_2} &\rightarrow \mathrm{IO_3} \\ \mathrm{I} + \mathrm{NO_2} &\rightarrow \mathrm{INO_2} \quad . \end{aligned}$$

These soluble gases can react on or within the aerosol phase. Thus the aerosol phase is no source for iodine but it provides an environment for iodine compounds to interact

with other species. By the transfer of the soluble iodine containing gases INO_2 and INO_3 into the aerosol phase iodine chemistry establishes a possible sink for nitrogen oxide in moderately polluted air masses. A significant denoxification of MBL air due to nitrogen uptake on aerosol was found by McFiggans et al. (2000). Iodine enhances this denoxification directly by building iodine nitrates and indirectly by the activation of bromine, which forms bromine nitrate, also leading to a faster transfer of nitrate into the aerosol phase.

INO_2 and INO_3 as well as HI or HOI are subject to a net transfer into the aerosol. After their uptake nitrate and water are produced, and iodine is usually released back into the gas phase in the form of one of the relatively insoluble gases I_2, IBr or ICl. Thus the activation of chlorine and bromine by iodine is intensified in polluted (i.e. NO_x rich) air masses:

$$\begin{aligned}
INO_3 + H_2O &\rightarrow HOI + HNO_3 \\
INO_2 + H_2O &\rightarrow HOI + HONO \\
HOI + X^- + H^+ &\rightarrow IX + H_2O \\
HI &\rightarrow I^- + H^+ \\
I^- + HOX + H^+ &\rightarrow IX + H_2O \quad ,
\end{aligned}$$

where X denotes Br, Cl or I.

Aerosol does not only provide a recycling surface area for iodine. Iodine enrichment factors normally reach values higher than 1000 (EF(I)>1000) in comparison to sea water (McFiggans et al., 2000). It is still an open question which iodine component accumulates in the aerosol. Cox et al. (1999) and Allan et al. (2001) emphasis gaseous OIO as the driving force for iodine enrichment in particles because of its relatively high photochemical stability, leading to iodate accumulation in the aerosol phase. Baker et al. (2000) and McFiggans et al. (2000) also favour iodate as a stable component but give no formation mechanism. Vogt et al. (1999) propose direct uptake of I_2O_2 onto the aerosol or uptake of IO followed by its self-reaction in the aerosol phase

$$\begin{aligned}
I_2O_2 + H_2O &\rightarrow HOI + IO_2^- + H^+ \\
IO + IO(+H_2O) &\rightarrow HOI + IO_2^- + H^+
\end{aligned}$$

leading to IO_2^- formation reacting further to iodate via

$$IO_2^- + H_2O_2 \rightarrow IO_3^- + H_2O$$

with subsequent accumulation in the aerosol phase. The theory of accumulation of iodate in the aerosol phase is supported by measurements of Wimschneider and Heumann (1995) who found concentrations for iodate much higher than for iodide in all measured aerosol size ranges for marine air over the South Atlantic Ocean.

Another hypothesis linked with iodine chemistry is the possibility of particle formation. O'Dowd et al. (2002a) showed in smog chamber experiments that particle formation from condensable iodine-containing vapours can occur. They suggest three different pathways. The concentration of gaseous iodine determines which pathway is the one dominating the nucleation process. Prerequisits for this process are the abundance of iodocarbons, ultraviolet radiation and the availability of ozone. The iodocarbons are photolysed by the radiation to yield iodine radicals. These react with ozone to form IO. Firstly, IO reacts with itself to produce OIO, which can nucleate to form I_2O_4 and higher order

iodine oxide polymers (this theorie is described in more detail by Hoffmann et al. (2001) and supported by Jimenez et al. (2003)). Secondly, the dimer I_2O_2 is produced in the self-reaction of IO. This also accumulates to higher polymers. Bloss et al. (2001) propose I_2O_2 as the main product of the IO self-reaction. At very low initial concentrations of iodocarbons the dominant reaction of particle formation is that of IO with HO_2 to yield HOI which then takes part in the particle formation. O'Dowd et al. (2002a) suggest that especially in coastal regions the iodine concentrations are high enough to make this process significant in nature. In their laboratory experiments they varied the initial CH_2I_2 mixing ratio from 50 nmol/mol down to 0.0015 nmol/mol and concluded that lower mixing ratios do not hinder or change the nucleation process but only slow it down. However, the measured concentrations of iodocarbons (see Table 2.1) clearly show that even the smallest concentration tested by O'Dowd et al. (2002a) is higher than those measured at Mace Head, Ireland, for which the particle formation by iodine was discussed. O'Dowd et al. (2002b) considered a second (iodine independent) way of particle formation. They conclude from measurements in the frame work of the PARFORCE (new PARticle FORmation and fate in the Coastal Environment) experiment that, according to Kulmala et al. (2002), the particle nucleation occurred by ternary nucleation of sulphuric acid, ammonia and water vapour. Whereas the sulphuric acid concentration may not have been high enough to grow the new particles into detectable sizes (Kulmala et al., 2002), the iodine vapour concentrations during low tide at daytime could have been capable to grow the newly built particles (about 1 nm) into a measureable particle size ($>$ 3 nm) (Mäkelä et al., 2002).

Most measurements of inorganic iodine species in the gas phase are performed with the DOAS instrument (Platt, 2000; Platt and Hönninger, 2003; Carpenter et al., 1999, 2001). The DOAS should be able to measure I_2, IO, and OIO. To the authors knowledge no I_2 concentrations have been reported in the literature. OIO was measured in a range from below the detection limit up to a mixing ratio of 3 pmol/mol by Allan et al. (2001) at Cape Grim, Australia. Even for IO the database is very poor. Allan et al. (2000) measured IO at Cape Grim in the range from below detection limit (i.e. $<$ 0.2 pmol/mol) up to 4 pmol/mol with an average of 1 pmol/mol. Alicke et al. (1999) report values above the detection limit up to mixing ratios of about 6 pmol/mol at noon for IO at Mace Head, Ireland, whereas Carpenter et al. (2001) found peaks of up to 3 pmol/mol for the same time and location.

2.0.4 Halogens in the Free Troposphere

Satellite and groundbased measurements increasingly provide evidence that BrO is abundant not only in the boundary layer but also in the free troposphere (van Roozendael et al., 2002; Wennberg, 1999). Here it can significantly contribute to ozone destruction. Harder et al. (1998), Frieß et al. (1999), Fitzenberger et al. (2000) as well as Platt and Hönninger (2003) report mixing ratios of about 1-2 pmol/mol BrO for the mid-latitudinal troposphere. At these mixing ratios the BrO self-reaction is of minor importance, whereas it is the main driving force for ozone destruction during the bromine explosion events in the polar regions. In the free troposphere the ozone destruction cycle initiated by the reaction of BrO and HO_2 (see Cycle IV) is more significant (Platt, 2000). This reaction pathway leads to a shift of the HO_2/OH ratio which could change the oxidising capacity of the local atmosphere.

The sources of bromine oxides in the free troposphere are still under discussion. Platt

(2000) proposes upward transport of BrO from the boundary layer as well as degradation of short-lived organo-halogen species in the free troposphere as possible sources. McElroy et al. (1999), who measured BrO in the polar free troposphere, suggest convection of BrO and of particles as ice crystals and small droplets, which then will provide a surface for heterogeneous reactions as main sources. Fitzenberger et al. (2000) extend this theory to the mid-latitudes and propose a heterogeneous activation mechanism, recycling HBr, HOBr and $BrNO_3$ on the surface of droplets or ice crystals to release BrCl or Br.

Von Glasow et al. (2004) were the first to consider halogens in a global model study of the free troposphere. They found ozone destruction in the free troposphere of up to 20% in a simulation with halogen chemistry in comparison to another without halogens.

Chapter 3

Model Descriptions

3.1 ECHAM5 - A Model Description

The General Circulation Model (GCM) ECHAM is based on the weather prediction model of the European Centre for Medium-range Weather Forecasts **EC**MWF in Reading, United Kingdom. The Max Planck Institute for Meteorology in **HAM**burg, Germany (MPI-MET) adapted it to a climate model. Version 5 of ECHAM (further denoted as ECHAM5) was extended at the Max Planck Institute for Chemistry in Mainz, Germany (MPI-C) by the comprehensive Modular Earth Submodel SYstem (MESSy, see Jöckel et al., 2005), providing the possibility to couple various submodels (i.e. processes) to the base model. MESSy is described in detail in Section 3.2.

ECHAM5 as climate model provides the dynamical core and the time management of ECHAM5/MESSy. Some processes that are also incorporated in the original ECHAM5 have been replaced by MESSy submodels in ECHAM5/MESSy, e.g. tracer transport by convection and cloud microphysics.

Various different model resolutions can be applied. The horizontal resolution ranges from T21 (as a technical test version) up to T159 (see Table 3.1 for more details). These are the standard resolutions, but higher resolutions are also possible if initial data are provided. The vertical resolution of the tropospheric version involves 19 (L19) or 31 (L31) layers, respectively, with the top layer at 10 hPa. The middle atmosphere version (MA-ECHAM5) reaching up to 0.01 hPa comprises 39 (L39) or 90 (L90) layers. For the studies shown here the tropospheric T31L31 version is applied exclusively. In the vertical direction a hybrid

Resolution	approx. Box Width ° × °	approx. Box Width km	Number of Boxes lon. × lat.	Time Step s
T21L19	5.6 × 5.6	621	64 × 32	2400
T31L31	4.2 × 4.2	467	96 × 48	1800
T42L31	2.8 × 2.8	311	128 × 64	1200
T63L31	2.1 × 2.1	233	192 × 96	720
T85L31	1.4 × 1.4	156	256 × 128	480
T106L31	1.1 × 1.1	122	320 × 160	360
T159L31	0.7 × 0.7	81	480 × 240	180

Table 3.1: Table of ECHAM5 model resolutions.

pressure coordinate system is used, which is terrain-following in the lower levels (σ) and merges in the upper levels into surfaces of constant pressure (p). The governing equations are the primitive equations of motion formulated for a moist atmosphere. The prognostic variables are vorticity, divergence, the logarithmic surface pressure, temperature, water vapour, cloud water and cloud ice. Time integration is done by a semi-implicit time integration scheme, the so-called 'leapfrog scheme'. ECHAM5 originally provides three different advection schemes. The default, a flux-form semi-Lagrangian mechanism (Lin and Rood, 1996; Lin et al., 1994), is applied in this study. This advection scheme is mass conserving by definition. But due to the implementation into ECHAM5 using hybrid pressure coordinates tracer advection is not fully mass conserving as described by Jöckel et al. (2001).

ECHAM5 also contains a relatively detailed cloud scheme including convection as well as large scale condensation and formation of cumulus and stratus clouds. These routines have been replaced by submodels in ECHAM5/MESSy (see Sections 3.2.6 and 3.2.9). For a detailed description of ECHAM5 see Roeckner et al. (2003) and the MPI-MET website[1].

3.1.1 Data Assimilation

It is possible to relax the ECHAM5 model atmosphere towards an observed state by applying a four parameter assimilation technique, the so-called nudging. The model is nudged towards the observed state by adding a non-physical tendency to the overall tendency of a prognostic model variable X:

$$\frac{\mathrm{dX}}{\mathrm{dt}} = \mathrm{F_m(X)} + \mathrm{G(X)[X_{obs} - X]} \quad . \tag{3.1}$$

$\mathrm{F_m(X)}$ is the model forcing for variable X, G(X) the relaxation coefficient and [X_{obs}-X] the difference between model and observation. More details about the nudging procedure can be found in Jeuken et al. (1996).

In this study the prognostic variables surface pressure p, divergence D, vorticity V and temperature T are nudged, with $\mathrm{G}(p) = 1.1574$, $\mathrm{G}(D) = 0.5787$, $\mathrm{G}(V) = 4.6296$ and $\mathrm{G}(T) = 1.1574$, respectively.

3.2 MESSy

The Modular Earth Submodel SYstem (MESSy) is a development of the MPI-C with contributions of the Deutsches Zentrum für Luft-und Raumfahrt (DLR) (see Jöckel et al., 2005). The first MESSy (version 0.9) was released in October 2004. Further information and a short description of each submodel of this MESSy version are available at the MESSy website[2]. The basic idea of MESSy is to organise the implementation of various processes into so-called submodels. Due to this modularisation it is possible to realise many different tasks within the same structure, e.g. processes such as emissions, convection or various diagnostic tools. All data required from the base model are provided via the MESSy data transfer/export interface (further denoted as data interface). This interface needs to be adopted if MESSy is connected to another base model.

[1] *http://www.mpimet.mpg.de/en/extra/models/echam/echam5.php*
[2] *http://www.messy-interface.org*

Table 3.2: List of MESSy submodels available in MESSy-version 0.9.1. For details see the MESSy website[2]. Submodels used in this study are written in bold face. All people responsible for the respective submodels are from MPI-C, contributions of other institutes are listed in footnotes.

Submodel Name	Function	Responsible
ADVECT	alternative ADVECTion (under construction)	P. Jöckel
AIRSEA	air-sea exchange over oceans	A. Pozzer
ATTILA[a]	lagrangian transport scheme	M. Traub/-P. Jöckel
CLOUD[b]	CLOUD model	H. Tost
CONVECT[c]	CONVECTion model	H. Tost
CVTRANS	new ConVective tracer TRANSport	H. Tost
D14CO	^{14}CO (diagnostics)	P. Jöckel
DRADON	^{222}Rn (diagnostics)	P. Jöckel
DRYDEP	DRY DEPosition of gases and aerosols	A. Kerkweg
EMDEP	EMissions and DEPosition	L. Ganzefeld
EQSAM	EQuilibrium Simplified Aerosol Model	S. Metzger
GM7[d]	Generalised Modal aerosol model	S. Metzger
H2O	correct H_2O and feedback	C. Brühl
HETCHEM	HETerogeneous CHEMistry (reaction rates)	B. Steil
JVAL	calculates J-VALues	R. Sander
LGTMIX	MIXing of LaGrangian Tracers	P. Jöckel
LNOX	Lightning NO_x	P. Jöckel
M7[e]	Modal aerosol model	A. Kerkweg
MECCA	calculation of gas phase chemistry	R. Sander
MECCA-MBL	calculation of aerosol phase chemistry	A. Kerkweg
OFFLEM	OFFLine EMissions	P. Jöckel
ONLEM	ONLine EMissions (gas and aerosol)	A. Kerkweg
PHOTO	calculation of PHOTOlysis rate coefficients	C. Brühl
PSC	Polar Stratospheric Clouds	J. Buchholz
PTRAC	Passive TRACer (diagnostics)	P. Jöckel
QBO[f]	'Quasi Biannual Oszillation' nudging	P. Jöckel
SCAV	SCAVenging and wet deposition of gases and aerosols	H.Tost
SCOUT	Selectable Column OUTput	P. Jöckel
SEDI	SEDImentation of aerosols	A. Kerkweg
STATATT	STATistic of ATTila	M. Traub
TNUDGE	Tracer NUDG(E)ing	P. Jöckel
TREXP	Tracer Release EXPeriment	P. Jöckel
TROPOP	diagnostic of TROPOPause and boundary layer height	P. Jöckel
VISO	Values on horizontal ISO-surfaces	P. Jöckel

[a] original code from DLR
[b] the original routines have been part of ECHAM5
[c] the original routines have been part of ECHAM5
[d] original box model from Wilson et al. (2001), see section 3.2.4
[e] original box model from Wilson et al. (2001), see section 3.2.4
[f] original code from MPI-MET

Each submodel is divided into a core or 'kernel' and an interface layer. The interface layer of the individual submodel collects the data needed by the submodel, e.g. temperature, pressure etc., from the MESSy data interface and transforms those into the format required by the core layer. The results of the core are delivered back to the data interface. The core contains the 'scientific' content of the submodel. It provides a stand-alone box or column process model. The exact structure and the way MESSy is implemented and connected to ECHAM5 are documented on websites (see below) and in Jöckel et al. (2005).

As mentioned above, MESSy comprises a large set of submodels and will be further extended in future. In the following subsections details are given only for those submodels that were used in this study. For a current list of MESSy submodels see Table 3.2 (version 0.9.1) or the MESSy website[2].

3.2.1 MECCA - A Gas Phase Chemistry Mechanism

MECCA (Module Efficiently Calculating the Chemistry of the Atmosphere) of Sander et al. (2005) is a gas phase chemistry model. It is a box model in its basic entity. As part of MESSy it is straightforward to implement into more dimensional, e.g. global models.

The core of each chemical model is the numerical solution of the set of differential equations determined by the considered species and reactions. In MECCA this is done with KPP (Kinetic PreProcessor; Sandu et al. (1997b,a)). It provides a variety of different integrators to be chosen by the user. Sandu et al. (1997b,a) performed a very extensive test of different integration methods and found that Rosenbrock solvers suited best for requirements of 3D atmospheric chemistry calculations. Usually the autonomous linearly-implicit 2-stage Rosenbrock solver (ROS2) (Verwer et al., 1997) with fixed time steps is used for integrations comprising only gas phase chemistry. But experience shows that this integrator is not stable enough for very stiff systems of differential equations. The ROS3 (Rosenbrock solver of third order) with automatic time stepping is more stable and thus more reliable. The reason is not so much the order of the Rosenbrock solver but rather the automatic time stepping. In the fixed time step method the user specifies the number and the length of the chemical substeps the solver uses for the integration, whereas in the 'automatic time step method' the KPP solver tests if the result of one integration step ranges within a given error interval. If this is not the case, the result of this integration is rejected and a smaller time step is applied for the integration step, thus stabilising the integration process. The main requirements of KPP are an equation file containing all chemical reactions including their rate coefficients and a species file which names all species occurring in the equation file.

MECCA is designed to meet various scientific needs. Thus the equation file provided by MECCA includes a large variety of reactions and each user is able to select the subset he/she is interested in by a shell-script.

MECCA comprises the stratospheric chemistry of ECHAM4/CHEM (Steil et al., 1998) and tropospheric chemistry including NMHC (Non-Methane HydroCarbon) chemistry of von Kuhlmann et al. (2003). The gas phase mechanism was extended by halogen and sulphur chemistry based on von Glasow et al. (2002) in the framework of this study.

Most of the required rate coefficients are dependent on actual model parameters as temperature or pressure. Thus each rate coefficient given in the KPP equation file can be

a) a plain number for constant rate coefficients

b) a (statement) function including e.g. a temperature or pressure dependence, like an Arrhenius-function

c) a variable which provides a rate coefficient if the calculation of this rate coefficient is more complex.

Examples for the latter type of rate coefficients are photolysis rate coefficients as well as rate coefficients for heteorogeneous reactions if the explicit calculation of aerosols or polar stratospheric clouds is omitted.

The MECCA box model calculates the photolysis rate coefficients itself. This algorithm was adopted from the MOCCA (Model Of Chemistry Considering Aerosols) chemistry box model[3]. No precalculation of heterogeneous reaction rate coefficients is performed in the MECCA box model, because MECCA includes a submodel for explicit aerosol chemistry calculation (MECCA-MBL, see next section).

In 3D simulations, photolysis rate coefficients are imported via the MESSy data interface from the submodel JVAL (see Section 3.2.3). The heterogeneous reaction rate coefficients are imported from other MESSy submodels (e.g. PSC or HETCHEM).

The gas phase chemistry and the photolysis reactions used in this study are listed in Table C.1 and C.2 of Appendix C, respectively. For a more detailed description and the full set of available reactions see Sander et al. (2005) and the supplement therein as well as the MECCA website[4].

3.2.2 MECCA-MBL

The submodel MECCA has been designed for gas phase chemistry only. In the framework of this study MECCA was extended by a submodel (called MECCA-MBL) to calculate simultaneously gas and aerosol phase chemistry within the same mechanism. MECCA-MBL comprises additional equations and species files covering liquid phase and gas-liquid phase transition reactions as well as the calculation of all coefficients required for computation of liquid phase chemistry. As noted above, the set of differential equations becomes very stiff if chemistry in two different phases is calculated simultaneously. Thus the Rosenbrock solver of third order with automatic time stepping has to be used in studies including aerosol chemistry.

Most of the reaction rate coefficients within the aerosol phase depend on aerosol properties. The required input parameters are the number distribution N, the ambient radius r_{amb} and the standard deviation σ of the radius distribution of the respective mode. These variables are assumed to be constant within the MECCA box model, whereas in 3D simulations they are imported from the aerosol submodel M7 (see Section 3.2.4) via the MESSy data interface. In this case the rate coefficients are calculated in each box for every time step.

The liquid water content[5] (lwc) of an aerosol mode j is given by

$$lwc_j = \frac{4}{3}\pi r_{j,\mathrm{amb}}^3 N_j^{\mathrm{tot}} \exp\left(\frac{9(\log\sigma_j)^2}{2(\log e)^2}\right) \tag{3.2}$$

(Sander, 1999). N_j^{tot} is the total number of particles in mode j. Equation 3.2 is only valid under the assumption that all particle components are dissolved in the water and no solid matter is left. For sea salt this is probably valid if the lwc is large enough. Hence the aerosol chemistry calculations are ignored if the aerosol water content is less than $10^{-12}\mathrm{m}^3(\mathrm{aq})/\mathrm{m}^3(\mathrm{air})$.

[3] by R. Sander, see *http://www.mpch-mainz.mpg.de/~sander/mocca*

[4] *http://www.mpch-mainz.mpg.de/~sander/messy/mecca/*

[5] For the units of formal parameters see Appendix B.

The exchange rates are precalculated in each grid box before the KPP-integration. The forward (k_exf) and backward (k_exb) exchange rates for a species X between gas and aerosol phase j are calculated according to Schwartz (1986)(see also Sander, 1999):

$$\begin{aligned} k\_exf_j(X) &= k_{j,\mathrm{mt}}(X) \cdot lwc_j \\ k\_exb_j(X) &= k_{j,\mathrm{mt}}(X) \cdot k_{\mathrm{H}}(X) \quad . \end{aligned} \tag{3.3}$$

$k_{j,\mathrm{mt}}(X)$ denotes the mass transfer coefficient and $k_{\mathrm{H}}(X)$ the inverse dimensionless Henry's law coefficient of species X in mode j.

The mass transfer coefficient for a single particle $k_{j,\mathrm{mt}}(X)$ with radius r_j is given by

$$k_{\mathrm{j,mt}}(X) = \left(\frac{r_j^2}{3D_g(X)} + \frac{4r_j}{3\bar{v}(X)\alpha(X)} \right)^{-1}$$

with D_g denoting the gas phase diffusion coefficient, α being the accommodation coefficient (see Table C.7) and $\bar{v}$ the mean molecular speed. D_g can be approximated following the kinetic gas theorie (see e.g. Wayne, 2000) as $D_g(X) = \lambda_{air}\bar{v}(X)/3$ with λ_{air} being the mean free path of air molecules. The mean molecular speed is given by $\bar{v}(X) = 8RT/(\pi M_X)$, where R is the universal gas constant, T the temperature and M_X the molar mass of species X. The averaged mass transfer coefficient for a modal aerosol distribution $\bar{k}_{\mathrm{j,mt}}$ is an integral over the particle radius:

$$\bar{k}_{\mathrm{j,mt}}(X) = \frac{4\pi}{3\ lwc_j} \int_{-\infty}^{+\infty} \left(\frac{r_j^2}{3D_g(X)} + \frac{4r_j}{3\bar{v}(X)\alpha(X)} \right)^{-1} r_j^3 \frac{\partial N_j}{\partial log r_j} dlogr_j \quad .$$

There is no analytical solution for this integral. Thus the mass transfer coefficient for the ambient mean radius of the mode is used in MECCA-MBL. To account for the differences between the integrated mean mass transfer coefficient and the mass transfer coefficient for the mean radius, a study with the box model MOCCA was performed, in which both of these coefficients have been calculated. Their comparison yields empiric correction factors f_j of about 0.84 and 0.55 for the accumulation and the coarse mode, respectively, resulting in

$$\tilde{k}_{j,\mathrm{mt}}(X) = f_j \frac{\bar{v}(X)}{r_j} \left(\frac{r_j}{\lambda_{\mathrm{air}}} + \frac{4}{3\alpha(X)} \right)^{-1} .$$

The inverse dimensionless Henry's law coefficient $k_{\mathrm{H}}(X)$ (in Equation 3.3) is calculated from the Henry's law coefficient k_{henry} (see Table C.6) as described by Sander (1999):

$$k_{\mathrm{H}}(X) = \frac{1}{k_{\mathrm{henry}}(X)TR} .$$

A summary of all reactions included into the aqueous phase mechanism with references for the respective reaction rates is listed in Appendix C. Presently MECCA-MBL is designed to calculate chemistry on one or two aerosol modes. In the present study only one mode (the so-called sea salt mode or coarse mode) is used for the simulations.

An important issue is the emission calculation of those ions associated with sea salt emissions, as Cl^-, Br^-, HCO_3^-, I^-, IO_3^- and Na^+. The NaCl mass emission flux is imported via the MESSy data interface from the submodel ONLEM (see Section 3.2.7). The chloride emission is calculated from this mass flux. All other ions abundant in sea water (and therefore emitted by sea salt production) are assumed to have a fixed ratio to Cl^- as listed in Table 3.3.

More details about MECCA-MBL can be found in a technical note (Sander et al., 2005) and its supplement.

Ion X	Ratio [X]/[Cl^-]
Cl^-	1.0
Br^-	$1.5 \cdot 10^-3$
HCO_3^-	$4.2 \cdot 10^-3$
I^-	$7.4 \cdot 10^{-8}/0.545$
IO_3^-	$2.64 \cdot 10^{-7}/0.545$

Table 3.3: Assumed ion abundance in sea water (see MOCCA manual for details: *http://www.mpch-mainz.mpg.de/˜sander/mocca*).

3.2.3 Photolysis

In 3D simulations MECCA relies on a submodel providing photolysis rate coefficients. For this purpose the submodel JVAL is used.

The physical core of JVAL is based on the spectral approach of Landgraf and Crutzen (1998). The photolysis rate coefficient J_X of the species X is given by

$$J_X = \int_I \sigma_X(\lambda)\phi_X(\lambda)F(\lambda)\ d\lambda\ ,$$

where $F(\lambda)$ denotes the spectral actinic flux, λ the wavelength, $\sigma_X(\lambda)$ the absorption cross-section and $\phi_X(\lambda)$ the quantum yield. I is the photochemically active spectral interval (178.6 nm $\leq \lambda \leq$ 752.5 nm). It is subdivided into eight bands (indexed by i) according to Landgraf and Crutzen (1998). They are chosen in the manner, that the contribution of each band can be calculated individually:

$$J_{i,X} = \int_{I_i} \sigma_X(\lambda)\phi_X(\lambda)F(\lambda)\ d\lambda\ .$$

To minimise the computational effort, each photolysis rate coefficient $J_{i,X}$ is further subdivided into the photolysis rate of a purely absorbing atmosphere $J^a_{i,X}$ and the part that includes the influence of light scattering by air molecules, aerosol and cloud droplets. The latter part can be neglected in the Schumann-Runge-Band (178.6 nm $\leq \lambda \leq$ 202.0 nm) because of the very strong O_2 absorption in this wavelength interval. Thus the photolysis rate coefficient for a gas X can be written as

$$J_X = J^a_{1,X} + \sum_{i=2}^{8} J^a_{i,X} \cdot \delta_i\ ,$$

where δ_i is the ratio of the actual actinic flux to the actinic flux for a purely absorbing atmosphere at an adequate fixed wavelength λ_i in the interval I_i:

$$\delta_i := \frac{F(\lambda_i)}{F^a(\lambda_i)}\ .$$

As a result the $J^a_{i,X}$ can be precalculated, and only the δ_i values have to be determined during the integration. This is done with a radiative transfer code taking into account absorption and scattering of molecules, particles and the earth's surface. More details concerning the photolysis algorithm can be found in Landgraf and Crutzen (1998) and on the MESSy website.

	Mode	SO_4^{2-}	OC	BC	DU	SS
1	nucleation soluble	x				
2	Aitken soluble	x	x	x		
3	accumulation soluble	x	x	x	x	x
4	coarse soluble	x	x	x	x	x
5	Aitken insoluble		x	x		
6	accumulation insoluble				x	
7	coarse insoluble				x	

Table 3.4: Distribution of aerosol components in the M7 modes: SO_4^{2-} = sulphate ; OC = organic carbon; BC = black carbon; SS = sea salt; DU = dust.

3.2.4 The Aerosol Module M7

One of the new approaches of this work is the calculation of halogen chemistry based on a prognostic aerosol distribution, which is provided by the aerosol submodel M7. This aerosol model was developed at the Joint Research Center of the European Commission (JRC) in Ispra, Italy (Wilson et al., 2001; Vignati et al., 2004). In its basic entity it is a box model and thus straightforward to include into MESSy.

M7 describes the aerosol distribution as seven independent modes in lognormal distribution. The total particle number as well as the masses of the components of each mode are calculated prognostically. The mean dry radius and the mean ambient radius are determined diagnostically, and the radius standard deviation for each mode is kept constant ($\sigma = 2.0$ for the coarse modes, $\sigma = 1.69$ otherwise). The seven modes are distinguished by composition and size. The radius spectrum is subdivided into four size ranges. Three modes contain insoluble aerosol compounds only, and four further modes include soluble sulphate and sea salt in addition to the insoluble components and are therefore called the 'soluble modes'. The smallest one is the nucleation mode consisting of sulphate only. It covers the particle size range up to 5 nm. The insoluble Aitken mode (5 to 50 nm) comprises organic and black carbon. The soluble Aitken mode consists of sulphate in addition to black and organic carbon. The insoluble accumulation and coarse modes only contain dust. The accumulation mode covers the radii from 50 to 500 nm, whereas the coarse mode describes particles larger than 500 nm. The soluble accumulation and coarse modes contain the insoluble compounds organic and black carbon as well as dust and furthermore the soluble components sulphate and sea salt. Table 3.4 summarises the distribution of the different components among the modes. This modal structure requires 18 mass tracers and 7 number tracers, i.e. 25 aerosol tracers in total. Because the condensation of H_2SO_4 on existing particles and nucleation of new particles (see list below) is treated in M7, a gas phase sulphuric acid tracer must be available. This tracer is provided by MECCA.
The following processes are taken into account in M7:

- Nucleation of sulphate particles:
  The process of nucleation affects only the nucleation mode and gas phase sulphate. For the calculation of this process the mechanism by Vehkamäki et al. (2002) is applied.

- Condensation of H_2SO_4 onto all modes:
  For soluble modes this results in a growth of the mean radius. Condensation onto insoluble aerosols makes the aerosol soluble and therefore transfers particles from the insoluble modes into the soluble modes of the same size.

- Coagulation of aerosols:
  Coagulation of two differently sized aerosols is assumed to yield an aerosol particle of the size range of the larger particle. Coagulation of two equally sized aerosol particles forms an aerosol particle of the same size. Coagulation of an insoluble particle with a soluble particle yields a soluble particle in the size range of the larger particle.
- Transition from smaller to larger modes:
  Due to the processes mentioned above, the mean radii of the modes increase over time. To maintain the size range of all modes, the transition of particles of one mode into the next larger mode is included. This is no physical or chemical process, but rather part of the algorithm.

More details about the box model M7 are given in Wilson et al. (2001) and Vignati et al. (2004). M7 was also implemented directly into ECHAM5 by P. Stier (MPI-MET). This version (ECHAM5-HAM) is described in more detail by Stier et al. (2005). Further information on the MESSy submodel M7 can be found on the MESSy website.

3.2.5 Sedimentation

The sedimentation submodel SEDI is based on the theory of aerosol sedimentation (see for example Pruppacher and Klett (1997), page 451). This MESSy submodel was developed as part of this thesis.

Only sedimentation of aerosol particles and their components is accounted for. The terminal sedimentation velocity[6] v_t is given by the Stokes velocity v_{Stokes} modified by the Cunningham-slip-flow correction f_{Csf} and the Slinn factor f_{Slinn}:

$$v_t = v_{\text{Stokes}} \cdot f_{\text{Slinn}} \cdot f_{\text{Csf}}$$

with

$$v_{\text{Stokes}} = \frac{2}{9} \left(\rho_{\text{aero}}(k) - \rho_{\text{air}}\right) \frac{g}{\eta} \, r(k)^2$$

$$f_{\text{Csf}} = 1 + 1.257 \frac{\lambda_{\text{air}}}{r(k)} + 0.4 \frac{\lambda_{\text{air}}}{r(k)} \, exp\left(-1.1 \Big/ \frac{\lambda_{\text{air}}}{r(k)} \right)$$

$$f_{\text{Slinn}} = \begin{cases} 1 & \text{bins} \\ \sigma(k)^{2ln\sigma(k)} & \text{lognormal modes} \end{cases},$$

where k denotes the respective aerosol mode, $\sigma(k)$ is the radius standard deviation, $\rho_{\text{aero}}(k)$ the aerosol density and $r(k)$ the ambient radius of aerosol mode k. η denotes the dynamic viscosity of air, g the gravitational acceleration and λ_{air} the mean free path of air molecules. v_{Stokes} is the sedimentation velocity of spheres. The Cunningham-slip-flow factor corrects for aerodynamic differences between ideal spheres and real non-spherical particles. In case of lognormal distributions the particle radius varies over a wide range. As the mean sedimentation velocity of all particles of a lognormal mode is larger than the sedimentation velocitiy for a particle of the mean radius, a correction factor has to be applied. This is the Slinn factor (Slinn and Slinn, 1980).

[6] For the units of formal parameters see Appendix B.

In the sedimentation scheme of zeroth order an upper limit is applied to the terminal velocity. This is given by the ratio of model layer thickness (Δz) to time step (Δt):

$$v_t \leq \frac{\Delta z}{\Delta t} .$$

This limitation prevents particles falling through more than one model layer within one model time step. SEDI also provides a sedimentation scheme of first order, which is not described here, because the zeroth order scheme is used for this study. For further information see also the MESSy website.

3.2.6 Scavenging and Wet Deposition

Scavenging by cloud and rain droplets as well as wet deposition are important loss processes for trace gases as well as for aerosols. ECHAM5 contains a simplified parameterisation only (J. Feichter, MPI-MET). New MESSy submodels dealing with the effect of cloud processes on tracers have been developed to handle these important processes in the same detailed way as the chemistry. In the following only a short description of the functionality is given. The reader is referred to Tost et al. (2005, in prep.) and to a forthcoming PhD thesis by H. Tost as well as the MESSy website.

A very important sink of trace gases and aerosols is scavenging followed by wet deposition. The SCAV submodel simulates large scale and convective SCAVenging in rain, snow and ice, accounting for nucleation and impaction scavenging.

For the scavenging of trace gases the same approach as in MECCA-MBL is used, i.e. the exchange between the gas phase and the droplets as well as the chemistry within the droplets are calculated with KPP. SCAV is fast enough for climate studies by limiting the SCAV chemistry to a small mechanism containing only the most soluble gases as HNO_3 and H_2SO_4. But it is also capable to deal with more complex mechanisms which contain a wider variety of trace gases (e.g. halogens, as required for this study).

The scavenging of aerosols is calculated using a size dependent coagulation/coalescence kernel. Thus a scavenging rate for each mode of an aerosol model is computed and assigned to the respective aerosol component tracers of this mode. The wet deposition flux of the trace gas or aerosol component, respectively, results from the concentration of each species in the precipitation.

Furthermore, coupling of aerosol and cloud chemistry is taken into account. The individual aerosol components (e.g. sulphate or chloride) are transferred to the droplets when the aerosol is scavenged. When droplets evaporate, the most volatile components are released into the gas phase, whereas the other ones become aerosol components of the largest available aerosol mode (which is the coarse mode in the present study).

3.2.7 Emissions

MESSy contains a number of emission submodels. The two submodels OFFLEM and ONLEM which deal with OFFLine and ONLine EMissions, respectively, are used in this study. The difference between online and offline emissions is that offline emissions do not depend on any model parameters. In contrast to this, online emissions are adjusted in every model time step due to time varying model parameters.
In OFFLEM emission fields contain prescribed emission fluxes. The user can select among three possibilities for each emission field:

a) The flux can be directly assigned to the tendency of a respective tracer.

b) The flux can be converted to a lower boundary condition which is processed in the vertical diffusion calculations.

c) The flux can be simply provided to the MESSy data interface for usage in other submodels.

To handle all emissions in the same way, the input fields have to fulfil two requirements. They have to be in netCDF[7] format, and the fluxes must be in units of molecules per square meter and second. OFFLEM was developed by P. Jöckel (MPI-C). In this study offline emission fields are used for CO, HCHO, CH_3OH, HCOOH, NH_3, NO_x and SO_2. The CO, HCHO, CH_3OH, HCOOH and NO_x fields are compilations of anthropogenic emissions provided by the EDGAR-database[8]. The biomass burning emissions are based on the work of Galanter et al. (2000). A detailed description of these emissions can be found in von Kuhlmann et al. (2003). They used the EDGAR-database version 2.0. L. Ganzeveld (MPI-C) updated these emissions to version 3.2 for the use in ECHAM5/MESSy. The NH_3 emission is derived from the GEIA inventory emission set[9] (Bouwman et al., 1997). The SO_2 emission data originate from the EDGAR-database version 3.2 and are scaled in a similar way as CO and NO_x (manuscript in prep. by L. Ganzeveld, 2005). NO_x emissions by aircraft are based on Schmitt and Brunner (1997).

ONLEM deals with the emissions which depend on model parameters and therefore have to be updated every time step. For example, sea salt emissions depend on the surface wind speed and on the land-sea and sea-ice masks of the model. The ONLEM submodel was written as part of this work. The content of the core routines is partially based on previous work as described below.
For sea salt emissions ONLEM provides three alternative schemes:

- MONAHAN: This scheme is based on the original Monahan function (Monahan, 1986). The sea salt mass emission flux $F_{SS,j}$ associated with mode j with radius r_j is calculated as follows:

$$F_{SS,j} = \frac{4}{3}\pi \cdot 1.15 \cdot 10^{-15} \cdot (1 + 0.057\ r_j^{1.05}) \cdot 10^{1.19e^{-B^2}}$$

$$\text{with} \qquad B = (0.380 - log(r_j))/0.650 \quad .$$

- LSCE: This scheme applies lookup tables, and it is a wind speed dependent interpolation between the emission functions of Monahan (1986) and Smith and Harrison (1998). The lookup tables have been designed especially for M7 emissions, because they are dependent on the aerosol mode definition. They have been provided by M. Schulz (Laboratoire des Sciences du Climat et de l'Environnement, Saclay), published in Guelle et al. (2001).

- AEROCOM: This scheme is based on offline fields, which give daily emission fluxes in units of kg (sea salt) per day and per gridbox (on a $1^\circ \times 1^\circ$ grid). These data are provided by the AEROCOM project. AEROCOM is an international global

[7] *http://my.unidata.ucar.edu/content/software/netcdf/index.html*
[8] *http://arch.rivm.nl/env/int/coredata/edgar/*
[9] *http://www.geiacenter.org*

AEROsol model interCOMparison project[10] which provides a database including emission and nudging data to enable the comparison. Because the AEROCOM B experiment is a model comparison for the year 2000, the sea salt emissions of AEROCOM are given for this year.

The organic and black carbon emissions used in this study also originate from the AEROCOM B experiment. They are classified into fossil fuel, biogenic fuel, wildfire emissions and Secondary Organic Aerosol (SOA) formation.

The mineral dust emissions depend on the soil moisture, a source strength factor, a threshold velocity and the clay fraction of the uppermost soil layer. A more detailed description of the source can be found in Balkanski et al. (2003). Timmreck and Schulz (2004) and Schulz et al. (1998) performed several sensitivity studies and tests.

In the framework of MESSy it is possible to run more than one aerosol model within the same model simulation. Because the distribution of the emissions onto the modes or bins of an aerosol model is dependent on the specific aerosol model, all aerosol emissions calculated in ONLEM are provided to the MESSy data interface and are not assigned to the aerosol tracers directly (see emission option c)). The changes in tracer concentration due to the emission fluxes calculated in ONLEM are determined in the specific aerosol model itself.

Apart from the aerosol emissions, ONLEM also computes trace gas emissions which are dependent on time varying model parameters. For these emissions all options listed above are valid. Dimethyl sulphide (DMS) emissions are based on Liss and Merlivat (1986) and depend on the wind speed. The CH_4 emission routine is a 'pseudo' emission, fixing the surface concentration of methane. This routine was developed by L. Ganzeveld (MPI-C). The soil-biogenic NO emissions depend on the leaf area index, soil wetness, soil temperature, the distribution of cultivation/agriculture, N-fertiliser loss, canopy reduction, and rice-emission reduction. The routine was originally developed by Van den Broek (pers. comm., 1995). More details are given in Ganzeveld et al. (2002) or on the MESSy website.

Finally, an important additional source of NO_x is lightning activity. These emissions are provided by the MESSy submodel LNOX (Lightning NO_x), which is based on Price et al. (1997) and has been extended by Grewe et al. (2001).

3.2.8 Dry Deposition

The submodel DRYDEP calculates the loss of trace gases and aerosol particles from the atmosphere to the earth's surface by turbulent transfer and uptake. If this loss process happens in absence of precipitation it is called DRY DEPosition. Deposition is a primary mechanism to clean the atmosphere. The process of trace gas and aerosol particle removal is implemented following Ganzeveld and Lelieveld (1995) and Stier et al. (2005):

Removal of Gases The dry deposition of trace gases is based on the big leaf approach as originally developed by Hicks et al. (1987). It was included and tested in a model by Ganzeveld and Lelieveld (1995) and Ganzeveld et al. (1998). This mechanism is implemented only for a few gases, namely O_3, NO, NO_2, HNO_3, SO_2 and particulate SO_4^{2-}. The latter is only important for a bulk sulphate aerosol and thus not applicable for the present study. The dry deposition velocities of other trace gases which are expected to have an important sink due to the dry deposition process are interpolated according to

[10] *http://nansen.ipsl.jussieu.fr/AEROCOM/*

their solubility and reactivity between the dry depostion velocities of SO_2 and O_3. The uptake resistances of the individual gases are interpolated based on their Henry's law coefficient and an estimated reactivity coefficient, where SO_2 is taken as reference for soluble non-reactive trace gases and O_3 for non-soluble reactive trace gases.
The dry deposition flux[11] $F_{\mathrm{dep}}(X)$ is given by

$$F_{\mathrm{dep}}(X) \quad = \quad c_g(X) \cdot v_d(X)$$

with $c_g(X)$ being the gas phase concentration. The dry deposition velocity $v_d(X)$ of a trace gas X depends on the aerodynamic resistance R_{aero}, the quasi-laminary boundary layer resistance $R_{\mathrm{qbr}}(X)$ and the surface resistance R_{surf}:

$$v_d(X) = \frac{1}{R_{\mathrm{aero}} + R_{\mathrm{qbr}}(X) + R_{\mathrm{surf}}} \quad ,$$

where R_{aero} is a function of the physical state of the atmosphere, $R_{\mathrm{qbr}}(X)$ is controlled by molecular diffusion and R_{surf} depends on the chemical, physical and biological properties of the surface.
The resistances are given as follows:

$$R_{\mathrm{aero}} \quad = \quad \frac{1}{u_\star \kappa}\left[\left(\frac{z-d}{z_0}\right) - \Psi\left(\frac{z-d}{L}\right)\right]$$

with $u_\star$ being the friction velocity, κ denotes von Karman constant, z the reference height, Ψ the dimensionless stability function. L is the Monin-Obukhov length, d the displacement height and z_0 denotes the roughness length.

$$R_{\mathrm{qbr}}(X) \quad = \quad \ln\left(\frac{z_{0\mathrm{m}}}{z_{0\mathrm{X}}}\right)\frac{1}{u_\star \kappa}\left(\frac{Sc}{Pr}\right)^{2/3} \quad ,$$

where $z_{0\mathrm{m}}$ and $z_{0\mathrm{X}}$ are the surface roughness length of momentum or of a trace gas X, respectively, Pr is the Prandtl number (0.72) and Sc the Schmidt number, which is defined as the ratio of kinematic viscosity of air to the molecular diffusivity of a trace gas. Normally $R_{\mathrm{qbr}}(X)$ is neglected because it is much smaller than R_{aero} and R_{surf}.

R_{surf} is dependent on the surface type. Over the ocean there is only a distinction between the sea ice covered fraction and the open ocean. In grid boxes over land, four different land types are taken into account: 1) the snow/ice covered fraction, 2) the water in the wet skin reservoir[12], 3) bare soil and 4) vegetation. For 1), 2) and 3), R_{surf} is set to the resistance of the respective type

$$R_{\mathrm{surf}} \quad = \quad R_{\mathrm{type}} \ ,$$

whereas the resistance for vegetation is calculated as

$$R_{\mathrm{surf}} \quad = \quad \left(\frac{LAI}{r_{\mathrm{leaf}}} + \frac{1}{r_{\mathrm{soil}}}\right)^{-1}$$

with LAI being the leaf area index, r_{soil} the soil resistance and r_{leaf} denoting the leaf/needle resistance, which is dependent on the serial mesophyll and stomatal resistance and a parallel cuticular resistance. For more details and further explanation see Ganzeveld and Lelieveld (1995).

[11] For the units of formal parameters see Appendix B.
[12] The wet skin reservoir is usually the humidity provided by the plants surface.

Removal of Aerosols and Aerosol compounds The implementation of the dry deposition of aerosols and its constituents is based on the implementation by P. Stier (MPI-MET) and L. Ganzeveld (MPI-C) in ECHAM5-HAM. Therefore this dry deposition scheme applies only for modal aerosol distributions. It is implemented in a similar way as the gas phase deposition. Thus according to the big leaf approach the deposition velocity of each aerosol mode is calculated depending on the six different surface types, the mean radius and the radius standard deviation of the aerosol mode (for more details see Stier et al., 2005).

3.2.9 Clouds and Convective Transport Processes

Some processes included in ECHAM5 have been substituted by MESSy submodels in ECHAM5/MESSy. The CLOUD submodel developed by H. Tost (MPI-C) is a modularised version of the ECHAM5 cloud routines. At the moment CLOUD consists of the same cloud microphysics scheme as the original ECHAM5 routines. In future a new cloud scheme might be implemented. Similarly, the CONVECT submodel replaces the ECHAM5 routines for the convective processes. In contrast to the CLOUD submodel, CONVECT already contains a variety of alternative convection schemes. A sensitivity analysis of different convection schemes is currently in preparation (H. Tost, 2005). In the present study the Tiedtke scheme is used (Tiedtke, 1989; Nordeng, 1994). The output of the cloud scheme as well as the convection scheme used in this study are the same as in the original ECHAM5 routines (they are only a modularised version of the ECHAM5 code), thus for more information see Roeckner et al. (2003). In addition, H. Tost implemented the submodel CVTRANS with currently five different ConVective TRANSport schemes. In this study a two-step mechanism has been chosen. Firstly, the tracers are transported up to the highest level where rain production occurs. Subsequently, the tracers are processed by the scavenging mechanism (Section 3.2.6), and then the transport in the layers above those levels where rain production takes place is calculated. All three submodels will be explained in more detail in forthcoming articles and a PhD thesis by H. Tost (see also the MESSy website).

3.2.10 Diagnostic Tools

Besides submodels describing physical or chemical processes also diagnostic tools have been included into MESSy. For this study the submodel TROPOP has been used. TROPOP diagnoses the TROPOPause and the boundary layer height.

Depending on the application, the tropopause is defined in many different ways. In MECCA-MBL the tropopause height is used to limit the region of aerosol chemistry to the troposphere. As for this application an easy estimate of this height is sufficient, the climatological mean tropopause height is used, provided by the World Meteorological Organisation (WMO).

Chapter 4

Results

4.1 Simulation Setup

The present study is the first one to address reactive halogen chemistry including the explicit simulation of halogen release based on a prognostically calculated aerosol distribution. Table 4.1 lists the simulations performed within this study. Since halogen release strongly depends on the available sea salt aerosol as well as on its renewal rate, different sea salt emission methods, their dependence on the 10m surface wind speeds and the resulting sea salt distribution are compared. Three integrations have been performed, one for each of the three sea salt emission methods contained in the submodel ONLEM (see Section 3.2.7). These simulations are labelled according to the method applied: LSCE, MONAHAN and AEROCOM. To show the impact of the underlying meteorology a fourth, nudged simulation using the LSCE emission scenario has been carried out (LSCE-NUDG). The model spinup period for all long-term simulations was three months, followed by a one year integration period. Since the sea salt distributions are not influenced by halogen chemistry, these simulations include only gas phase chemistry in MECCA to provide a realistic gas phase H_2SO_4 concentration to the aerosol submodel M7. In contrast to these aerosol physics simulations, the other four long-term simulations include gas and aerosol phase chemistry. They have been performed to show the effects of different chemistry setups. In addition to the base simulation containing the complete halogen chemistry (i.e. all equations listed in Appendix C), two further integrations have been performed: in the first all halogen reactions in gas and aerosol phase are excluded (NOHAL). The second simulation (CL) includes chlorine chemistry, but bromine chemistry is neglected. Because one year of integration is not representative for a free running climate model, the base simulation containing the full halogen chemistry (CLIM) was integrated for five years (2000-2004). The sensitivity simulations are integrated for one year, thus often only the first year of the base integration is compared to the others. This is indicated by the abbreviation CLIM2000. As the dynamics impact the aerosol chemistry by modifying the sea salt distribution, an additional simulation applying the nudging method and including the same chemistry as the base integration has been carried out (abbreviated MBLNUDG). In addition to the one year integrations, during which output intervals must be relatively high (in these simulations 14 hours), a shorter time period has been simulated to enable data output every time step (i.e. 30 minutes) to investigate the diurnal cycles. The relevant short-term simulations are labelled with a 'D-' in front of the above mentioned acronyms.

In the following, Section 4.2 provides an evaluation of the sea salt sensitivity integrations. Because this study is one of the first global model studies that does not prescribe

Table 4.1: List of model simulations: The colour coding of the acronyms is equal to the line colours in the figures shown later. In all aerosol chemistry simulations emissions according to M. Schulz are applied.

Acronym	Integration Time	Output Interval	Simulation Description
long-term aerosol physics simulations			
LSCE	1 year	14 hours	sea salt emissions after Schulz
MONAHAN	1 year	14 hours	sea salt emissions after Monahan
AEROCOM	1 year	14 hours	AEROCOM sea salt emissions
LSCE-NUDG	1 year	14 hours	nudged simulation; sea salt emissions after Schulz
long-term aerosol chemistry simulations			
CLIM	5 years	14 hours	chemistry for coarse mode, 'base simulation'
CLIM2000	1 year	14 hours	acronym for the first year of the CLIM simulation
NOHAL	1 year	14 hours	aerosol chemistry without halogens
CL	1 year	14 hours	aerosol chemistry without bromine but with chlorine
MBLNUDG	1 year	14 hours	same as base simulation, but nudged
short-term aerosol physics simulations			
D-LSCE	14 days	30 minutes	sea salt emissions after Schulz
short-term aerosol chemistry simulations			
D-CLIM	14 days	30 minutes	'base simulation', chemistry for coarse mode
D-NOHAL	14 days	30 minutes	as base simulation, but chemistry without halogens
D-CL	14 days	30 minutes	as base simulation, but chemistry with chlorine and without bromine
D-MBLNUDG	14 days	30 minutes	same as base simulation, but nudged

the aerosol pH, but calculates it prognostically as part of the multi-phase chemistry mechanism, in Section 4.3 the resulting aerosol pH distributions are discussed in detail. Section 4.4 is dedicated to reactive halogen chemistry in the marine boundary layer (MBL) evolving in the CLIM and the MBLNUDG simulations. Especially the BrO distributions are investigated here. In Section 4.5 the influence of the reactive halogen chemistry on other trace gases is examined, focussing on ozone chemistry. Results of the short-term integrations are presented in Section 4.6.

4.2 Atmospheric Sea Salt Distributions

Halogen chemistry in the MBL strongly depends on the sea salt emissions, which in turn vary strongly with the wind velocity. Two of the three emission methods included in the MESSy submodel ONLEM are direct functions of the 10m wind speed. These are the methods according to Monahan (1986) and M. Schulz (Guelle et al., 2001), referred to as MONAHAN and LSCE, respectively. The third scenario includes offline emission

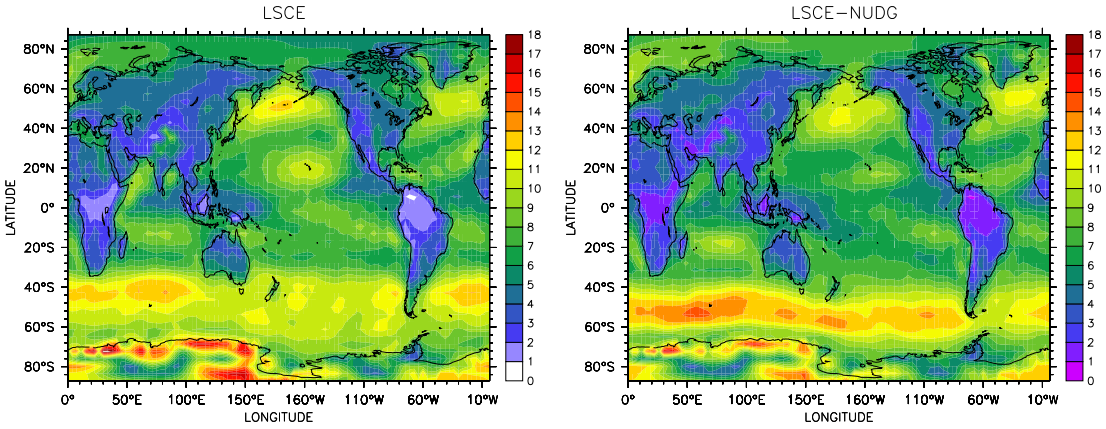

Figure 4.1: Annually averaged 10m wind speed [m/s]. Left: free simulation (LSCE); right: nudged simulation (LSCE-NUDG).

fields provided by the project AEROCOM, which originate from a model simulation by Gong et al. (2003). They used a slightly modified compilation of the Monahan emission function, but not the same as in the LSCE scenario. For each of these three setups a one year integration was performed to compare the resulting sea salt distributions (see first part of Table 4.1). For the simulations the MECCA gas phase chemistry mechanism was used in addition to the aerosol physics provided by the aerosol submodel M7. The dynamics and thus the wind fields produced by a climate model differ from observations by nature. Therefore, as a sensitivity study a fourth nudged simulation has been carried out using the LSCE emission scenario (acronym: LSCE-NUDG). For details about the nudging see Section 3.1.1.

Before comparing the three sea salt emission scenarios, first the underlying wind fields and their deviations depending on the different implied dynamics are evaluated. Figure 4.1

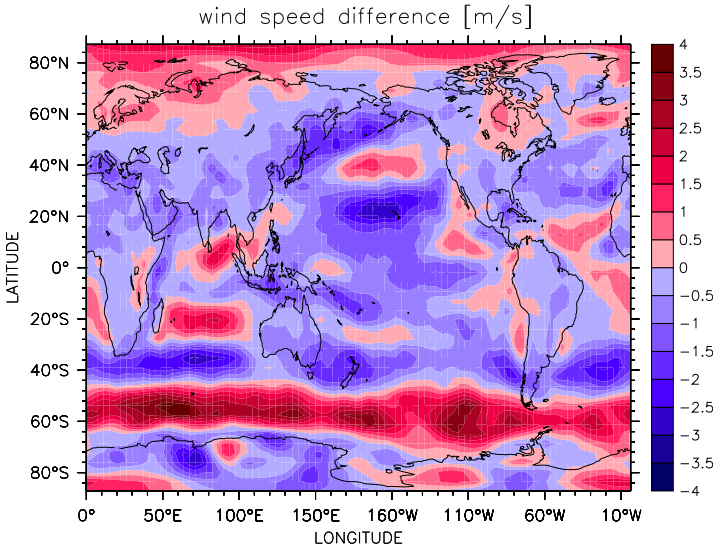

Figure 4.2: Difference of annually averaged 10m wind speed (nudged simulation - free simulation).

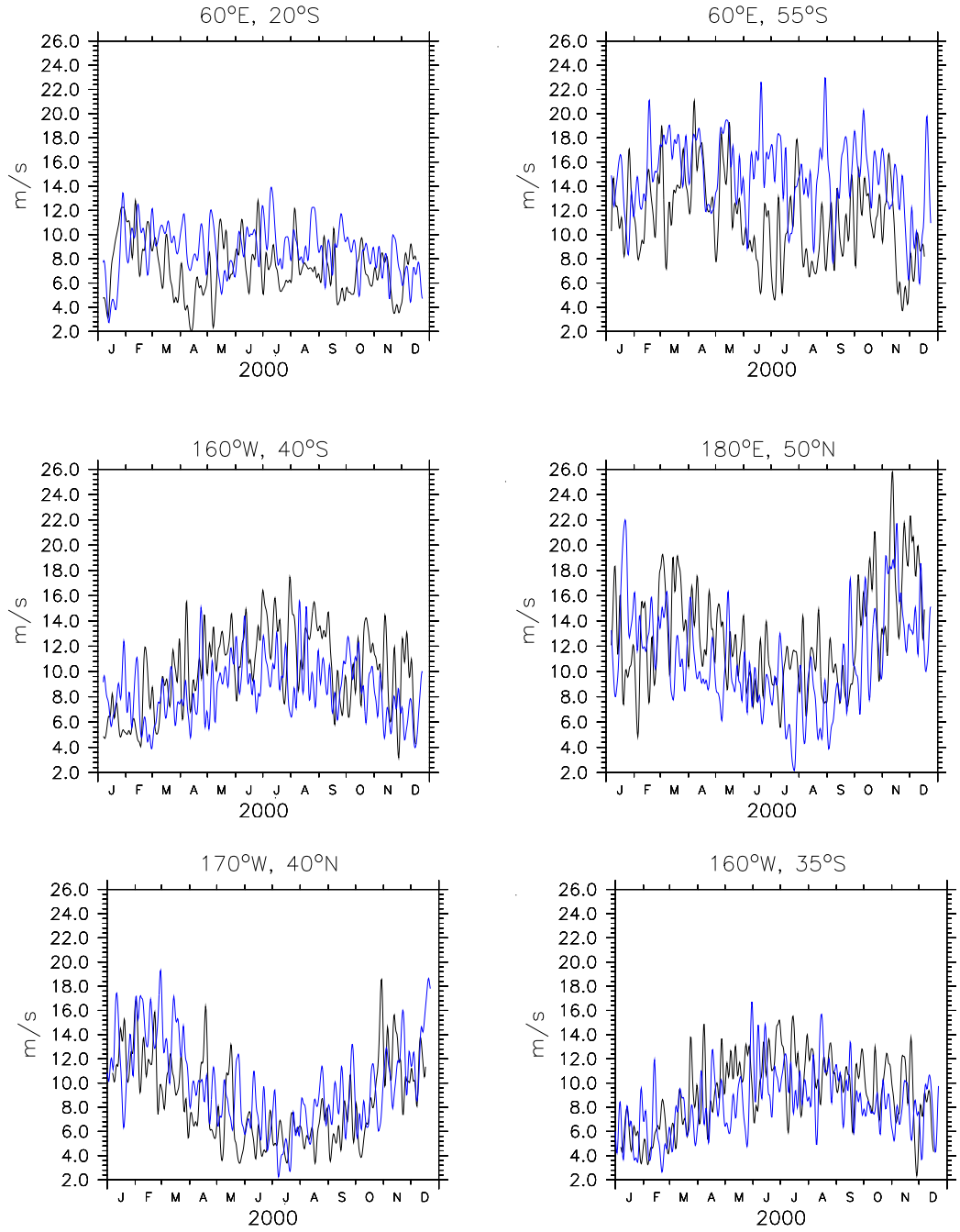

Figure 4.3: Local annual cycles of 10m wind speed at six distinct sites. Black lines represent the climatological simulation and blue lines the nudged integration.

displays the distribution of the annually averaged 10m wind speed in the free simulation and in the nudged simulation. Figure 4.2 shows the differences of the annually averaged 10m wind speed between both integrations. The nudged simulation produces up to 4 m/s higher wind speeds than the free integration in the Southern Ocean storm track region. In contrast, in the latitudinal band between 30°S and 40°S the free integration simulates up to 3.5 m/s higher wind speeds. Similar differences occur in the northern hemisphere, hence the nudged model results suggest stronger meridional gradients of the 10m winds.

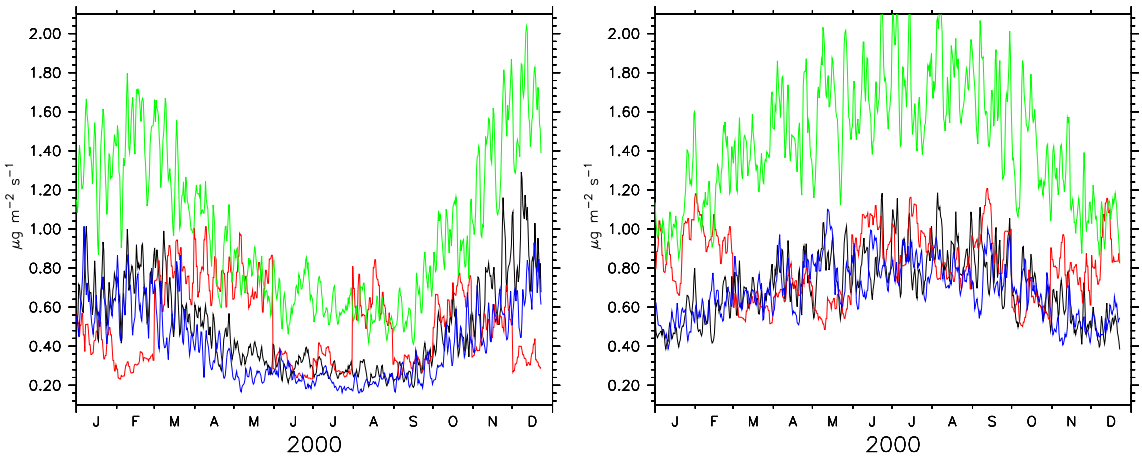

Figure 4.4: Time evolution of hemispherically averaged sea salt mass emission fluxes. Left: northern hemisphere; right: southern hemisphere; black: LSCE simulation; red: AEROCOM simulation; green: MONAHAN simulation; blue: LSCE-NUDG simulation.

The climatological simulation produces higher wind speeds slightly south of the Bering Sea and around 20°N over the Pacific Ocean. The former maximum is shifted more southward in the nudged integration. In addition, the nudged simulation produces higher average wind speed at 20°S in the Indian Ocean and in the North Atlantic (around 55°N). One possible reason is that the meteorological fields introduced by the nudging into the climate model have been calculated at higher resolution (the resolution of the ECMWF model) and therefore represent more realistically spatial gradients. In addition, part of the difference is associated with regular interannual meteorological variability. To look into this in some more detail, the seasonal cycles at some locations where large differences in the annual average of the 10m wind speed occur are shown in Figure 4.3. Black and blue lines denote the climatological and the nudged simulation, respectively. Over the Indian Ocean (60°E, 20°S) the nudged integration produces slightly larger wind speeds during most of the year than the free one. The difference is largest in the autumn (March-May), when the wind speeds can differ up to 6 m/s. As an example for the Southern Ocean storm track region the results at 60°E, 55°S are shown. Here the wind speed of the nudged simulation is larger most of the time reaching maximum differences larger than 15 m/s (the mean difference is 4 m/s). In contrast to the Southern Ocean storm track region, where the nudged simulation produces higher wind speeds throughout the year, the latitudinal band slightly more north (approximately 30°S to 45°S) shows higher wind speeds for the climatological integration. The site at 160°W, 40°S is located exactly in this latitudinal band. The 10m wind speeds of the free simulation are approximately 2 m/s higher than those of the nudged integration. The panels for the locations 180°E, 50°N and 170°W, 40°N show the seasonal cycles for two locations near the peaks showing up in the North Pacific in Figure 4.2. At 170°W, 40°N the winds of the nudged simulation are slightly higher troughout the year, whereas at 180°E, 50°N the winds are higher for the free integration.

To summarise, most of the differences of the annually averaged wind speed shown in Figure 4.2 prevail throughout the year. Nevertheless, the wind speed shows the expected seasonal behaviour reaching maxima in winter and minima in summer. An interesting exception is displayed in the last panel of Figure 4.3 for 160°W, 35°S. From April to

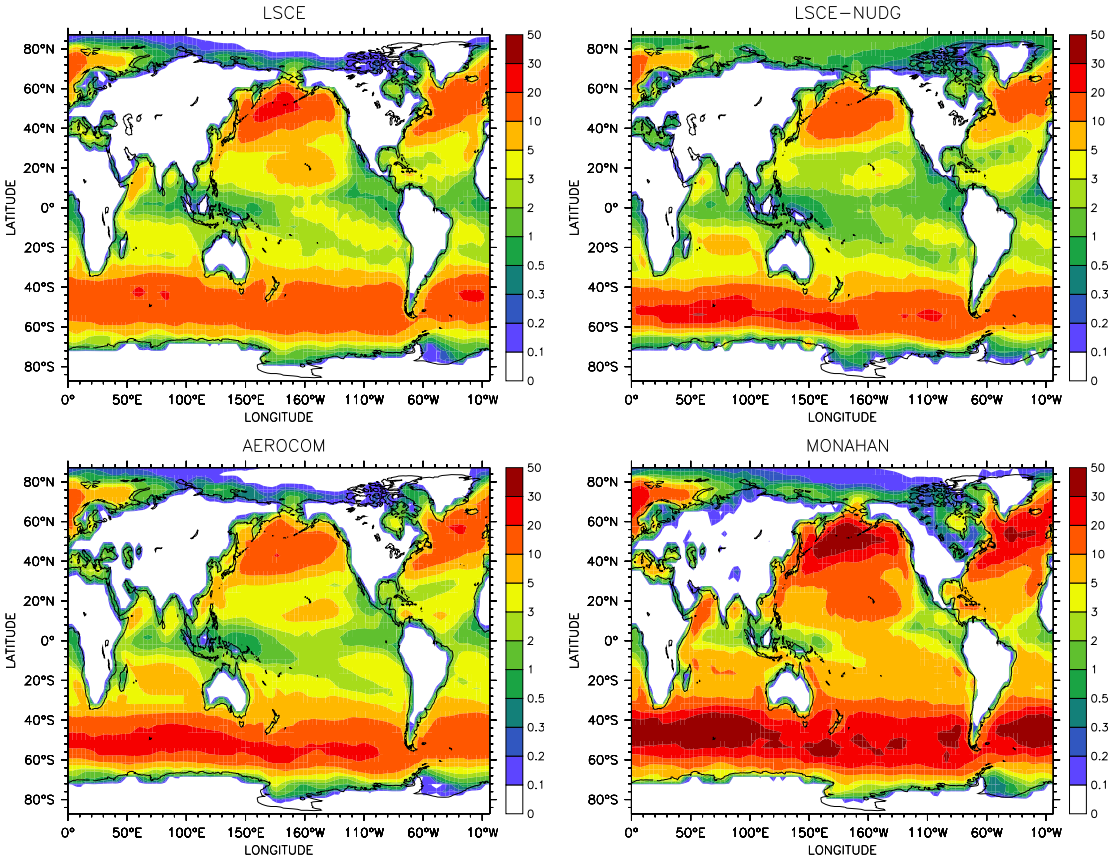

Figure 4.5: Annually averaged sea salt emission fluxes [10^{-10} kg m^{-2} s^{-1}]: upper left: LSCE; upper right: LSCE-NUDG; lower left: AEROCOM; lower right: MONAHAN.

November the free simulation produces approximately 5 m/s higher wind speeds than the nudged one, whereas in the other months the nudged winds are appoximately 5 m/s higher. This is due to a longitudinal shift in the wind speed patterns between the climatological and the nudged integration.

Since sea salt emissions depend on the wind velocity, the differences pointed out for the 10m winds show up in the sea salt emissions as well. Figure 4.4 displays the evolution of sea salt emission fluxes averaged per hemisphere in μg(NaCl) m^{-2} s^{-1} for the four emission scenarios. As in the previous pictures, black and blue lines denote the LSCE and the LSCE-NUDG simulation, respectively. Figure 4.5 shows the distribution of the annually averaged sea salt emission fluxes. The sea salt emission fluxes displayed in the upper panels of Figure 4.5 correspond well to the wind speed patterns (Figure 4.1). The differences between the free and the nudged integration pointed out for the annually averaged wind speed are basically the same for the annually averaged sea salt emission fluxes. The seasonal cycles (Figure 4.4) with maxima during winter as well as the differences between the emission fluxes reflect the differences in the wind patterns (see Figure 4.3). These differences lead to an enhanced sea salt production south of 40°S in the nudged integration and a reduced sea salt production between 20°N and 20°S.

The green and the red line in Figure 4.4 present the MONAHAN and the AEROCOM simulation, respectively. As the MONAHAN emissions are calculated online from the 10m wind speed, they show the same seasonal behaviour as the LSCE emissions. But in

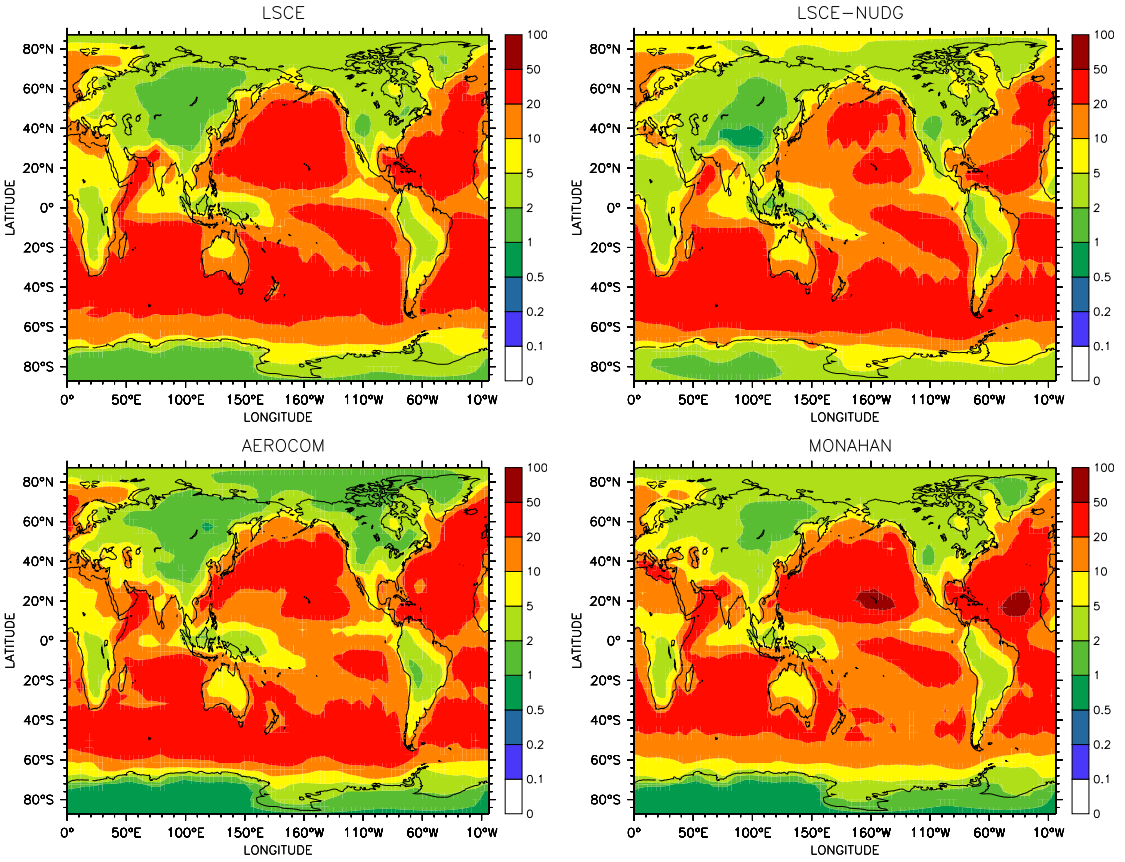

Figure 4.6: Column burdens of annually averaged integrated sea salt mass [mg m^{-2}]: upper left: LSCE; upper right: LSCE-NUDG; lower left: AEROCOM; lower right: MONAHAN.

contrast to the LSCE results the emitted sea salt mass is nearly twice as high, as also indicated by the column burdens shown in Figure 4.6. These differences are larger in the winter when wind velocities are higher. This is in line with several studies (e.g. Guelle et al., 2001) reporting that the Monahan function produces too high sea salt emissions at higher wind speeds. This is the reason why some global models use a combination of the two emission scenarios of Monahan (1986) and of Smith and Harrison (1998) (e.g. Stier et al. (2005) or the TOMCAT model used by Xin Yang in group of A. Cox in Cambridge, UK, pers. comm.).

The mass of emitted sea salt in the AEROCOM scenario is in the range of that emitted in the LSCE simulation. But in contrast to the other three emission scenarios, there is no distinct seasonal cycle in the AEROCOM sea salt emissions. This is remarkable, because the emissions were precalculated for AEROCOM using the Monahan (1986) emission function, thus a similar seasonal cycle was expected. Furthermore, the AEROCOM hemispheric averages show some curious 'jumps' from one month to the other (Figure 4.4).

The annually averaged emission fluxes (Figure 4.5) show basically the same pattern for AEROCOM as for the LSCE emissions. Only in the Southern Ocean storm track region the AEROCOM emissions produce slightly more sea salt mass. The resulting three-dimensional atmospheric sea salt distribution does not only depend on the emission flux but also on the removal processes and on the dynamics. Figure 4.6 shows the annually

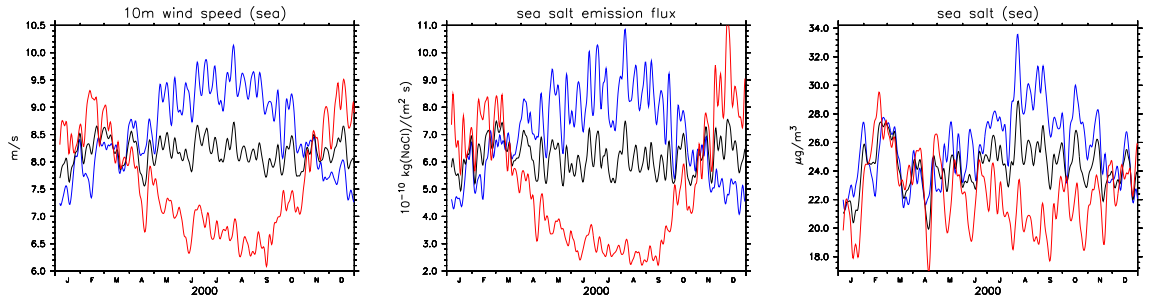

Figure 4.7: Annual variability of the 10m wind speed, the sea salt emission flux and the sea salt mass over the oceans (CLIM simulation). Black: global mean; red: northern hemispheric mean; blue: southern hemispheric mean.

averaged and vertically integrated sea salt mass in mg(NaCl) m^{-2} (i.e. the column burden). The MONAHAN sea salt column burden is the highest of all four scenarios as expected from the higher emission fluxes. The AEROCOM scenario gives the smallest integrated column mass especially over the northern continents. Most interesting are the differences between the LSCE and the LSCE-NUDG integration, because these differences are direct consequences of the nudging and thus they are an effect of a change in the dynamics due to nudging. The aerosol columns over the northern ocean are smaller in the nudged than in the free simulation because of the lower wind speeds in the nudged integration. The sea salt columns over the southern hemispheric ocean are basically the same. Obviously the nudged simulation produces smaller sea salt columns over the continents. Especially high mountains like the Himalaya and the Andes become visible due to smaller columns within the nudged simulation. The nudging data are based on the ECMWF model, which has a higher resolution than the ECHAM5. This means that the height of mountains is better resolved and thus the mountains are a stronger barrier for air mass transport. At least this shows up in the smaller sea salt column burdens over higher mountains. In contrast to this the burdens over Antarctica are higher in the nudged than in the free integration. This may be a result of the higher sea salt emission fluxes in the Southern Ocean storm track as well as an effect of different dynamical patterns. Thus in the following only the simulations using the LSCE emission scenario are considered. As the aerosol chemistry integrations CLIM and MBLNUDG provide the same aerosol physics as the LSCE and LSCE-NUDG simulation, respectively, in the following only the CLIM and the MBLNUDG integration are compared.

To summarise, the LSCE scenario provides the most realistic sea salt emissions of the three different available emissions schemes, since the MONAHAN scenario produces too much sea salt and the AEROCOM scenario lacks a seasonal cycle.

Figure 4.7 displays the large-scale annual variability of the 10m wind speed (left panel), the sea salt mass emission flux (middle panel) and the sea salt mass (right panel) over the oceans. The black, red and blue lines denote the global, northern hemispheric and southern hemispheric means, respectively. The 10m wind speeds do not vary significantly in the global mean. However, for the two hemispheres distinct seasonal cycles with minima in summer and maxima in winter appear. The sea salt emissions strongly depend on the surface wind speed. Thus their annual cycles mirror the wind speed distribution. The non-linear dependence of these two quantities is evident by the fact that in winter the sea salt emission flux is three times as high as in summer, while the wind speed is higher by

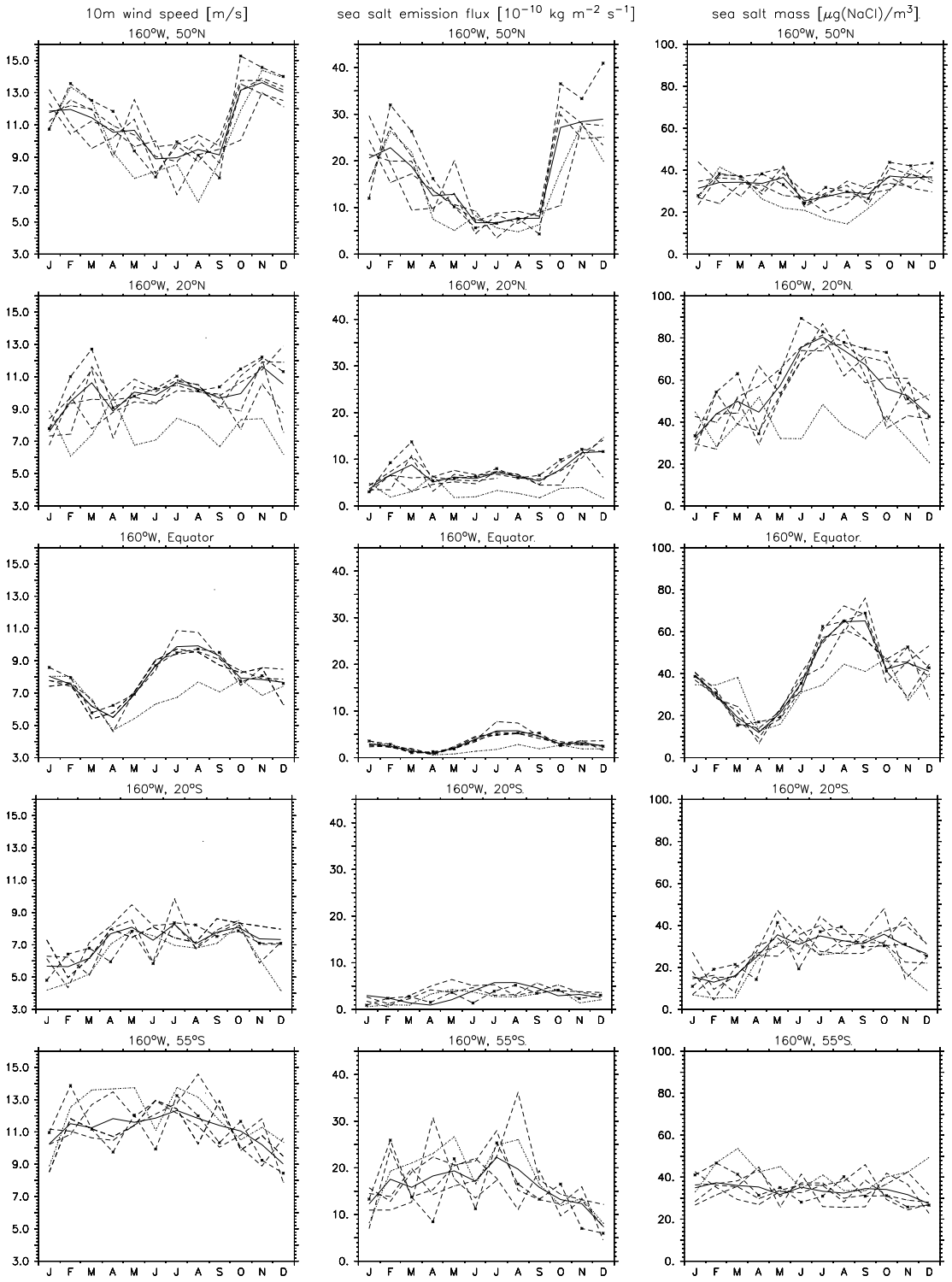

Figure 4.8: Climatological annual variability of the 10m wind speed, the sea salt emission flux and the sea salt mass. Bold line: climatological mean (5 years); dashed line: single years (2000-2004); dotted line: nudged simulation (year 2000).

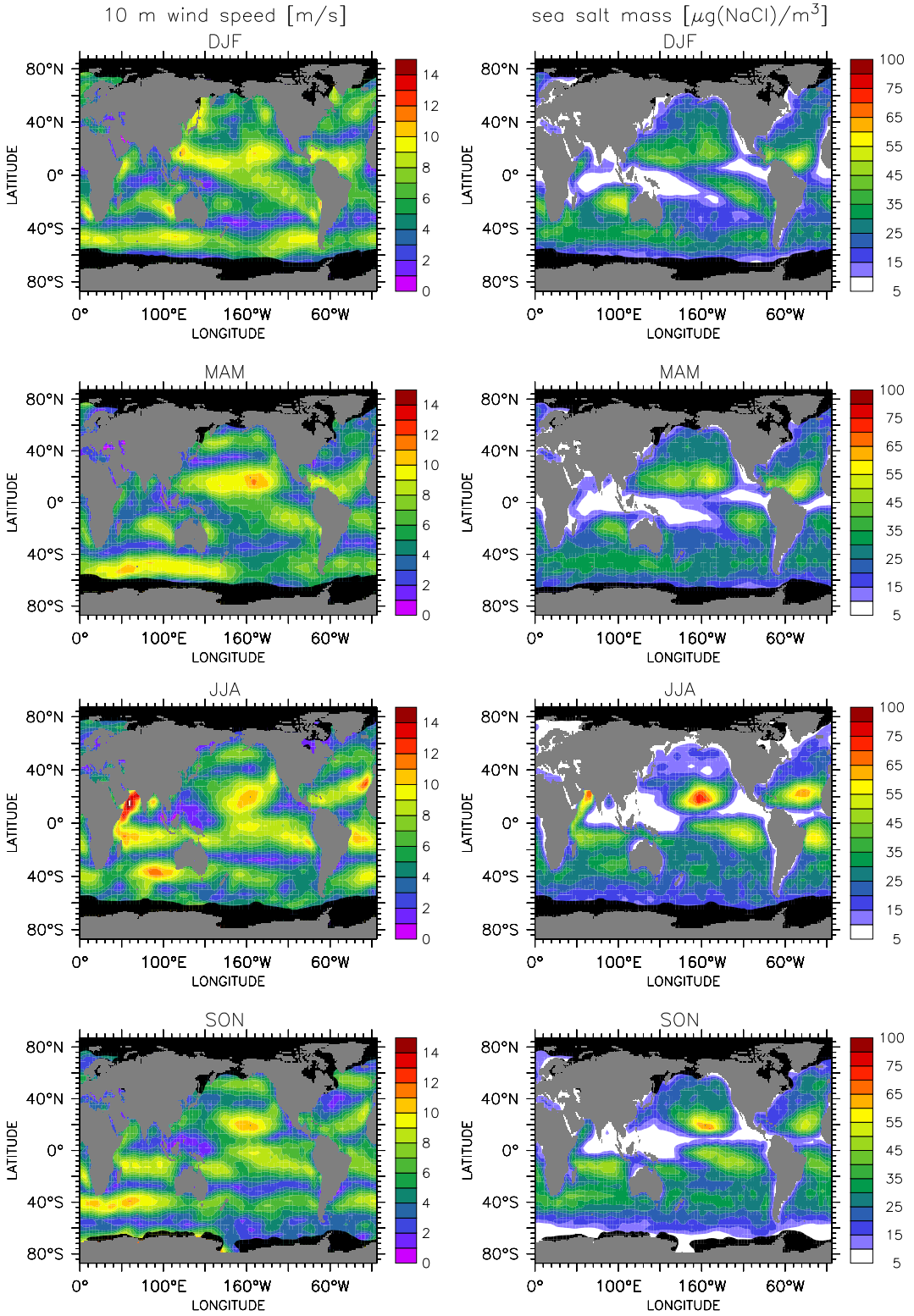

Figure 4.9: Seasonally averaged 10m wind speed and sea salt mass in the marine boundary layer for the climatological simulation (CLIM2000). The title of each panel refers to the months of the respective season displayed.

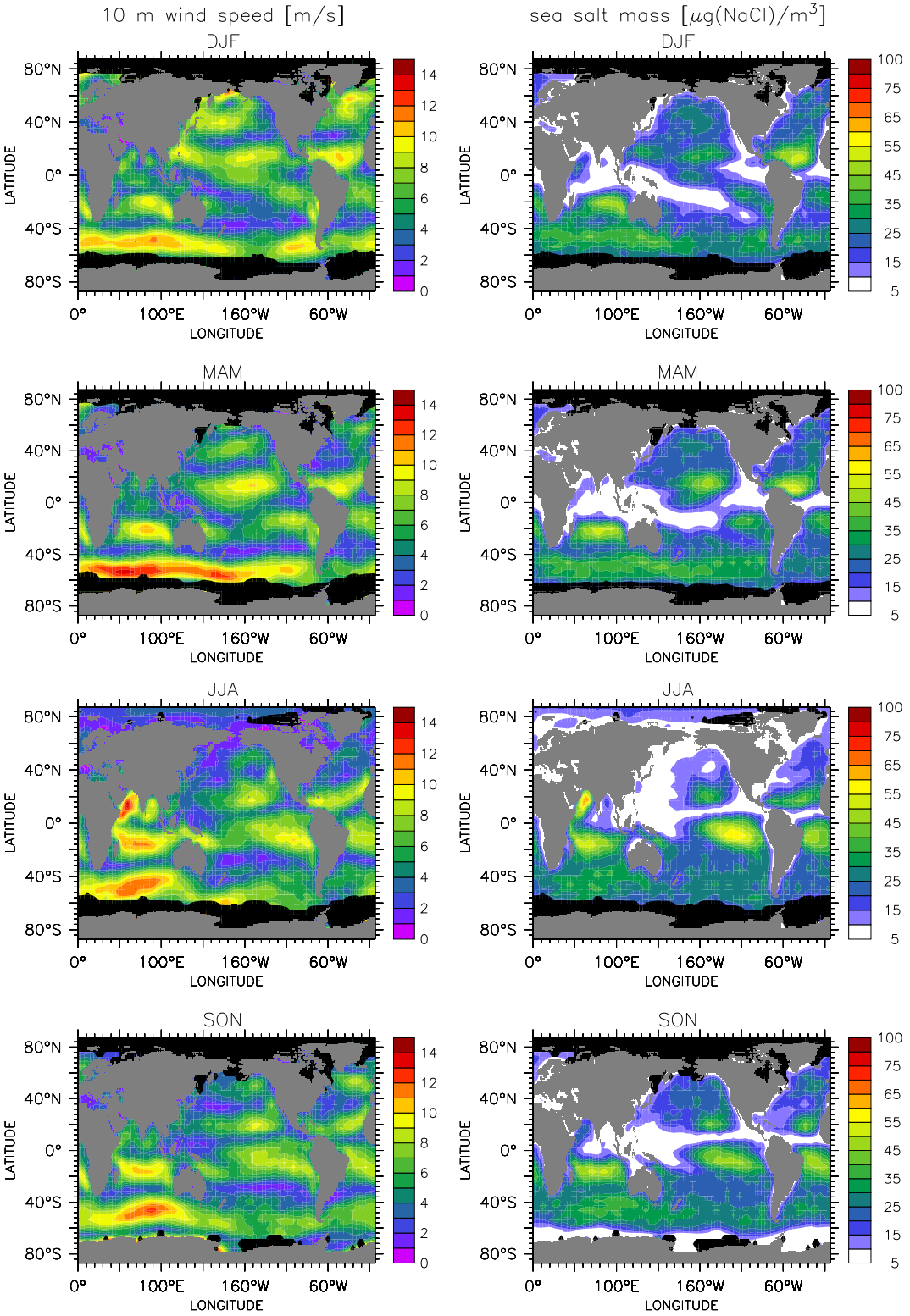

Figure 4.10: Seasonally averaged 10m wind speed and sea salt mass in the marine boundary layer for the nudged simulation (MBLNUDG).

a factor of roughly 1.3 only. The annual cycle of sea salt emissions in both hemispheres does not lead to a distinct cycle of the sea salt mass, which stays roughly constant with only a slight deviation during the period from August to November. The seasonal cycle in the emissions does not result in a marked seasonal cycle in the atmospheric sea salt load, mainly because of the shift of sea salt emissions to larger particles at higher wind speed. These larger particles are rapidly removed by dry deposition, sedimentation and scavenging followed by wet deposition. Thus the sea salt mass in the air is not necessarily higher than at lower wind speed, as confirmed in Figure 4.8. Here the 10m wind speed, the sea salt mass emissions flux and the marine boundary layer mean sea salt mass are displayed. The monthly mean values of the five year average of the CLIM simulation (bold line) as well as the monthly means of each year of this integration (dashed lines, 2000-2004) are shown. The year 2000 is additionally marked by asterisks, because this year is often compared to other simulations. In addition, the monthly means of the nudged integration (dotted line) are displayed. For comparison five sites located at 160°W longitude and at the latitudes of 50°N, 20°N, the equator, 20°S and 55°S have been selected. Obviously, by comparing the two northern locations, higher wind speed leads to higher sea salt emission fluxes, but does not necessarily yield a higher sea salt mass concentration. This is mostly due to the different meteorological conditions (meaning horizontal and vertical transport as well as the above mentioned removal processes) influencing the sea salt mass concentration in addition to the emission flux. This is illustrated by a comparison of the nudged with the climatological parameters at the same site. At the two northern locations and the equator the nudged wind velocity in summer is smaller than for the other simulations. For each individual site this leads to smaller emission fluxes and to lower sea salt mass concentrations.

Figures 4.9 and 4.10 display the seasonal[1] mean wind speed and the marine boundary layer mean sea salt mass for the climatological and the nudged simulation, respectively. Obviously, the wind speed maxima are associated with maxima in the sea salt mass. Thus in the climatological simulation much more sea salt occurs over the northern hemispheric oceans, whereas in the nudged integration more sea salt is abundant in the southern hemispheric storm track region. In addition, a marked maximum in wind speed as well as in the sea salt mass shows up over the Indian Ocean during the period from June to August. The occurrence of this maximum corresponds to the summer monsoon period, which is associated with relatively high wind speeds from the south-west.

It is rather difficult to compare simulation results to measurements and they are even harder to compare if a relatively low model resolution was chosen (as in this study). Whereas measurements are mostly performed at single, distinct locations, the model grid box is approximately 500 km × 500 km wide and represents an average over this area. Nevertheless some comparisons are presented in the following. Stier et al. (2005) showed a comparison of their model results performed with ECHAM5-HAM in T63L31 in a nudged mode with the data of different measurement networks. Their Table 10 is adapted in Table 4.2 of this study and expanded by two additional columns listing the annual average values for the climatological (CLIM) and the nudged (MBLNUDG) simulation. Obviously the present study's results deviate slightly more from measurements than the relatively high resolution model results presented by Stier et al. (2005). They argued that their measurements were in good agreement with the measurements of the University of Miami network. The agreement for the measurement sites for the IMPROVE network was not

[1]DJF: December, January, February; MAM: March, April, May; JJA: June, July, August and SON: September, October, November

Table 4.2: Averaged aerosol mass concentration measurements and model results. The first five columns are adopted from Table 10 of Stier et al., (2005). The last two columns show model results of the present study (CLIM and MBLNUDG simulations).

Location	Longitude [°E]	Latitude [°N]	Measurements [$\frac{\mu m}{m^3}$]	Model (HAM) [$\frac{\mu m}{m^3}$]	Model (MESSy) (CLIM) [$\frac{\mu m}{m^3}$]	Model (MESSy) (MBLNUDG) [$\frac{\mu m}{m^3}$]
IMPROVE Network[a]						
Acadia	-68.3	44.4	0.6	6.5	15.9	14.2
Badlands	-101.9	43.7	0.0	0.2	0.8	0.4
Bandelier	-106.3	35.8	0.0	0.3	0.9	0.6
Big Bend	-103.2	29.3	0.2	1.7	1.7	1.1
Boundary Waters	-91.5	48.0	0.1	1.0	0.6	0.5
Denali	-149.0	63.7	0.1	0.5	1.0	1.1
Everglades	-80.7	25.4	1.0	10.1	26.9	16.9
Gila Wilderness	-108.2	33.2	0.1	0.8	2.0	1.2
Mammoth Cave	-86.3	37.3	0.2	0.8	1.4	0.7
Mount Rainier	-122.1	46.8	0.2	2.7	6.3	5.9
Okefenokee	-82.1	30.7	0.7	4.8	7.1	4.5
Virgin Island	-64.8	18.3	1.7	13.9	45.5	37.9
University of Miami Network						
Catham Island, New Zealand	-176.5	-43.9	13.8	27.3	30.9	31.2
Cape Point, South Africa	18.5	-34.3	10.4	18.3	32.5	29.6
Cape Grim, Tasmania	144.7	-40.7	19.8	22.6	25.6	23.1
Invercargill, New Zealand	168.4	-46.4	7.1	20.9	24.1	28.2
Marsh, King George Island	-58.3	-62.2	3.5	18.1	17.6	26.3
Marion Island	37.8	-46.9	10.5	45.6	38.8	43.8
Mawson, Antarctica	62.5	-67.6	0.3	0.8	5.35	18.7
Palmer Station, Antarctica	-64.1	-64.8	3.2	9.1	7.5	13.0
Reunion Island	55.8	-21.2	11.6	23.2	13.4	42.6
Wellington, New Zealand	174.9	-41.3	10.4	15.7	21.3	22.1
Yate, New Caledonia	167.0	-22.1	31.9	18.0	29.3	27.3
Norfolk Island	168.0	-29.1	26.0	19.0	31.3	26.4
American Samoa	-170.6	-14.2	5.5	9.5	17.8	12.9
Midway Island	-177.4	28.2	14.3	17.7	42.2	23.5
Oahu, Hawaii	-157.7	21.3	14.9	21.1	63.1	40.2
Cheju, Korea	126.5	33.5	16.4	11.5	14.9	10.2
Hedo, Okinawa, Japan	128.2	26.9	23.3	15.4	29.2	19.6
Fanning Island	-159.3	3.9	14.8	17.7	22.5	23.6
Barbardos	-59.4	13.2	17.4	21.5	45.1	41.0
Izana, Tenerife	-16.5	28.3	0.0	20.1	42.3	31.1
Bermuda	-64.9	32.3	13.4	16.0	26.8	21.2
Heimaey, Iceland	-20.3	63.4	25.7	14.3	19.0	15.8
Mace Head, Ireland	-9.9	53.3	19.8	18.4	33.4	28.4
Miami	-80.2	25.8	8.5	10.6	26.9	17.8

[a] *http://vista.cira.colostate.edu/improve*

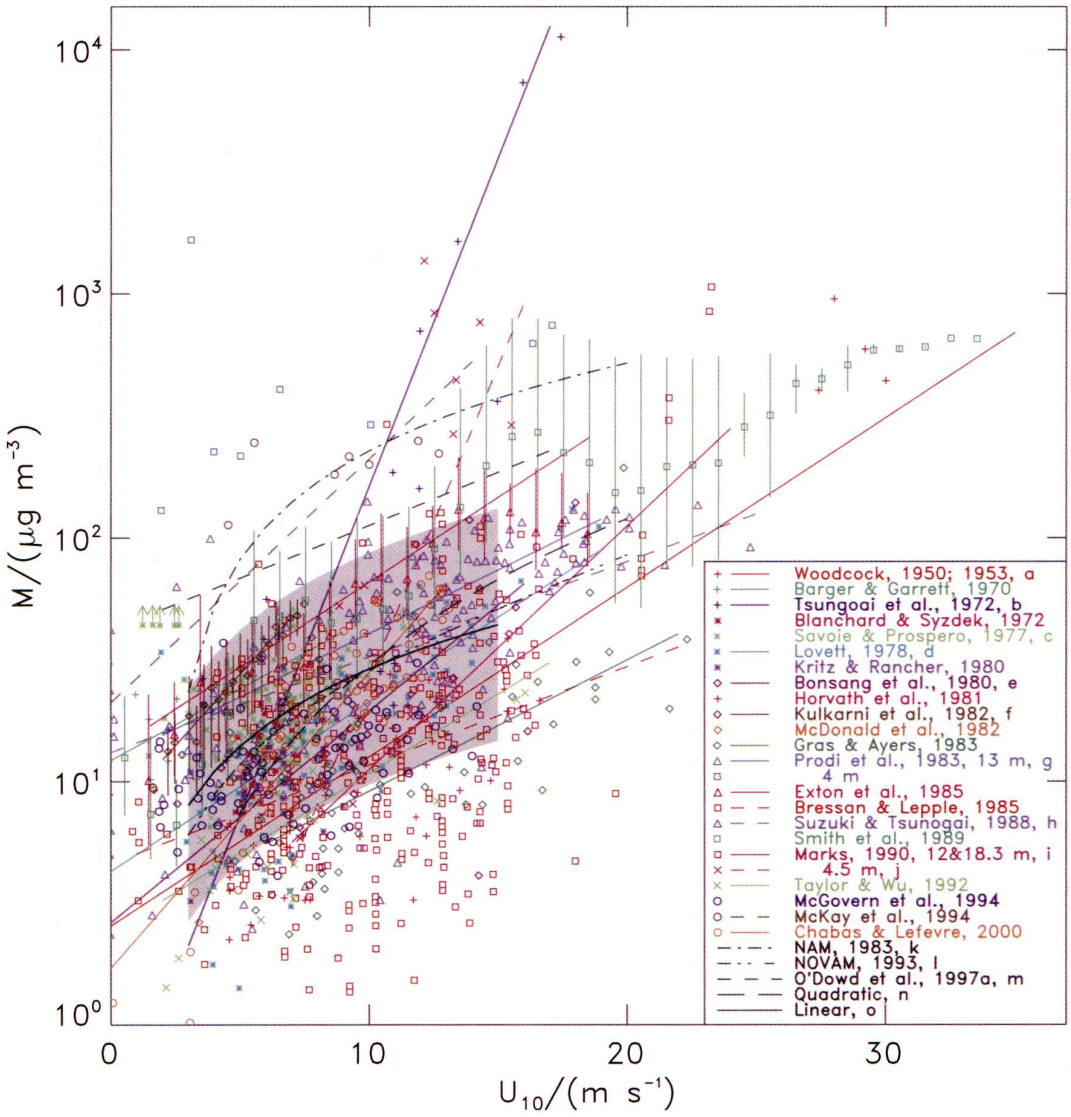

Figure 4.11: Sea salt aerosol mass against 10m wind speed, from different measurements. Figure 17 (page 130) of Lewis and Schwartz, 'Sea Salt Aerosol Production: Mechanisms, Methods, Measurements and Models - A Critical Review', 2004, Copyright [2004] American Geophysical Union. Reproduced by permission of American Geophysical Union.

so well because most of these sites are continental, and thus numerical diffusion along the strong gradients of sea salt along the coast lines may explain these differences. This argument is probably valid for this model study as well. The resolution of the model study is expected to have a significant influence. Since Stier et al. (2005) used a horizontal resolution twice as high it seems reasonable that their model results fit better with the measurements than the results from the present study. The models ECHAM5-HAM and ECHAM5/MESSy have some parts used for aerosol modelling in common, whereas other parts used for aerosol modelling are different: they both use the same base model (ECHAM) providing the dynamics, the same microphysical core for the aerosol calculation (M7) and similar emission and dry deposition methods. However, other processes

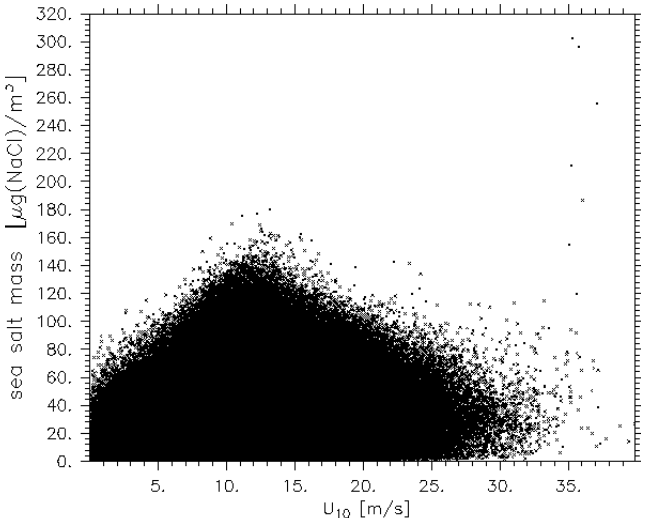

Figure 4.12: Scatter plot of sea salt mass concentration versus 10m wind speed for the CLIM simulation.

such as wet deposition and sedimentation as well as the sulphate chemistry are modelled differently. The displayed values for the nudged simulation generally are in slightly better agreement with the measurements than the free integration especially for the locations of the IMPROVE network. This again points to the fact that the nudged simulation creates more realistic wind fields than the climatological one. Additionally it has to be noticed, that the number of sea salt aerosol measurements over the remote ocean is very small.

Most data are obtained in measurement campaigns limiting the validity of these data to a specific region and to a time frame of a few weeks. Figure 4.11 shows a figure taken from Lewis and Schwartz (2004). They review measurements and model results related to sea salt. The figure displays measurements of sea salt aerosol mass plotted against the 10m wind speed. Most of the measurements are in the range of approximately 5 to 100 $\mu g/m^3$, which correspond to the modelled sea salt mass concentrations of this study. As also reviewed by Lewis and Schwartz (2004), most of the authors assume a linear dependence between the logarithm of the sea salt mass and the wind speed yielding increased sea salt mass for increased wind speed. But almost all of these measurements were taken in situations, when the wind speed was below of 15 m/s. The simulations performed during the present study show that the sea salt mass increases up to a wind speed of approximately 15 m/s and decreases at higher wind speed. This is illustrated in Figure 4.12, which shows the sea salt mass in the lowest model layer over the oceans plotted against the 10m wind speed for the CLIM simulation. Even though this scatter plot has no statistical meaning, it is obvious that the sea salt mass decreases for wind speeds higher than 15 m/s. The main reason for this is a combination of more efficient removal processes and faster vertical and horizontal transport. It may also partly be a model artefact associated with the modal description of the aerosol: the mean radius is shifted to larger values at higher wind speeds causing smaller particles in the same mode to sediment relatively faster. Thus the modal treatment of the aerosol distribution may lead to an overestimation of the removal processes at higher wind speed.

Number concentrations of sea salt aerosol are reported more often than sea salt masses. Figures 4.13 and 4.14 show the modelled seasonal averaged number concentrations of

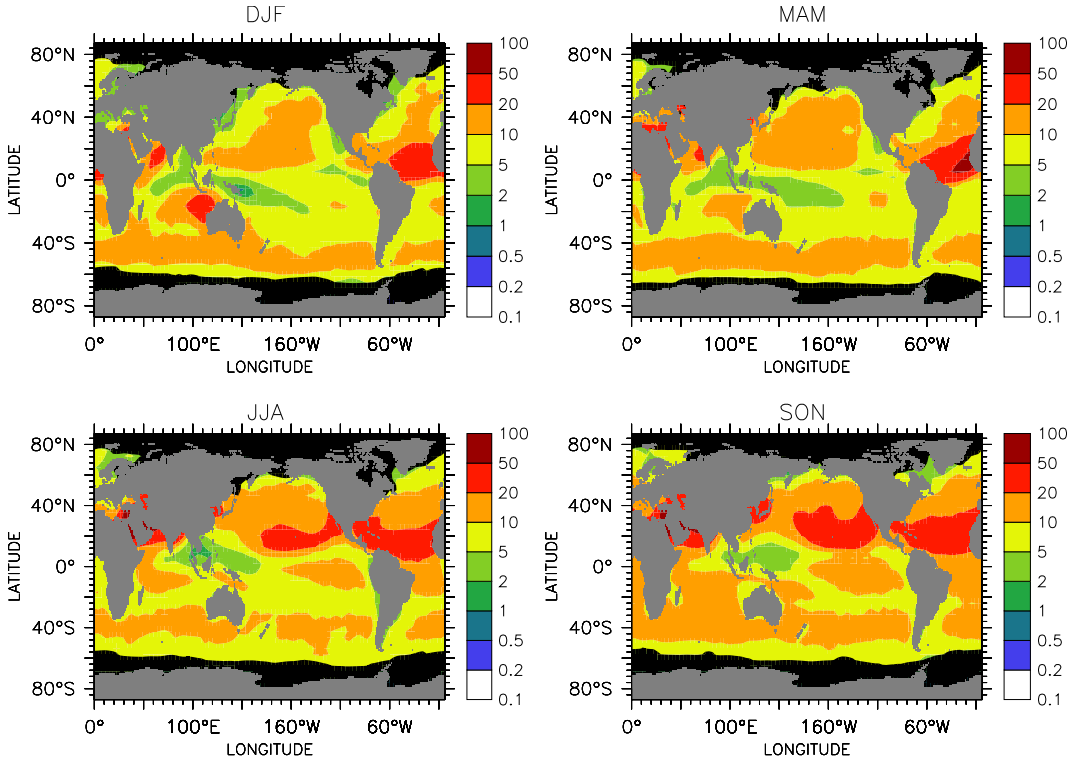

Figure 4.13: Seasonal averages of sea salt (coarse mode) aerosol number concentrations [cm^{-3}] in the lowest model layer for the climatological simulation (CLIM2000).

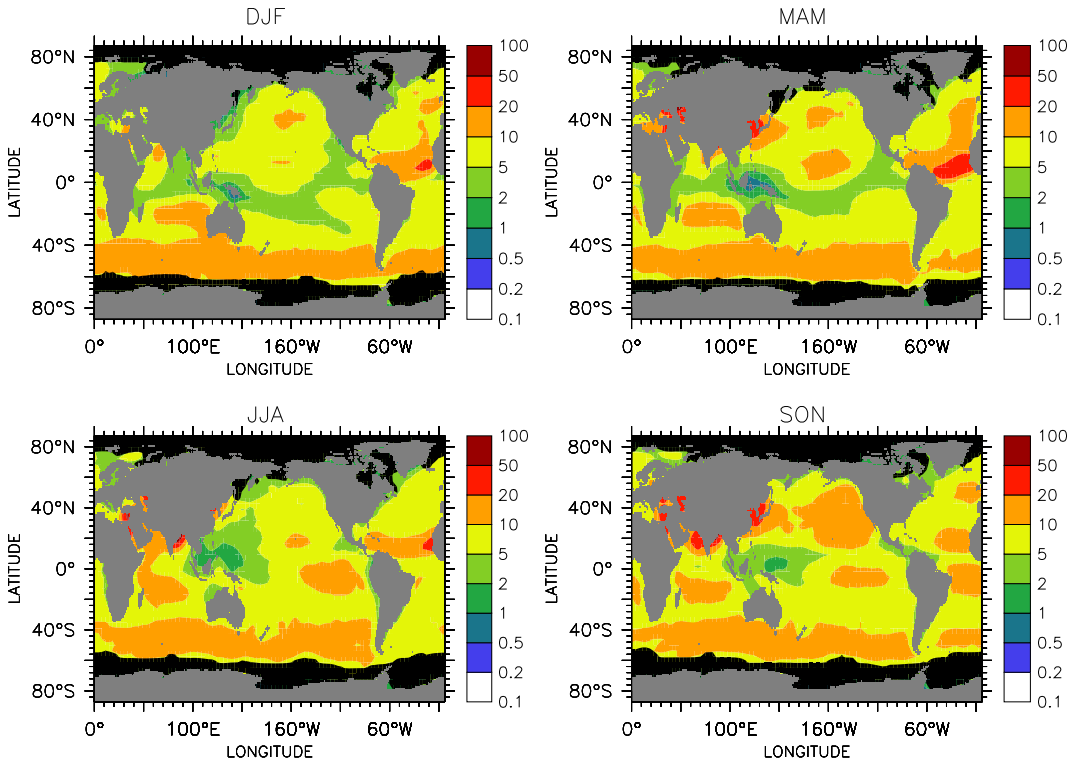

Figure 4.14: Seasonal averages of sea salt (coarse mode) aerosol number concentrations [cm^{-3}] in the lowest model layer for the nudged simulation (MBLNUDG).

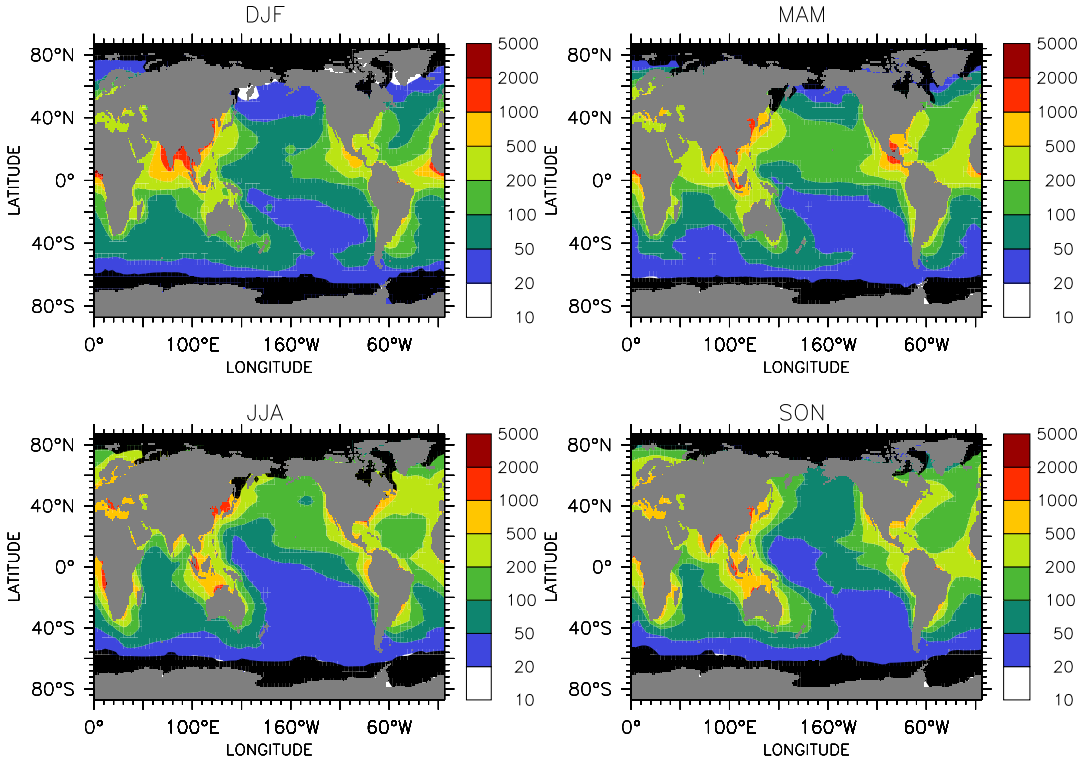

Figure 4.15: Seasonal averages of the sum of accumulation and coarse mode number concentrations [cm^{-3}] in the lowest model layer for the nudged simulation (MBLNUDG).

coarse mode aerosol for the climatological and the nudged simulation, respectively. Lewis and Schwartz (2004) summarise, that number concentrations ranging from below 1 cm^{-3} to 200 cm^{-3} have been reported, which would be in rough correspondence with the modelled number concentrations. Most of the reviewed measurements were between 1 cm^{-3} to 20 cm^{-3}. There are some difficulties in comparing measured data with the model results, as most of the time the measured and the modelled radii intervals do not exactly match. In addition, the measurements have some uncertainties, for example, a time dependence seems to be evident with smaller number concentrations reported in the early studies increasing to larger ones in more recent studies. Small values were reported in the 1970s and 1980s from < 1 cm^{-3} up to 10 cm^{-3} as an upper limit (for details about these studies see Lewis and Schwartz, 2004). More recent studies show higher values. O'Dowd and Smith (1993) measured concentrations in a range of 2 cm^{-3} to 80 cm^{-3} in October/November 1989 over the North-east Atlantic for sea salt aerosols ranging from 0.01 μm to 3 μm. Therefore the measured number concentrations correspond to the sum of the number concentrations of the coarse and the accumulation mode. Thus Figure 4.15 shows the sum of the seasonal number concentration averages of the accumulation and the coarse mode for the nudged simulation. The modelled number concentrations are higher than the measured ones from O'Dowd and Smith (1993) by a factor of 2. From the figures shown in this article, a mean particle number concentration for coarse mode aerosol (0.6 μm $-$ 3 μm) of around 5 cm^{-3} - 10 cm^{-3} can be deduced. For the North-east Atlantic the model predicts concentrations between 10 cm^{-3} - 20 cm^{-3} for the climatological and 5 cm^{-3} - 20 cm^{-3} for the nudged simulation, thus somewhat overestimating the measured number concentration. O'Dowd (2002) reports a constant particle concentration of 50 cm^{-3} for particles

larger than 0.3 μm for the Irish coast. This relatively high value is underpredicted by the model studies and should be mostly attributed to a coastal effect (e.g. enhanced wave breaking), which can not be resolved in a model containing gridboxes of approximately 500 km $\times$ 500 km. Bates et al. (1998) and Murphy et al. (1998) both report measurements from ACE1[2]. Even though taking part in the same campaign they report slightly different values. Bates et al. (1998) measured number concentrations of about 15 cm^{-3} in clean marine air and 23 cm^{-3} in continentally influenced air for a particles > 0.3 μm. Murphy et al. (1998) report concentrations of 30 cm^{-3} for particles > 0.16 μm. This is in good agreement with the model results of the present study. Guazzotti et al. (2001) measured aerosol during the Indian Ocean Experiment from February to March 1999 and found values from less than 1 cm^{-3} to 5 cm^{-3}. The model results indeed show smaller aerosol concentrations over the Indian Ocean, but again the modelled number concentrations for sea salt are overestimated compared to the measurements. To summarise, the model is in fair agreement with the reported measurements considering its limitations. It tends to overestimate the mass as well as the number concentrations of the sea salt aerosol mode. This effect is smaller in the nudged simulation, which again points to the fact that the nudged simulation is more realistic regarding the dynamics. It also provides some confidence that in future model applications at higher resolutions the model results will improve. The differences between the nudged and the climatological integrations have to be kept in mind (especially higher emission between 40°S and 60°S and smaller column burdens over the North Pacific) when discussing the halogen chemistry.

4.3 Aerosol pH

The aerosol pH is a key factor with regard to aerosol chemistry. It is rather difficult to measure, and in most model studies requiring the aerosol pH it is prescribed or deduced with a rough parameterisation. Thus quantitative knowledge about the aerosol pH (especially its global distribution) is very scarce. As the aerosol chemistry is calculated explicitly within this model study, the H^+ concentration is calculated prognostically. To evaluate the influence of the chemical composition on the results, integrations with different chemical setups have been performed (see Section 'long-term aerosol chemistry simulations' in Table 4.1). In addition to these simulations comprising the complete chemistry mechanism as listed in Appendix C (the CLIM and MBLNUDG simulations), an integration without halogen chemistry but including aerosol chemistry was carried out (the so-called NOHAL simulation). Futhermore an integration including chlorine but neglecting bromine chemistry was performed (the CL simulation). Figure 4.16 displays annually averaged values of the fully prognostically calculated aerosol pH as determined by these four different model setups. The aerosol in the NOHAL simulation is clearly much more acidic as in the other integrations, thus illustrating the importance of the HCl/Cl^- buffer of the sea salt aerosol. As discussed in Section 2.0.2, the Cl^- is able to buffer the aerosol pH to a significant amount. If a gas phase acid enters the aerosol phase and the aerosol is sufficiently acidified, HCl is formed, which degases because of its relatively high volatility, consuming an H^+ and thus keeping the aerosol pH constant. This works as long as chloride is still abundant in the aerosol to a sufficient amount. This process is missing in the simulation without halogens, thus the condensation of a gas phase acid onto the aerosol directly leads

[2]The First Aerosol Characterization Experiment (ACE1) took place from 15th November to 14th December 1995, in a region south-south-east from Tasmania, Australia in the Southern Ocean.

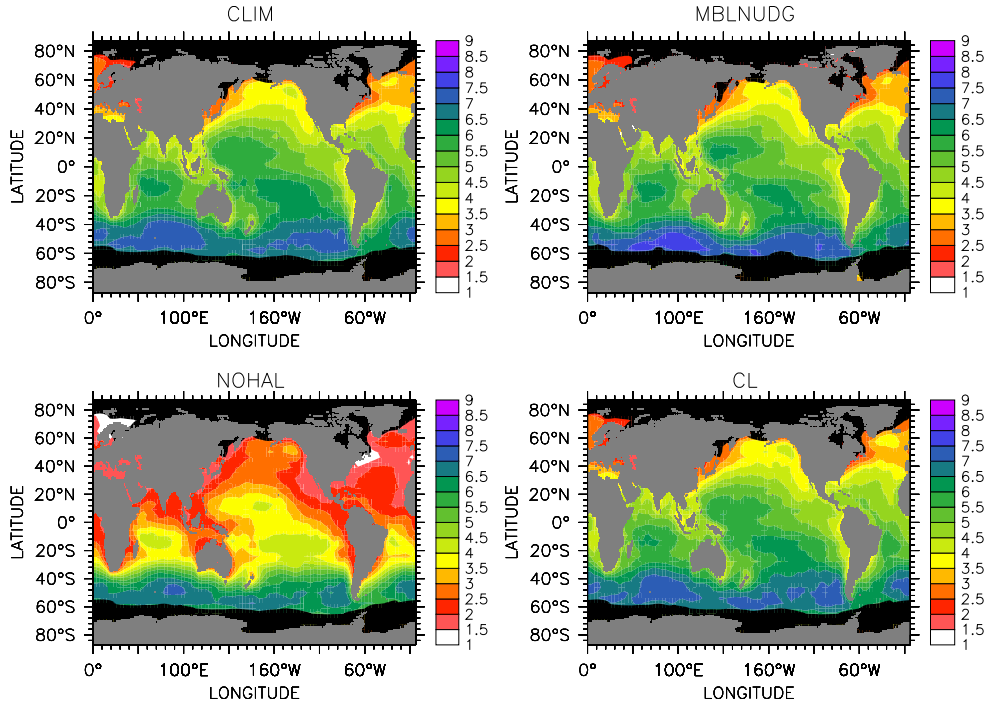

Figure 4.16: Annually averaged aerosol pH shown for the four integrations CLIM, MBLNUDG, NOHAL and CL.

to a further acidification of the aerosol and thus to very low aerosol pHs.

In general two major factors determine the aerosol pH: the abundance of gas phase acids and the emission of new alkaline sea salt particles. The combination of both factors leads to the north-south gradient in the aerosol pH (see Figure 4.16). In the northern hemisphere gas phase acids are relatively abundant. Apart from DMS oxidation, gas phase acids originate predominantly from the outflow of big urban and industrial centers, mostly located in the northern hemisphere. This air enriched in acids and/or their precursors is transported over the ocean by the synoptic weather systems and provides enough acidity to lower the aerosol pH even over the remote ocean. As the equator is a barrier for air mass transport and the acid production in the southern hemisphere is smaller, acids are less abundant in the southern hemisphere and the aerosol is less acidic. The sea water pH is around 8 and the aerosol pH would be at approximately 10.5 through the equilibration with ambient moisture, without taking up any acids. Therefore the emission of sea salt aerosol yields more alkaline aerosol. Thus the aerosol is expected to be more alkaline where high wind speeds lead to high sea salt emissions. As discussed above the nudged simulation produces higher wind speeds in the region between 40°S and 60°S and consequently higher sea salt emissions, showing up in Figure 4.16 as a band of slightly higher aerosol pH than in the CLIM and CL simulations. In the northern hemisphere the same effect would be expected, since the climatological simulation produces higher wind speeds over the south of the North Atlantic and North Pacific Oceans. The aerosol pHs for the three simulations comprising chlorine chemistry look quite similar in the northern hemisphere, again due to the HCl/Cl^- buffer. In the nudged simulation, in which less sea salt is emitted, this buffer keeps the pH in the same range as in the simulations with higher sea salt emission, as the fresh sea salt aerosol is rapidly acidified because of the high acid supply in the

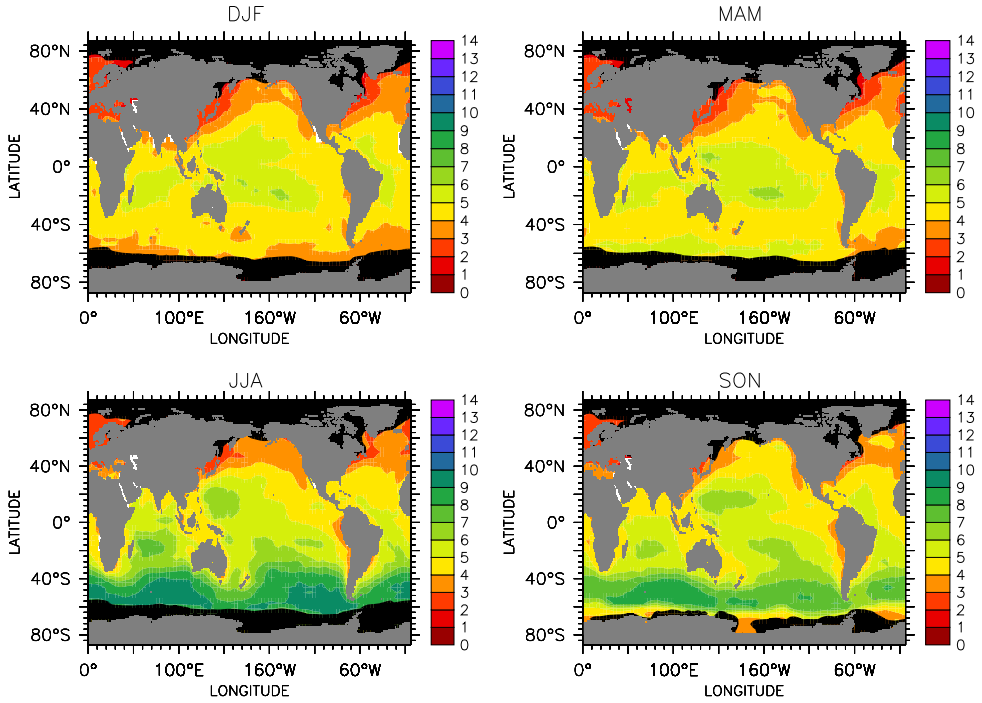

Figure 4.17: Seasonal averages of the aerosol pH for the nudged simulation (MBLNUDG).

northern hemisphere, i.e. within a range where the HCl/Cl^- buffer is active. Therefore the effect that the aerosol is more alkaline in the simulations creating higher wind speeds is not visible in the northern hemisphere. Figure 4.17 displays the seasonal changes of the aerosol pH. As the pH values do not differ much, only the aerosol pHs for the nudged simulation are shown. Distinct seasonal differences show up in this figure. The aerosol is significantly more acidic in the northern hemisphere than in the southern hemisphere and the aerosol is always highly acidified at the east coasts of America and Asia as well as in the European Atlantic region reaching values lower than 3. Over the North Atlantic the sea salt aerosol is acidified down to pH values lower than 4 throughout the year, whereas the aerosol in the North Pacific region is slightly less acidic especially in autumn. The differences between the two oceans may be related to the different size of the oceans. As the distance between the continents is less in the Atlantic region, the polluted air masses cross the ocean more easily. Since the region and thus the amount of aerosol that needs to be acidified is much smaller, the aerosol is more constantly acidified over the Atlantic Ocean.

In contrast to the northern hemisphere, the southern hemispheric aerosol pH shows a marked seasonal cycle, mainly driven by the Southern Ocean storm track region. The aerosol is highly alkaline (up to a pH of 11) in the southern hemispheric winter, when the highest wind speeds occur. A gradient forms from this region of high alkalinity to the equator, where a pH of around 6 prevails. The alkalinity of the storm track region is smaller in the spring and autumn months. The gradient completely disappears in the southern hemispheric summer, and the whole hemisphere is characterised by an aerosol pH of around 4 to 6. This is caused by the lower wind speeds in the summer months reducing sea salt emissions and thus production of alkalinity within the aerosol. The very high pH values developing in the Southern Ocean are to some degree a model artefact. As

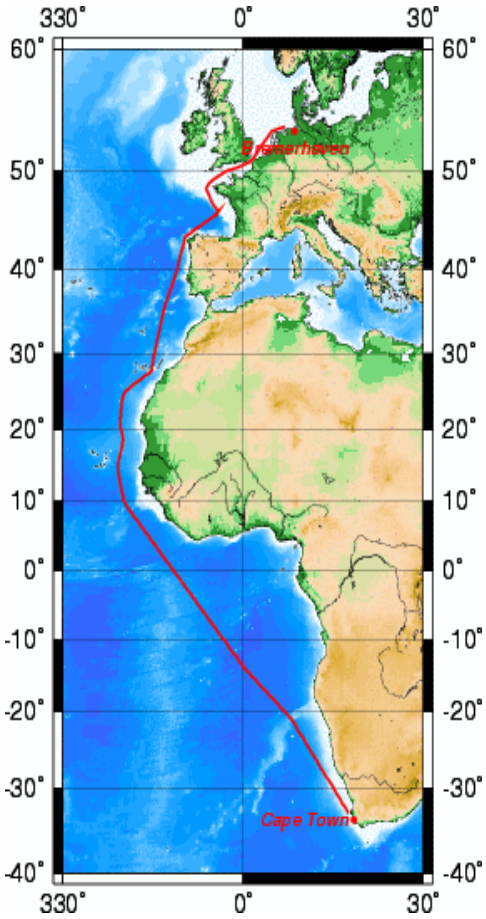

Figure 4.18: Cruise of the research vessel 'Polarstern' from Bremerhaven, Germany to Cape Town, South Africa in October 2003 (Keene et al. 2005, EGU conference).

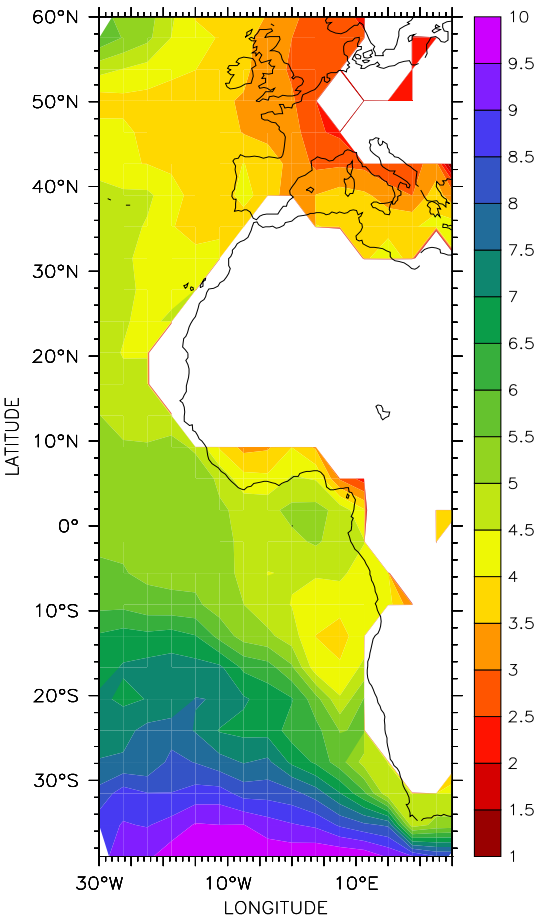

Figure 4.19: Modelled aerosol pH during October 2000 for the nudged simulation (MBLNUDG).

explained in the discussion about the sea salt mass distribution (Section 4.2) high wind speeds do not necessarily lead to a higher sea salt load, because the emitted particles are larger and thus are removed very efficiently from the atmosphere. In nature the large sea salt particles are emitted by the ocean and fall back to the sea just before they can equilibrate with their environment. These particles would not be a source of any alkalinity for the sea salt remaining in the air. Intrinsic to numerical simulations, process splitting is the only way in ECHAM5/MESSy to simulate the complex system. In the model, emissions of the aerosol ions (which are the source of alkalinity) into the coarse mode are calculated first within MECCA-MBL. Because of the modal treatment, a mixture of freshly emitted and aged sea salt evolves instantaneously. Afterwards this new mixture is subject to the removal processes dry deposition, sedimentation and wet deposition. On average this leads to a more efficient removal of aged sea salt and a larger supply of fresh salt in the model compared to the natural process. To summarise, this error originates from the process splitting. It causes an overestimation not only of the alkalinity but also of the halide ion source provided by sea salt in the model. It is planned to reduce this

error in future studies by calculation of a net aerosol ion emission from the sum of sea salt emission and the dry removal fluxes.

Measurements of sea salt aerosol pHs are very scarce. Pszenny et al. (2004) report measurements at Hawaii, USA between 4th and 29th September 1999 with pH values ranging from 4.5 to 5.4. This fits reasonably well with the model results in which pH values range between 4 and 6 throughout the year. Keene and Savoie (1998) present measurement results for a site directly located at the coast of Bermuda obtained in a campaign during April and May 1996. The pH ranged between 2.48 and 3.48. During a campaign in May 1997, aerosol pHs for the same site ranged from approximately 3.5 to 5.3 (the upper limit of the measurements) (Keene et al., 2002). This is in the range of the aerosol pH of the CLIM simulations during May (not shown). On a poster at the EGU General Assembly 2005 Keene et al. (2005) showed aerosol pH values measured during a ship cruise from Bremerhaven, Germany to Cape Town, South Africa in October 2003. They reported pH values around 2 to 3.5 for the European influenced air. Along the northern and the southern African west coast they measured pH values of approximately 4 to 4.5. The aerosol pH was highest in the ITCZ (inner tropical convergence zone) region with a value of approximately 4.8. Figure 4.18 shows the cruise track and Figure 4.19 displays the modelled mean aerosol pH for October 2000. In the model simulation a similar pH distribution along the cruise track is evident compared to the measurements, with highest pH values in the ITCZ, smaller ones at the northern and southern African west coast and the lowest values in regions where air masses are influenced by European outflow.

To conclude, the results of the model simulations fit reasonably well with the few available sea salt aerosol pH measurements. However, the measurement sites are exclusively located near to the coast. Thus a comparison of the modelled aerosol pH values over the open and remote ocean and thus an evaluation of the degree of the overprediction of hydrogencarbonate emissions by the model is presently not possible.

4.4 Reactive Halogen Chemistry

The parameters driving halogen chemistry, such as wind speed, sea salt emissions and the aerosol pH, have already been discussed in some detail so far. In this section the chemistry of the reactive halogen species is analysed. Since BrO is often used as an indicator for reactive halogen chemistry, the section focuses on BrO. As discussed in detail in Chapter 2, BrO is abundant where a high sea salt production and a sufficient supply of acids concur. This is confirmed by Figure 4.20 displaying the global annual mean BrO distribution on a logarithmic scale. The CLIM2000 simulation, showing the highest wind speeds over the North Pacific, produces most fresh sea salt and thus the highest annual mean BrO concentrations in this region. A second BrO maximum between 0°N and 30°N occurs in the Atlantic region[3]. Its magnitude is approximately the same for all three simulations, which is in line with the wind speed and pH values shown in the figures above. The MBLNUDG integration reveals additional maxima of the same order of magnitude (≈ 1 pmol/mol) around the equator and slightly lower over the Pacific as well as the Atlantic Ocean. These maxima also occur in the climatological simulations, but they are an order of magnitude smaller than the northern hemispheric maxima. As discussed before, the nudging influences the dynamics of the atmosphere. Thus the abundance of the second maxima

[3]The locations of these maxima are henceforth denoted as 'central Pacific' and 'central Atlantic'.

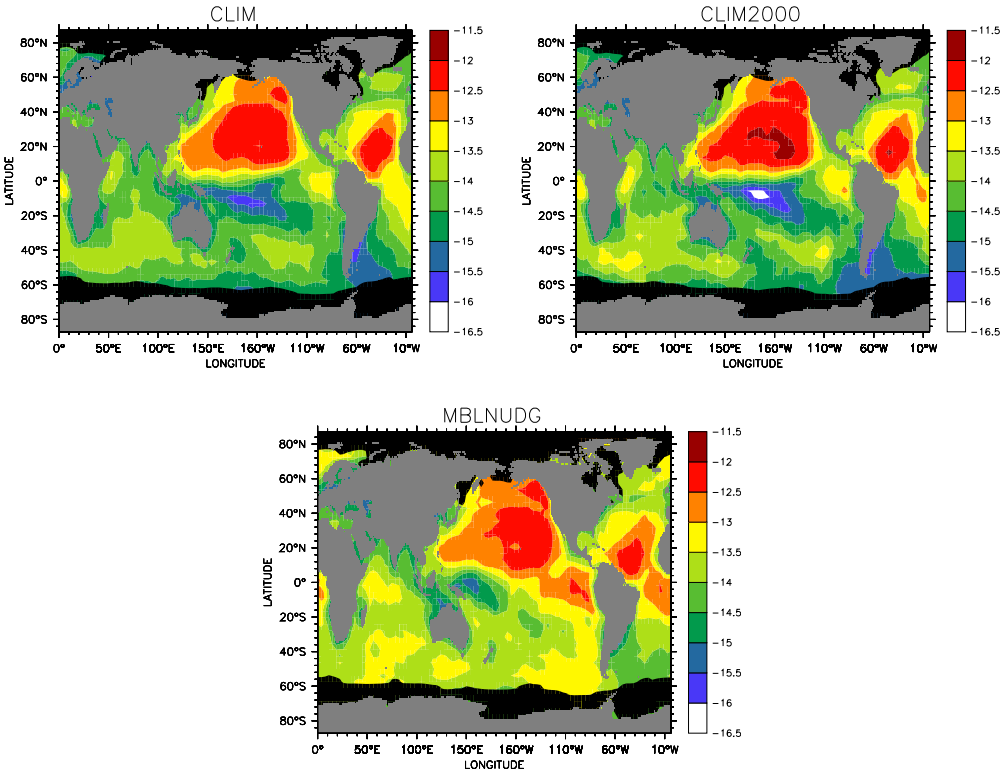

Figure 4.20: Annual mean BrO mixing ratios (mol/mol) on a logarithmic scale: upper left: CLIM, upper right: CLIM2000; bottom: MBLNUDG.

in the MBLNUDG simulation may result from the different transport of acids leading to higher bromine release in the area of these additional maxima. Over the Southern Ocean the wind speeds of the MBLNUDG simulation are higher than the wind speeds over the central Pacific of the climatological simulation. But nevertheless the resulting BrO mixing ratios are much lower for this region, even for the nudged integration. This is due to the much lower abundance of acids in the southern hemisphere. Most urban and industrial centers in Asia, North America and Europe are located in the northern hemisphere. Thus in the southern hemisphere the aerosol is less strongly acidified resulting in less efficient BrO release as for example in the central Pacific. Nevertheless the simulation with the highest wind speeds lead to the highest BrO mixing ratios. Thus the MBLNUDG integration produces between 10^{-14} and 10^{-13} mol/mol, CLIM between $10^{-14.5}$ and $10^{-13.5}$ mol/mol and the year 2000 integration (CLIM2000) between 10^{-15} and 10^{-14} mol/mol in the Southern Ocean storm track region. The maximum in the northern hemisphere shows that the main precursors for reactive halogen chemistry are the supply of 'fresh sea salt and polluted air', where the expression 'polluted air' refers to the abundance of acids, which are important for the acidification of the aerosol to catalyse the halogen release. The opposite, i.e. only low sea salt load and clean air, leads to very low BrO mixing ratios, which is obvious from the marked minimum of BrO in the Pacific Ocean directly south of the equator.

Figure 4.21 displays the seasonal averages of the BrO distribution on a logarithmic scale for the CLIM2000 simulation. Maxima over the northern hemispheric oceans dominate this distribution throughout the year. Especially in northern hemispheric spring (MAM)

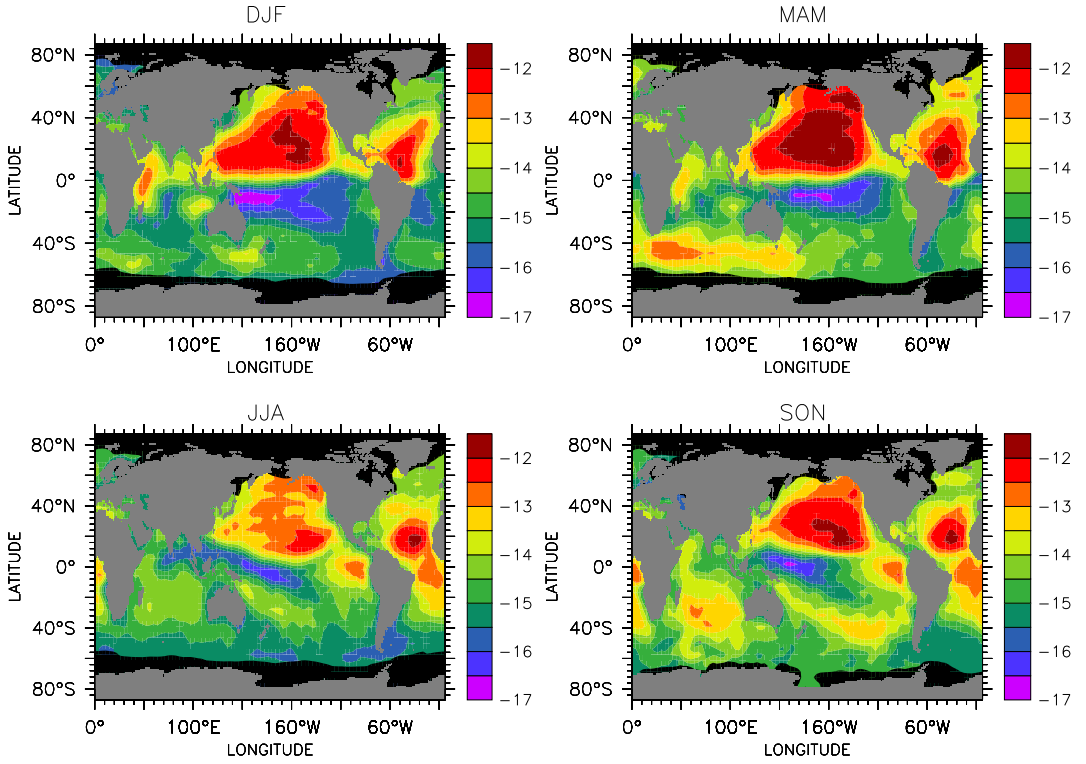

Figure 4.21: Seasonal averages of boundary layer BrO mixing ratios (mol/mol) on a logarithmic scale for the climatological simulation (CLIM2000).

the average is larger than 1 pmol/mol over a vast region of the North Pacific. If these concentrations occur in reality, they would be measurable throughout this season, as the detection limits of current instruments are around 1 pmol/mol. Therefore this may be conceived as evidence that these values are too high in comparison to measurements. However, very few measurement campaigns have been performed in the central Pacific. There are some reasons (already discussed), why the model produces too high amounts of BrO. Firstly, too high sea salt emissions are produced by fairly high 10m wind speeds in the CLIM simulation in contrast to the MBLNUDG integration, especially over the central Pacific. Secondly, the model produces too high aerosol ion emissions because of the process splitting applied to the sea salt emission and deposition processes, as already pointed out for hydrogencarbonate in the previous section. The halide ion emissions are also overpredicted leading to an overestimation of halogen release and an underprediction of the depletion of the aerosol with respect to bromine and chlorine, especially in the North Pacific and the North Atlantic, where acid supply is high enough to substantially acidify the aerosol.

The modelled BrO mixing ratios may actually be an order of magnitude too high, which would make a big difference for the possibilities to measure them, considering the detection limits of available instruments. In the entire North Pacific region high values of 0.05 to 5 pmol/mol persist throughout the year. In the North Atlantic these high values are reached in the latitudinal range between 0°N and approximately 30°N. At higher latitudes less than 0.01 pmol/mol are simulated most of the year. By taking a closer look at the relationship between the pH (Figure 4.17) and the BrO mixing ratios (Figure 4.21) one may conclude, that the high BrO mixing ratios evolve where the pH is

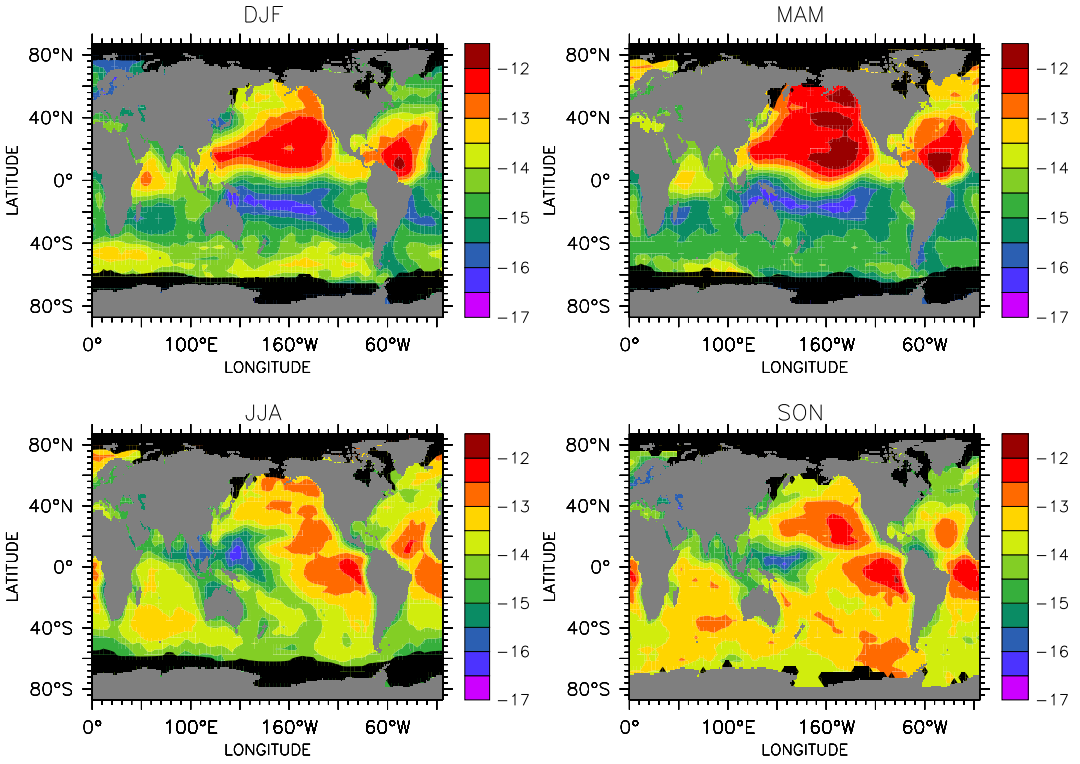

Figure 4.22: Seasonal averages of boundary layer BrO mixing ratios (mol/mol) on a logarithmic scale for the nudged simulation (MBLNUDG).

around 5, and that smaller BrO concentrations occur at lower pH values (as in the north of the North Atlantic). This conclusion is misleading, however, because the pH values themselves are a result of the abundance and the recycling of sea salt aerosol. Thus higher sea salt amounts lead to higher bromine release as long as the acid supply is high enough to acidify the fresh sea salt and thus cause the high BrO concentrations over the northern hemispheric oceans. In the southern hemisphere apparently less BrO is available. This is caused by minor abundance of sea salt and acidity, causing higher pH values and less bromine release into the atmosphere. During the southern hemispheric winter and spring significant amounts of BrO occur over the South Atlantic as well as over the Indian Ocean in spring. The minimum of BrO over the South Pacific near the equator is striking. This coincides with the marked minimum of sea salt in this region, which is caused by the dynamics of the ITCZ.

The BrO maxima in the northern hemisphere also show up in the nudged integration (Figure 4.22), but the amount of BrO is remarkably smaller. Apparently BrO mixing ratios in the southern hemisphere are much higher than in the climatological simulation. Since the sea salt mass distribution and the aerosol pH of both simulations are similar and since both integrations only differ in the dynamics' simulation, the main reason must be the circulation pattern. The question why the nudged simulation produces much more BrO in the southern hemisphere than the climatological one is postponed to the evaluation of the ozone distribution.

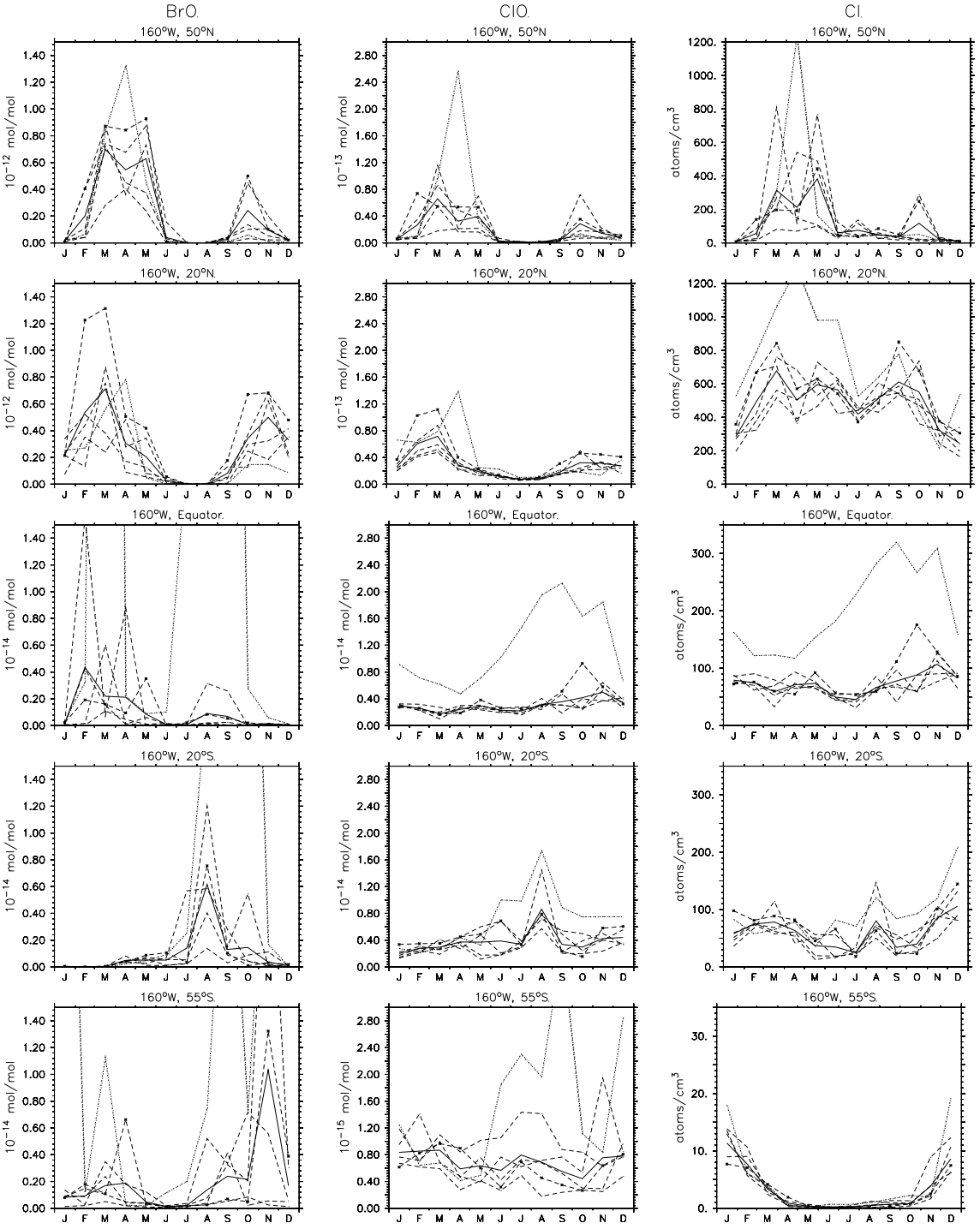

Figure 4.23: Climatological annual variability of the BrO mixing ratio, ClO mixing ratio and Cl concentration. Bold line: climatological mean (5 years); dashed lines: single years (2000-2004); dotted line: nudged simulation (year 2000).

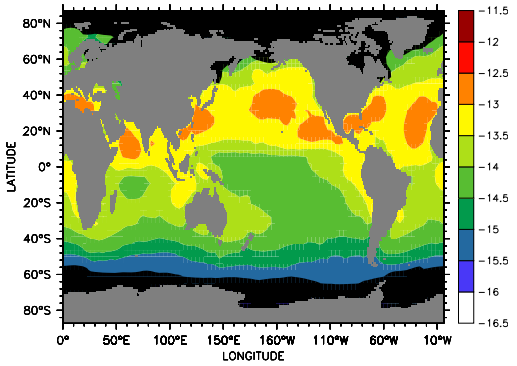

Figure 4.24: Annual average of ClO (mol/mol) on a logarithmic scale for the CLIM2000 simulation.

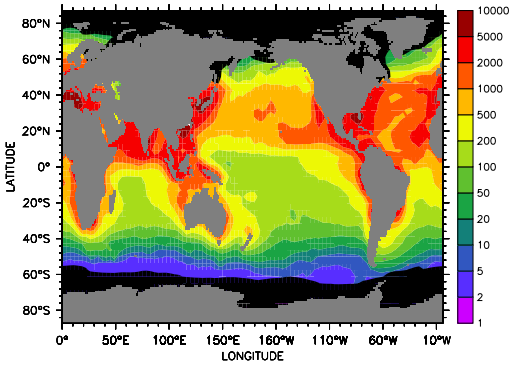

Figure 4.25: Annual average of Cl radical concentration (atoms/cm^3) for the CLIM2000 simulation.

The left column of Figure 4.23 displays the annual cycles[4] of BrO for the climatological mean, the single years (2000-2004) and the nudged simulation at the same five sites as already shown in Figure 4.8 (160°W and 50°N, 20°N, equator, 20°S and 55°S). A marked annual cycle with two peaks in the spring and in the autumn develops in the northern hemisphere. In the southern hemisphere the mixing ratios are much smaller and a distinct annual cycle is lacking. The origin of the two-peak structure in the northern hemisphere is still an open question. The minimum in the summer months is easy to understand, since the sea salt emissions are very low in this time of the year, only small amounts of fresh sea salt and a small bromide source are available and thus the BrO mixing ratios are small, too. In contrast, the sea salt emissions are high in the winter months. But at this time again high sea salt emissions do not necessarily mean a high sea salt load. The right column of Figure 4.8 displaying the sea salt mass shows a distinct minimum for the winter months in the northern hemisphere, which coincides with the wintertime BrO structure. The sea salt is acidified to a high degree (between pH 4 and 4.5) throughout the year. Hence the BrO mixing ratios strongly depend on the available sea salt mass as long as the aerosol is sufficiently acidic. A second minor reason may also be that photochemistry is less efficient in the winter months in the northern hemisphere. The BrO mixing ratios developing in the southern hemisphere are much smaller, but in correspondence with the seasonal cycles shown in Figure 4.21, the BrO mixing ratios produced in the nudged simulation are approximately an order of magnitude higher than the climatological ones.

The same two-peak structure as for BrO occurs in the annual cycle[5] of ClO in the northern hemisphere for the same reasons (see middle column of Figure 4.23). The release of BrCl from the aerosol to the gas phase is the most efficient way to drive chlorine out of the slightly acidified aerosol (pH $\approx$ 5). ClO shows the same annual cycle as BrO because the main chlorine release process is directly coupled to the bromine release mechanism. At daytime degassed BrCl is rapidly photolysed to Br and Cl radicals. The right column of Figure 4.23, which displays the annual cycle of Cl radicals, confirms the ideas discussed above indicating that less efficient halogen release takes place in the winter months of the northern hemisphere. As the incoming radition is smallest in winter and the daylight

[4]Note, that a scale by two orders of magnitude smaller was chosen for the BrO panels showing the sites on the southern hemisphere and the equator.

[5]Note, that the scales chosen for the ClO panels differ by two orders of magnitude dependent on the site.

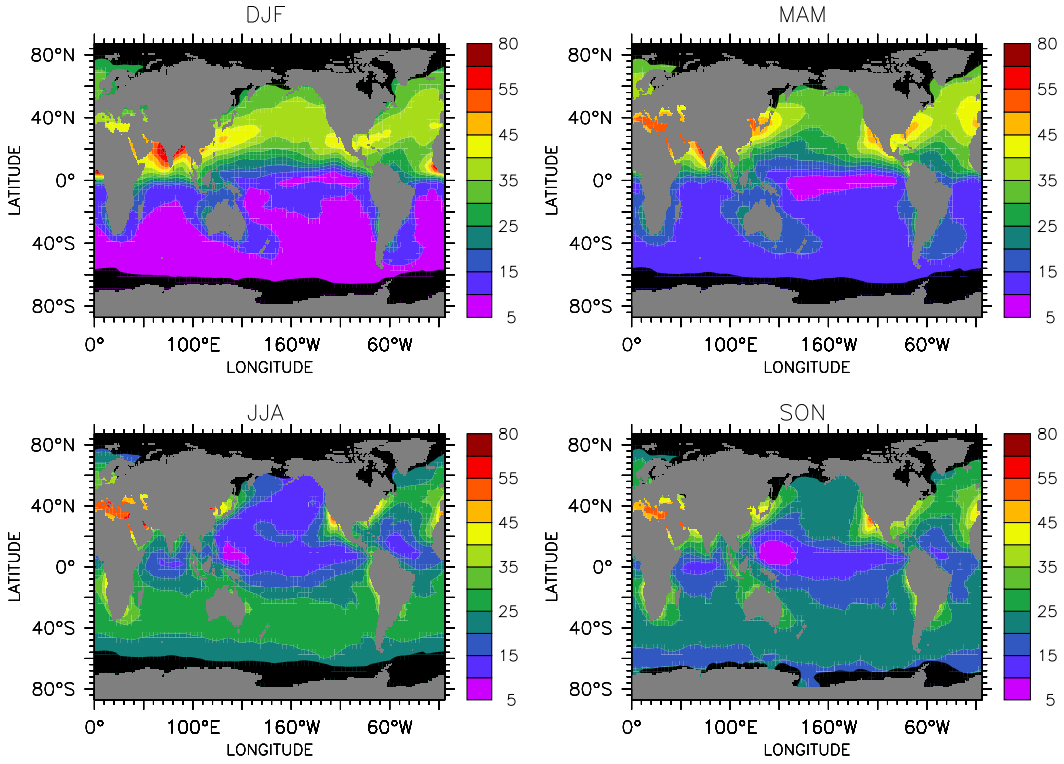

Figure 4.26: Seasonal averages of boundary layer ozone (nmol/mol) for the climatological simulation (CLIM2000).

periods are shorter, the photolysis of the released Br_2 and BrCl is less efficient than during the rest of the year. This is confirmed by the Cl annual cycles showing minima in the winter months at the four sites at 50°N and 20°N on the northern hemisphere as well as 20°S and 55°S on the southern hemisphere, respectively. Figures 4.24 and 4.25 display global distributions of the annual averages of ClO and Cl radicals for the CLIM2000 simulation, respectively. Maximum values are reached in the northern hemisphere for the same reasons as for BrO.

To conclude, the model results show realistic patterns of RHS chemistry, but according to the few available measurements over the open ocean (as listed in Section 2.0.2), the model may overestimate bromine release in the northern hemisphere and underpredicts it in the sourthern hemisphere. Two explanations have been proposed, which are both related to the model setup. The next section goes into more detail about the interaction of halogens with other trace gases.

4.5 Influences of Reactive Halogens on Other Trace Gases

Halogen chemistry influences the ozone concentrations, because the catalytic cycle of bromine release as well as the gas phase cycle consume O_3 (see Cycles III and IV in Chapter 2). Figure 4.26 shows the seasonal ozone distribution for the CLIM integration. Marked seasonal hemispheric cycles occur in both hemispheres. The ozone mixing ratios reach minima as small as 10 nmol/mol in summer in both hemispheres, whereas the maxima in winter show ozone mixing ratios up to 50 nmol/mol in the northern hemisphere

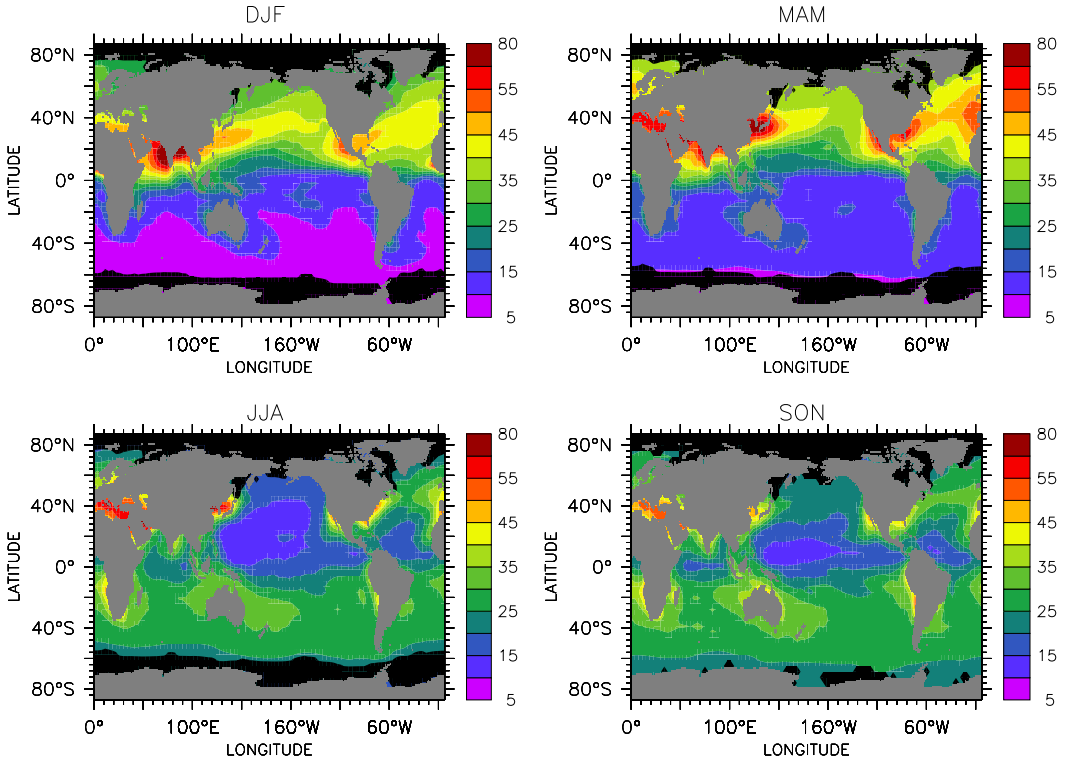

Figure 4.27: Seasonal averages of boundary layer ozone (nmol/mol) for the nudged simulation (MBLNUDG).

and up to 30 nmol/mol in the southern hemisphere. The nudged simulation (see Figure 4.27) shows a very similar seasonal cycle as the climatological one. However, the ozone mixing ratios are higher in the southern hemisphere except for DJF in the nudged simulation. BrO is expected to be a marker for active halogen chemistry and thus higher BrO mixing ratios should point to stronger ozone destruction. But in this case the nudged simulation produces higher BrO mixing ratios as well as higher O_3 mixing ratios than the climatological integration. The main reason causing higher O_3 concentrations as well as higher BrO concentrations is the larger transport of ozone from the continents over the ocean due to the different dynamics applied by the nudging. The higher level of ozone (in comparison to the climatological simulation) then leads to a higher production of BrO because the latter is also coupled to the amount of available ozone.

The effect of bromine chemistry reducing ozone due to its fast recycling (see Chapter 2, Cycles III-V) is larger in the free troposphere than in the boundary layer (von Glasow et al., 2004). Nevertheless, an influence on ozone is also detectable in the MBL. Figure 4.28 displays the ratio of the annual mean ozone mixing ratios of the CLIM versus the NOHAL simulation[6]. In the CLIM simulation compared to the NOHAL simulation ozone is reduced in regions where high BrO mixing ratios are predicted. Its loss reaches up to 9% over the central Pacific Ocean and up to 7% over the central Atlantic Ocean. With the exception of some coastal areas, ozone decreases over all oceans. In the southern hemisphere ozone is consistently lower by 2-4% in the simulation including bromine (CLIM). It has to be kept in mind, that these are annual averages, whereas the effects can be larger under some

[6]The NOHAL simulation is an integration including aerosol chemistry but omitting halogen reactions.

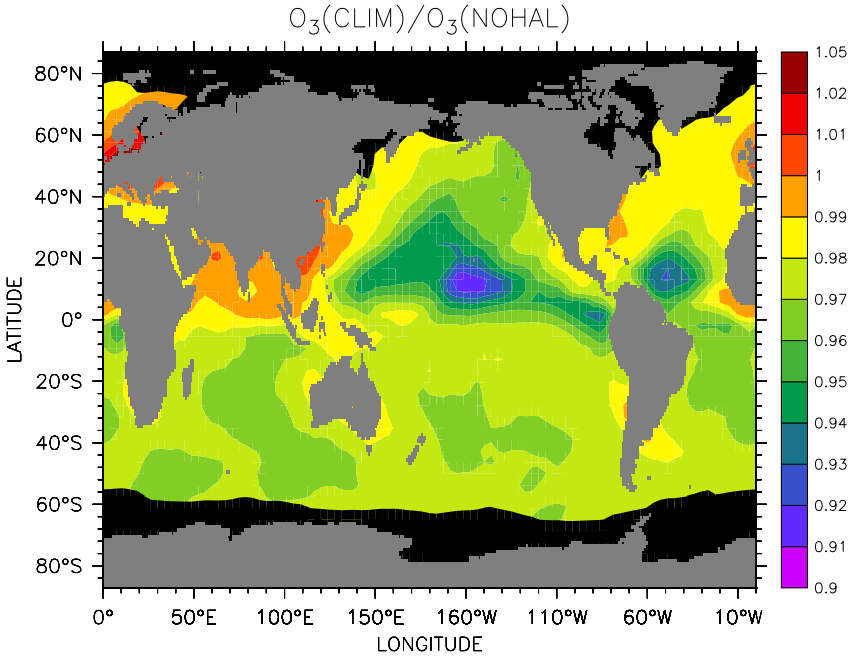

Figure 4.28: Ratio of the annual mean mixing ratios of ozone: CLIM/NOHAL.

conditions and sometimes even no effect on ozone is detectable. Thus the ratios of the ozone mixing ratios shown here indicate that halogens have a significant effect on ozone even in the MBL.

Next, a comparison of the modelled ozone concentrations with measurements shows whether the model performs well in reproducing ozone mixing ratios. Two databases have been selected for this comparison. The first one is a database containing ship-borne ozone measurements over the Atlantic Ocean during the period from 1977 to 2002 (Lelieveld et al., 2004). Here, the period from 1995 to 2002 is used because the data coverage is more comprehensive. Table 4.3 lists seasonal averages of ozone mixing ratios for 20° latitude bands from 60°N to 60°S. The averages have been calculated for the eight years of measured data and for the nudged simulations dealing with full halogen chemistry (MBLNUDG) and only with gas phas chemistry (LSCE-NUDG). In the measured data the aforementioned contrast between the hemispheres is also evident. The northern hemisphere shows higher ozone mixing ratios than the southern hemisphere throughout the year. This contrast is highest in the first half of the year, when ozone mixing ratios in the southern hemisphere are about half of those in the northern hemisphere. The difference decreases in the second half of the year, showing only slightly higher values for the northern hemisphere in SON, whereas O_3 mixing ratios in the southern hemisphere are relatively high owing to biomass burning emissions. This pattern is reflected by the LSCE-NUDG integration. In this simulation the contrasts between the hemispheres are even higher. In DJF and MAM the modelled ozone mixing ratios are higher in the northern and lower in the southern hemisphere than the measured ones, thus increasing the gradient between both hemispheres. During the other two seasons the model produces lower ozone mixing ratios in the northern and higher ones in the southern hemisphere in comparison to the measured data, thus the gradient between the hemispheres is reduced. As bromine chemistry generally leads to a reduction of ozone, one would expect the MBLNUDG integration to produce lower

Table 4.3: Measured and modelled seasonal mean ozone mixing ratios (nmol/mol) and 1-σ standard deviations for 20° latitude bands over the Atlantic Ocean. The measurement database is the same as used in Lelieveld et al. (2004).

	DJF		MAM		JJA		SON	
	Mean nmol/mol	σ	Mean nmol/mol	σ	Mean nmol/mol	σ	Mean nmol/mol	σ
Measured Seasonal Averages 1995-2002								
40°N-60°N	28.0	11.6	33.3	14.0	34.9	11.4	28.5	11.1
20°N-40°N	37.5	6.9	36.9	13.1	33.0	10.2	34.2	8.1
0°N-20°N	31.2	8.2	29.4	8.8	23.5	6.7	24.9	7.4
0°S-20°S	15.0	4.7	18.1	6.1	27.4	6.9	23.4	6.4
20°S-40°S	15.4	4.2	20.6	5.9	28.5	4.8	25.3	6.3
40°S-60°S	13.3	3.2	21.1	6.0	27.9	4.7	20.9	5.0
Modelled Seasonal Averages 2000 (LSCE-NUDG)								
40°N-60°N	36.2	8.3	45.3	9.6	30.8	12.9	30.7	7.6
20°N-40°N	41.9	7.1	43.7	11.1	26.0	14.4	30.0	9.5
0°N-20°N	32.1	10.7	28.3	8.3	19.8	5.9	20.4	6.2
0°S-20°S	12.2	4.1	17.4	4.9	32.2	7.2	26.4	7.7
20°S-40°S	9.6	4.6	15.8	5.1	31.0	6.1	28.0	8.1
40°S-60°S	8.6	3.6	13.0	3.7	27.5	5.4	25.3	7.0
Modelled Seasonal Averages 2000 (MBLNUDG)								
40°N-60°N	33.0	4.7	37.8	7.7	27.8	11.1	30.6	7.2
20°N-40°N	34.9	5.5	36.0	10.2	25.7	12.5	30.6	10.3
0°N-20°N	32.9	13.8	21.4	7.5	16.6	5.8	19.0	7.7
0°S-20°S	11.2	4.2	15.2	4.6	27.1	6.1	18.6	5.8
20°S-40°S	10.8	4.6	17.6	5.0	27.9	3.7	21.0	7.0
40°S-60°S	10.1	3.2	15.3	4.2	24.9	3.1	18.9	5.3

ozone mixing ratios than the LSCE-NUDG simulation. This is only valid for the northern hemisphere throughout the year and the southern hemisphere during JJA and SON. In the first half of the year the MBLNUDG integration shows higher ozone concentrations than the LSCE-NUDG simulation for the southern hemisphere, thus indicating a smaller gradient between the hemispheres than the LSCE-NUDG simulation and a larger one than the measurements. During the rest of the year the differences between the hemispheres are similar to the measurements but at lower ozone mixing ratios. Figures 4.29 and 4.30 show the annual averages of the ozone measurements by Lelieveld et al. (2004) and the CLIM simulation, respectively. The general ozone concentration distribution is quite similar, especially the north-south gradients displayed by the measurements are well covered by the model. However, the absolute averaged modelled ozone mixing ratios are smaller than the measurements in almost all Atlantic regions. The largest differences occur along the American east coast, where the measurements show much higher ozone concentrations than the model results. There are two possible explanations for these differences. The

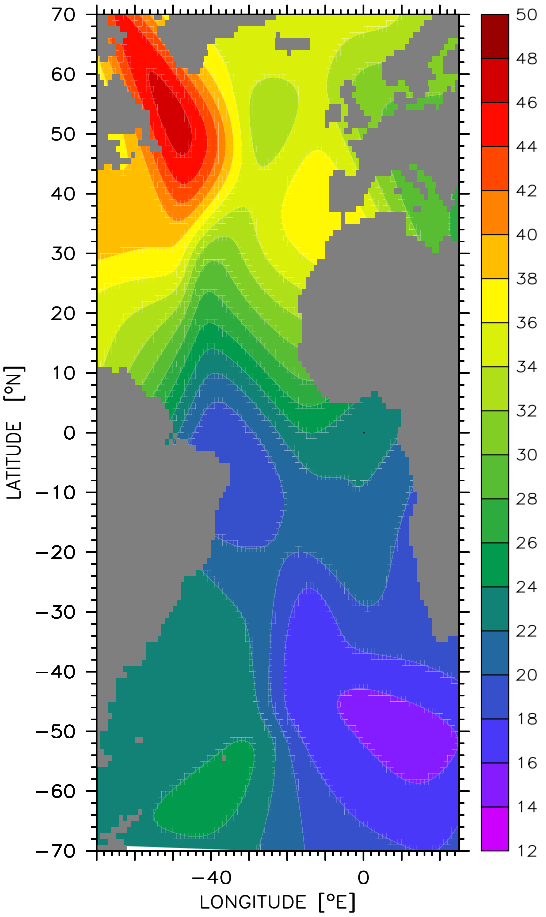

Figure 4.29: Measured annual mean ozone mixing ratios (nmol/mol) for the years 1995-2002 over the Atlantic Ocean using the Atlantic ship measurement database by Lelieveld et al. (2004).

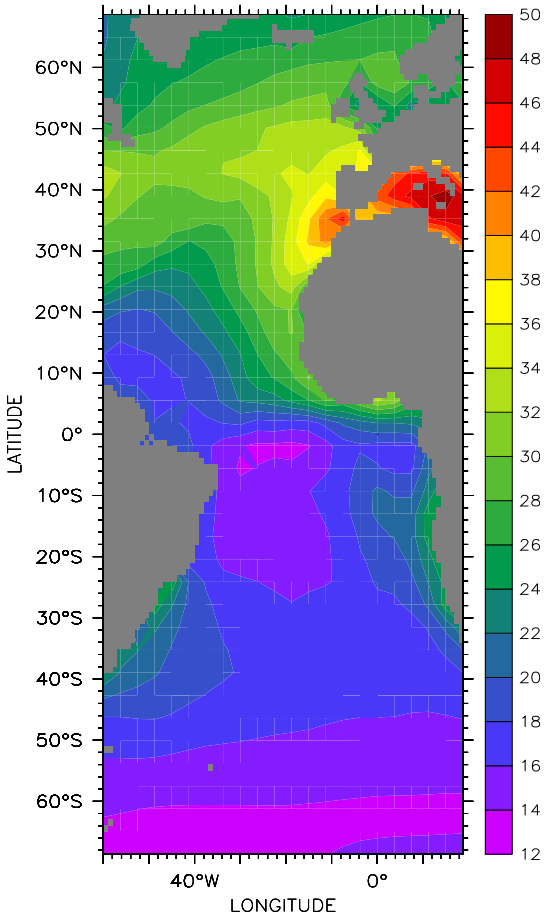

Figure 4.30: Modelled annual mean ozone mixing ratios (nmol/mol) for the Atlantic Ocean region using the data for the five years long CLIM simulation (2000-2004).

first one is part of the model setup: the emission inventories used for continental emissions in the present study are not fully up to date[7], thus may be underestimating the continental ozone production and the outflow over the oceans. The second reason is the chosen gridding function for the measurements: since the data set results from ship-borne measurements, the distribution of the data in time and space depends on the ship tracks. Because the gridding function applies to each data point the same weight, the averages for one region shown for the measurements may be shifted to the average of one specific season.

To summarise, the simulations (MBLNUDG and CLIM) including bromine chemistry show slightly smaller ozone mixing ratios in comparison to the measurements most of the time. It must be emphasised that the modelled mixing ratios are within the 1-σ standard deviation of the measured data. As eight years of horizontally scattered measurements

[7]For the ongoing model evaluation of ECHAM5/MESSy a comprehensive, completely tested emission data set is provided. Unfortunately this was not available for the simulations shown here, thus a prior version of these data set had to be used.

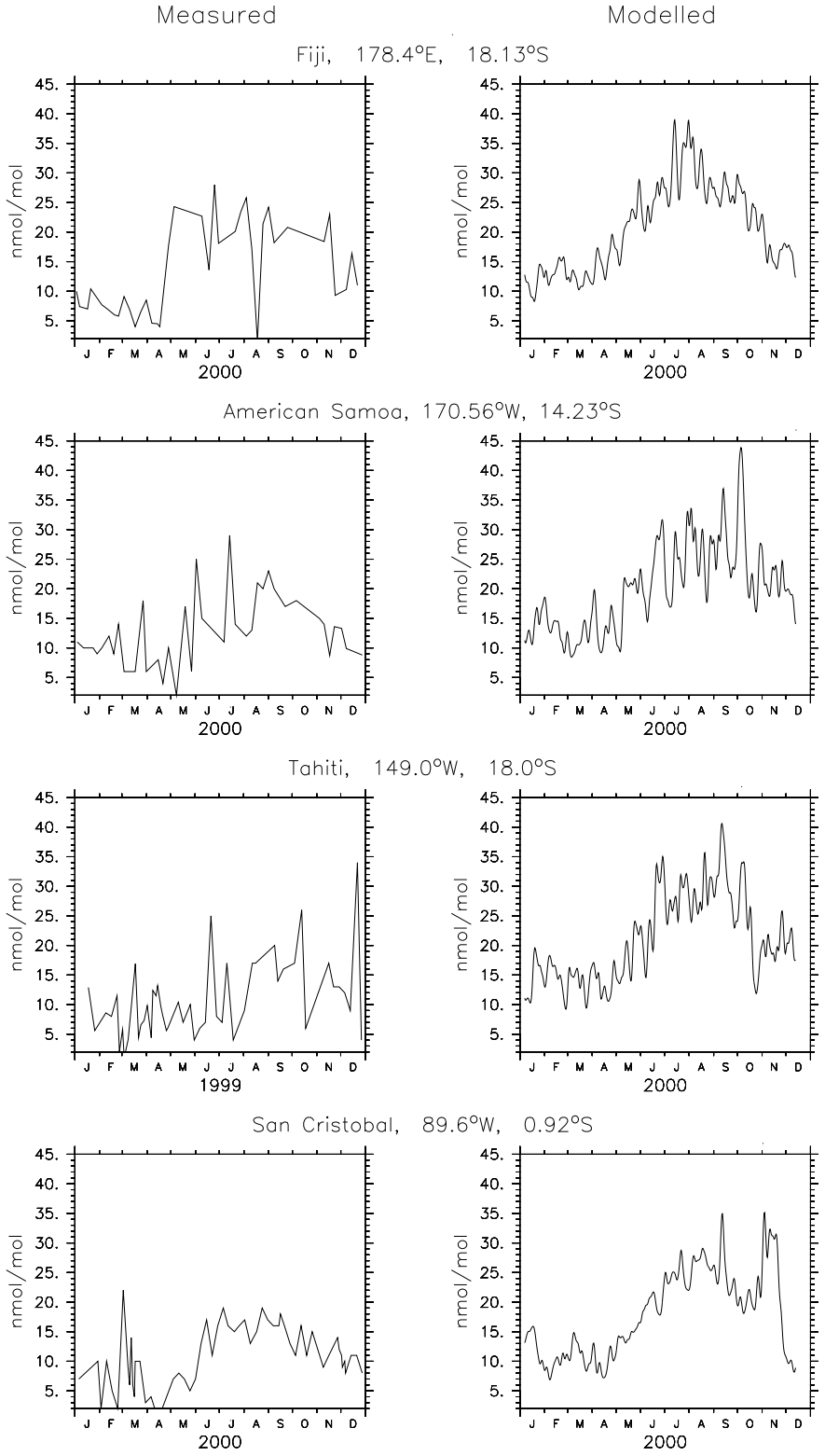

Figure 4.31: Ozone mixing ratios: comparison of model surface data (MBLNUDG simulation) with the lowest measurement levels of ozonesonde data from the SHADOZ network.

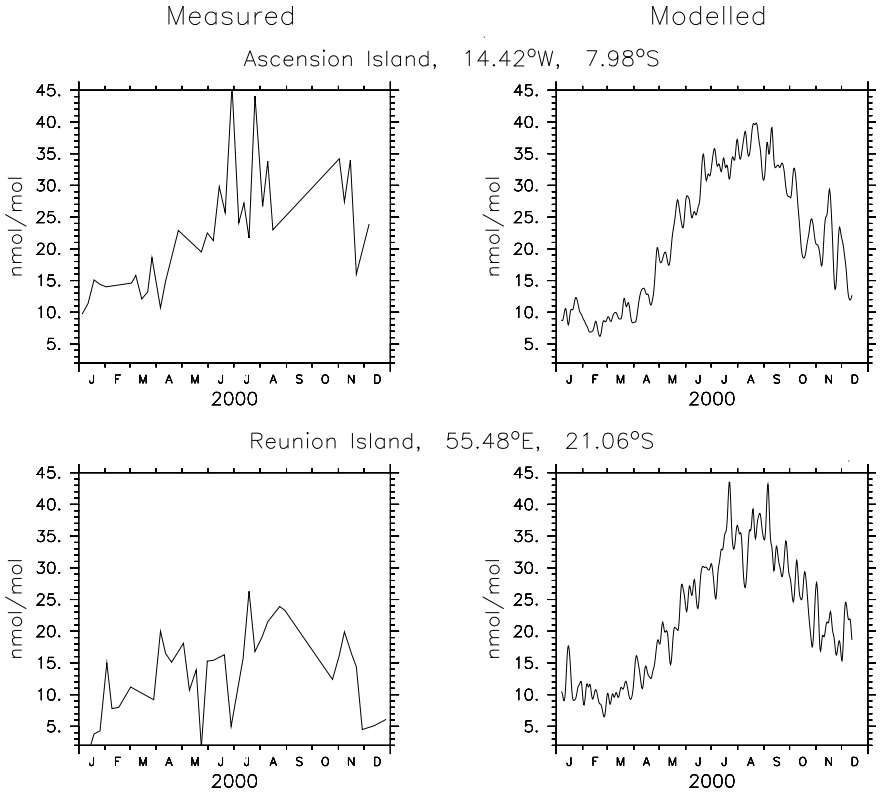

Figure 4.31: (continued)

have been compared with one year and five years of model integration for the Table 4.3 and the Figure 4.30, respectively, the conclusion seems justified, that the correspondence between the measurements and the modelled data is quite reasonable.

The second data set is provided by the Southern Hemispheric ADditional OZonesondes (SHADOZ) project (Thompson et al., 2003a,b). Figure 4.31 shows the comparison of the MBLNUDG simulation with measurements at six stations of the SHADOZ network, all located on islands within the tropics. As the ozonesonde measurements have not been performed on a regular time interval, the database is relatively small. The displayed annual cycles are calculated from the lowest data points provided by the ozonesonde measurements in 2000 with the exception of Tahiti, where no data set for 2000 is available (the year 1999 is shown). As the SHADOZ data are not very well resolved in time compared to the modelled ones, the seasonal cycle is not as clearly resolved as by the model simulation. Nevertheless, in both cases annual cycles appear with maxima in the period between July and September and with minima in the southern hemispheric summer months. Especially these minima reveal higher ozone mixing ratios in the simulations than in the measurements. Additionally, the maxima given by the model are higher with the exception of Ascension Island. In general, the model overpredicts the ozone concentration for these six sites in the year 2000. This contrasts the results shown above, where the model simulations are lower than the measurement data from the Atlantic Ocean data set in the latitude band from equator to 20°S. The reason is that the data set provided by Lelieveld et al. (2004) is only valid for the Atlantic Ocean, and the only island located in the Atlantic Ocean provided by the SHADOZ network is Ascension Island, that is exactly the one site

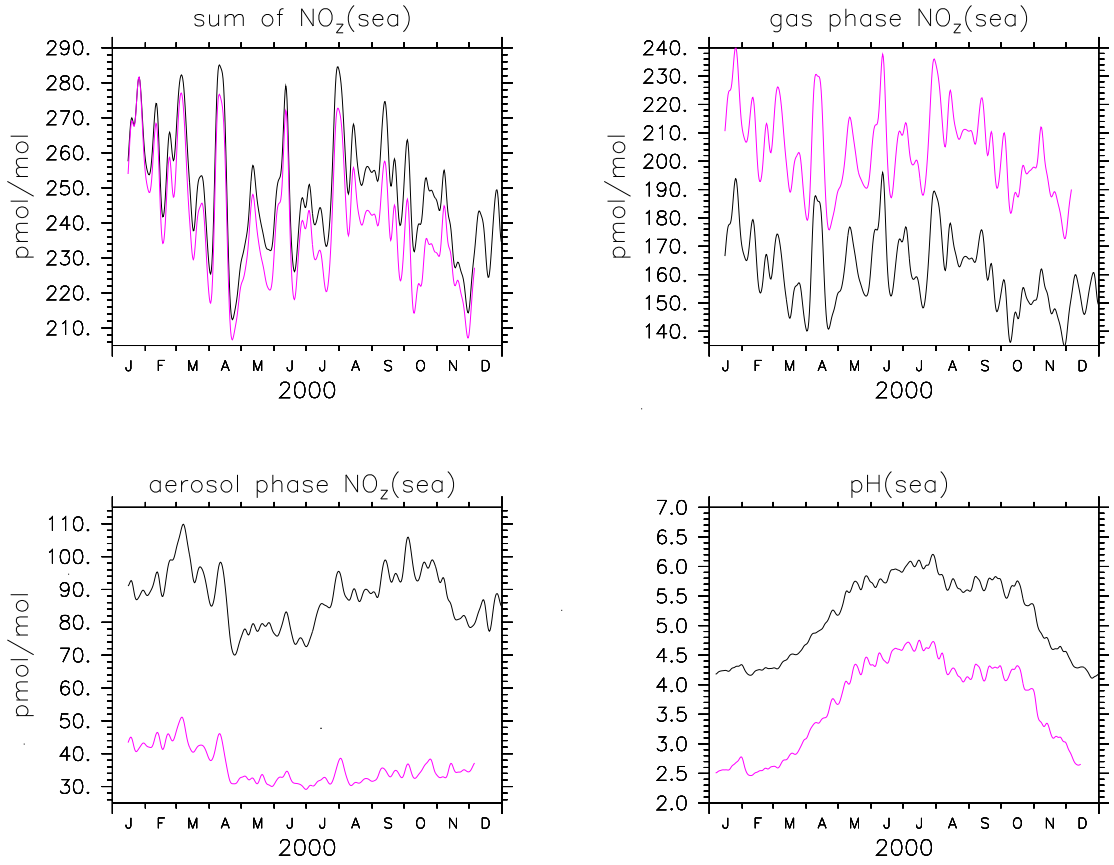

Figure 4.32: Sum of NO_z, gas phase NO_z and NO_z dissolved in the aerosol phase. The fourth panel displays the aerosol pH of both simulations. Black line: CLIM2000; purple line: NOHAL.

at which the modelled ozone mixing ratios are not significantly higher than the measured ones. Most of the other islands are located in the Pacific Ocean (with the exception of Reunion Island, which is located in the Indian Ocean), and the results for the Atlantic Ocean cannot be transferred to the Pacific Ocean. A second difference between the two measurement data sets is that the Atlantic Ocean data set is from ship-borne measurements, whereas the SHADOZ measurements are stationary providing a better resolved database in time for these locations.

To conclude, the model seems to perform well as the modelled ozone mixing ratios are within the 1-σ standard deviation of the measured data from the Atlantic Ocean database (Lelieveld et al., 2004). No statistical statement can be made about the data of the SHADOZ network, but the model reproduces the seasonal cycles shown by the ozonesonde measurements.

Not only ozone is directly affected by halogen chemistry, but also the nitrogen oxide chemistry. Figure 4.32 displays the NO_z partitioning[8] between gas and aerosol phase for the CLIM2000 (black line) and the NOHAL (purple line) simulation. The upper left panel shows the sum of nitrogen oxides in the gas phase and the aerosol phase. Even if the CLIM2000 simulation contains slightly more NO_z, both integrations cover mainly the same amount of NO_z. By looking at the mixing ratios in the gas phase (upper right

[8] $NO_z = NO + NO_2 + NO_3 + N_2O_5 + HONO + HNO_3 + HNO_4 + NO_3^-(aero) + HNO_3(aero)$

panel) and in the aerosol phase (lower left panel) it becomes obvious that the partitioning between the phases is completely different for both chemical setups. In the simulation with halogen chemistry most of the NO_z remains in the aerosol phase, whereas without halogen chemistry most NO_z is in the gas phase. These large differences in the partitioning of NO_z are a consequence of the chlorine chemistry. In the CLIM2000 simulation chloride buffers the pH of the aerosol (see lower right panel in Figure 4.32). If acid enters the aerosol phase, HCl is released to the gas phase and the pH stays constant (see Chapter 2, Equation 2.1). As the global mean aerosol pH ranges between 4 to 6 in the CLIM2000 integration, HNO_3 is taken up by the aerosol in this simulation. No HCl buffer exists in the NOHAL simulation, thus the aerosol pH ranges between 2.5 and 4.5 and less HNO_3 is taken up by the aerosol.

4.6 Short-term Chemical Cycles

Annual and seasonal averages as well as global means of the most important quantities driving reactive halogen chemistry have been the focal point of the present evaluation so far. This section is dedicated to the details of the chemistry in the global model. For this reason the chemistry in individual boxes in the lowest model layer is studied for a 14-day period in October 2000.

Five simulations have been performed starting from their annual integration on the 14th of October and simulating the time period until the 31st of October. The output interval of these integrations was 30 minutes (i.e. each model time step). The first simulation is the aerosol physics integration, which contains only gas phase chemistry (D-LSCE). The second and the third simulation (D-CLIM and D-MBLNUDG) include full aerosol chemistry as given in Appendix C. Additional simulations excluding the bromine chemistry (D-CL) and excluding all halogen chemistry (D-NOHAL) have been performed to separate the influences by aerosol, chlorine and bromine chemistry. In the following figures the simulations are distinguished by line colours. The D-CLIM integration is denoted by

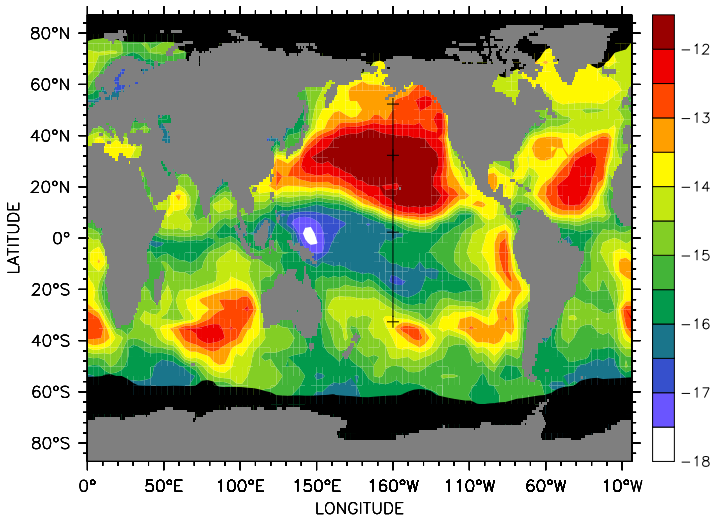

Figure 4.33: BrO mixing ratio (mol/mol) average during the 14-day period from 16th to 29th October 2000 on a logarithmic scale for the CLIM simulation. The four sites have been marked with crosses, connected with a line.

black lines, the D-LSCE, D-NOHAL and the D-CL simulations are displayed by red lines, purple lines and blue lines, respectively. Four sites in the Pacific Ocean have been chosen for a detailed investigation of halogen chemistry. They are located at 160°W longitude, and 50°N, 30°N, 0°S and 35°S latitude. Figure 4.33 shows the average BrO distribution for the 14-day period from the 16th to 29th October 2000. This figure illustrates that the locations have been chosen to represent a wide range of simulated BrO mixing ratios.

The panels in the first row of Figure 4.34 show the BrO short-term cycles[9] (as given by the D-CLIM simulation), displayed for the four locations from north to south (in the figures from left to right). The orders of magnitude of the BrO mixing ratios range from a minimum of 0.001 pmol/mol at the equator, and from 0.01 pmol/mol to 0.1 pmol/mol at 35°S and 50°N, respectively, to the maximum of more than 1 pmol/mol at 30°N. This enables a more detailed evaluation, e.g. to test how different conditions affect BrO concentrations and how reactive bromine interacts with other trace gases. The average BrO mixing ratios given above correspond well to the average values displayed in Figure 4.33. The site at 30°N is located near the maximum in the peak over the North Pacific Ocean. The 50°N site is placed in a more moderately affected part of the Pacific Ocean. The equator site is located near the minimum of the BrO distribution, though not directly in the minimum. Why this minimum appears, which is also apparent in the sea salt distribution, is discussed later in this section. The site at 35°S is located near the Southern Ocean storm track region, but not exactly within it. This yields very moderate BrO concentrations showing a minimum of reactive halogen chemistry.

At all locations the BrO mixing ratios show the typical diurnal variation. The distinct morning and evening peaks as well as the intermediate minimum at noon are consequences of the different photolytic properties of Br_2 and BrCl on the one hand and O_3 on the other hand, as pointed out by von Glasow et al. (2002). In the morning the solar spectrum is shifted towards the longer wavelengths in the lower parts of the atmosphere. In this wavelength interval Br_2 and BrCl are more easily photolysed than O_3. This causes a delay in the ozone photolysis, which has a feedback on the HO_x chemistry[10]. Since the reaction with HO_2 is the dominant sink for BrO (apart from photolysis), the delay in HO_2 formation, caused by the delayed onset of O_3 photolysis, explains the increase of the BrO concentration. Later in the day the HO_x chemistry is fully active and HO_2 is an efficient sink for BrO, thus causing the minimum of BrO mixing ratios at noon. The evening peak occurs for the same reasons as the morning peak. The variation of the daily maxima is affected by many different parameters. The second, third and fourth rows of Figure 4.34 display the most abundant acids in the gas phase (=SO_2+H_2SO_4+HNO_3), the aerosol liquid water content (LWC) and the aerosol pH, respectively. Figure 4.35 shows the bromine enrichment factors, the precipitation rates, the sea salt mass concentrations and the sea salt number concentrations in the same arrangement as in Figure 4.34. The aerosol liquid water content is approximately 1 to $2{\cdot}10^{-11}$ $m^3(aq)/m^3(air)$ at all four sites, but it is slightly higher in the two southern locations. The aerosol pH behaves very differently in these four examples. At 30°N and the equator the pH is fairly constant in comparison to the other two locations.

The most acidic aerosol is present at the location at 30°N. Most of the time the pH ranges between 4.5 and 5.5, thus enabling an efficient halogen release and bromine recycling indicated by the very high BrO mixing ratios. On 19th October a decrease of

[9]Note: As the BrO mixing ratios differ by several orders of magnitude, the scales of the plots have been adjusted to the respective order of magnitude for each location.

[10]HO_x = OH + HO_2

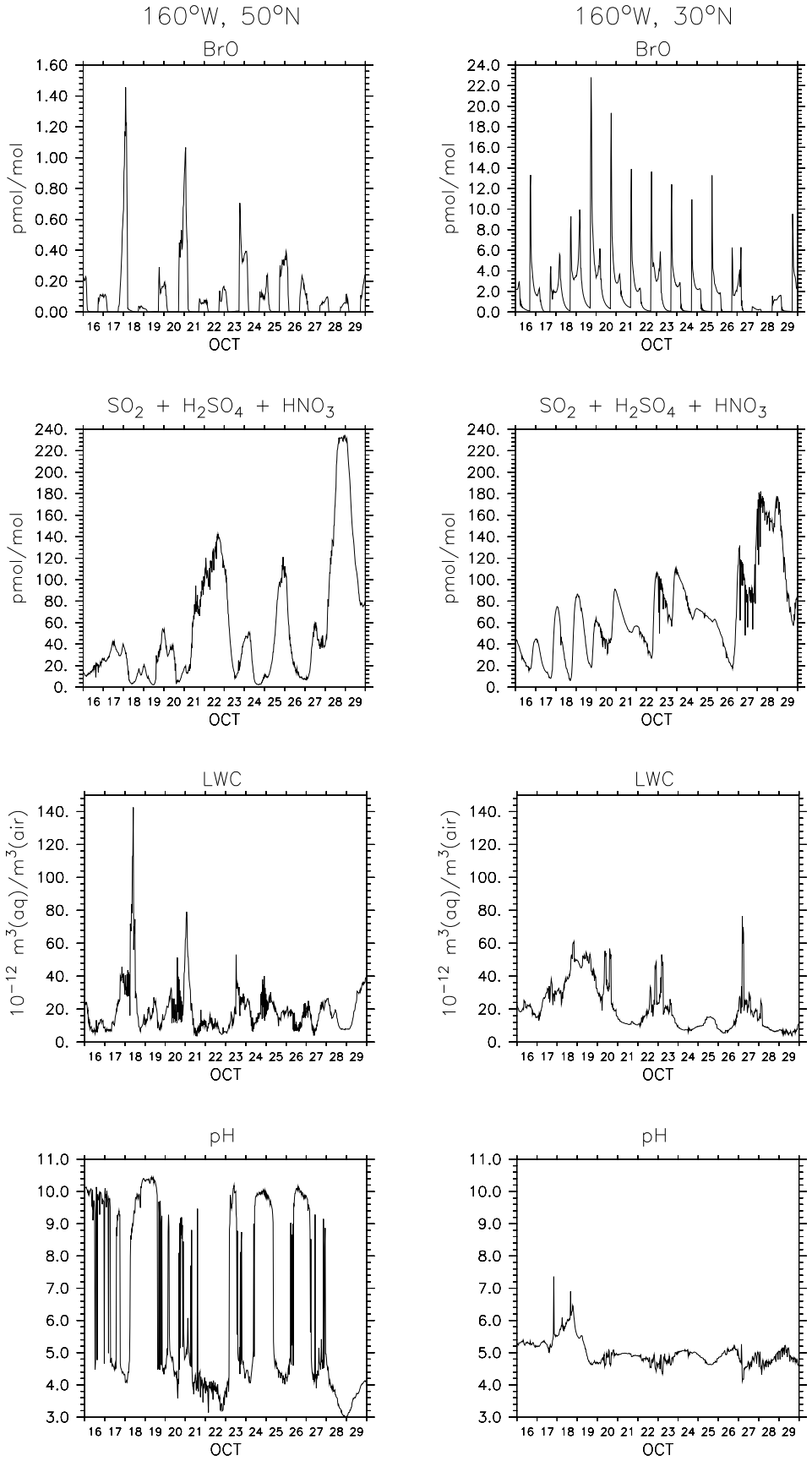

Figure 4.34: Time series of BrO, gas phase acids (=SO_2 + H_2SO_4 + HNO_3), aerosol liquid water content (LWC) and aerosol pH at 160°W and 50°N, 30°N, equator and 35°S (from left to right) for the period 16th to 29th October 2000 (D-CLIM simulation).

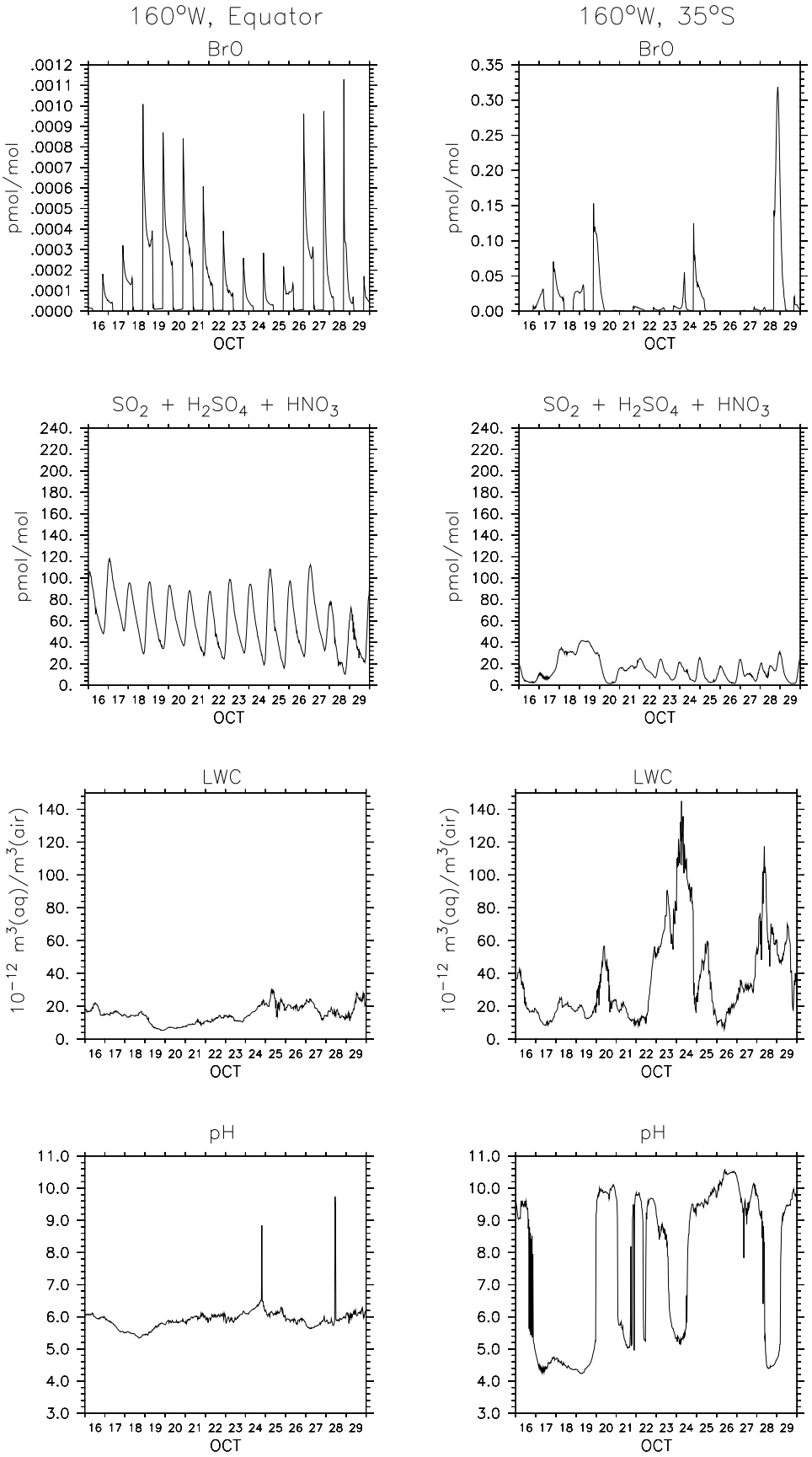

Figure 4.34: (continued)

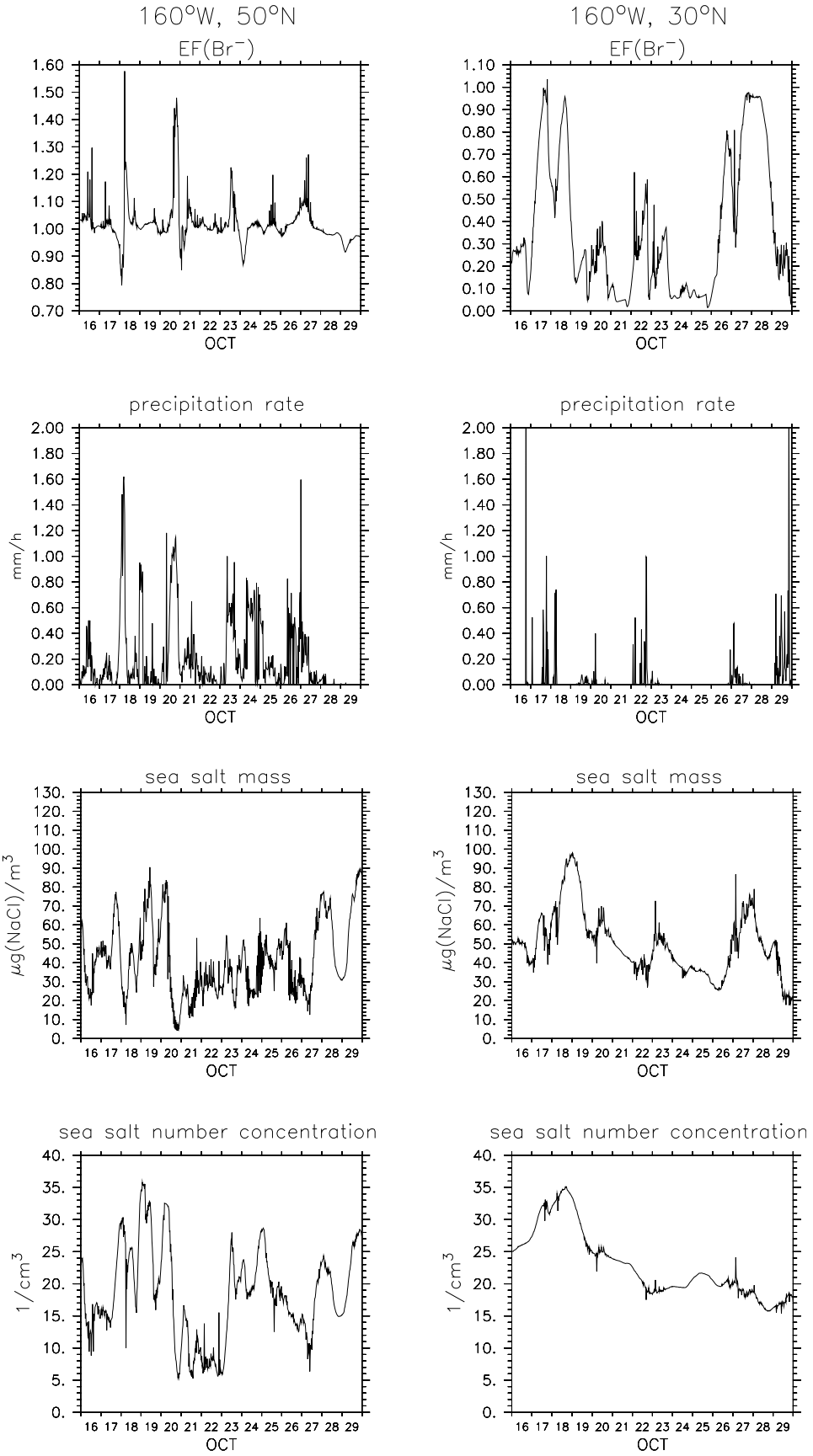

Figure 4.35: Time series of EF(Br^-), precipitation rate (in mm/h), sea salt mass and number concentration (μg/m^3 and cm^{-3}, respectively) at 160°W and 50°N, 30°N, equator and 35°S for the period 16th to 29th October 2000 (D-CLIM simulation).

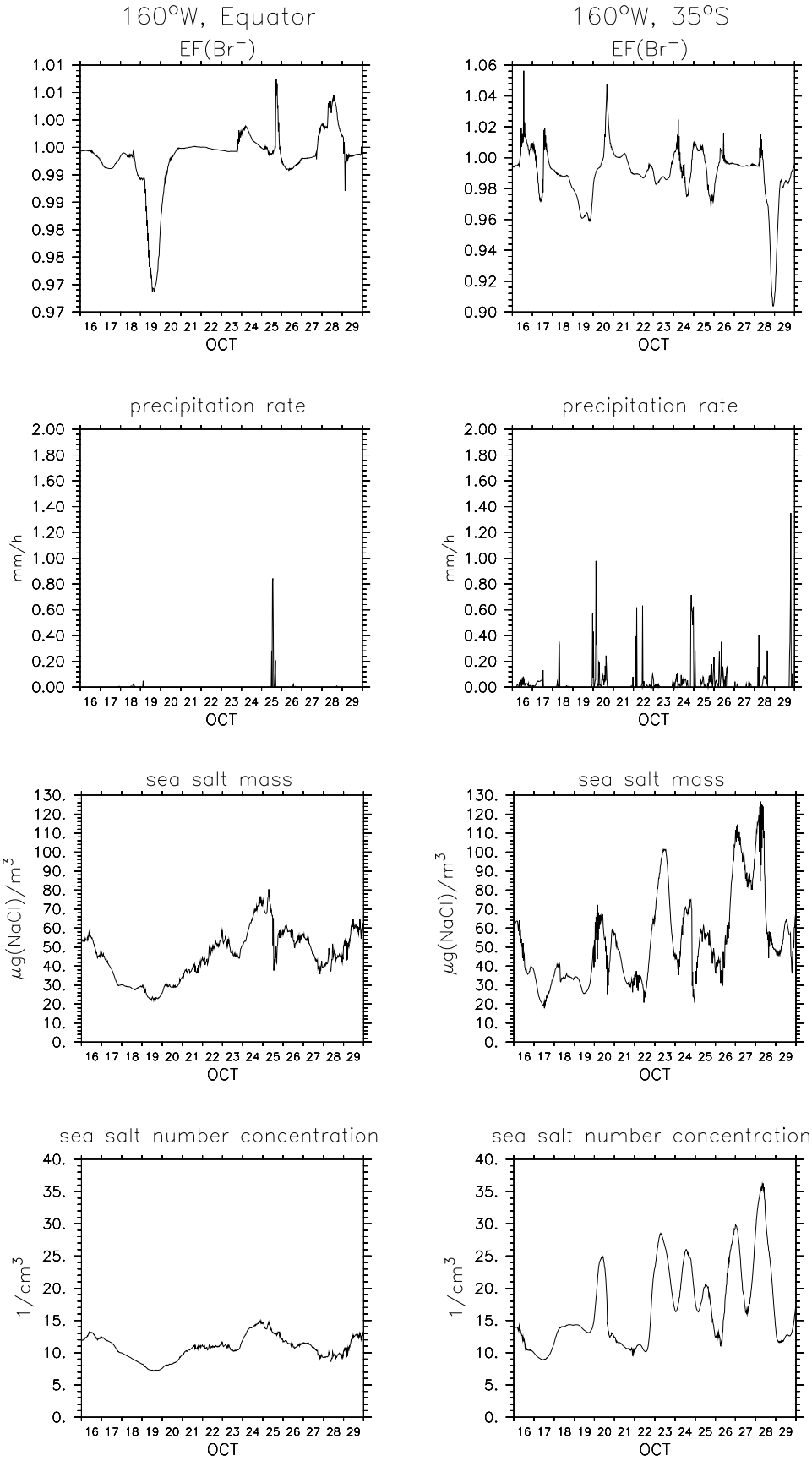

Figure 4.35: (continued)

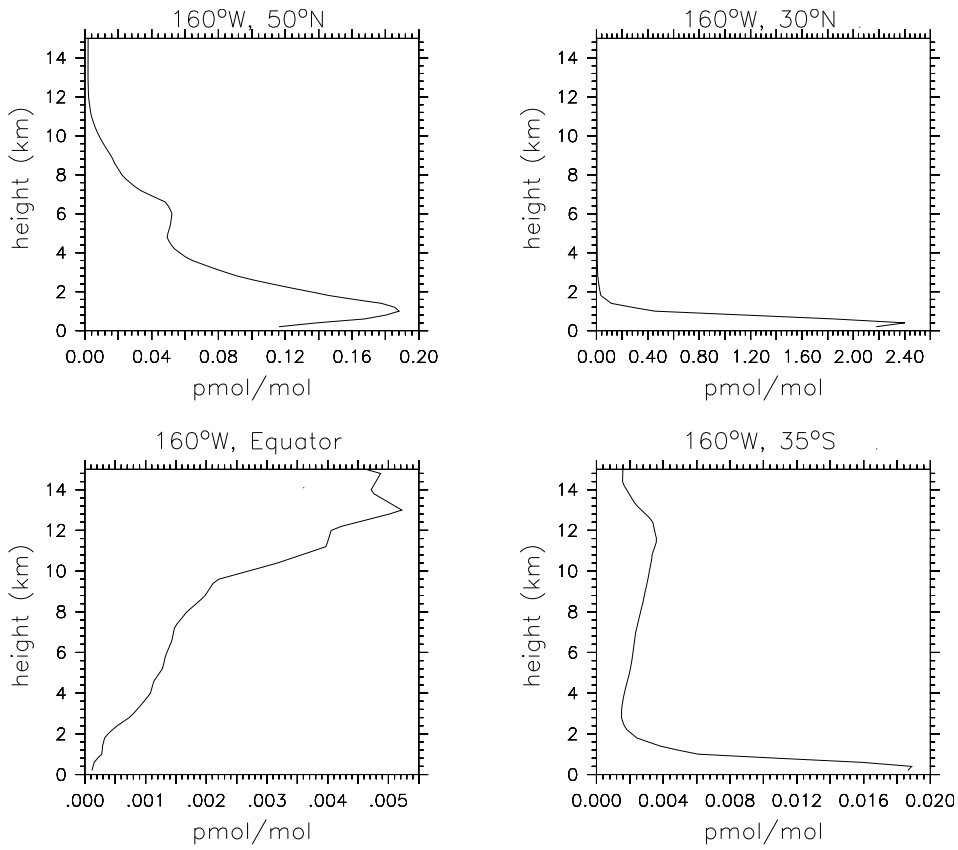

Figure 4.36: Averaged vertical profiles of BrO (pmol/mol) at 160°W and 50°N, 30°N, the equator and 35°S for the period 16th to 29th October 2000 (D-CLIM simulation).

the pH to about 4.8 results in an increase of the BrO maxima. These relatively high BrO mixing ratios decrease during the following days whereas the pH is relatively constant. This is caused by a strong depletion in bromine (see the first row of Figure 4.35). On 26th October the enrichment factor increases and reaches a value of nearly 1 (i.e. no depletion) for the two following days. During this period the pH stays at a low level, the acid mixing ratio reaches an extended maximum, but the BrO concentration is drastically reduced. This is due to a rain event that takes place from 26th to 27th October (see second row of Figure 4.35). This figure only shows the precipitation reaching the surface. The rain event itself starts at the end of 25th October, but during the first day (26th October) the rain droplets completely evaporate in the lowest model layers, thus no rain reaches the surface on that day. On the one hand the rain efficiently removes BrO, on the other hand it leads to an enhancement of the enrichment factor as the rain droplets evaporate. The last effect is caused by the scavenging of halogens from the gas phase into the cloud or rain droplets. This increases the ratio of bromide to sodium, as sodium is not scavenged. Thus the enrichment factor increases as soon as evaporation takes place. It is evident from the BrO daily cycles, that the BrO mixing ratio starts to recover after the rain stops.

At the second location where the pH stays relatively constant (i.e. the site at the equator), the pH ranges between 5.5 and 6.5. Thus the aerosol is here one order of magnitude more alkaline than the aerosol at 30°N. The amount of available gas phase acids is similar at both points, but the aerosol liquid water content is slightly higher at the equator.

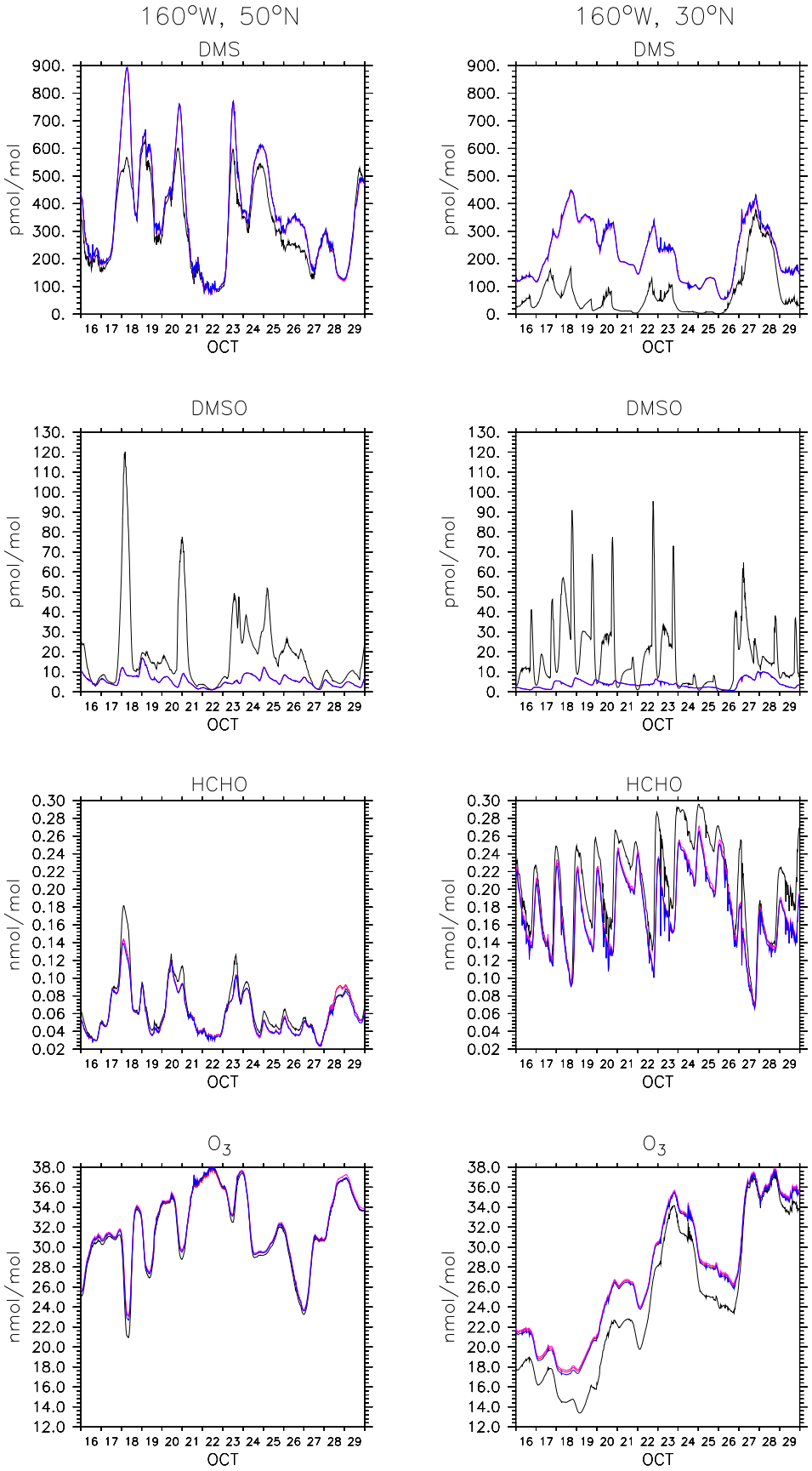

Figure 4.37: Time series of DMS, DMSO, HCHO and O_3 at 160°W and 50°N (left) and 30°N (right) for the period 16th to 29th October 2000. The simulations are distinguished by line colours: D-CLIM = black line; D-LSCE = red line; D-NOHAL = purple line and D-CL = blue line.

However, this is not the only reason for the different BrO mixing ratios. As pointed out above, the location near the equator produces the least BrO of all four locations, whereas at 30°N the highest mixing ratios are reached. The last two rows of Figure 4.35 show the sea salt mass and the number concentrations. The mass concentrations are similar, but the number concentrations are significantly lower at the equator. Therefore, the particles at the equator are larger and thus less efficiently acidified and depleted (compare first row of the same figure). Due to its low depletion the aerosol theoretically could have been a source of bromine. The (second) reason for the low efficiency of the release process is the short residence time of sea salt and BrO in the MBL. At the equator located within the ITCZ, convection is a dominating process, causing fast upward transport of aerosols as well as trace gases. This is illustrated by Figure 4.36 displaying the 14-day average vertical profiles of BrO at the four distinct sites. In contrast to the other three sites, the mixing ratios at the equator increase from the surface to the tropopause, where a distinct maximum appears. This is caused by the upward transport of BrO and its precursors from the MBL in combination with influences by downward transport of stratospheric bromine.

To conclude, the convective conditions dominate the situation near the equator. This location is an example that restriction of the evaluation to chemical quantities only (known to influence the halogen chemistry) would not be enough to understand the complex feedbacks within a global model. The vertical profiles at the other three locations show a structure with a maximum some hundred meter above the ocean's surface. This is in agreement with the results of von Glasow et al. (2002) obtained with the column model MISTRA-MPIC. They found that the BrO concentration increases from the surface up to the boundary layer top. Above the boundary layer the concentrations rapidly decrease, which is reproduced by ECHAM5/MESSy. The vertical distribution is not as detailed and pronounced as in MISTRA-MPIC, but it is well reproduced in view of the coarse vertical resolution of ECHAM5/MESSy compared to MISTRA-MPIC.

The most striking difference between the two locations discussed so far and the two others is the presence of rain: At 30°N some distinct rain events occur and at the equator only two short rain events happen, whereas it rains more often at the other two locations, especially at 50°N. A correlation between high pH values and the occurrence of stronger rain events is apparent. At 50°N the pH values decrease significantly when the rain rate is lower than approximately 0.5 mm/h. The same is also valid for the location at 35°S where the pH increases to about 9.5 at a rain rate of more than approximately 0.5 mm/h. The behaviour of the pH is directly reflected in the BrO mixing ratios at both locations. When the pH is low, the BrO mixing ratios are high. This is not only due to the efficient release of bromine by the acidified aerosol, an additional effect is that BrO resides longer in the air when the rain rate is small. A small or absent rain rate indicates that scavenging near the surface ceases because the rain has already partly evaporated in this lowest part of the atmosphere. These correlations are confirmed by the variation of the enrichment factors (first row of Figure 4.35). The aerosol is depleted when the rain rate is almost zero, leading to low aerosol pH which enables an efficient bromine release and thus BrO formation. During all rain events (except the very small ones) the enrichment factor is nearly 1, and the aerosol pH is high which reduces the release of bromine to almost zero. At the end of these rain events the enrichment factor of bromine shows a large peak. This is due to the evaporating rain. As explained above, bromine is taken up by cloud and rain droplets. If these droplets evaporate, the halide ions become part of the aerosol. Thus the aerosol is enriched because the scavenging followed by evaporation is a source of halide ions but not for sodium.

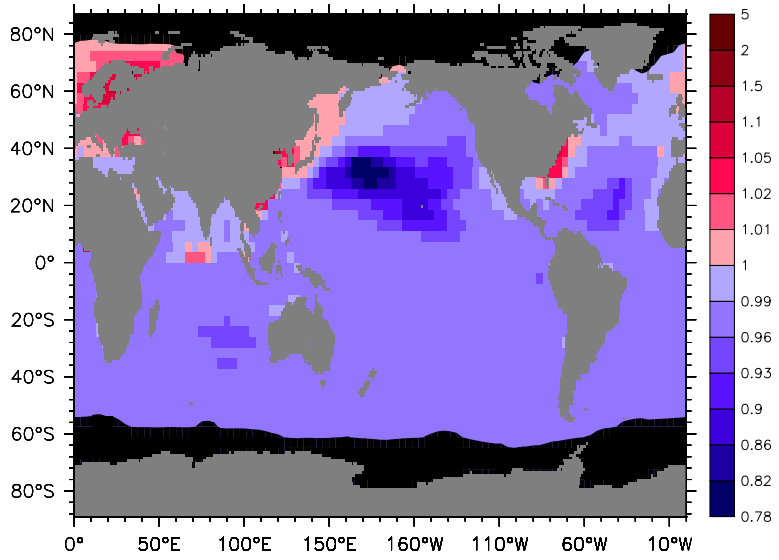

Figure 4.38: Ratio of 14-day O_3 averages of the D-CLIM to the D-LSCE simulation.

After discussing the BrO mixing ratios and the reason for their variation, the impact of halogen chemistry on other trace gases is evaluated. Figure 4.37 shows the short-term cycles of DMS, DMSO, HCHO and ozone at 160°N and 50°N (left column) as well as 30°N (right column) for the four different short-term simulations D-CLIM, D-LSCE, D-NOHAL and D-CL. The BrO mixing ratios at the equator and at 35°S are so small that an impact on the considered trace gases would not be detectable. Therefore, these results are not displayed here. As discussed by von Glasow et al. (2004) DMS is oxidised by BrO and OH yielding DMSO. Thus the consideration of bromine chemistry should have a significant influence on the concentrations of DMS and DMSO. This is confirmed by Figure 4.37 (see first two rows). The higher the BrO values are, the larger is the difference between the DMS concentrations of the simulations without bromine and the D-CLIM simulation. Here the curves for the three simulations without bromine (D-LSCE, D-NOHAL and D-CL) coincide, thus only the D-CL integration (blue line) is visible because it is on top of the other two lines. The DMSO formation depends strongly on the available BrO. This leads to the same morning and evening peaks in the DMSO diurnal cycle already discussed for BrO.

Wagner et al. (2002) discussed the influence of halogen chemistry on formaldehyde (HCHO). To evaluate this, they performed a box model study. In sensitivity studies they used different fixed mixing ratios for BrO (up to 5 pmol/mol) and found only a slight reduction of HCHO concentrations (smaller than 1%). In a second sensitivity study they tested different Cl radical concentrations. HCHO was increased by 22% compared to the base simulation without halogen chemistry, if high Cl concentrations of about 10^5 atoms/cm^3 were applied. The diurnal cycles of formaldehyde in the present study (see third row of Figure 4.37) show a difference for the HCHO mixing ratio in the D-CLIM integration compared to the other three integrations. The lines displaying the simulations without bromine are again one on top of the other. As at the two considered sites Cl radical concentrations of 100 atoms/cm^3 (not shown) are seldomly exceeded, no effect of Cl concentrations on HCHO was detected in agreement with the study of Wagner et al. (2002). The formaldehyde mixing ratios developing in the D-CLIM integration are slightly

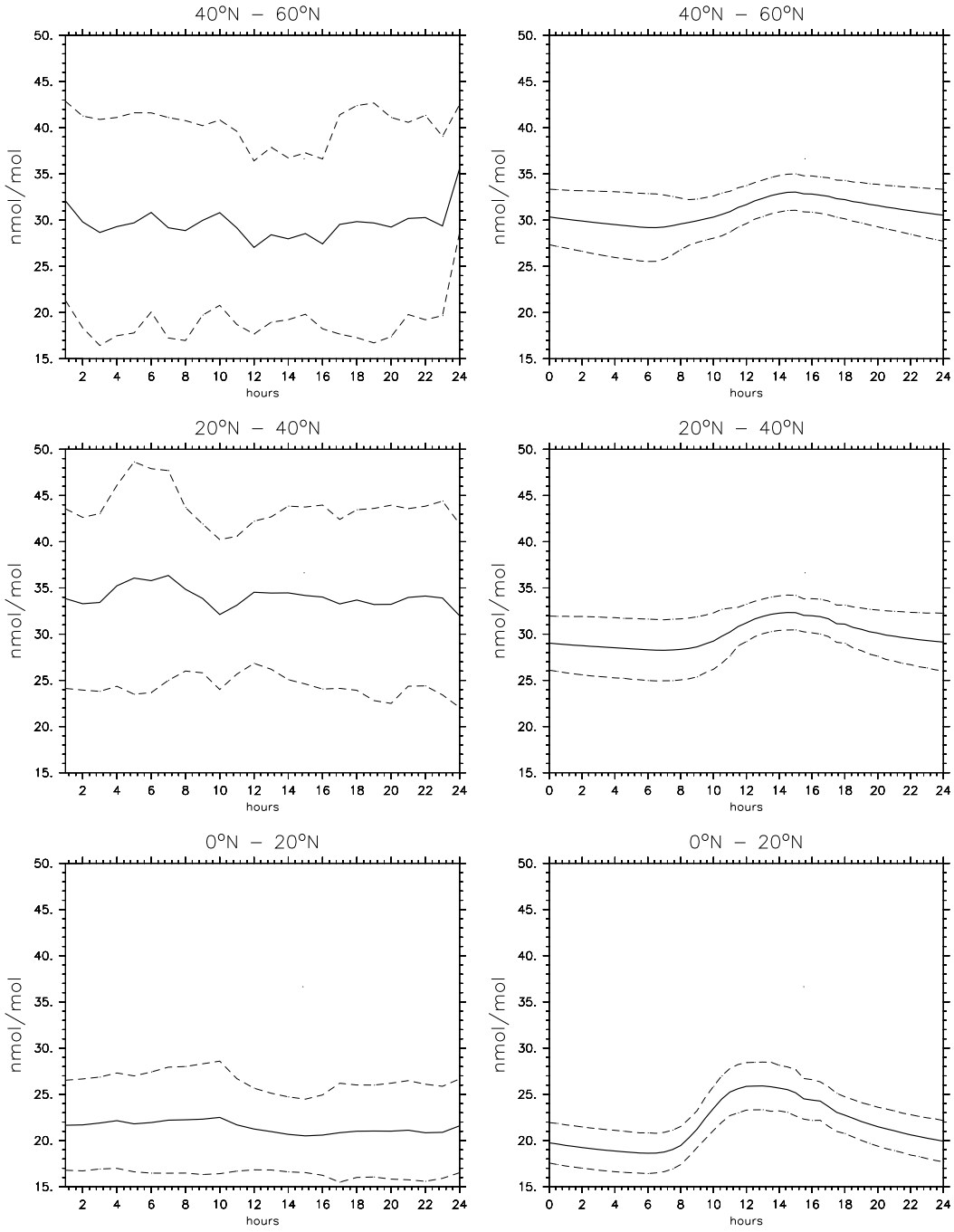

Figure 4.39: Comparison of averaged diurnal cycles of ozone mixing ratios (nmol/mol) for October (in UTC) from measurements over the Atlantic Ocean (Lelieveld et al., 2004) (left column) and from the 14-day model integration D-MBLNUDG (right column) for the same latitude bands as in Table 4.3. The dashed lines show the 1-σ standard deviation of the averaged diurnal cycles.

higher than in the other simulations (between 0.1 to 0.4 nmol/mol, which corresponds to an increase of approximately 4% to 16%). This is more than predicted by Wagner et al. (2002). But the highest deviations in HCHO do not correspond directly to the maxima in

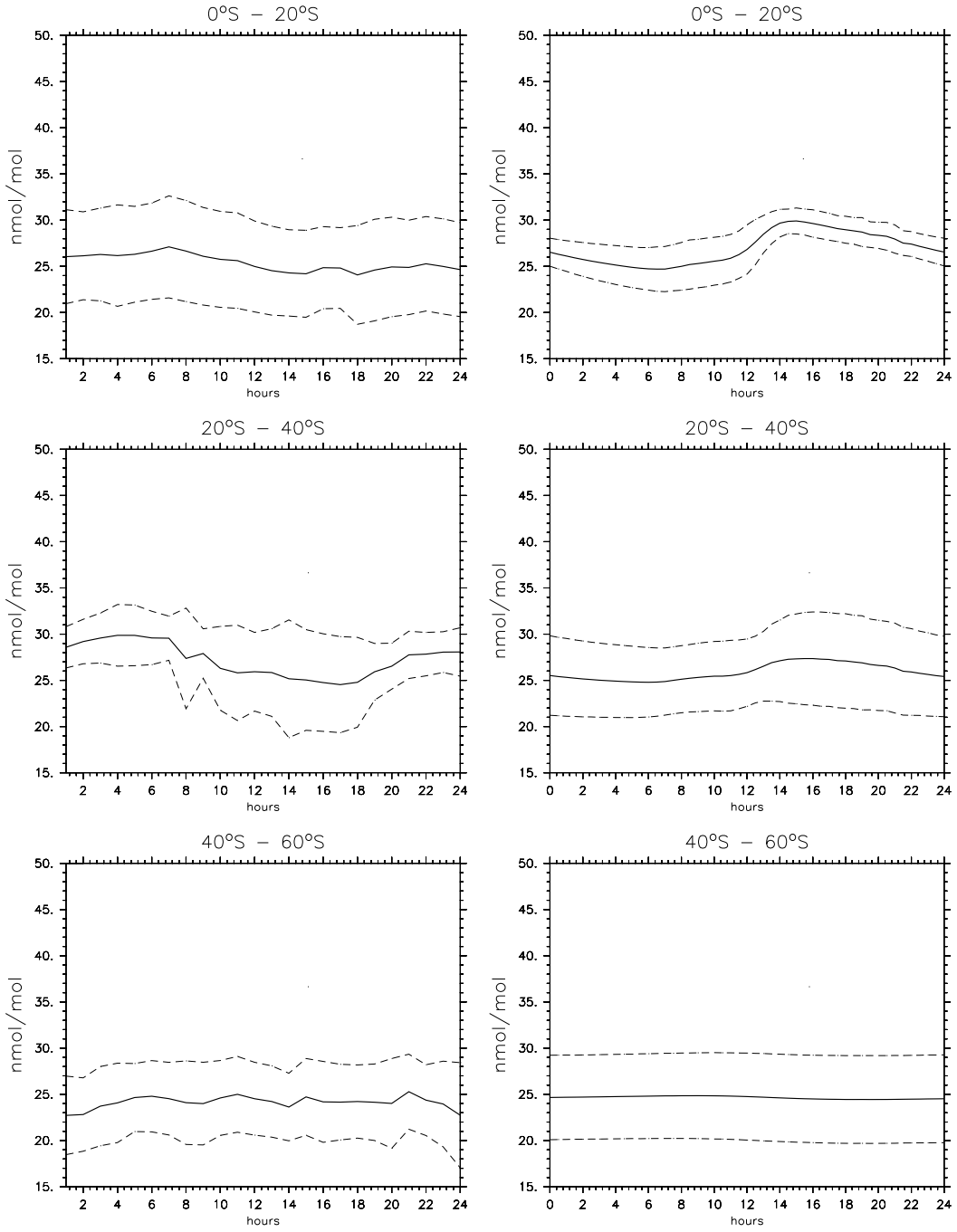

Figure 4.39: (continued)

the BrO mixing ratios. This leads to the conclusion that the formaldehyde concentration is not affected directly by BrO but by other trace gases that are modified by varying BrO concentrations.

The last row of Figure 4.37 displays the ozone mixing ratios. By comparing these panels with the panels showing the BrO mixing ratios (Figure 4.34) for both locations it becomes evident that ozone is continuously substantially reduced when BrO mixing ratios are high. At 30°N where BrO mixing ratios are higher than 1 pmol/mol, the ozone mixing ratios

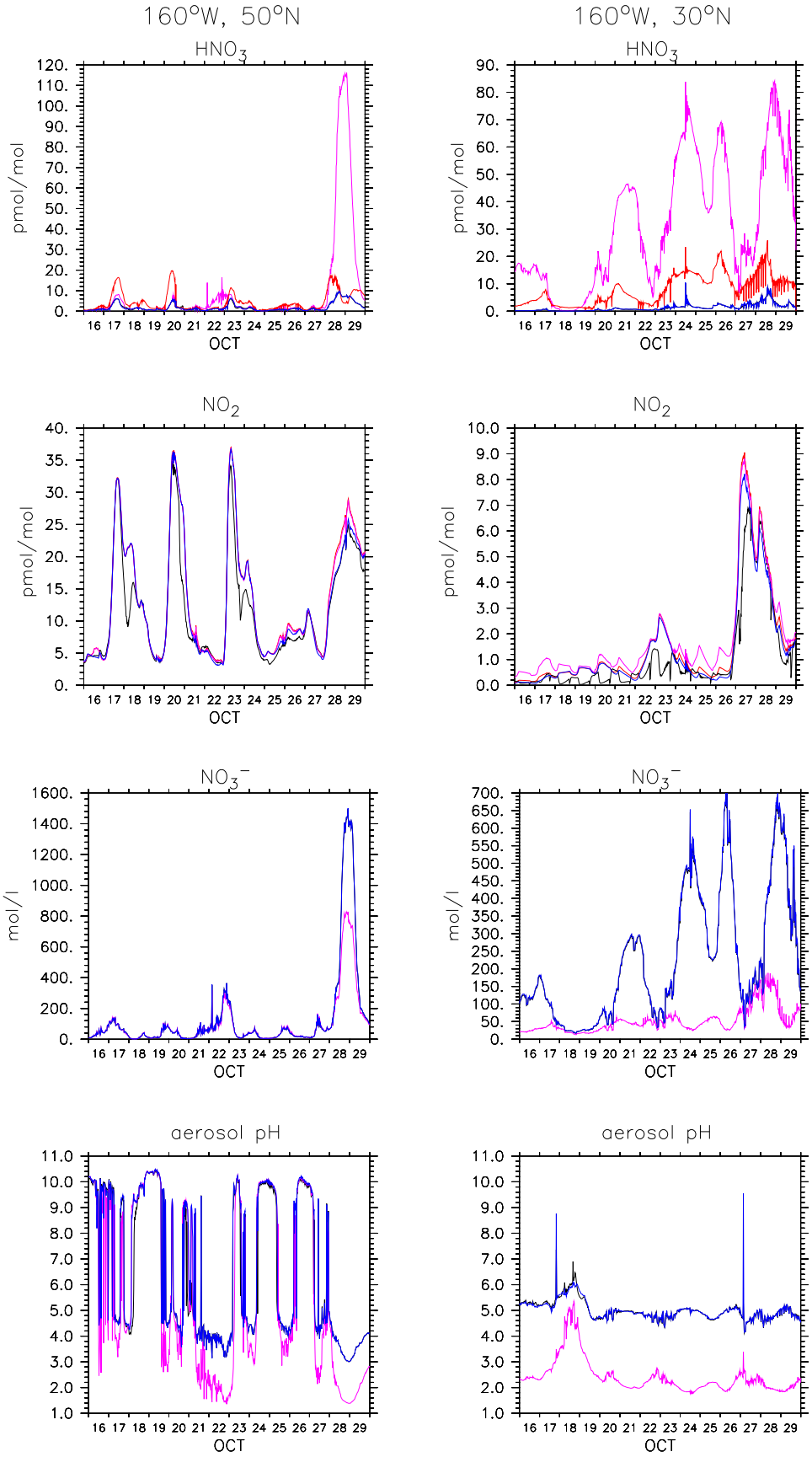

Figure 4.40: Time series of HNO_3, NO_2, NO_3^- and aerosol pH at 160°W and 50°N, 30°N, the equator and 35°S for the period 16th to 29th October 2000. Simulations are distinguished by line colours: D-CLIM = black line; D-LSCE = red line; D-NOHAL = purple line and D-CL = blue line.

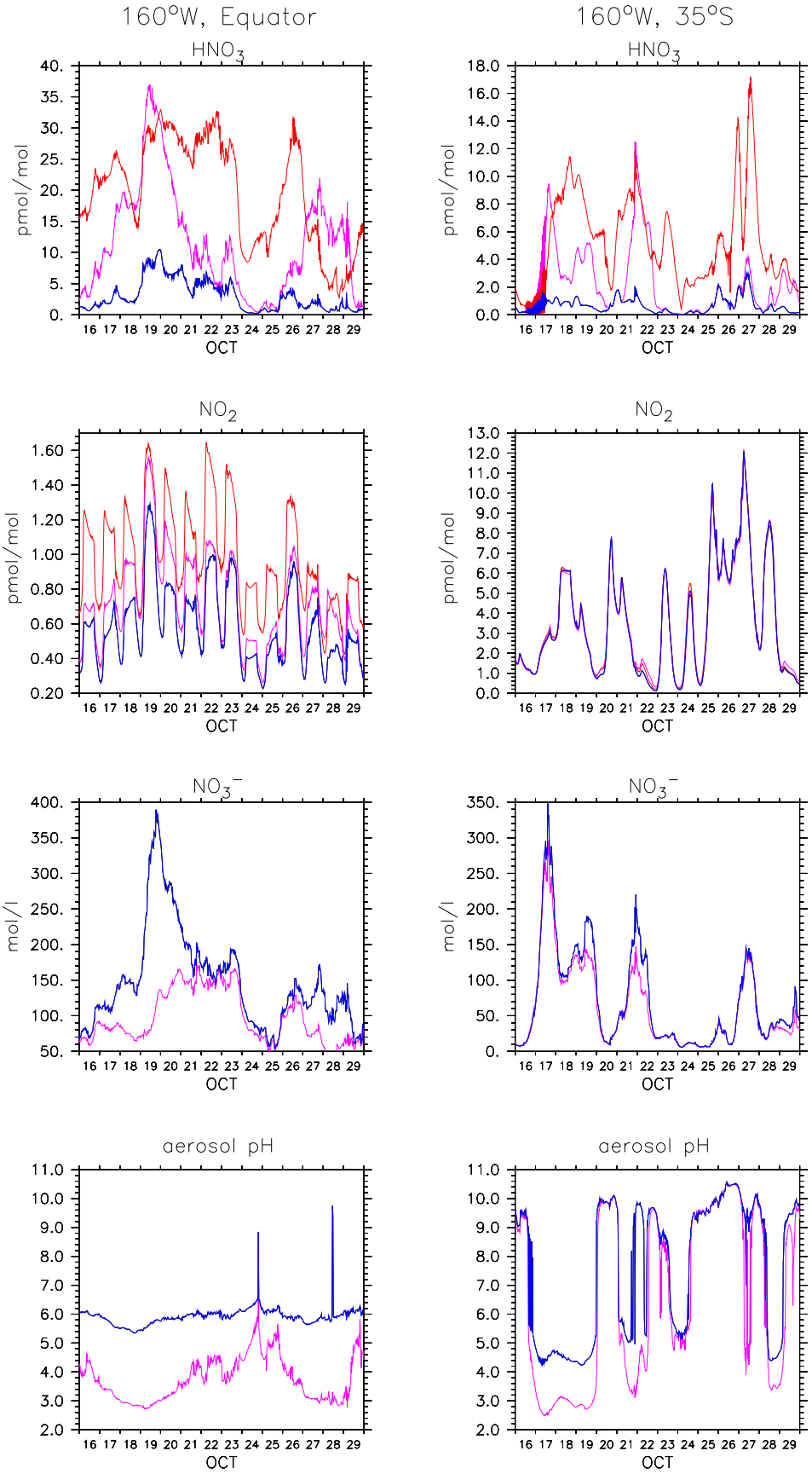

Figure 4.40: (continued)

are up to 4 nmol/mol ($\approx 20\%$) lower in the simulation with bromine chemistry (D-CLIM) than in the three other simulations. Figure 4.38 displays the ratio of the 14-day averages of ozone mixing ratios of the D-CLIM and the D-LSCE simulation. It shows up to 20% less ozone in the simulation with bromine chemistry, exactly in the regions where the high BrO concentrations occur. This effect is very large and probably an upper limit, since the model tends to overestimate reactive bromine. Figure 4.39 displays the averaged diurnal cycles of ozone for measured and modelled data. For comparison, the Atlantic Ocean ship-borne ozone measurements from Lelieveld et al. (2004) have been used (see also Section 4.5). In the left column of Figure 4.39 the diurnal cycles averaged over the eight Octobers from 1995 to 2002 are shown. In the right column the diurnal cycles (14-day averages) of the nudged integration containing the full halogen chemistry (D-MBLNUDG) are displayed. Here the same 20° latitude bands are shown as in Table 4.3. The modelled ozone mixing ratios are always within the 1-σ intervals of the measurements. At most latitude bands the mean modelled ozone mixing ratios are very similar to the measured ones, they are only significantly smaller at 20°N -40 °N and 20°S - 40°S. The modelled ozone mixing ratios reveal a more pronounced diurnal cycle with a maximum between 12 and 15 hours depending on the latitude. The only exception is the latitudinal band from 40°S - 60°S where the simulated ozone concentration stays almost constant. To summarise, the model covers the range of the ozone mixing ratios well for the single latitudinal bands in the Atlantic Ocean. However, the diurnal variations differ between the measurements and the model, as the measurements show no distinct diurnal cycle. The absence of a pronounced diurnal cycle may be an artefact of the number and distribution of the measurements, which are relatively sparse for some latitudinal bands. The ships may have passed the same locations at approximately the same times.

Looking back at the ozone short-term cycles (Figure 4.37, last row) it becomes apparent that the curves of the simulations without bromine (D-LSCE, D-NOHAL and D-CL) are very similar. Nevertheless they slightly differ. The D-LSCE integration simulates the highest ozone concentrations. By including aerosol chemistry (D-NOHAL) the ozone mixing ratio slightly reduces, and the same happens after including chlorine chemistry (D-CL). But only the additional treatment of bromine (D-CLIM) results in remarkably less ozone. Thus ozone is also slightly influenced by aerosol chemistry as well as by chlorine chemistry, whereas most of this is caused by the effect of aerosols and chlorine on nitrogen chemistry.

Figure 4.40 displays the diurnal cycles of some interesting nitrogen oxides illustrating the influences of chlorine and aerosol chemistry in the same way as Figure 4.37. The effect of bromine chemistry on some nitrogen species is negligibly small. Thus for those species the blue line is on top of the black line. The main process influencing the nitrogen oxide concentrations is the uptake onto the aerosol, where the uptake itself is regulated by the aerosol pH, which is buffered by HCl in the simulations including chlorine chemistry. Thus in the D-CL and the D-CLIM simulations nitrogen oxides are taken up by the aerosol, whereas the D-NOHAL simulation sometimes reaches very low aerosol pH values, so that HNO_3 is released back to the gas phase. In these cases the D-NOHAL integration shows higher gas phase nitric acid concentrations than the D-LSCE simulation, in which aerosol chemistry and thus uptake on aerosol is completely missing. This effect is clearly visible in the diurnal cycles of HNO_3 (upper row of Figure 4.40), where the purple line (marking the D-NOHAL simulation) exceeds the red line (marking the pure gas phase simulation) several times. These events coincide with the decrease of the pH to rather low values in the D-NOHAL simulation (see last row of Figure 4.40). The HNO_3 mixing ratios in

the D-CL and the D-CLIM integrations are always lower than in the D-NOHAL and the D-LSCE simulations. According to this, in the simulations including halogens the aerosol often contains more nitrate than in the D-NOHAL integration (see third row of Figures 4.40). Bromine enhances mainly the uptake of NO_2 onto the aerosol, thus the NO_2 mixing ratios (second row of Figure 4.40) deviate between the D-CL simulation and the D-CLIM simulation. No effect at all is evident for the location at 35°S as the BrO concentrations are to small to significantly influence NO_x chemistry. At the equator only the difference between aerosol uptake on unbuffered and buffered aerosol shows up. At the other two locations, where fairly high amounts of BrO occur, NO_2 is affected significantly. At 50°N, the D-CLIM simulation shows less gas phase NO_2 than the other integrations when the BrO reaches mixing ratios higher than approximately 0.4 pmol/mol (see Figure 4.34, first row). As the site at 30°N has a daytime average of more than 2 pmol/mol until the 26th October, the NO_2 mixing ratios in the D-CLIM simulation are always smaller than in the other three integrations. The effect of NO_2 reduction is mostly due to the reaction of BrO with NO_2 forming $BrNO_3$, which is efficiently taken up by the aerosol.

In this section the details of halogen and aerosol chemistry have been shown at four sites located in the Pacific Ocean being characterised by production of very different amounts of BrO. The various competing influences of bromine, chlorine and aerosol chemistry as well as of dynamics and microphysics have been illustrated.

Chapter 5

Discussion

This thesis focuses on the global modelling of halogen chemistry in the marine boundary layer (MBL). It is the first model study using a prognostically calculated sea salt distribution to reach this goal. As sea salt is the dominant source of chlorine and bromine in the MBL, its prognostic calculation is an important step forward. Not only the sea salt aerosol distribution, but also the sources of chloride and bromide within the aerosol are computed online. In addition, the release and recycling of halogens are determined within this global model study by explicitly calculating gas-aerosol multi-phase chemistry, until now only achieved with box and column models (Vogt et al., 1996; von Glasow et al., 2002; Toyota et al., 2001). Previous global model studies used prescribed aerosol distributions or parameterisations of halogen release and of the recycling process (von Glasow et al. (2004) and Xin Yang, Cambridge, group of A. Cox, pers. comm.). These studies were restricted to aerosol chemistry parameterisations for several reasons. First, only few aerosol models have been included into global models so far. The explicit calculation of the aerosol physics and the multi-phase chemistry requires high additional computational efforts for a climate model. In addition to the aerosol size and mass distributions, the explicit calculation of aerosol chemistry within a global model is computationally very expensive[1]. This is not tolerable for many areas of research especially since global modelling requires relatively long integrations. The intent of previous modelling efforts was limited to obtaining a rough estimate of the halogen chemistry to assess its effects on a global scale. This project started with a model setup describing a more comprehensive system, accounting for the important processes, and simplify the model in a second step with the constraint that it still shows the same results but that the computing time decreases to a tolerable amount. The last step would be of high importance to be able to perform a 'halogen forecast' e.g. for measurement campaigns. This is of course a highly ambitious goal, not really intended to be reached within this thesis work. As illustrated in the previous chapter, some processes should still be improved for a 'fully featured' tropospheric halogen chemistry calculation. The first steps have been done and the first prognostically calculated global halogen chemistry of the MBL is presented within this thesis. In the fol-

[1]For example, the 15 month integration (3 month model spinup and 12 month integration) of the LSCE simulation (the integration without aerosol chemistry, but with gas phase chemistry and aerosol physics) took approximately 2 1/2 days on one node of an IBM p575 Power5 system[2]. To simulate the same time period for the CLIM scenario (the simulation with full chlorine and bromine chemistry), approximately 11 1/2 days (i.e. 4 to 5 times longer) were necessary. This increase in simulation time is about the same if the horizontal resolution of the model would be doubled.

[2]Node characteristics: 8-way compute nodes (eServer p575), equipped with 1.9 GHz Power5 processors, with a peak performance of 60.8 GFlop/s and 32 GB of main memory per node.

lowing, the achievements so far, the difficulties occurred within the simulations presented here, and solutions and further steps are discussed in detail.

5.1 Numerical Stiffness of the Chemical Solver

The halogen chemistry mechanism implemented into MECCA-MBL was adopted from the MISTRA-MPIC model (von Glasow et al., 2002). During the first attempts to perform global simulations it became evident that the global model could not cope with the complete mechanism included in MISTRA, although the computational costs were not the primary problem. The limiting factor for the chemistry calculations within MECCA is the numerical stability of the solver. Even if the Rosenbrock solver of third order with automatic time stepping (see Section 3.2.2) is chosen, the solver sometimes crashes[3]. Why does the chemistry perform well in MISTRA-MPIC and in the MECCA-MBL box model, but not in a 3D simulation? The most stringent constraints are given by the boundary conditions. A box or a column model always assumes 'ideal' conditions. The meteorology is constant or slowly developing within these models. Changes in trace gas concentrations, not caused by chemistry, originate from emissions and possibly from entrainment and detrainment at the box or column borders. Thus only small changes occur in tracer concentrations, being no real challenge for the numerical stability of the chemistry solver. In contrast, the global model simulates a wide range of meteorological conditions in one time step: e.g. at the same time there is winter in one hemisphere and summer in the other one, there are simultaneously day and night on earth as well as windy and also calm conditions and so on. This may cause strong gradients for the meteorological variables as well as for the chemical tracers[4]. Thus the meteorological conditions can sometimes change much faster in a global model than in box or column models, thus leading to much higher variations in tracer concentrations in the global model. For example, advection can strongly change the concentrations of trace gases during one time step. Not only the concentrations but also the ratios of the different concentrations can change rapidly, because advection depends on the gradient of each individual trace gas. Other processes usually not resolved in 0D and 1D models are large scale and convective cloud processes. These also lead to large trace gas concentration changes. Hence changes in the tracer concentrations between the calls of the chemical solver can be much higher in a global model than in box and column models. This creates conditions far from the chemical equilibrium, sometimes causing unrealistic reaction rates yielding negative concentrations within one time step of the solver. This should be prevented by the automatic time step control of the Rosenbrock solver. However, in some cases this control mechanism fails owing to the large range of ambient conditions. This problem only occurs if gas phase and aerosol chemistry are simultaneously calculated within the same mechanism associated with fast tracer transfer between phases. The solver with automatic time step control is stable for all simulations performed with MECCA as long as only gas phase chemistry is applied.

To prevent the integrator from crashing, one has to avoid situations in which high instabilities occur. This could be achieved by circumventing reactions with very high reaction rates, e.g., by applying an equilibrium assumption instead of resolving the equi-

[3]The chemical integration produces unreasonable values as mixing ratios > 1 mol/mol or NaN (Not A Number). The latter mostly happens because of a divison by a numerical zero within the matrix inversion in the Rosenbrock solver.

[4]The term 'tracer' includes the gas phase species as well as the species dissolved in the aerosol, i.e. all chemical active compounds.

librium explicitly. This method is not yet widely used within MECCA-MBL, because it requires a complete rearrangement of the equation file. However, it is discussed to be used in future.

The second possibility is the reduction of the system. So far the original aerosol chemistry mechanism adopted from MISTRA-MPIC was reduced to the most important equations. Tables C.3 - C.5 show this reduced subset of reactions (for a complete list of the available reactions see the MECCA/MECCA-MBL website[5]). A further crucial reduction of the system, required to stabilise it, was its limitation to the gas phase and only one aerosol mode. Every additional mode interacting with the gas phase makes the calculation of the gas phase concentrations rather complex. Additionally every aerosol mode is associated with its own liquid water content, which directly influences most of the reaction rates of this mode. Thus the reaction rates of each mode can range in orders of magnitude dependent on the liquid water content. Therefore, the aerosol chemistry in the present study is restricted to the coarse (i.e. the sea salt aerosol) mode. This has consequences for the results of this study. As pointed out by von Glasow et al. (2002) sulphate aerosol significantly influences halogen chemistry, because it recycles reactive bromine and chlorine. HCl, HBr, HOBr and $BrNO_3$ are scavenged by sulphate aerosol and due to the low pH they are rapidly transformed into Br_2 or BrCl, which instantaneously degas. The recycling on sulphate aerosol can be more efficient than on sea salt aerosol (von Glasow et al., 2002). This process is missing in the model study presented in this thesis, as the sulphate aerosol reactions are neglected because of the numerical instability of the chemical solver. Thus the effect of the reactive halogen species (RHS) may be underpredicted in this model due to the missing sulphate aerosol chemistry in areas where sulphate aerosol concentrations are relatively high and where the sea salt aerosol is not highly acidic.

5.2 Uncertainties Influencing the Emission Fluxes

Some inconsistencies in the model setup of the halogen chemistry in MESSy/MECCA-MBL related to sea salt emissions have been noticed during the evaluation of the results. On the one hand the sea salt emissions are strongly influenced by the simulated model dynamics. On the other hand, the emissions of halide ions as well as of hydrogencarbonate are enhanced because of the process splitting of emission and deposition calculations.

5.2.1 Dynamics

The sea salt emission flux is strongly dependent on the surface wind speed, which itself is regulated by the model dynamics. The modelled dynamics are affected by the model setup, for which the chosen resolution is important. The coarser the resolution, the more unrealistic the model may be.

Resolution

For this study the horizontal resolution of T31 was chosen, which is the lowest one resolving synoptical disturbances such as cyclones and high-pressure areas. It was not possible to

[5] *http://www.mpch-mainz.mpg.de/~sander/messy/mecca/*

choose a higher resolution because of the enormous increase in computing time[6]. By the comparison of the climatological (CLIM) and the nudged simulation (MBLNUDG) it became evident that the resolution of T31 is not sufficient to resolve some dynamical details. In contrast to the CLIM scenario the MBLNUDG simulation is driven by the dynamics of the ECMWF model which has a higher resolution (T159), thus showing more dynamical details. Therefore model simulations performed at low horizontal resolution should be nudged integrations to get more realistic results.

Input Data

Apart from the resolution the input data chosen for a model simulation influence the dynamics of a model to a significant degree. This does not necessarily aim at the initial data, since in most cases the model results after 3 months of spinup time should be independent of the initial data. The regularly applied boundary conditions influence the dynamics most. These are in case of the ECHAM5 mainly the sea surface temperatures (SSTs), which are prescribed by an independent data set. In this model study a climatological mean of the annual SST cycles is applied. Another choice would have been to use the measured yearly data sets provided by AMIP[7] (Atmospheric Model Intercomparison Project). The used climatological mean is determined from these yearly data sets. SSTs represent a key factor in the dynamics developing in the model, thus the choice should have a significant influence. In this thesis no sensitivity analysis addressing this point was included because of a lack in the availability of the complete AMIP data set for the year 2000.

Nudging

Instead of a sensitivity study with the yearly AMIP data set, a comparison between a completely climatological and a nudged simulation has been performed. The constraints of a nudged integration are even higher than those imposed by the AMIP SST data. As the reanalysis simulations of the ECMWF are integrations performed by an operational weather prediction model, in which all available observational data have been assimilated, this is the global information nearest to reality. Thus a nudged ECHAM5 simulation can be conceived as more realistic than a climatological integration. The climatological simulations produce too high wind speeds in the northern hemisphere and too low ones in the Southern Ocean storm track region. As these differences in wind speeds lead to differences in the sea salt emission fluxes, a direct influence of the applied dynamics on the modelled halogen chemistry is evident. Hence, a difference in dynamics changes the emission patterns and in that way the modelled RHS chemistry. Additionally, acid transport from the big cities at the east coast of America and Asia over the northern oceans is influenced by dynamics.

[6] A doubling of the horizontal resolution would yield in a simulation time four times as high. Usually the time step is halfed if the resolution is doubled due to the Courant-Friedrich-Levy criteria. This would lead to a computing time eight times as high. In terms of the computing times given above this would yield a simulation time of approximately 3 months for the first 15 months for the CLIM scenario and the 5 1/4 year integration would have taken approximately 10 months.

[7] http://www-pcmdi.llnl.gov/projects/amip/index.php

5.2.2 Process Splitting of Emission and Deposition Calculations

The calculation of halide emissions from the sea salt emission mass flux represents another difficult task. Based on the assumptions that sea water has a relatively constant composition of the abundant ions and that the calculated sea salt mass fluxes consist of NaCl only, the chloride emission flux is calculated from the sea salt emission mass flux, and subsequently the bromide and the hydrogencarbonate fluxes are scaled with the constant ratios as listed in Table 3.3. This way of emission calculation has a hidden problem. The surface wind speed triggers the wave motion of the ocean. The higher the surface wind speed the higher are the waves and the more sea spray is produced. In reality the droplets produced can undergo two different processes. The smaller ones remain air-borne and equilibrate with their environment. However, larger droplets sediment instantaneously to the ocean, thus they do not influence the chemistry. In the model the aerosol distribution is exactly modelled in this way. First the emission of sea salt mass and particle number is calculated from the emission flux, and afterwards the removal processes as dry deposition, sedimentation and wet deposition are applied. The critical point is that this process splitting is applied to the chemistry in the same way. Thus the ion emissions are calculated from the sea salt emission flux as explained above. These newly emitted ions are added to the chemical tracers of the aerosol. Thus a new aerosol composition is introduced and this mixture undergoes the removal processes with the aerosol particles. In the end the modelled aerosol is 'too fresh', because in reality removal processes deposit much more fresh sea salt. A solution to this problem would be to apply a net emission flux calculated from the difference of the emission and the dry deposition flux of sea salt. This is planned for a future model study.

In the simulations shown in the present study process splitting is applied, which means that the renewal of sea salt is overpredicted and its lifetime is underestimated. As a consequence, the emissions of chloride, bromide and hydrogencarbonate are too high. In case of hydrogencarbonate this is equivalent to an overpredicted supply of alkalinity to the aerosol. In areas of low acid supply this leads to much too alkaline aerosol as it prevails over the Southern Oceans (see for example Figure 4.17). Significant halogen release happens only in acidified aerosol because the release as well as the recycling are acid catalysed. Thus the overprediction of alkalinity supply to the aerosol leads to less RHS chemistry in areas of low available acids. In contrast, the overprediction of alkalinity has little impact on RHS chemistry in areas where acid concentrations are high. The acids rapidly titrate the aerosol and thus efficient halogen release is possible at any time. This occurs in the results shown for the central Pacific Ocean and central Atlantic Ocean.

The effect of the overestimation of the halide ion emissions is coupled to the aerosol pH, as the release of halogens to the gas phase is acid catalysed. Thus the overestimation of the halide emission has a negligible impact around the Southern Ocean storm track regions. The only exception is the southern hemispheric summer, the season when the aerosol pH is low enough to allow for efficient halogen release (see Figure 4.17). In contrast, the aerosol pH over the northern hemispheric oceans is high enough to account for efficient halogen release most of the time. In this case the overprediction of the halide ion emission results in additional halogen release. This is the reason for the very high BrO mixing ratios modelled over the northern oceans (see Figures 4.20, 4.21, and 4.33). Consequently the overestimation of the ion concentrations is twofold in this region: on the one hand the effective emission fluxes are too high because of the process splitting applied in the calculation of the new concentrations due to the emission and deposition fluxes. On the

other hand the emission fluxes themselves are overestimated in this region related to the dynamics (especially in the climatological simulations).

The overrating of the RHS chemistry because of too high emissions is counteracted by the effect of slowing down this chemistry by the neglect of sulphate aerosol (see above). The net effect is an overestimation of RHS in the northern hemisphere and an underestimation in the southern hemisphere where not enough acidity is available to titrate the sea salt aerosol.

5.3 Interactions between Chemical and Physical Processes

The last section of the previous chapter was dedicated to the evaluation of interactions between different processes driving halogen chemistry. The impact of halogen chemistry on other trace gases has been investigated as well. These results are unaffected by the fact that the global distribution of RHS chemistry is not yet fully realistically simulated. Evaporation of cloud and rain droplets leads to an increase in the enrichment factors, which is due to the uptake of halogen containing gases by the droplets. When the droplets evaporate, the halide ions remain in the aerosol phase, thus enriching the aerosol phase in chloride and bromide because no liquid phase sodium is gained by this process.

Another important aspect is the vertical transport. If the aerosol is transported rapidly upward after emission (as shown for the site near the equator in Section 4.6) the time to initiate efficient halogen chemistry near the surface is lacking.

5.4 Impact of RHS chemistry

One of the main conclusions of this thesis is that significant RHS chemistry develops everywhere, where sufficient fresh sea salt is produced and the acid supply is high enough. In this case halogen release causes high BrO mixing ratios in the MBL during daytime showing a significant impact on other trace gases. High BrO mixing ratios are indicative for reactive halogen chemistry. Thus the largest effects of halogens are expected where the highest BrO mixing ratios occur.

5.4.1 ... on Ozone

The effect of BrO on ozone is confirmed by the results shown in Section 4.6. The high BrO mixing ratios produced at 30°N result in strong depletions in O_3. The ozone reductions due to bromine chemistry shown in the Sections 4.5 and 4.6 confirm the results of other model studies (von Glasow et al., 2004 and Xin Yang, pers. comm.), indicating that sufficient BrO concentrations lead to substantial ozone depletions. The absolute rate of ozone destruction can not be predicted from the present model study as the above discussed issues enhance the BrO production in the northern hemisphere and reduce it in the southern hemisphere, leading to an over- or underestimation of ozone destruction in the respective hemisphere. However, the modelled ozone concentrations compare reasonably well with ozone measurements.

5.4.2 ... on DMS and DMSO

Von Glasow and Crutzen (2004) discussed the possible role of BrO in the DMS oxidation process. They pointed to the increasing importance of the addition pathway of the DMS

oxidation in the presence of BrO, thus shifting particle formation and particle growth by sulphur containing species towards particle growth instead of formation of new particle by H_2SO_4. The feedback on particle formation was not studied within this thesis, but a reduction of DMS concentrations and an increase of DMSO concentrations in the simulation including bromine chemistry in comparison to the simulations without bromine chemistry points to the important role of BrO in DMS oxidation.

5.4.3 ... on HCHO

A direct impact of BrO and Cl radicals on formaldehyde was not detectable within this study, which is in accordance with Wagner et al. (2002). However, the HCHO concentrations differ somewhat between the sensitivity integrations, but these differences are not in direct correspondence to the BrO and Cl concentration changes. Thus they have to be indirect effects of changes in other trace gas concentrations due to the abundance of BrO and Cl.

5.4.4 ... on Uptake of Nitrogen Oxides and Nitric Acid

In addition to the influence of bromine on trace gases the importance of Cl^-/HCl buffering within the aerosol was shown based on a sensitivity study with two model simulations including and excluding chlorine chemistry. The buffered aerosol takes up most of the nitrogen oxides, whereas the pH of the unbuffered aerosol is too low, so that HNO_3 is released back into the gas phase when the aerosol water content decreases (see Figures 4.32 and 4.40). Furthermore the effect of bromine chemistry was shown, leading to enhanced denoxification as BrO reacts with NO_2 to bromine nitrate, which is efficiently taken up by the aerosol, thus decreasing the nitrogen dioxide concentration.

The most critical aspect in modelling RHS chemistry is the aerosol pH, because halogen chemistry responds very sensitively to it. Thus the simulation of aerosol pH (mainly the emission of hydrogencarbonate) needs to be improved in future.

Chapter 6

Conclusions

Within the scope of this thesis results were presented of the first global study of halogen chemistry in the marine boundary layer using a general circulation model (GCM) and explicitly calculating halogen chemistry in the gas phase and the aerosol phase as well as the transfer between both phases. It was pointed out that the explicit treatment of this complex system leads to some difficulties, mainly due to the extensive computer time required and the numerical stiffness of the chemical solver. Nevertheless, this study shows that it is possible to adopt a model setup including gas and aerosol phase chemistry as well as prognostic calculations of the aerosol distribution on a global scale. Even if there is evidence that the absolute values of the modelled species' concentrations do not fully comply with measurements, some typical mechanisms driving reactive halogen chemistry as well as some typical patterns of the horizontal distributions could be identified:

- High BrO concentrations develop where acid supply and production of fresh sea salt are relatively high.
- BrO oxidises DMS to a significant amount, thus strengthening the importance of the addition pathway of DMS oxidation[1].
- No influence of BrO on formaldehyde is detectable in agreement with Wagner et al. (2002).
- Bromine release is closely coupled to the aerosol pH.
- The sea salt aerosol pH is buffered by two processes: the alkaline aerosol is buffered by hydrogencarbonate, whereas the more important buffer is Cl^-/HCl. A sensitivity study showed that in comparison to the few available sea salt aerosol pH measurements the aerosol not containing the Cl^-/HCl buffer was by far too acidic.
- Sea salt aerosol enhances the denoxification of polluted air masses, since bromine nitrate and nitric acid are more efficiently taken up by the Cl^-/HCl buffered aerosol.

At present the model likely overestimates the BrO concentrations in the northern hemisphere and underpredicts them in the southern hemisphere, as a consequence of the process splitting applied to the calculations of emission and deposition fluxes. But apart from the absolute values the pattern is expected to stay the same, if a combined treatment of those

[1] This is (following von Glasow and Crutzen, 2004) equivalent to the strengthening of particle growth due to DMS oxidation instead of primary particle formation by H_2SO_4 (Figure 2.2).

fluxes is applied. High peaks (larger than 1 pmol/mol BrO on average) can develop over the North Pacific as well as the North Atlantic. These are abundant throughout the year and reach a maximum in the northern hemispheric spring. The peaks are caused by the interaction of relatively strong sea salt emission fluxes as well as the constant supply of gas phase acids, advected from the urban and industrial centers of the continents. In the southern hemisphere the simulated BrO mixing ratios are significantly smaller (2-3 orders of magnitude on an average). They are assumed to be underpredicted because of too high emissions of alkalinity (hydrogencarbonate) associated with sea water.

The contrasts in the halogen chemistry of the hemispheres are less marked if the model is forced to the dynamics provided by the ECMWF reanalysis data. This is due to the lower surface wind speeds developing in the nudged simulation in the northern hemisphere, thus causing smaller emissions of halogen ions followed by less halogen release. In the southern hemisphere the surface wind speeds developing in the nudged simulation are somewhat higher in the summer compared to the climatological simulation. As the southern hemispheric summer is the season during which the aerosol is sufficiently acidified to release bromine in a substantial amount, this yields a higher BrO formation. Thus the contrast between both hemispheres is considerably sharper in the climatological simulation than in the nudged integration.

To conclude, the model calculates quite realistic marine boundary layer halogen chemistry. To further improve the results (i.e. be closer to the few available measurements) future model studies should account for the following:

- Simulations should be performed as nudged integrations, since the climatological integration produces too strong surface winds and thus too high sea salt emissions.

- For the halide and hydrogencarbonate emissions, a net emission flux resulting from the difference of sea salt emission and dry deposition flux should be applied.

- The emissions of halocarbons should be added to the model setup.

- If possible, the chemistry of the sulphate aerosol mode should also be taken into account.

These steps should lead to further improvement of the already very promising model results.

Appendix A

Abbreviations

Abbreviation	Meaning
1D	one-dimensional
3D	three-dimensional
ACE1	First Aerosol Characterization Experiment
AEROCOM	emission scenario and abbreviation of one simulation, see Table 4.1
AMIP	Atmospheric Model Intercomparison Project
ASTEX	Atlantic Stratocumulus Transition EXperiment
CCN	Cloud Condensation Nuclei
CL	abbreviation of respective simulation, see Table 4.1
CLIM	abbreviation of respective simulation, see Table 4.1
CLIM2000	abbreviation of respective simulation, see Table 4.1
CPU	Central Processing Unit
CTM	Chemical Transfer Model
DLR	Deutsches Zentrum für Luft-und Raumfahrt
D-CL	abbreviation of respective simulation, see Table 4.1
D-CLIM	abbreviation of respective simulation, see Table 4.1
D-LSCE	abbreviation of respective simulation, see Table 4.1
D-MBLNUDG	abbreviation of respective simulation, see Table 4.1
D-NOHAL	abbreviation of respective simulation, see Table 4.1
DJF	Season: December, January, February
DMS	DiMethyl Sulphide
DOAS	Differential Optical Absorption Spectroscopy
ECHAM5	climate model (description see Chapter 3.1)
ECHAM5-HAM	An ECHAM5 version containing P. Stier's (MPI-MET) implementation of the aerosol model M7
ECMWF	European Center for Medium-range Weather Forecast
FT	Free Troposphere
GCM	General Circulation Model
INDOEX	INDian Ocean EXperiment
ITCZ	InnerTropical Convergence Zone
JJA	Season: June, July, August
JRC	Joint Research Center of the European Commission, Ispra, Italy

Abbreviation	Meaning
JVAL	MESSy submodel calculating photolysis rates
KPP	Kinetic PreProcessor (software integrating differential equation sets)
LSCE	emission scenario and abbreviation of one simulation, see Table 4.1
LSCE-NUDG	abbreviation of respective simulation, see Table 4.1
M7	aerosol model included in ECHAM5/MESSy
MAGE	Marine Aerosol and Gas Exchange
MAM	Season: March, April, May
MATCH	Model of Atmospheric Transport and CHemistry
MBL	Marine Boundary Layer
MBLNUDG	bbreviation of respective simulation, see Table 4.1
MECCA	MESSy submodel calculating gas phase chemistry
MECCA-MBL	submodel of MECCA to calculate MBL halogen chemistry
MESSy	Modular Earth Submodel SYstem
MISTRA	MIcrophysical STRAtus (one-dimensional microphysical model)
MISTRA-MPIC	MPI-C verison of MISTRA, comprising additionally to the original MISTRA a chemistry mechanism describing MBL halogen chemistry
MOCCA	box Model Of Chemistry Considering Aerosols
MONAHAN	emission scenario and abbreviation of respective simulation, see Table 4.1
MPI	Max Planck Institute
MPI-C	Max Planck Institute for Chemistry, Mainz, Germany
MPI-MET	Max Planck Institute for Meteorology, Hamburg, Germany
MSA	Methane Sulphonic Acid
MSIA	Methane SulphInic Acid
NMHC	Non-Methane HydroCarbon
NOHAL	abbreviation of respective simulation, see Table 4.1
nss	non-sea salt
OFFLEM	OFFLine EMission submodel of MESSy
ONLEM	ONLine EMission submodel of MESSy
PHOENICS	Particles of Human Origin Extinguishing Natural solar radiation In Climate Systems (*http://phoenics.chemistry.uoc.gr*)
PSC	Polar Stratospheric Clouds; also synonym for the MESSy submodel calculating PSCs
RHS	Reactive Halogen Species
SCAV	SCAVenging model within MESSy
SEAMAC	size-SEgregated Aerosol model of the Marine Air Chemistry
SHADOZ	Southern Hemispheric Additional OZonesondes
SON	Season: September, October, November
SST	Sea Surface Temperature
TROPOP	MESSy submodel
VOC	Volatile Organic Compound

Appendix B

Variable Definitions

Variable	Description	SI-unit
c_g	gas phase concentration	molecules/m^3
D_g	gas phase diffusion coefficient	m^2/s
d	displacement height	m
$F(\lambda)$	spectral actinic flux	W/(m^2 m)
$F_{SS,j}$	sea salt emission mass flux	kg/(m^2 s)
F_{dep}	dry deposition flux	molecules/(m^2 s)
$F_m(X)$	model forcing for X	
f_j	correction factor	1
f_{Csf}	Cunningham slip flow correction factor	1
f_{Slinn}	Slinn correction factor for sedimentation velocity	1
$G(X)$	relaxation coefficient	
g	gravitational acceleration	m/s^2
I	photochemically active spectral interval (178.6 nm $\leq \lambda \leq$ 752.5 nm)	m
J_X	photolysis rate coefficient	1/s
$J_{i,X}$	photolysis rate coefficient for spectral interval i	1/s
$J^a_{i,X}$	photolysis rate coefficient for spectral interval i for a purely absorbing atmosphere	1/s
k_exb	backward exchange rate	1/s
k_exf	forward exchange rate	1/s
k_{H}	inverse dimensionless Henry's law coefficient	1
k_{henry}	Henry's law coefficient	mol/ (m^3_{aq} Pa)
k_{mt}	accommodation coefficient	1/s
L	Monin-Obukhov-length	m
LAI	Leaf Area Index	m^2
lwc	liquid water content	m^3(water)/ m^3(air)
M_X	molar mass of species X	kg/mol
N	number concentration of aerosol model	1/m^3
N^{tot}_j	total number concentration of one aerosol model j	1/m^3
Pr	Prandtl number (0.72)	1
R	gas constant for dry air	J/ (mol K)
R_{aero}	aerodynamic resistance	s/m

Variable	Description	SI-unit
R_{qbr}	quasi-laminar boundary layer resistance	s/m
R_{surf}	surface resistance	s/m
R_{type}	surface resistance of soil type 'type'	s/m
r_{leaf}	leaf/needle resistance	s/m
r_{soil}	soil resistance	s/m
r	radius of the total particle	m
r_{amb}	ambient radius	m
Sc	Schmidt number = (kinematic viscosity of air)/ (molecular diffusivity of trace gas)	1
T	temperature	K
Δt	time step	s
$u_\star$	friction velocity	m/s
$\bar{v}$	mean molecular velocity	m/s
v_{d}	dry deposition velocity	m/s
v_{Stokes}	Stokes velocity	m/s
v_{t}	terminal sedimentation velocity	m/s
X	denotes one species/tracer or variable	
z	height	m
z_0	roughness length	m
$z_{0\mathrm{m}}$	roughness length of momentum	m
$z_{0\mathrm{X}}$	roughness length of trace gas	m
Δz	layer thickness	m
α	accommodation coefficient	1
δ_i	ratio of the actual actinic flux to the actinic flux for a purely absorbing atmosphere	1
η	dynamic viscosity	kg/(m s)
κ	von Karman constant (0.4)	1
λ_{air}	mean free path of air	m
λ	wavelength	m
$\rho_{\mathrm{aero}}(k)$	aerosol density of mode k	kg/m^3
ρ_{air}	density of air	kg/m^3
σ	standard deviation (of a mode)	1
$\sigma_X(\lambda)$	absorption cross-section of species X at wavelength λ	m^2
$\phi_X(\lambda)$	quantum yield of species X at wavelength λ	1
Ψ	dimensionless stability function	1

Appendix C

MECCA Reaction Tables

Table C.1: Gas Phase Reactions

#	Reaction	Rate Coefficient
G1000	$O_2 + O(^1D) \rightarrow O(^3P) + O_2$	`3.2E-11*EXP(70./temp)`
G1001	$O_2 + O(^3P) \rightarrow O_3$	`6.E-34*((temp/300.) **(-2.4))*cair`
G2100	$H + O_2 \rightarrow HO_2$	`k_3rd(temp,cair,5.7E-32, 1.6,7.5E-11,0.,0.6)`
G2104	$OH + O_3 \rightarrow HO_2$	`1.7E-12*EXP(-940./temp)`
G2105	$OH + H_2 \rightarrow H_2O + H$	`5.5E-12*EXP(-2000./temp)`
G2107	$HO_2 + O_3 \rightarrow OH$	`1.E-14*EXP(-490./temp)`
G2109	$HO_2 + OH \rightarrow H_2O$	`4.8E-11*EXP(250./temp)`
G2110	$HO_2 + HO_2 \rightarrow H_2O_2$	`k_HO2_HO2`
G2111	$H_2O + O(^1D) \rightarrow 2\ OH$	`2.2E-10`
G2112	$H_2O_2 + OH \rightarrow H_2O + HO_2$	`2.9E-12*EXP(-160./temp)`
G3101	$N_2 + O(^1D) \rightarrow O(^3P) + N_2$	`1.8E-11*EXP(110./temp)`
G3103	$NO + O_3 \rightarrow NO_2 + O_2$	`3.E-12*EXP(-1500./temp)`
G3106	$NO_2 + O_3 \rightarrow NO_3 + O_2$	`1.2E-13*EXP(-2450./temp)`
G3108	$NO_3 + NO \rightarrow 2\ NO_2$	`1.5E-11*EXP(170./temp)`
G3109	$NO_3 + NO_2 \rightarrow N_2O_5$	`k_NO3_NO2`
G3110	$N_2O_5 \rightarrow NO_2 + NO_3$	`k_NO3_NO2/ (3.E-27*EXP(10990./temp))`
G3200	$NO + OH \rightarrow HONO$	`k_3rd(temp,cair,7.E-31, 2.6,3.6E-11,0.1,0.6)`
G3201	$NO + HO_2 \rightarrow NO_2 + OH$	`3.5E-12*EXP(250./temp)`
G3202	$NO_2 + OH \rightarrow HNO_3$	`k_3rd(temp,cair,2.E-30, 3.,2.5E-11,0.,0.6)`
G3203	$NO_2 + HO_2 \rightarrow HNO_4$	`k_NO2_HO2`
G3204	$NO_3 + HO_2 \rightarrow NO_2 + OH + O_2$	`3.5E-12`
G3205	$HONO + OH \rightarrow NO_2 + H_2O$	`1.8E-11*EXP(-390./temp)`
G3206	$HNO_3 + OH \rightarrow H_2O + NO_3$	`k_HNO3_OH`
G3207	$HNO_4 \rightarrow NO_2 + HO_2$	`k_NO2_HO2/ (2.1E-27*EXP(10900./temp))`
G3208	$HNO_4 + OH \rightarrow NO_2 + H_2O$	`1.3E-12*EXP(380./temp)`

Table C.1: Gas Phase Reactions (continued)

#	Reaction	Rate Coefficient
G4101	$CH_4 + OH \rightarrow CH_3O_2 + H_2O$	1.85E-20*EXP(2.82*log(temp) -987./temp)
G4102	$CH_3OH + OH \rightarrow HCHO + HO_2$	7.3E-12*EXP(-620./temp)
G4103a	$CH_3O_2 + HO_2 \rightarrow CH_3OOH$	4.1E-13*EXP(750./temp) /(1.+1./497.7*EXP(1160./ temp))
G4103b	$CH_3O_2 + HO_2 \rightarrow HCHO + H_2O + O_2$	4.1E-13*EXP(750./temp) /(1.+497.7*EXP(-1160./ temp))
G4104	$CH_3O_2 + NO \rightarrow HCHO + NO_2 + HO_2$	2.8E-12*EXP(300./temp)
G4105	$CH_3O_2 + NO_3 \rightarrow HCHO + HO_2 + NO_2$	1.3E-12
G4106a	$CH_3O_2 + CH_3O_2 \rightarrow 2\ HCHO + 2\ HO_2$	9.5E-14*EXP(390./temp) /(1.+1./26.2*EXP(1130./ temp))
G4106b	$CH_3O_2 + CH_3O_2 \rightarrow HCHO + CH_3OH$	9.5E-14*EXP(390./temp) /(1.+26.2*EXP(-1130./ temp))
G4107	$CH_3OOH + OH \rightarrow .7\ CH_3O_2 + .3\ HCHO + .3\ OH + H_2O$	k_CH3OOH_OH
G4108	$HCHO + OH \rightarrow CO + H_2O + HO_2$	9.52E-18*EXP(2.03*log(temp) +636./temp)
G4109	$HCHO + NO_3 \rightarrow HNO_3 + CO + HO_2$	3.4E-13*EXP(-1900./temp)
G4110	$CO + OH \rightarrow H + CO_2$	1.57E-13+cair*3.54E-33
G4111	$HCOOH + OH \rightarrow HO_2$	4.E-13
G6100	$Cl + O_3 \rightarrow ClO$	2.3E-11*EXP(-200./temp)
G6102	$ClO + ClO \rightarrow Cl_2O_2$	k_ClO_ClO
G6103	$Cl_2O_2 \rightarrow ClO + ClO$	k_ClO_ClO/ (1.27E-27*EXP(8744./temp))
G6202	$Cl + H_2O_2 \rightarrow HCl + HO_2$	1.1E-11*EXP(-980./temp)
G6204	$ClO + HO_2 \rightarrow HOCl$	2.7E-12*EXP(220./temp)
G6205	$HCl + OH \rightarrow Cl + H_2O$	2.6E-12*EXP(-350./temp)
G6300	$ClO + NO \rightarrow NO_2 + Cl$	6.4E-12*EXP(290./temp)
G6301	$ClO + NO_2 \rightarrow ClNO_3$	k_3rd(temp,cair,1.8E-31, 3.4,1.5E-11,1.9,0.6)
G6302	$ClNO_3 \rightarrow ClO + NO_2$	6.918E-7*exp(-10909./temp) *cair
G6304	$ClNO_3 + Cl \rightarrow Cl_2 + NO_3$	6.5E-12*EXP(135./temp)
G6400	$Cl + CH_4 \rightarrow HCl + CH_3O_2$	9.6E-12*EXP(-1360./temp)
G6401	$Cl + HCHO \rightarrow HCl + CO + HO_2$	8.1E-11*EXP(-30./temp)
G6402	$Cl + CH_3OOH \rightarrow CH_3O_2 + HCl$	5.7E-11
G6403	$ClO + CH_3O_2 \rightarrow HO_2 + Cl + HCHO$	3.3E-12*EXP(-115./temp)
G7100	$Br + O_3 \rightarrow BrO$	1.7E-11*EXP(-800./temp)
G7102a	$BrO + BrO \rightarrow Br + Br$	2.4E-12*EXP(40./temp)
G7102b	$BrO + BrO \rightarrow Br_2$	2.8E-14*EXP(869./temp)
G7200	$Br + HO_2 \rightarrow HBr$	1.5E-11*EXP(-600./temp)

Table C.1: Gas Phase Reactions (continued)

#	Reaction	Rate Coefficient
G7201	$BrO + HO_2 \rightarrow HOBr$	3.4E-12*EXP(540./temp)
G7202	$HBr + OH \rightarrow Br + H_2O$	1.1E-11
G7300	$Br + BrNO_3 \rightarrow Br_2 + NO_3$	4.9E-11
G7301	$BrO + NO \rightarrow Br + NO_2$	8.8E-12*EXP(260./temp)
G7302	$BrO + NO_2 \rightarrow BrNO_3$	k_BrO_NO2
G7303	$BrNO_3 \rightarrow BrO + NO_2$	k_BrO_NO2/ (5.44E-9*exp(14192./temp) *1.E6*R_gas*temp/ (atm2Pa*N_A))
G7400	$Br + HCHO \rightarrow HBr + CO + HO_2$	1.7E-11*EXP(-800./temp)
G7401	$Br + CH_3OOH \rightarrow CH_3O_2 + HBr$	2.66E-12*EXP(-1610./temp)
G7402a	$BrO + CH_3O_2 \rightarrow HOBr + HCHO$	0.8/1.1*5.7E-12
G7402b	$BrO + CH_3O_2 \rightarrow Br + HCHO + HO_2$	0.3/1.1*5.7E-12
G7403	$CH_3Br + OH \rightarrow H_2O + Br$	2.35E-12*EXP(-1300./temp)
G7600	$Br + BrCl \rightarrow Br_2 + Cl$	3.3E-15
G7601	$Br + Cl_2 \rightarrow BrCl + Cl$	1.1E-15
G7602	$Br_2 + Cl \rightarrow BrCl + Br$	1.2E-10
G7603a	$BrO + ClO \rightarrow Br + OClO$	9.5E-13*EXP(550./temp)
G7603b	$BrO + ClO \rightarrow Br + Cl$	2.3E-12*EXP(260./temp)
G7603c	$BrO + ClO \rightarrow BrCl$	4.1E-13*EXP(290./temp)
G7604	$BrCl + Cl \rightarrow Br + Cl_2$	1.5E-11
G9200	$SO_2 + OH \rightarrow H_2SO_4 + HO_2$	k_3rd(temp,cair,3.E-31, 3.3,1.5E-12,0.,0.6)
G9400a	$DMS + OH \rightarrow CH_3SO_2 + HCHO$	1.13E-11*EXP(-253./temp)
G9400b	$DMS + OH \rightarrow DMSO + HO_2$	k_DMS_OH
G9401	$DMS + NO_3 \rightarrow CH_3SO_2 + HNO_3 + HCHO$	1.9E-13*EXP(520./temp)
G9402	$DMSO + OH \rightarrow .6\ SO_2 + HCHO + .6\ CH_3O_2 + .4\ HO_2 + .4\ CH_3SO_3H$	1.E-10
G9403	$CH_3SO_2 \rightarrow SO_2 + CH_3O_2$	1.9E13*EXP(-8661./temp)
G9404	$CH_3SO_2 + O_3 \rightarrow CH_3SO_3$	3.E-13
G9405	$CH_3SO_3 + HO_2 \rightarrow CH_3SO_3H$	5.E-11
G9600	$DMS + Cl \rightarrow CH_3SO_2 + HCl + HCHO$	3.3E-10
G9700	$DMS + Br \rightarrow CH_3SO_2 + HBr + HCHO$	9.E-11*EXP(-2386./temp)
G9701	$DMS + BrO \rightarrow DMSO + Br$	2.54E-14*EXP(850./temp)

Notes and References:

temp: temperature of air

C(KPP_X): concentration of X in molecules/cm^3

cair: conversion factor mol/mol $\rightarrow$ molecules/cm^3

exp: FORTRAN notation: exp(y) $\equiv e^y$

E: FORTRAN notation: x.E-y $\equiv x \cdot 10^y$

k_3rd: Funktion of 3rd order rate coefficients as given by

```
ELEMENTAL REAL(dp) FUNCTION k_3rd(temp,cair,k0_300K,n,kinf_300K,m,fc)
INTRINSIC LOG10

  REAL(dp),  INTENT(IN) ::  temp          ! temperature [K]
  REAL(dp),  INTENT(IN) ::  cair          ! air concentration [molecules/cm3]
  REAL,      INTENT(IN) ::  k0_300K       ! low pressure limit at 300 K
  REAL,      INTENT(IN) ::  n             ! exponent for low pressure limit
  REAL,      INTENT(IN) ::  kinf_300K     ! high pressure limit at 300 K
  REAL,      INTENT(IN) ::  m             ! exponent for high pressure limit
  REAL,      INTENT(IN) ::  fc            ! broadening factor (usually fc=0.6)
  REAL                  ::  zt_help, k0_T
  REAL                  ::  kinf_T, k_ratio

  zt_help  =  300./temp
  k0_T     =  k0_300K * zt_help**(n) * cair                    ! k_0 at current T
  kinf_T   =  kinf_300K * zt_help**(m)                         ! k_inf at current T
  k_ratio  =  k0_T/kinf_T
  k_3rd    =  k0_T/(1.+k_ratio)*fc**(1./(1.+LOG10(k_ratio)**2))
END FUNCTION k_3rd
```

G1000, G1001: Sander et al. (2003b)

G2100, G2104, G2105, G2107, G2109: Sander et al. (2003b)

G2110: The rate coefficient is: `k_HO2_HO2 = (1.5E-12*EXP(19./temp)+1.7E-33*EXP(1000./temp)*cair)*(1.0_dp+1.4E-21*EXP(2200./temp)*C(KPP_H2O))`. The value for the first (pressure-independent) part is from Christensen et al. (2002), the water term from Kircher and Sander (1984)

G2111, G2112: Sander et al. (2003b)

G3101, G3103, G3106, G3108: Sander et al. (2003b)

G3109: The rate coefficient is: `k_NO3_NO2 = k_3rd(temp,cair,2.0E-30,4.4,1.4E-12,0.7,0.6)`. Sander et al. (2003b)

G3110: The rate coefficient is defined as backward reaction of G3109 divided by the equilibrium constant; Sander et al. (2003b)

G3200, G3201, G3202: Sander et al. (2003b)

G3203: The rate coefficient is: `k_NO3_HO2 = k_3rd(temp,cair,1.8E-31,3.2,4.7E-12,1.4,0.6)`;Sander et al. (2003b)

G3204, G3205: Sander et al. (2003b)

G3206: The rate coefficient is: `k_HNO3_OH = 2.4E-14*EXP(460./temp)+1./((1./6.5E-34*EXP(1335./temp)*cair)+(1./2.7E-17*EXP(2199./temp)))` Sander et al. (2003b)

G3207: The rate coefficient is defined as backward reaction of G3203 divided by the equilibrium constant. Sander et al. (2003b)

G3208: Sander et al. (2003b)

G4101: Atkinson (2003)

G4102: Sander et al. (2003b)

G4103a, G4103b: Sander et al. (2003b); product distribution is from Elrod et al. (2001)

G4104: Sander et al. (2003b)

G4105: Atkinson et al. (1999)

G4106a, G4106b: Sander et al. (2003b)

G4107: The rate coefficient is: `k_CH3OOH_OH = 3.8E-12*EXP(200./temp)`; Sander et al. (2003b)

G4108: Sivakumaran et al. (2003)

G4109: same temperature dependence assumed as for $CH_3CHO+NO_3$; (Sander et al., 2003b)

G4110: McCabe et al. (2001)

G4111: Sander et al. (2003b)

G6100: Sander et al. (2003b)

G6102: The rate coefficient is: `k_ClO_ClO = k_3rd(temp,cair,1.6E-32,4.5,2.E-12, 2.4,0.6)`; Sander et al. (2003b)

G6103: The rate coefficient is defined as backward reaction of G6102 divided by the equilibrium constant; Sander et al. (2003b)

G6202: Sander et al. (2003b)

G6204: Sander et al. (2003b); At low temperatures, there may be a minor reaction channel leading to O_3+HCl. See Finkbeiner et al. (1995) for details. It is neglected here.

G6205, G6300, G6301: Sander et al. (2003b)

G6302: Anderson and Fahey (1990)

G6304, G6400, G6401, G6402, G6403: Sander et al. (2003b)

G7100, G7102a, G7102b, G7200, G7201, G7202: Sander et al. (2003b)

G7300: Orlando and Tyndall (1996)

G7301: Sander et al. (2003b)

G7302: The rate coefficient is: `k_BrO_NO2 = k_3rd(temp,cair,5.2E-31,3.2,6.9E-12, 2.9,0.6)`; Sander et al. (2003b)

G7303: The rate coefficient is defined as backward reaction of G7302 divided by the equilibrium constant (Orlando and Tyndall, 1996); (Sander et al., 2003b)

G7400: Sander et al. (2003b)

G7401: Mallard et al. (1993)

G7402a, G7402b: Aranda et al. (1997)

G7403: Sander et al. (2003b)

G7600, G7601, G7602: Mallard et al. (1993)

G7603a, G7603b, G7603c: Sander et al. (2003b)

G7604: Mallard et al. (1993)

G9200: Sander et al. (2003b)

G9400a: Atkinson et al. (2004); Abstraction path: the assumed reaction sequence (omitting H_2O and O_2 as products) according to Yin et al. (1990) is:

$$\begin{aligned}
\mathrm{DMS + OH} &\rightarrow \mathrm{CH_3SCH_2} \\
\mathrm{CH_3SCH_2 + O_2} &\rightarrow \mathrm{CH_3SCH_2OO} \\
\mathrm{CH_3SCH_2OO + NO} &\rightarrow \mathrm{CH_3SCH_2O + NO_2} \\
\mathrm{CH_3SCH_2O} &\rightarrow \mathrm{CH_3S + HCHO} \\
\mathrm{CH_3S + O_3} &\rightarrow \mathrm{CH_3SO} \\
\mathrm{CH_3SO + O_3} &\rightarrow \mathrm{CH_3SO_2} \\
\hline
\mathrm{DMS + OH + NO + 2O_3} &\rightarrow \mathrm{CH_3SO_2 + HCHO + NO_2} \quad .
\end{aligned}$$

Neglecting the effect on O_3 and NO_x, the remaining reaction is:

$$\mathrm{DMS + OH + O_3 \rightarrow CH_3SO_2 + HCHO}$$

G9400b: Atkinson et al. (2004); Addition path: The rate coefficient is: `k_DMS_OH = 1.0E-39*EXP(5820./temp)*C(KPP_O2)/(1.+5.0E-30*EXP(6280./temp)*C(KPP_O2))`.

G9401: Atkinson et al. (2004)

G9402: Hynes and Wine (1996)

G9403, G9404, G9405: Barone et al. (1995)

G9600: Atkinson et al. (2004)

G9700: Jefferson et al. (1994)

G9701: Ingham et al. (1999)

Table C.2: Photolysis Reactions

#	Reaction	Rate Coefficient
J1001a	$O_3 + h\nu \rightarrow O(^1D)$	J_O1D
J1001b	$O_3 + h\nu \rightarrow O(^3P)$	J_O3P
J2101	$H_2O_2 + h\nu \rightarrow 2\ OH$	J_H2O2
J3101	$NO_2 + h\nu \rightarrow NO + O(^3P)$	J_NO2
J3103a	$NO_3 + h\nu \rightarrow NO_2 + O(^3P)$	J_NO2O
J3103b	$NO_3 + h\nu \rightarrow NO$	J_NOO2
J3104	$N_2O_5 + h\nu \rightarrow NO_2 + NO_3$	J_N2O5
J3200	$HONO + h\nu \rightarrow NO + OH$	J_HONO
J3201	$HNO_3 + h\nu \rightarrow NO_2 + OH$	J_HNO3
J3202	$HNO_4 + h\nu \rightarrow .667\ NO_2 + .667\ HO_2 + .333\ NO_3 + .333\ OH$	J_HNO4
J4100	$CH_3OOH + h\nu \rightarrow HCHO + OH + HO_2$	J_CH3OOH
J4101a	$HCHO + h\nu \rightarrow H_2 + CO$	J_COH2
J4101b	$HCHO + h\nu \rightarrow H + CO + HO_2$	J_CHOH
J6000	$Cl_2 + h\nu \rightarrow Cl + Cl$	J_Cl2
J6100	$Cl_2O_2 + h\nu \rightarrow 2\ Cl$	J_Cl2O2
J6101	$OClO + h\nu \rightarrow ClO + O(^3P)$	J_OClO
J6201	$HOCl + h\nu \rightarrow OH + Cl$	J_HOCl
J6300	$ClNO_2 + h\nu \rightarrow Cl + NO_2$	J_ClNO2
J6301	$ClNO_3 + h\nu \rightarrow Cl + NO_3$	J_ClNO3
J7000	$Br_2 + h\nu \rightarrow Br + Br$	J_Br2
J7100	$BrO + h\nu \rightarrow Br + O(^3P)$	J_BrO
J7200	$HOBr + h\nu \rightarrow Br + OH$	J_HOBr
J7300	$BrNO_2 + h\nu \rightarrow Br + NO_2$	J_BrNO2
J7301	$BrNO_3 + h\nu \rightarrow Br + NO_3$	J_BrNO3
J7600	$BrCl + h\nu \rightarrow Br + Cl$	J_BrCl

Notes:
J-values are calculated with the external MESSy-module JVAL and then supplied to the MECCA chemistry.

Table C.3: Heterogeneous Reactions

#	Reaction	Rate coefficient
H1001f	$O_3 \rightarrow O_3(aq)$	`k_exf(cs,KPP_O3)`
H1001b	$O_3(aq) \rightarrow O_3$	`k_exb(cs,KPP_O3)`
H2102f	$H_2O_2 \rightarrow H_2O_2(aq)$	`k_exf(cs,KPP_H2O2)`
H2102b	$H_2O_2(aq) \rightarrow H_2O_2$	`k_exb(cs,KPP_H2O2)`
H3200f	$NH_3 \rightarrow NH_3(aq)$	`k_exf(cs,KPP_NH3)`
H3200b	$NH_3(aq) \rightarrow NH_3$	`k_exb(cs,KPP_NH3)`
H3201	$N_2O_5 \rightarrow HNO_3(aq) + HNO_3(aq)$	`k_exf_N2O5(cs)*C(KPP_H2O_cs)`
H3203f	$HNO_3 \rightarrow HNO_3(aq)$	`k_exf(cs,KPP_HNO3)`
H3203b	$HNO_3(aq) \rightarrow HNO_3$	`k_exb(cs,KPP_HNO3)`
H4100f	$CO_2 \rightarrow CO_2(aq)$	`k_exf(cs,KPP_CO2)`
H4100b	$CO_2(aq) \rightarrow CO_2$	`k_exb(cs,KPP_CO2)`
H6000f	$Cl_2 \rightarrow Cl_2(aq)$	`k_exf(cs,KPP_Cl2)`
H6000b	$Cl_2(aq) \rightarrow Cl_2$	`k_exb(cs,KPP_Cl2)`
H6200f	$HCl \rightarrow HCl(aq)$	`k_exf(cs,KPP_HCl)`
H6200b	$HCl(aq) \rightarrow HCl$	`k_exb(cs,KPP_HCl)`
H6201f	$HOCl \rightarrow HOCl(aq)$	`k_exf(cs,KPP_HOCl)`
H6201b	$HOCl(aq) \rightarrow HOCl$	`k_exb(cs,KPP_HOCl)`
H6300	$N_2O_5 + Cl^-(aq) \rightarrow ClNO_2 + NO_3^-(aq)$	`k_exf_N2O5(cs)*5.E2`
H6301	$ClNO_3 \rightarrow HOCl(aq) + HNO_3(aq)$	`k_exf_ClNO3(cs)*C(KPP_H2O_cs)`
H6302	$ClNO_3 + Cl^-(aq) \rightarrow Cl_2(aq) + NO_3^-(aq)$	`k_exf_ClNO3(cs)*5.E2`
H7000f	$Br_2 \rightarrow Br_2(aq)$	`k_exf(cs,KPP_Br2)`
H7000b	$Br_2(aq) \rightarrow Br_2$	`k_exb(cs,KPP_Br2)`
H7200f	$HBr \rightarrow HBr(aq)$	`k_exf(cs,KPP_HBr)`
H7200b	$HBr(aq) \rightarrow HBr$	`k_exb(cs,KPP_HBr)`
H7201f	$HOBr \rightarrow HOBr(aq)$	`k_exf(cs,KPP_HOBr)`
H7201b	$HOBr(aq) \rightarrow HOBr$	`k_exb(cs,KPP_HOBr)`
H7300	$N_2O_5 + Br^-(aq) \rightarrow BrNO_2 + NO_3^-(aq)$	`k_exf_N2O5(cs)*3.E5`
H7301	$BrNO_3 \rightarrow HOBr(aq) + HNO_3(aq)$	`k_exf_BrNO3(cs)*C(KPP_H2O_cs)`
H7302	$BrNO_3 + Br^-(aq) \rightarrow Br_2(aq) + NO_3^-(aq)$	`k_exf_BrNO3(cs)*3.E5`
H7600f	$BrCl \rightarrow BrCl(aq)$	`k_exf(cs,KPP_BrCl)`
H7600b	$BrCl(aq) \rightarrow BrCl$	`k_exb(cs,KPP_BrCl)`
H7601	$ClNO_3 + Br^-(aq) \rightarrow BrCl(aq) + NO_3^-(aq)$	`k_exf_ClNO3(cs)*3.E5`
H7602	$BrNO_3 + Cl^-(aq) \rightarrow BrCl(aq) + NO_3^-(aq)$	`k_exf_BrNO3(cs)*5.E2`
H9100f	$SO_2 \rightarrow SO_2(aq)$	`k_exf(cs,KPP_SO2)`
H9100b	$SO_2(aq) \rightarrow SO_2$	`k_exb(cs,KPP_SO2)`
H9200	$H_2SO_4 \rightarrow H_2SO_4(aq)$	`k_exf(cs,KPP_H2SO4)`
H9401	$CH_3SO_3H \rightarrow CH_3SO_3^-(aq) + H^+(aq)$	`k_exf(cs,KPP_CH3SO3H)`

Notes and References:
The forward (`k_exf`) and backward (`k_exb`) rate coefficients are calculated in the file `messy_mecca_mbl.f90` using the accommodation coefficients in subroutine `mecca_mbl_alpha` and Henry's law constants in subroutine `mecca_mbl_henry`.

k_{mt} = mass transfer coefficient

lwc = liquid water content of aerosol mode

cs = index for mode to which this chemistry equation is applied

H3201, H6300, H7300: Behnke et al. (1994), Behnke et al. (1997)

H6301, H6302, H7601: The total uptake is determined by $k_{\mathrm{mt}}(\mathrm{ClNO_3})$. The relative rates are assumed to be the same as for N_2O_5 (H3201, H6300, H7300).

H7301, H7302, H7602: The total uptake is determined by $k_{\mathrm{mt}}(\mathrm{BrNO_3})$. The relative rates are assumed to be the same as for N_2O_5 (H3201, H6300, H7300).

For the 9 heterogeneous reactions H3201, H6300, H7300, H6301, H6302, H7601, H7301, H7302, H7602 the following equation is valid:

$fhet(X,Y) = k_{\mathrm{mt}}(X) \times lwc \times f(Y)[Y]/Het_T$, with f($H_2O$) = 1, f($Cl^-$) = 5.0E2, and $f(Br^-)$ = 3.0E5, $[Y]$ = concentration of Y; $\mathrm{Het_T} = [\mathrm{H_2O}] + \mathrm{f}(\mathrm{Cl^-})[\mathrm{Cl^-}] + \mathrm{f}(\mathrm{Br^-})[\mathrm{Br^-}]$

X and Y are given for each reactions as denoted in following Table:

X	Y		
	H_2O	Cl^-	Br^-
N_2O_2	H3201	H6300	H7300
$ClNO_3$	H6301	H6302	H7601
$BrNO_3$	H7301	H7302	H7602

Table C.4: Acid-Base and other Equilibria

#	Reaction	$K_0[M^{m-n}]$	$\frac{-\Delta H}{R}[K]$	Reference
EQ21	$H_2O \rightleftharpoons H^+ + OH^-$	1.0E-16	-6716	Chameides (1984)
EQ30	$NH_4^+ \rightleftharpoons H^+ + NH_3$	5.88E-10	-2391	Chameides (1984)
EQ32	$HNO_3 \rightleftharpoons H^+ + NO_3^-$	15.0		Davis and de Bruin (1964)
EQ40	$CO_2 \rightleftharpoons H^+ + HCO_3^-$	4.3E-7	-913	Chameides (1984)
EQ61	$HCl \rightleftharpoons H^+ + Cl^-$	1.7E6	6896	Marsh and McElroy (1985)
EQ71	$HBr \rightleftharpoons H^+ + Br^-$	1.0E9		Lax (1969)
EQ73	$BrCl + Cl^- \rightleftharpoons BrCl_2^-$	3.8	1143	Wang et al. (1994)
EQ74	$BrCl + Br^- \rightleftharpoons Br_2Cl^-$	1.8E4		Wang et al. (1994)
EQ75	$Br_2 + Cl^- \rightleftharpoons Br_2Cl^-$	1.3		Wang et al. (1994)
EQ90	$SO_2 \rightleftharpoons H^+ + HSO_3^-$	1.7E-2	2090	Chameides (1984)
EQ91	$HSO_3^- \rightleftharpoons H^+ + SO_3^{2-}$	6.0E-8	1120	Chameides (1984)
EQ92	$HSO_4^- \rightleftharpoons H^+ + SO_4^{2-}$	1.2E-2	2720	Seinfeld (1998)
EQ93	$H_2SO_4 \rightleftharpoons H^+ + HSO_4^-$	1.0E3		Seinfeld (1998)

Notes:
m, n are the numbers of products on the left and right hand side, respectively.

Table C.5: Aqueous Phase Reactions

#	Reaction	k_0 $[M^{1-n}s^{-1}]$	$-E_a/R[K]$
A6204	$Cl_2 \rightarrow Cl^- + HOCl + H^+$	2.2E1	-8012
A6208	$HOCl + Cl^- + H^+ \rightarrow Cl_2$	2.2E4	-3508
A7202	$Br_2 \rightarrow Br^- + HOBr + H^+$	9.7E1	
A7208	$HOBr + Br^- + H^+ \rightarrow Br_2$	1.6E10	
A7602	$Br^- + HOCl + H^+ \rightarrow BrCl$	1.3E6	
A7603	$HOBr + Cl^- + H^+ \rightarrow BrCl$	2.3E10	
A7604	$BrCl \rightarrow Cl^- + HOBr + H^+$	3.0E6	
A9101	$SO_3^{2-} + O_3 \rightarrow SO_4^{2-}$	1.5E9	-5300
A9206	$HSO_3^- + O_3 \rightarrow SO_4^{2-} + H^+$	3.7E5	-5500
A9209	$HSO_3^- + H_2O_2 \rightarrow SO_4^{2-} + H^+$	5.2E6	-3650
A9601	$SO_3^{2-} + HOCl \rightarrow Cl^- + HSO_4^-$	7.6E8	
A9605	$HSO_3^- + HOCl \rightarrow Cl^- + HSO_4^- + H^+$	7.6E8	
A9702	$SO_3^{2-} + HOBr \rightarrow Br^- + HSO_4^-$	5.0E9	
A9705	$HSO_3^- + HOBr \rightarrow Br^- + HSO_4^- + H^+$	5.0E9	

Notes and References: n is the order of the reaction.

A6204: Ayers et al. (1996)

A6208: Ayers et al. (1996)

A7202: Beckwith et al. (1996)

A7208: Beckwith et al. (1996)

A7602: Kumar and Margerum (1987)

A7603: Liu and Margerum (2001)

A7604: Liu and Margerum (2001)

A9101: Hoffmann (1986)

A9206: Hoffmann (1986)

A9209: Martin and Damschen (1981)

A9601: Fogelman et al. (1989)

A9605: assumed to be the same as for SO_3^{2-} + HOCl (A9601).

A9702: Troy and Margerum (1991)

A9705: assumed to be the same as for SO_3^{2-} + HOBr (A9702).

Table C.6: Henry's Law Coefficients

Species	$K_H^0[M/atm]$	$-\Delta_{soln}H/R[K]$	Reference
O_3	$1.2{\cdot}10^{-2}$	2560	Chameides (1984)
H_2O_2	$1.0{\cdot}10^{5}$	6338	Lind and Kok (1994)
NH_3	$5.8{\cdot}10^{1}$	4085	Chameides (1984)
N_2O_5	∞		
HNO_3	$1.7{\cdot}10^{5}$	8694	Lelieveld and Crutzen (1991)
CO_2	$3.1{\cdot}10^{-2}$	2423	Chameides (1984)
HCHO	$7.0\cdot10^{3}$	6425	Chameides (1984)
Cl_2	$9.1\cdot10^{-2}$	2500	Wilhelm et al. (1977)
HCl	1.2	9001	Brimblecombe and Clegg (1989)
HOCl	$6.7{\cdot}10^{2}$	5862	Huthwelker et al. (1995)
$ClNO_3$	∞		
Br_2	$7.6{\cdot}10^{-1}$	4094	Dean (1992)
HBr	1.3	10239	Brimblecombe and Clegg (1989)
HOBr	$9.3{\cdot}10^{1}$	=HOCl	Vogt et al. (1996)
$BrNO_3$	∞		
BrCl	$9.4{\cdot}10^{-1}$	5600	Bartlett and Margerum (1999)
DMSO	$5.0{\cdot}10^{4}$	=HCHO	De Bruyn et al. (1994)
SO_2	1.2	3120	Chameides (1984)
H_2SO_4	∞		
CH_3SO_3H	∞		

Table C.7: Accommodation Coefficients

Species	α^0	$-\Delta_{soln}H/R[K]$	Reference
O_3	0.002	(at 292 K)	DeMore et al. (1997)
H_2O_2	0.077	2769	Worsnop et al. (1989)
NH_3	0.06	(at 295 K)	DeMore et al. (1997)
N_2O_5	0.1	(at 195-300 K)	DeMore et al. (1997)
HNO_3	0.5	(at RT)	Abbatt and Waschewsky (1998)
CO_2	0.01	2000	estimated
HCHO	0.04	(at 260-270 K)	DeMore et al. (1997)
Cl_2	0.038	6546	Hu et al. (1995)
HCl	0.074	3072	Schweitzer et al. (2000)
HOCl	=HOBr	=HOBr	estimated
$ClNO_3$	0.1	(at RT)	Koch and Rossi (1998)
Br_2	0.038	6546	Hu et al. (1995)
HBr	0.031	3940	Schweitzer et al. (2000)
HOBr	0.5	(at RT)	Abbatt and Waschewsky (1998)
$BrNO_3$	0.8	0	Hanson et al. (1996)
BrCl	$=Cl_2$	$=Cl_2$	estimated
DMSO	0.048	2578	De Bruyn et al. (1994)
SO_2	0.11	0	DeMore et al. (1997)
H_2SO_4	0.65	(at 303 K)	Pöschl et al. (1998)
CH_3SO_3H	0.076	1762	De Bruyn et al. (1994)

Appendix D

SCAV Reaction Tables

Table D.1: Heterogeneous Reactions

#	Reaction	Rate Coefficient
H1000f	$O_2 \rightarrow O_2(aq)$	`k_exf(KPP_O2)`
H1000b	$O_2(aq) \rightarrow O_2$	`k_exb(KPP_O2)`
H1001f	$O_3 \rightarrow O_3(aq)$	`k_exf(KPP_O3)`
H1001b	$O_3(aq) \rightarrow O_3$	`k_exb(KPP_O3)`
H2100f	$OH \rightarrow OH(aq)$	`k_exf(KPP_OH)`
H2100b	$OH(aq) \rightarrow OH$	`k_exb(KPP_OH)`
H2101f	$HO_2 \rightarrow HO_2(aq)$	`k_exf(KPP_HO2)`
H2101b	$HO_2(aq) \rightarrow HO_2$	`k_exb(KPP_HO2)`
H2102f	$H_2O_2 \rightarrow H_2O_2(aq)$	`k_exf(KPP_H2O2)`
H2102b	$H_2O_2(aq) \rightarrow H_2O_2$	`k_exb(KPP_H2O2)`
H3100f	$NO \rightarrow NO(aq)$	`k_exf(KPP_NO)`
H3100b	$NO(aq) \rightarrow NO$	`k_exb(KPP_NO)`
H3101f	$NO_2 \rightarrow NO_2(aq)$	`k_exf(KPP_NO2)`
H3101b	$NO_2(aq) \rightarrow NO_2$	`k_exb(KPP_NO2)`
H3102f	$NO_3 \rightarrow NO_3(aq)$	`k_exf(KPP_NO3)`
H3102b	$NO_3(aq) \rightarrow NO_3$	`k_exb(KPP_NO3)`
H3200f	$NH_3 \rightarrow NH_3(aq)$	`k_exf(KPP_NH3)`
H3200b	$NH_3(aq) \rightarrow NH_3$	`k_exb(KPP_NH3)`
H3201	$N_2O_5 \rightarrow HNO_3(aq) + HNO_3(aq)$	`k_exf_N2O5*C(KPP_H2O_l)`
H3202f	$HONO \rightarrow HONO(aq)$	`k_exf(KPP_HONO)`
H3202b	$HONO(aq) \rightarrow HONO$	`k_exb(KPP_HONO)`
H3203f	$HNO_3 \rightarrow HNO_3(aq)$	`k_exf(KPP_HNO3)`
H3203b	$HNO_3(aq) \rightarrow HNO_3$	`k_exb(KPP_HNO3)`
H3204f	$HNO_4 \rightarrow HNO_4(aq)$	`k_exf(KPP_HNO4)`
H3204b	$HNO_4(aq) \rightarrow HNO_4$	`k_exb(KPP_HNO4)`
H4100f	$CO_2 \rightarrow CO_2(aq)$	`k_exf(KPP_CO2)`
H4100b	$CO_2(aq) \rightarrow CO_2$	`k_exb(KPP_CO2)`
H4101f	$HCHO \rightarrow HCHO(aq)$	`k_exf(KPP_HCHO)`
H4101b	$HCHO(aq) \rightarrow HCHO$	`k_exb(KPP_HCHO)`
H4102f	$CH_3O_2 \rightarrow CH_3OO(aq)$	`k_exf(KPP_CH3O2)`
H4102b	$CH_3OO(aq) \rightarrow CH_3O_2$	`k_exb(KPP_CH3O2)`

Table D.1: Heterogeneous Reactions (continued)

#	Reaction	Rate Coefficient
H4103f	$HCOOH \rightarrow HCOOH(aq)$	`k_exf(KPP_HCOOH)`
H4103b	$HCOOH(aq) \rightarrow HCOOH$	`k_exb(KPP_HCOOH)`
H4104f	$CH_3OOH \rightarrow CH_3OOH(aq)$	`k_exf(KPP_CH3OOH)`
H4104b	$CH_3OOH(aq) \rightarrow CH_3OOH$	`k_exb(KPP_CH3OOH)`
H4105f	$CH_3OH \rightarrow CH_3OH(aq)$	`k_exf(KPP_CH3OH)`
H4105b	$CH_3OH(aq) \rightarrow CH_3OH$	`k_exb(KPP_CH3OH)`
H6000f	$Cl_2 \rightarrow Cl_2(aq)$	`k_exf(KPP_Cl2)`
H6000b	$Cl_2(aq) \rightarrow Cl_2$	`k_exb(KPP_Cl2)`
H6200f	$HCl \rightarrow HCl(aq)$	`k_exf(KPP_HCl)`
H6200b	$HCl(aq) \rightarrow HCl$	`k_exb(KPP_HCl)`
H6201f	$HOCl \rightarrow HOCl(aq)$	`k_exf(KPP_HOCl)`
H6201b	$HOCl(aq) \rightarrow HOCl$	`k_exb(KPP_HOCl)`
H7000f	$Br_2 \rightarrow Br_2(aq)$	`k_exf(KPP_Br2)`
H7000b	$Br_2(aq) \rightarrow Br_2$	`k_exb(KPP_Br2)`
H7200f	$HBr \rightarrow HBr(aq)$	`k_exf(KPP_HBr)`
H7200b	$HBr(aq) \rightarrow HBr$	`k_exb(KPP_HBr)`
H7201f	$HOBr \rightarrow HOBr(aq)$	`k_exf(KPP_HOBr)`
H7201b	$HOBr(aq) \rightarrow HOBr$	`k_exb(KPP_HOBr)`
H7600f	$BrCl \rightarrow BrCl(aq)$	`k_exf(KPP_BrCl)`
H7600b	$BrCl(aq) \rightarrow BrCl$	`k_exb(KPP_BrCl)`
H9100f	$SO_2 \rightarrow SO_2(aq)$	`k_exf(KPP_SO2)`
H9100b	$SO_2(aq) \rightarrow SO_2$	`k_exb(KPP_SO2)`
H9200	$H_2SO_4 \rightarrow H_2SO_4(aq)$	`k_exf(KPP_H2SO4)`

Notes and References:
The forward (`k_exf`) and backward (`k_exb`) rate coefficients are calculated in the file `messy_scav_base.f90`.

H3201: $\mathrm{k\_exf\_N2O5} = \mathrm{k_{mt}}(N_2O_5) \times \mathrm{lwc}/([H_2O] + 5.0\mathrm{E}2 \cdot [Cl^-] + 3.0\mathrm{E}5 \cdot [Br^-])$ with k_{mt} = mass transfer coefficient; lwc = liquid water content of aerosol mode and [X] concentration of X; see Behnke et al. (1994), Behnke et al. (1997)

Table D.2: Photolysis Reactions

#	reaction	rate coefficient
PH01	$H_2O_2 + h\nu \rightarrow 2\ OH$	`J_H2O2` $\cdot$ 2.33

Notes:
J-values are calculated with the external MESSy-module JVAL and then supplied to the SCAV chemistry.

Table D.3: Acid-Base and other Equilibria

#	Reaction	$K_0[M^{m-n}]$	$-\Delta H/R[K]$	Reference
EQ20	$HO_2 \rightleftharpoons O_2^- + H^+$	1.6E-5		Weinstein-Lloyd and Schwartz (1991)
EQ21	$H_2O \rightleftharpoons H^+ + OH^-$	1.0E-16	-6716	Chameides (1984)
EQ30	$NH_4^+ \rightleftharpoons H^+ + NH_3$	5.88E-10	-2391	Chameides (1984)
EQ31	$HONO \rightleftharpoons H^+ + NO_2^-$	5.1E-4	-1260	Schwartz and White (1981)
EQ32	$HNO_3 \rightleftharpoons H^+ + NO_3^-$	15		Davis and de Bruin (1964)
EQ33	$HNO_4 \rightleftharpoons NO_4^- + H^+$	1.E-5		Warneck (1999)
EQ40	$CO_2 \rightleftharpoons H^+ + HCO_3^-$	4.3E-7	-913	Chameides (1984)
EQ41	$HCOOH \rightleftharpoons H^+ + HCOO^-$	1.8E-4		Weast (1980)
EQ61	$HCl \rightleftharpoons H^+ + Cl^-$	1.7E6	6896	Marsh and McElroy (1985)
EQ62	$HOCl \rightleftharpoons H^+ + ClO^-$	3.2E-8		Lax (1969)
EQ71	$HBr \rightleftharpoons H^+ + Br^-$	1.0E9		Lax (1969)
EQ72	$HOBr \rightleftharpoons H^+ + BrO^-$	2.3E-9	-3091	Kelley and Tartar (1956)
EQ90	$SO_2 \rightleftharpoons H^+ + HSO_3^-$	1.7E-2	2090	Chameides (1984)
EQ91	$HSO_3^- \rightleftharpoons H^+ + SO_3^{2-}$	6.0E-8	1120	Chameides (1984)
EQ92	$HSO_4^- \rightleftharpoons H^+ + SO_4^{2-}$	1.2E-2	2720	Seinfeld (1998)
EQ93	$H_2SO_4 \rightleftharpoons H^+ + HSO_4^-$	1.0E3		Seinfeld (1998)

Note: m,n are the numbers of products on the left and right hand side, respectively.

Table D.4: Aqueous Phase Reactions

#	Reaction	k_0 $[M^{1-n}s^{-1}]$	$\frac{-E_a}{R}[K]$
A1000	$O_3 + O_2^- \rightarrow OH + OH^-$	1.5E9	
A2100	$OH + O_2^- \rightarrow OH^-$	1.0E10	
A2101	$OH + OH \rightarrow H_2O_2$	5.5E9	
A2102	$HO_2 + O_2^- \rightarrow H_2O_2 + OH^-$	1.0E8	-900
A2103	$HO_2 + OH \rightarrow H_2O$	7.1E9	
A2104	$HO_2 + HO_2 \rightarrow H_2O_2$	9.7E5	-2500
A2105	$H_2O_2 + OH \rightarrow HO_2$	2.7E7	-1684
A3100	$NO_2^- + O_3 \rightarrow NO_3^-$	5.0E5	-6950
A3101	$NO_2 + NO_2 \rightarrow HNO_3 + HONO$	1.0E8	
A3102	$NO_4^- \rightarrow NO_2^-$	8.0E1	
A3200	$NO_2 + HO_2 \rightarrow HNO_4$	1.8E9	
A3201	$NO_2^- + OH \rightarrow NO_2 + OH^-$	1.0E10	
A3202	$NO_3 + OH^- \rightarrow NO_3^- + OH$	8.2E7	-2700
A3203	$HONO + OH \rightarrow NO_2$	1.0E10	
A3204	$HONO + H_2O_2 \rightarrow HNO_3$	4.6E3	-6800
A4100	$CO_3^- + O_2^- \rightarrow HCO_3^- + OH^-$	6.5E8	
A4101	$CO_3^- + H_2O_2 \rightarrow HCO_3^- + HO_2$	4.3E5	
A4102	$HCOO^- + CO_3^- \rightarrow 2\ HCO_3^- + HO_2$	1.5E5	
A4103	$HCOO^- + OH \rightarrow OH^- + HO_2 + CO_2$	3.1E9	-1240
A4104	$HCO_3^- + OH \rightarrow CO_3^-$	8.5E6	
A4105	$HCHO + OH \rightarrow HCOOH + HO_2$	7.7E8	-1020
A4106	$HCOOH + OH \rightarrow HO_2 + CO_2$	1.1E8	-991
A4107	$CH_3OO + O_2^- \rightarrow CH_3OOH + OH^-$	5.0E7	
A4108	$CH_3OO + HO_2 \rightarrow CH_3OOH$	4.3E5	
A4109	$CH_3OH + OH \rightarrow HCHO + HO_2$	9.7E8	
A4110a	$CH_3OOH + OH \rightarrow CH_3OO$	2.7E7	-1715
A4110b	$CH_3OOH + OH \rightarrow HCHO + OH$	1.1E7	-1715
A9100	$SO_3^- + O_2 \rightarrow SO_5^-$	1.5E9	
A9101	$SO_3^{2-} + O_3 \rightarrow SO_4^{2-}$	1.5E9	-5300
A9102	$SO_4^- + O_2^- \rightarrow SO_4^{2-}$	3.5E9	
A9103	$SO_4^- + SO_3^{2-} \rightarrow SO_3^- + SO_4^{2-}$	4.6E8	
A9104	$SO_5^- + O_2^- \rightarrow HSO_5^- + OH^-$	2.3E8	
A9200	$SO_3^{2-} + OH \rightarrow SO_3^- + OH^-$	5.5E9	
A9201	$SO_4^- + OH \rightarrow HSO_5^-$	1.0E9	
A9202	$SO_4^- + HO_2 \rightarrow SO_4^{2-} + H^+$	3.5E9	
A9203	$SO_4^- + H_2O \rightarrow SO_4^{2-} + H^+ + OH$	1.1E1	-1110
A9204	$SO_4^- + H_2O_2 \rightarrow SO_4^{2-} + H^+ + HO_2$	1.2E7	
A9205	$HSO_3^- + O_2^- \rightarrow SO_4^{2-} + OH$	3.0E3	
A9206	$HSO_3^- + O_3 \rightarrow SO_4^{2-} + H^+$	3.7E5	-5500
A9207	$HSO_3^- + OH \rightarrow SO_3^-$	4.5E9	
A9208	$HSO_3^- + HO_2 \rightarrow SO_4^{2-} + OH + H^+$	3.0E3	
A9209	$HSO_3^- + H_2O_2 \rightarrow SO_4^{2-} + H^+$	5.2E6	-3650
A9210	$HSO_3^- + SO_4^- \rightarrow SO_3^- + SO_4^{2-} + H^+$	8.0E8	
A9212	$HSO_3^- + HSO_5^- \rightarrow 2\ SO_4^{2-} + 2\ H^+$	7.1E6	

Table D.4: Aqueous phase reactions (continued)

#	Reaction	k_0 $[M^{1-n}s^{-1}]$	$\frac{-E_a}{R}[K]$
A9300	$SO_3^{2-} + NO_2 \rightarrow SO_4^{2-} + 2\ HONO - NO_2$	2.0E7	
A9301	$SO_4^- + NO_3^- \rightarrow SO_4^{2-} + NO_3$	5.0E4	
A9302	$SO_4^{2-} + NO_3 \rightarrow NO_3^- + SO_4^-$	1.0E5	
A9303	$HSO_3^- + NO_2 \rightarrow HSO_4^- + 2\ HONO - NO_2$	2.0E7	
A9304	$HSO_3^- + NO_3 \rightarrow SO_3^- + NO_3^- + H^+$	1.4E9	-2000
A9305	$HSO_3^- + HNO_4 \rightarrow HSO_4^- + NO_3^- + H^+$	3.1E5	
A9400	$SO_3^{2-} + HCHO \rightarrow CH_2OHSO_3^- + OH^-$	1.4E4	
A9401	$SO_3^{2-} + CH_3OOH \rightarrow SO_4^{2-} + CH_3OH$	1.6E7	-3800
A9402	$HSO_3^- + HCHO \rightarrow CH_2OHSO_3^-$	4.3E-1	
A9403	$HSO_3^- + CH_3OOH \rightarrow SO_4^{2-} + H^+ + CH_3OH$	1.6E7	-3800
A9404	$CH_2OHSO_3^- + OH^- \rightarrow SO_3^{2-} + HCHO$	3.6E3	

Notes and References: n is the order of the reaction.

A1000: Sehested et al. (1983)

A2100, A2103 : Sehested et al. (1968)

A2101: Buxton et al. (1988)

A2102, A2104: Christensen and Sehested (1988)

A2105: Christensen et al. (1982)

A3100: Damschen and Martin (1983)

A3101: Lee and Schwartz (1981)

A3102, A3200: Warneck (1999)

A3201: Wingenter et al. (1999)

A3202: Exner et al. (1992)

A3203: Barker et al. (1970)

A3204: Damschen and Martin (1983)

A4100, A4101, A4102, A4104: Ross et al. (1992)

A4103, A4105, A4106: Chin and Wine (1994)

A4107, A4108, A4110a,b: Jacob (1986)

A4109: Buxton et al. (1988)

A9100: Huie and Neta (1987)

A9101: Hoffmann (1986)

A9102: Jiang et al. (1992)

A9103: Huie and Neta (1987)

A9104: Buxton et al. (1996)

A9200: Buxton et al. (1988)

A9201, A9202: Jiang et al. (1992)

A9203: Herrmann et al. (1995)

A9204: Wine et al. (1989)

A9205: D. Sedlak, pers. comm. (1993)

A9206: Hoffmann (1986)

A9207: Buxton et al. (1988)

A9208: D. Sedlak, pers. comm. (1993)

A9209: Martin and Damschen (1981)

A9210: Huie and Neta (1987)

A9212: Betterton and Hoffmann (1988)

A9300: Clifton et al. (1988)

A9301: Exner et al. (1992)

A9302: Logager et al. (1993)

A9303: Clifton et al. (1988)

A9304: Exner et al. (1992)

A9305: Warneck (1999)

A9400, A9402: Boyce and Hoffmann (1984)

A9401, A9403: Huie and Neta (1987)

A9404: Seinfeld (1998)

List of Tables

2.1 Measurements of organic-iodines 18

3.1 Table of model resolutions 25
3.2 List of MESSy submodels 27
3.3 Assumed ion abundance in sea water 31
3.4 M7: compound distribution over modes 32

4.1 List of model simulations 40
4.2 Averaged aerosol mass concentrations 51
4.3 Measured and modelled seasonal mean ozone mixing ratio 69

C.1 Gas Phase Reactions 105
C.2 Photolysis Reactions 111
C.3 Heterogeneous Reactions 112
C.4 Acid-Base and other Equilibria 114
C.5 Aqueous Phase Reactions 115
C.6 Henry's Law Coefficients 116
C.7 Accommodation Coefficients 116

D.1 Heterogeneous Reactions 117
D.2 Photolysis Reactions 119
D.3 Acid-Base and other Equilibria 119
D.4 Aqueous Phase Reactions 120

Bibliography

Abbatt, J. and Waschewsky, G.: Heterogeneous Interactions of HOBr, HNO_3, O_3, and NO_2 with Deliquescent NaCl Aerosols at Room Temperature, J. Phys. Chem. A, 102, 3719–3725, 1998.

Alicke, B., Hebestreit, K., Stutz, J., and Platt, U.: Iodine oxide in the marine boundary layer, Nature, 397, 572–573, 1999.

Allan, B., McFiggans, G., Plane, J., and Coe, H.: Oberservations of iodine monoxide in the remote marine boundary layer, J. Geophys. Res., 105, 14 363–14 369, 2000.

Allan, B., Plane, J., and McFiggans, G.: Observations of OIO in the remote marine boundary layer, Geophys. Res. Lett., 28, 1945–1948, 2001.

Allan, B. J.: A spectroscopic study of radical chemistry in the troposphere, Ph.D. thesis, University of East Anglia, Great Britain, 1998.

Anderson, L. C. and Fahey, D. W.: Studies with $ClONO_2$: Thermal dissociation rate and catalytic conversion to NO using an NO/O_3 chemiluminescence detector, J. Phys. Chem., 94, 644–652, 1990.

Aranda, A., Le Bras, G., La Verdet, G., and Poulet, G.: The BrO + CH_3O_2 reaction: Kinetics and role in the atmospheric ozone budget, Geophys. Res. Lett., 24, 2745–2748, 1997.

Ashworth, S. H., Allan, B. J., and Plane, J. M. C.: High resolution spectroscopy of the OIO radical: Implications for the ozone-depleting potential of iodine, Geophys. Res. Lett., 29, doi:10.1029/2001GL013851, 2002.

Atkinson, R.: Kinetics of the gas-phase reactions of OH radicals with alkanes and cycloalkanes, Atmos. Chem. Phys., 3, 2233–2307, 2003.

Atkinson, R., Baulch, D. L., Cox, R. A., Hampson, Jr., R. F., Kerr, J. A., Rossi, M. J., and Troe, J.: Summary of evaluated kinetic and photochemical data for atmospheric chemistry: Web version August 1999, `http://www.iupac-kinetic.ch.cam.ac.uk/`, 1999.

Atkinson, R., Baulch, D. L., Cox, R. A., Crowley, J. N., Hampson, R. F., Hynes, R. G., Jenkin, M. E., Rossi, M. J., and Troe, J.: Evaluated kinetic and photochemical data for atmospheric chemistry: Volume I – gas phase reactions of O_x, HO_x, NO_x and SO_x species, Atmos. Chem. Phys., 4, 1461–1738, 2004.

Ayers, G., Gillett, R., Cainey, J., and Dick, A.: Chloride and Bromide Loss from Sea-Salt Particles in Southern Ocean Air, J. Atmos. Chem., 33, 299–319, 1999.

Ayers, G. P., Penkett, S. A., Gillett, R. W., Bandy, B., Galbally, I. E., Meyer, C. P., Elsworth, C. M., Bentle, S. T., and Forgan, B. W.: The Annual Cycle of Peroxides and Ozone in Marine Air at Cape Grim, Tasmania, J. Atmos. Chem., 23, 221 – 252, 1996.

Baker, A. R., Thompson, D., Campos, M. L. A. M., Perry, S. J., and Jickells, T. D.: Iodine concentration and availability in atmospheric aerosol, Atmos. Environ., 34, 4331–4336, 2000.

Balkanski, Y., Schulz, M., Claquin, T., Moulin, C., and Ginoux, P.: Global emissions of mineral aerosol: Formulation and validation using satellite imagery, chap. Emission of Atmospheric Tracer Compounds, pp. 253–282, Kluwer Acad., Norwell, Mass., 2003.

Barker, G. C., Fowles, P., and Stringer, B.: Pulse radiolytic induced transient electrical conductance in liquid solutions, Trans. Faraday Soc., 66, 1509–1519, 1970.

Barone, S. B., Turnipseed, A. A., and Ravishankara, A. R.: Role of adducts in the atmospheric oxidation of dimethyl sulfide, Faraday Discuss., 100, 39–54, 1995.

Barrie, L. A., Bottenheim, J. W., Schnell, R. C., Crutzen, P. J., and Rasmussen, R. A.: Ozone destruction and photochemical reactions at polar sunrise in the lower Arctic atmosphere, Nature, 334, 138–141, 1988.

Bartlett, W. P. and Margerum, D. W.: Temperature dependencies of the Henry's law constant and the aqueous phase dissociation constant of bromine chloride, Environ. Sci. Technol., 33, 3410–3414, 1999.

Bates, T. S., Kapustin, V. N., Quinn, P. K., Covert, D. S., Coffman, D. J., Mari, C., Dirkee, P. A., Bruyn, W. J. D., and Saltzman, E. S.: Processes controlling the distribution of aerosol particles in the lower marine boundary layer during the First Aerosol Charaterization Experiment (ACE1), J. Geophys. Res., 103, 16 369–16 383, 1998.

Beckwith, R. C., Wang, T. X., and Margerum, D. W.: Equilibrium and kinetics of bromine hydrolysis, Inorg. Chem., 35, 995–1000, 1996.

Behnke, W., Scheer, V., and Zetzsch, C.: Production of $BrNO_2$, Br_2 and $ClNO_2$ from the Reaction between Sea Spray Aerosol and N_2O_5, J. Aer. Sc., 25, Suppl.1, S277 – S278, 1994.

Behnke, W., George, C., Scheer, V., and Zetzsch, C.: Production and decay of $ClNO_2$ from the reaction of gaseous N_2O_5 with NaCl solution: Bulk and aerosol experiments, J. Geophys. Res., 102, 3795–3804, 1997.

Bell, N., Hsu, L., Jacob, D., Schultz, M., Blake, D., Butler, J., King, D., Lobert, J., and Maier-Reimer, E.: Methyl iodide: Atmospheric budget and use as a tracer of marine convection in global models, J. Geophys. Res., 107, 4340, doi:10.1029/2001JD001151, 2002.

Betterton, E. A. and Hoffmann, M. R.: Oxidation of aqueous SO_2 by peroxymonosulfate, J. Phys. Chem., 92, 5962–5965, 1988.

Bloss, W. J., Rowley, D. M., Cox, R. A., and Jones, R. L.: Kinetics and Products of the IO Self-Reaction, J. Phys. Chem. A, 105, 7840–7854, 2001.

Bobrowski, N., Hönninger, G., Galle, B., and Platt, U.: Detection of bromine monoxide in a volcanic plume, Nature, 423, 273–276, 2003.

Bott, A.: A numerical model of the cloud-topped planetary boundary layer: Impact of aerosol particles on the radiative forcing of stratiform clouds, Q. J. R. Meteorol. Soc., 123, 631–656, 1997.

Bott, A., Trautmann, T., and Zdunkowski, W.: A numerical model of the cloud-topped planetary boundary layer: Radiation, turbulence and spectral microphysics in marine stratus, Q. J. R. Meteorol. Soc., 122, 635–667, 1996.

Bouwman, A., Lee, D., Asman, W., Dentener, F., Van der Hoek, K., and Olivier, J.: A global high-resolution emission inventory for ammonia, Global Biogeochem. Cycles, 11, 561–587, 1997.

Boyce, S. D. and Hoffmann, M. R.: Kinetics and mechanism of the formation of hydroxymethanesulfonic acid at low pH, J. Phys. Chem., 88, 4740–4746, 1984.

Brimblecombe, P. and Clegg, S. L.: Erratum, J. Atmos. Chem., 8, 95, 1989.

Buxton, G. V., Greenstock, C. L., Helman, W. P., and Ross, A. B.: Critical review of rate constants for reactions of hydrated electrons, hydrogen atoms and hydroxyl radicals ($\cdot$OH/$\cdot$O$^-$) in aqueous solution, J. Phys. Chem. Ref. Data, 17, 513–886, 1988.

Buxton, G. V., McGowan, S., Salmon, G. S., Williams, J. E., and Wood, N. D.: A study of the spectra and reactivity of oxysulphur-radical anions involved in the chain oxidation of S(IV): A pulse and γ-radiolysis study, Atmos. Environ., 30, 2483–2493, 1996.

Carpenter, L., Sturges, W., Penkett, S., Liss, P., Alicke, B., Hebestreit, K., and Platt, U.: Short-lived alkyl iodides and bromides at Mace Head, Ireland: Links to biogenic sources and halogen oxide production, J. Geophys. Res., 104, 1679–1689, 1999.

Carpenter, L., Hebestreit, K., Platt, U., and Liss, P.: Coastal zone production of IO precursors: a 2-dimensional study, Atmos. Chem. Phys., 1, 9–18, 2001.

Carslaw, N., Carpenter, L., Plane, J., Allan, B., Burgess, R., Clemitshaw, K., Coe, H., and Penkett, S.: Simultaneous observations of nitrate and peroxy radicals in the marine boundary layer, J. Geophys. Res., 102, 18 917–18 933, 1997a.

Carslaw, N., Plane, J. M., Coe, H., and Cuevas, E.: Observations of the nitrate radical in the free troposphere at Izana de Tenerife, J. Geophys. Res., 102, 10 613–10 622, 1997b.

Chameides, W.: The Photochemistry of a Remote Marine Stratiform Cloud, J. Geophys. Res., 89, 4739–4755, 1984.

Chameides, W. and Davis, D.: Iodine: Its possible role in tropospheric photochemistry, J. Geophys. Res., 85, 7383–7398, 1980.

Chatfield, R. and Crutzen, P.: Are there interactions of iodine and sulfur species in marine air photochemistry ?, J. Geophys. Res., 95D, 22 319–22 341, 1990.

Chin, M. and Wine, P. H.: A temperature-dependent competitive kinetics study of the aqueous-phase reactions of OH radicals with formate, formic acid, acetate, acetic acid, and hydrated formaldehyde, in: Aquatic and Surface Photochemistry, edited by Helz, G. R., Zepp, R. G., and Crosby, D. G., pp. 85–96, A. F. Lewis, NY, 1994.

Christensen, H. and Sehested, K.: HO_2 and O_2^- radicals at elevated temperatures, J. Phys. Chem., 92, 3007–3011, 1988.

Christensen, H., Sehested, K., and Corfitzen, H.: Reactions of hydroxyl radicals with hydrogen peroxide at ambient and elevated temperatures, J. Phys. Chem., 86, 1588–1590, 1982.

Christensen, L. E., Okumura, M., Sander, S. P., Salawitch, R. J., Toon, G. C., Sen, B., Blavier, J.-F., and Jucks, K. W.: Kinetics of $HO_2 + HO_2 \rightarrow H_2O_2 + O_2$: Implications for stratospheric H_2O_2, Geophys. Res. Lett., 29, doi:10.1029/2001GL014525, 2002.

Cicerone, R. J.: Halogens in the atmosphere, Rev. Geophys. Space Phys., 19, 123–139, 1981.

Clifton, C. L., Altstein, N., and Huie, R. E.: Rate constant for the reaction of NO_2 with sulfur(IV) over the pH range 5.3–13, Environ. Sci. Technol., 22, 586–589, 1988.

Cox, R., Bloss, W., Jones, R., and Rowley, D.: OIO and the Atmospheric Cycle of Iodine, Geophys. Res. Lett., 26, 1857–1860, 1999.

Damschen, D. E. and Martin, L. R.: Aqueous aerosol oxidation of nitrous acid by O_2, O_3 and H_2O_2, Atmos. Environ., 17, 2005–2011, 1983.

Davis, D., Crawford, J., Liu, S., McKeen, S., Bandy, A., Thornton, D., Rowland, F., and Blake, D.: Potential impact of iodine on tropospheric levels of ozone and other critical oxidants, J. Geophys. Res., 101, 2135–2147, 1996.

Davis, Jr., W. and de Bruin, H. J.: New activity coefficients of 0-100 per cent aqueous nitric acid, J. Inorg. Nucl. Chem., 26, 1069 – 1083, 1964.

De Bruyn, W. J., Shorter, J. A., Davidovits, P., Worsnop, D. R., Zahniser, M. S., and Kolb, C. E.: Uptake of gas phase sulfur species methanesulfonic acid, dimethylsulfoxide, and dimethyl sulfone by aqueous surface, J. Geophys. Res., 99, 16 927 – 16 932, 1994.

Dean, J. A.: Lange's Handbook of Chemistry, McGraw-Hill, Inc., 1992.

DeMore, W. B., Sander, S. P., Golden, D. M., Hampson, R. F., Kurylo, M. J., Howard, C. J., Ravishankara, A. R., Kolb, C. E., and Molina, M. J.: Chemical Kinetics and Photochemical Data for Use in Stratospheric Modeling, Tech. Rep. JPL Publication 97-4, Jet Propulsion Laboratory, Pasadena, CA, 1997.

Elrod, M. J., Ranschaert, D. L., and Schneider, N. J.: Direct kinetics study of the temperature dependence of the CH_2O branching channel for the $CH_3O_2 + HO_2$ reaction, Int. J. Chem. Kinetics, 33, 363–376, 2001.

Erickson III, D. J., Seuzaret, C., Keene, W. C., and Gong, S. L.: A general circulation model based calculation of HCl and $ClNO_2$ production from sea-salt dechlorination: Reactive chlorine emissions inventory, J. Geophys. Res., 104D, 8347–8372, 1999.

Exner, M., Herrmann, H., and Zellner, R.: Laser-based studies of reactions of the nitrate radical in aqueous solution, Ber. Bunsenges. Phys. Chem., 96, 470–477, 1992.

Finkbeiner, M., Crowley, J. N., Horie, O., Müller, R., Moortgat, G. K., and Crutzen, P. J.: Reaction between HO_2 and ClO: Product formation between 210 and 300 K, J. Phys. Chem., 99, 16 264–16 275, 1995.

Fitzenberger, R., Rösch, R., Camy-Peyret, C., Chipperfield, M., Harder, H., Platt, U., Sinnhuber, B.-M., Wagner, T., and Pfeilsticker, K.: First Profile Measurements of Tropospheric BrO, Geophys. Res. Lett., 27, 2921–2924, 2000.

Fogelman, K. D., Walker, D. M., and Margerum, D. W.: Non-metal redox kinetics: Hypochlorite and hypochlorous acid reactions with sulfite, Inorg. Chem., 28, 986 – 993, 1989.

Frieß, U., Otten, C., Chipperfield, M., Wagner, T., Pfeilsticker, K., and Platt, U.: Intercomparison of measured and modelled BrO slant column amounts for the Arctic winter and spring 1994/95, Geophys. Res. Lett., 26, 1861–1864, 1999.

Gabriel, R., von Glasow, R., Sander, R., Andreae, M., and Crutzen, P.: Bromide content of sea-salt aerosol particles collected over the Indian Ocean during INDOEX 1999, J. Geophys. Res., 107, 8032, doi:10.1029/2001JD001133, 2002.

Galanter, M., Levy, H., and Carmichael, G.: Impacts of biomass burning on tropospheric CO, NO_x, and O_3, J. Geophys. Res., 105, 6633–6653, 2000.

Ganzeveld, L. and Lelieveld, J.: Dry deposition parameterization in a chemistry general circulation model and its influence on the distribution of reactive trace gases, J. Geophys. Res., 100, 20 999–21 012, 1995.

Ganzeveld, L., Lelieveld, J., and Roelofs, G.-J.: A dry deposition parameterization for sulfur oxides in a chemistry and general circulation model, J. Geophys. Res., 103, 5679–5694, 1998.

Ganzeveld, L., Lelieveld, J., Dentener, F., Krol, M., and Roelofs, G.-J.: Atmosphere-biosphere trace gas exchange simulated with a single-column model, J. Geophys. Res., 107, 4297, doi:10.1029/2001JD000684, 2002.

Gong, S. L., Barrie, L. A., Blanchet, J.-P., von Salzen, K., Lohmann, U., Lesins, G., Spacek, L., Zhang, L. M., Girard, E., Lin, H., Leaitch, R., Leighton, H., Chylek, P., and Huang, P.: Canadian Aerosol Module: A size-segregated simulation of atmospheric aerosol processes for climate and air quality models 1. Module development, J. Geophys. Res., 108D, doi:10.1029/2001JD002002, 2003.

Grewe, V., Brunner, D., Dameris, M., Grenfell, J. L., Hein, R., Shindell, D., and Staehelin, J.: Origin and variability of upper tropospheric nitrogen oxides and ozone at northern mid-latitudes, Atmos. Environ., 35, 3421–3433, 2001.

Guazzotti, S. A., Coffee, K. R., and Parther, K. A.: Continuous measurements of size-resolved particle chemistry during INDOEX-Intensive Field Phase 99, J. Geophys. Res., 106, 28 607–28 627, 2001.

Guelle, W., Schulz, M., Balkanski, Y., and Dentener, F.: Influence of the source formulation on modeling the atmospheric global distribution of sea salt aerosol, J. Geophys. Res., 106, 27 509–27 524, 2001.

Hanson, D. R., Ravishankara, A. R., and Lovejoy, E. R.: Reaction of $BrONO_2$ with H_2O on submicron sulfuric acid aerosol and the implications for the lower stratosphere, J. Geophys. Res., 101D, 9063–9069, 1996.

Harder, H., Camy-Peyret, C., Ferlemann, F., Fitzenberger, R., Hawat, T., Osterkamp, H., Schneider, M., Perner, D., Platt, U., Vradelis, P., and Pfeilsticker, K.: Stratospheric BrO profiles measured at different latitudes and seasons: Atmospheric observations, Geophys. Res. Lett., 25, 3843–3846, 1998.

Hebestreit, K., Stutz, J., Rosen, D., matveiv, V., Peleg, M., Luria, M., and Platt, U.: DOAS Measurements of Tropospheric Bromine Oxide in Mid-Latitudes, Science, 283, 55–57, 1999.

Herrmann, H., Reese, A., and Zellner, R.: Time resolved UV/VIS diode array absorption spectroscopy of SO_x^- (x=3, 4, 5) radical anions in aqueous solution, J. Mol. Struct., 348, 183–186, 1995.

Hicks, B., Baldocchi, D., Meyer, T., Hosker, R. P., and Matt, D.: A preliminary multiple resistance routine for deriving dry deposition velocities from measured quantities, Water Air Soil Pollut., 36, 311–330, 1987.

Hoffmann, M. R.: On the kinetics and mechanism of oxidation of aquated sulfur dioxide by ozone, Atmos. Environ., 20, 1145 – 1154, 1986.

Hoffmann, T., O'Dowd, C. D., and Seinfeld, J. H.: Iodine oxide homogeneous nucleation: An explanation for coastal new particle production, Geophys. Res. Lett., 28, 1949–1952, 2001.

Hönninger, G. and Platt, U.: Observations of BrO and its vertical distribution during surface ozone depletion at Alert., Atmos. Environ., 36, 2481–2489, 2002.

Hu, J. H., Shi, Q., Davidovits, P., Worsnop, D. R., Zahniser, M. S., and Kolb, C. E.: Reactive uptake of Cl_2 and Br_2 by aqueous surfaces as a function of Br^- and I^- ion concentration: The effect of chemical reaction at the interface, J. Phys. Chem., 99, 8768 – 8776, 1995.

Huebert, B. J., Zhuang, L., Howell, S., Noone, K., and Noone, B.: Sulfate, nitrate, methanesulfonate, chloride, ammonium, and sodium measurements from ship, island, and aircraft during the Atlantic Stratocumulus Transition EXperiment/Marine Aerosol Gas Exchange, J. Geophys. Res., 101D, 4413–4423, 1996.

Huie, R. E. and Neta, P.: Rate constants for some oxidations of S(IV) by radicals in aqueous solutions, Atmos. Environ., 21, 1743–1747, 1987.

Huthwelker, T., Clegg, S. L., Peter, T., Carslaw, K., Luo, B. P., and Brimblecombe, P.: Solubility of HOCl in water and aqueous H_2SO_4 to stratospheric temperatures, J. Atmos. Chem., 21, 81–95, 1995.

Hynes, A. J. and Wine, P. H.: The atmospheric chemistry of dimethylsulfoxide (DMSO) kinetics and mechanism of the OH + DMSO reaction, J. Atmos. Chem., 24, 23–37, 1996.

Ingham, T., Bauer, D., Sander, R., Crutzen, P. J., and Cowley, J.: Kinetics and Products of the Reaction BrO + DMS and Br + DMS at 298 K, J. Phys. Chem. A, 103, 7199–7209, 1999.

Jacob, D.: Chemistry of OH in Remote Clouds and Its Role in the Production of Formic Acid and Peroxymonosulfate, J. Geophys. Res., 91, 9807–9826, 1986.

James, J., Harrison, R., Savage, N., Allen, A., Grenfell, J., Allan, B., Plane, J., Hewitt, C., Davison, B., and Robertson, L.: Quasi-Lagrangian investigation into dimethyl sulfide oxidation in maritime air using a combination of measurements and model, J. Geophys. Res., 105, 26 379–26 392, 2000.

Jefferson, A., Nicovich, J. M., and Wine, P. H.: Temperature-dependent kinetics studies of the reactions $Br(^2P_{3/2}) + CH_3SCH_3 \leftrightarrow CH_3SCH_2 + HBr$. Heat of formation of the CH_3SCH_2 radical, J. Phys. Chem., 98, 7128–7135, 1994.

Jenkin, M., Cox, R., and Candeland, D.: Photochemical aspects of tropospheric iodine behaviour, J. Atmos. Chem., pp. 359–375, 1985.

Jeuken, A., Siegmund, P., Heijboer, L., Feichter, J., and Bengtson, L.: On the potential of assimilating meteorological analysis in a climate model for the purpose of model validation, J. Geophys. Res., 101, 16 939–16 950, 1996.

Jiang, P.-Y., Katsumura, Y., Nagaishi, R., Domae, M., Ishikawa, K., Ishigure, K., and Yoshida, Y.: Pulse radiolysis study of concentrated sulfuric acid solutions. Formation mechanism, yield and reactivity of sulfate radicals, J. Chem. Soc. Faraday Trans., 88, 1653–1658, 1992.

Jimenez, J. L., Bahreini, R., Cocker III, D. R., Zhuang, H., Varutbangkul, V., Flagan, R., Seinfeld, J., O'Dowd, C., and Hoffmann, T.: New particle formation from photooxidation of diiodomethane (CH_2I_2), J. Geophys. Res., 108, 4318, doi:10.1029/2002JD002452, 2003.

Jöckel, P., von Kuhlmann, R., Lawrence, M., Steil, B., Brenninkmeijer, C., Crutzen, P., Rasch, P., and Eaton, B.: On an fundamental problem in implementing flux-form advection schemes for tracer transport in 3-dimensional general circulation and chemistry transport models, Q. J. R. Meteorol. Soc., 127, 1035–1052, 2001.

Jöckel, P., Sander, R., Kerkweg, A., Tost, H., and Lelieveld, J.: Technical Note: The Modular Earth Submodel System (MESSy) - a new approach towards Earth System Modeling, Atmos. Chem. Phys., 5, 433–444, 2005.

Kanaya, Y., Yokouchi, Y., Matsumoto, J., Nakamura, K., Kato, S., Tanimoto, H., Furutani, H., Toyota, K., and Akimoto, H.: Implications of iodine chemistry for daytime HO_2 levels at Rishiri Island, Geophys. Res. Lett., 29, doi:10.1029/2001GL014061, 2002.

Keene, W. and Savoie, D.: The pH of deliquesced sea-salt aerosol in polluted air, Geophys. Res. Lett., 25, 2181–2184, 1998.

Keene, W. C., Pszenny, A. A. P., Maben, J. R., O'Halloran, T., Wall, A., Kerkweg, A., and Sander, R.: Latitudinal Variation in Volatile and Particulate Inorganic Halogens over the Eastern North and South Atlantic Oceans, geophysical Research Abstracts, EGU General Assembly 2005.

Keene, W. C., Sander, R., Pszenny, A. A., Vogt, R., Crutzen, P. J., and Galloway, J. N.: Aerosol pH in the marine boundary layer: A review and model evaluation, J. Aer. Sc., 29, 339–356, 1998.

Keene, W. C., Pszenny, A. A. P., Maben, J. R., and Sander, R.: Variation of marine aerosol acidity with particle size, Geophys. Res. Lett., 29, doi:10.1029/2001GL013881, 2002.

Kelley, C. M. and Tartar, H. V.: On the system: bromine-water, J. Am. Chem. Soc., 78, 5752–5756, 1956.

Kircher, C. C. and Sander, S. P.: Kinetics and mechanism of HO_2 and DO_2 disproportionations, J. Phys. Chem., 88, 2082–2091, 1984.

Koch, T. G. and Rossi, M. J.: Direct measurement of surface residence times: Nitryl chloride and chlorine nitrate on alkali halides at room temperature, J. Phys. Chem. A, 102, 9193–9201, 1998.

Kulmala, M., Korhonen, P., Napari, I., Karlsson, A., Berresheim, H., and O'Dowd, C.: Aerosol formation during PARFORCE: Ternary nucleation of H_2SO_4, NH_3 and H_2O, J. Geophys. Res., 107, 8111, doi:10.1029/2001JD000900, 2002.

Kumar, K. and Margerum, D. W.: Kinetics and mechanism of general-acid-assisted oxidation of bromide by hypochlorite and hypochlorous acid, Inorg. Chem., 26, 2706–2711, 1987.

Landgraf, J. and Crutzen, P.: An Efficient Method for Online Calculation of Photolysis and Heating Rates, J. Atmos. Sci., 55, 863–878, 1998.

Lax, E.: Taschenbuch für Chemiker und Physiker, Springer Verlag, Berlin, 1969.

Lee, Y.-N. and Schwartz, S. E.: Reaction kinetics of nitrogen dioxide with liquid water at low partial pressure, J. Phys. Chem., 85, 840–848, 1981.

Lelieveld, J. and Crutzen, J.: The Role of Clouds in Tropospheric Photochemistry, J. Atmos. Chem., 12, 229–267, 1991.

Lelieveld, J., van Aardenne, J., Fischer, H., de Reus, M., Williams, J., and Winkler, P.: Increasing Ozone over the Atlantic Ocean, Science, 304, 1483–1487, 2004.

Leser, H., Hönninger, G., and Platt, U.: MAX-DOAS measurements of BrO and NO_2 in the marine boundary layer, Geophys. Res. Lett., 30, doi:10.1029/2002GL015811, 2003.

Lewis, E. R. and Schwartz, S. E.: Sea Salt Aerosol Production: Mechanisms, Methods, Measurements and Models - A Critical Review, American Geophysical Union. Washington, DC, 2004.

Lin, S. and Rood, R.: Multidimensional flux form semi-Lagrangian transport schemes, Mon. Wea. Rev., 124, 2046–2070, 1996.

Lin, S.-J., Chao, W., Sud, Y., and Walker, G. K.: A class of the van Leer-type transport schemes and its applications to the moisture transport in a General Circulation Model, Mon. Wea. Rev., 122, 1575–1593, 1994.

Lind, J. A. and Kok, G. L.: Correction to "Henry's law determinations for aqueous solutions of hydrogen peroxide, methylhydroperoxide, and peroxyacetic acid" by John A. Lind and Gregory L. Kok, J. Geophys. Res., 99D, 21 119, 1994.

Liss, P. and Merlivat, L.: The Role of Air-Sea Exchange in Geochemical Cycling, chap. Air-Sea Gas Exchange Rates: Introduction and Synthesis, pp. 113–127, D. Reidel Publishing Company, 1986.

Liu, Q. and Margerum, D. W.: Equilibrium and kinetics of bromine chloride hydrolysis, Environ. Sci. Technol., 35, 1127–1133, 2001.

Logager, T., Sehested, K., and Holcman, J.: Rate constants of the equilibrium reactions $SO_4 + HNO_3 \longleftrightarrow HSO_4^- + NO_3$ and $SO_4 + NO_3 \longleftrightarrow SO_4^{2-} + NO_3$., Radiat. Phys. Chem., 41, 539 – 543, 1993.

Lovelock, J., Maggs, R., and Wade, R.: Halogenated Hydrocarbons in and over the Atlantic, Nature, 241, 194–196, 1973.

Mäkelä, J., Hoffmann, T., Holzke, C., Väkevä, M., Suni, T., Mattila, T., Aalto, P., Tapper, U., Kauppinen, E., and O'Dowd, C.: Biogenic iodine emissions and identification of end-products in coastal ultrafine particles during nucleation bursts, J. Geophys. Res., 107, 8110, doi: 10.1029/2001JD000580, 2002.

Mallard, W. G., Westley, F., Herron, J. T., Hampson, R. F., and Frizzel, D. H.: NIST Chemical Kinetics Database: Version 5.0, National Institute of Standards and Technology, Gaithersburg, MD, 1993.

Marsh, A. R. W. and McElroy, W. J.: The dissociation constant and Henry's law constant of HCl in aqueous solution, Atmos. Environ., 19, 1075–1080, 1985.

Martin, L. R. and Damschen, D. E.: Aqueous oxidation of sulfur dioxide by hydrogen peroxide at low pH, Atmos. Environ., 15, 1615–1621, 1981.

Matveev, V., Peleg, M., Rosen, D., Tov-Alper, D. S., Hebestreit, K., Stutz, J., Platt, U., Blake, D., and Luria, M.: Bromine oxide - ozone interaction over the Dead Sea, J. Geophys. Res., 106D, 10 375–10 387, 2001.

McCabe, D. C., Gierczak, T., Talukdar, R. K., and Ravishankara, A. R.: Kinetics of the reaction OH + CO under atmospheric conditions, Geophys. Res. Lett., 28, 3135–3138, 2001.

McElroy, C. T., McLinden, C. A., and McConnell, J. C.: Evidence for bromine monoxide in the free troposphere during the Arctic polar sunrise, Nature, 397, 338–341, 1999.

McFiggans, G., Plane, J. M., Allan, B. J., Carpenter, L. J., Coe, H., and O'Dowd, C.: A modeling study of iodine chemistry in the marine boundary layer, J. Geophys. Res., 105, 14 371–14 385, 2000.

Misra, A. and Marshall, P.: Computational Investigations of Iodine Oxides, J. Phys. Chem. A, 102, 9056–9060, 1998.

Molina, M. and Rowland, F.: Stratospheric sink for chlorofluoromethanes: chlorine atom-catalysed destruction of ozone, Nature, 249, 810–812, 1974.

Monahan, E. C.: The Role of Air-Sea Exchange in Geochemical Cycling, chap. The Ocean as a Source for Atmospheric Particles, pp. 129–163, D. Reidel Publishing Company, 1986.

Murphy, D., Thomson, D., Middlebrook, A., and Schein, M.: In situ single-particle characterization at Cape Grim, J. Geophys. Res., 103, 16 485–16 491, 1998.

Nagao, I., Matsumoto, K., and Tanaka, H.: Sunrise ozone destruction found in the subtropical marine boundary layer, Geophys. Res. Lett., 26, 3377–3380, 1999.

Nordeng, T.: Extended versions of the convective parameterization scheme at ECMWF and their impact on the mean and transient activity of the model in the tropics, Tech. Rep. 206, ECMWF, 1994.

O'Dowd, C., Jimenez, J., Bahreini, R., Flagan, R., Seinfeld, J., Hämerl, K., Pirjola, L., Kulmala, M., Jennings, S., and Hoffmann, T.: Marine aerosol formation from biogenic iodine emissions, Nature, 417, 632–636, 2002a.

O'Dowd, C. D.: On the spatial extent and evolution of coastal aerosol plumes, J. Geophys. Res., 107, 8105, doi:10.1029/2001JD000422, 2002.

O'Dowd, C. D. and Smith, M. H.: Physicochemical Properties of Aerosols Over the Northeast Atlantic: Evidence for Wind-Speed-Related Submicron Sea-Salt Aerosol Production, J. Geophys. Res., 98, 1137–1149, 1993.

O'Dowd, C. D., Hämeri, K., Mäkelä, J. M., Pirjola, L., Kumala, M., Jennings, S. G., Berresheimer, H., Hansson, H.-C., de Leeuw, G., Kunz, G. J., Allan, A. G., Hewitt, C. N., Jackson, A., Viisanen, Y., and Hoffmann, T.: A dedicated study of New Particle Formation and Fate in the Coastal Environment (PARFORCE): Overview of objectives and achievements, J. Geophys. Res., 107, 8108, 10.1029/2001JD000555, 2002b.

Oram, D. and Penkett, S.: Observations in Eastern England of Elevated Methyl Iodide Concentrations in Air of Atlantic Origin, Atmos. Environ., 28, 1159–1174, 1994.

Orlando, J. J. and Tyndall, G. S.: Rate coefficients for the thermal decomposition of $BrONO_2$ and the heat of formation of $BrONO_2$, J. Phys. Chem., 100, 19 398–19 405, 1996.

Platt, U.: Reactive Halogen Species in the Mid-latitude Troposphere - Recent Discoveries, Water Air Soil Pollut., 123, 229–244, 2000.

Platt, U. and Hönninger, G.: The role of halogen species in the troposphere, Chemosphere, 52, 325–338, 2003.

Platt, U. and Janssen, C.: Observation and role of the free radicals NO_3, ClO, BrO, and IO in the troposphere, Faraday Discuss., 100, 175–198, 1995.

Platt, U., Perner, D., and Pätz, H.: Simultaneous Measurements of Atmospheric CH_2O, O_3, and NO_2 by Differential Optical Absorption, J. Geophys. Res., 84, 6329–6335, 1979.

Pöschl, U., Canagaratna, M., Jayne, J. T., Molina, L. T., Worsnop, D. R., Kolb, C. E., and Molina, M. J.: Mass accommodation coefficient of H_2SO_4 vapor on aqueous sulfuric acid surfaces and gaseous diffusion coefficient of H_2SO_4 in N_2/H_2O, J. Phys. Chem. A, 102, 10 082–10 089, 1998.

Price, C., Penner, J., and Prather, M.: NO_x from lightning, 1. Global distribution based on lightning physics, J. Geophys. Res., 102, 5929–5941, 1997.

Pruppacher, H. and Klett, J.: Microphysics of Clouds and Precipitation, 2nd edition, Kluwer, Dordrecht, 954 pp., 1997.

Pszenny, A., Keene, W., Jacob, D., Fan, S., Maben, R., Zetwo, M., Springer-Young, M., and Galloway, J.: Evidence of inorganic Chlorine gases other than hydrogen chloride in marine surface air, Geophys. Res. Lett., 20, 699–702, 1993.

Pszenny, A. A. P., Moldanová, J., Keene, W. C., Sander, R., Maben, J. R., Martinez, M., Crutzen, P. J., Perner, D., and Prinn, R. G.: Halogen cycling and aerosol pH in the Hawaiian marine boundary layer, Atmos. Chem. Phys., 4, 147–168, 2004.

Rasmussen, R., Khalil, M., Gunawardena, R., and Hoyt, S.: Atmospheric Methyl Iodide (CH_3I), J. Geophys. Res., 87, 3086–3090, 1982.

Reifenhäuser, W. and Heumann, K. G.: Determinations of methyl iodide in the Antarctic atmosphere and the South Polar Sea, Atmos. Environ., 26A, 2905–2912, 1992.

Roeckner, E., Bäuml, G., Bonaventura, L., Brokopf, R., Esch, M., Giorgetta, M., Hagemann, S., Kirchner, I., Kornblueh, L., Manzini, E., Rhodin, A., Schlese, U., Schulzweida, U., and Tompkins, A.: The atmospheric general circulation model ECHAM5, Tech. rep., Max Planck-Institute for Meteorology, 2003.

Ross, A. B., Mallard, W. G., Helman, W. P., Bielski, B. H. J., Buxton, G. V., Cabelli, D. E., Greenstock, C. L., Huie, R. E., and Neta, P.: NDRL-NIST Solution Kinetics Database: - Ver. 1, National Institute of Standards and Technology, Gaithersburg, MD, 1992.

Sander, R.: Modeling Atmospheric Chemistry: Interactions between Gas-phase Species and Liquid Cloud/Aerosol Particles, Surv. Geophys., 20, 1–31, 1999.

Sander, R. and Crutzen, P.: Model study indicating halogen activation and ozone destruction in polluted air masses transported to the sea, J. Geophys. Res., 101, 9121–9138, 1996.

Sander, R., Rudich, Y., von Glasow, R., and Crutzen, P.: The role of $BrNO_3$ in marine tropospheric chemistry: A model study, Geophys. Res. Lett., 26, 2857–2860, 1999.

Sander, R., Keene, W., Pszenny, A., Arimoto, R., Ayers, G., Baboukas, E., Cainey, J., Crutzen, P., Duce, R., Hönninger, G., Huebert, B., Maenhaut, W., Mihalopoulos, N., Turekian, V., and Dingenen, R. V.: Inorganic bromine in the marine boundary layer: a critical review, Atmos. Chem. Phys., 3, 1301–1336, 2003a.

Sander, R., Kerkweg, A., Jöckel, P., and Lelieveld, J.: Technical Note: The new comprehensive atmospheric chemistry module MECCA, Atmos. Chem. Phys., 5, 445–450, 2005.

Sander, S. P., Finlayson-Pitts, B. J., Friedl, R. R., Golden, D. M., Huie, R. E., Kolb, C. E., Kurylo, M. J., Molina, M. J., Moortgat, G. K., Orkin, V. L., and Ravishankara, A. R.: Chemical Kinetics and Photochemical Data for Use in Atmospheric Studies, Evaluation Number 14, JPL Publication 02-25, Jet Propulsion Laboratory, Pasadena, CA, 2003b.

Sandu, A., Verwer, J. G., Blom, J. G., Spee, E., Carmichael, G. R., and Potra, F. A.: Benchmarking Stiff ODE Solvers for Atmospheric Chemistry Problems II. Rosenbrock Solvers, Atmos. Environ., 31, 3459–3472, 1997a.

Sandu, A., Verwer, J. G., van Loon, M., Carmichael, G. R., Potra, F. A., Dabdub, D., and Seinfeld, J. H.: Benchmarking Stiff ODE Solvers for Atmospheric Chemistry Problems I. Implicit vs Explicit, Atmos. Environ., 31, 3151–3166, 1997b.

Schall, C. and Heumann, K. G.: GC determination of volatile organoiodine and organobromine compounds in Arctic seawater and air samples, Fresenius J. Anal. Chem., 346, 717–722, 1993.

Schmitt, A. and Brunner, B.: Emissions from aviation and their development over time, in: Pollutants from air traffic - results of atmospheric research 1992-1997. Final Report on the BMBF Verbundprogramm ,,Schadstoffe in der Luftfahrt, Tech. rep., DLR-Mitteilung 97-04, 301 pp., [Available from: Deutsches Zentrum für Luft- und Raumfahrt, Oberpfaffenhofen and Cologne], 1997.

Schulz, M., Balkanski, Y., Guelle, W., and Dulac, F.: Role of aerosol size distribution and source location in a three-dimensional simulation of a Saharan dust episode tested against satellite-derived optical thickness, J. Geophys. Res., 103, 10 579–10 592, 1998.

Schwartz, S.: Chemistry of Multiphase Atmospheric Systems, vol. G6, chap. Mass-Transport Considerations Pertinent to Aqueous Phase Reactions of Gases in Liquid-Water Clouds, pp. 415–471, NATO ASI Series, 1986.

Schwartz, S. E. and White, W. H.: Solubility equilibria of the nitrogen oxides and oxyacids in dilute aqueous solution, in: Advances in Environmental Science and Engineering, edited by Pfafflin, J. R. and Ziegler, E. N., vol. 4, pp. 1–45, Gordon and Breach Science Publishers, NY, 1981.

Schwarz, A.: Entwicklung einer online Kopplungsmethode von GC mit ECD- und ICPMS-Detektion zur Bestimmung biogener Kohlenwasserstoffe in Meerwasser und der Atmosphäre, Ph.D. thesis, Johannes Gutenberg-Universität, Fachbereich Chemie und Pharmazie, 2003.

Schweitzer, F., Mirabel, P., and George, C.: Multiphase Chemistry of N_2O_5, $ClNO_2$, and $BrNO_2$, J. Phys. Chem. A, 102, 3942–3952, 1998.

Schweitzer, F., Mirabel, P., and George, C.: Uptake of hydrogen halides by water droplets, J. Phys. Chem. A, 104, 72–76, 2000.

Sehested, K., Rasmussen, O. L., and Fricke, H.: Rate constants of OH with HO_2, O_2^-, and $H_2O_2^+$ from hydrogen peroxide formation in pulse-irradiated oxygenated water, J. Phys. Chem., 72, 626–631, 1968.

Sehested, K., Holcman, J., and Hart, E. J.: Rate constants and products of the reactions of e_{aq}^-, O_2^- and H with ozone in aqueous solutions, J. Phys. Chem., 87, 1951–1954, 1983.

Seinfeld, J. u. S. P.: Atmospheric chemistry and physics, John Wiley & Sons, New York, Chichester, Weinheim, 1998.

Sievering, H., Ennis, G., Gorman, E., and Nagamoto, C.: Size distributions and statistical analysis of nitrate, excess sulfate, and chloride deficit in the marine boundary layer during GCE/CASE/WATOX, Global Biogeochem. Cycles, 4, 395–405, 1990.

Singh, H., Salas, L., and Stiles, R.: Methyl Halides in and over the Eastern Pacific 40° N - 32° S, J. Geophys. Res., 88, 3084–3090, 1983.

Sivakumaran, V., Hölscher, D., Dillon, T. J., and Crowley, J. N.: Reaction between OH and HCHO: temperature dependent rate coefficients (202-399 K) and product pathways (298 K), Phys. Chem. Chem. Phys., 5, 4821–4827, 2003.

Slinn, S. and Slinn, W.: Predictions for Particle Deposition on Natural Waters, Atmos. Environ., 14, 1013–1016, 1980.

Smith, M. H. and Harrison, M.: The Sea Spray Generation Function, J. Aer. Sc., pp. S189–S190, suppl.1, 1998.

Solberg, S., Schmidbauer, N., Semb, A., Stordal, F., and Hov, Ø.: Boundary layer ozone depletion as seen in the Norwegian Arctic in spring, J. Atmos. Chem., 23, 301–332, 1996.

Solomon, S.: Progress towards a quantitative understanding of Antarctic ozone depletion, Nature, 347, 347–354, 1990.

Solomon, S., Garcia, R., and Ravishankara, A.: On the role of iodine in ozone depletion, J. Geophys. Res., 99D, 20 491–20 499, 1994.

Spicer, C., Chapman, E., Finlay-Pitts, B., Plastridge, R., Hubbe, J., Fast, J., and Berkowitz, C.: Unexpectedly high concentrations of molecular chlorine in coastal air, Nature, 394, 353–356, 1998.

Steil, B., Dameris, M., Brühl, C., Crutzen, P., Grewe, V., Ponater, M., and Sausen, R.: Development of a chemistry module for GCMs: first results of a multiannual integration, Ann. Geophys., 16, 205–228, 1998.

Stier, P., Feichter, J., Kinne, S., Kloster, S., Vignati, E., Wilson, J., Ganzeveld, L., Tegen, I., Werner, M., Balkanski, Y., Schulz, M., and Boucher, O.: The Aerosol-Climate Model ECHAM5-HAM, Atmos. Chem. Phys., 5, 1125–1156, 2005.

Stutz, J., Ackermann, R., Fast, J. D., and Barrie, L.: Atmospheric reactive chlorine and bromine at the Great Salt Lake, Utah, Geophys. Res. Lett., 29, doi:10.1029/2002GL014812, 2002.

Thompson, A. M., Witte, J. C., McPeters, R. D., Oltmans, S. J., Schmidlin, F. J., Logan, J. A., Fujiwara, M., Kirchhoff, V. W., Posny, F., Coetze, G. J., Hoegger, B., Kawakami, S., Ogawa, T., Johnson, B. J., Vömel, H., and Labow, G.: Southern Hemispheric Additional Ozonesondes SHADOZ 1998-2000 tropical ozone climatology 1. Comparison with Total Ozone Mapping Spectrometer (TOMS) and ground-based measurements, J. Geophys. Res., 8238, doi:10.1029/2001JD000967, 2003a.

Thompson, A. M., Witte, J. C., Oltmans, S. J., Schmidlin, F. J., Logan, J. A., Fujiwara, M., Kirchhoff, V. W., Posny, F., Coetze, G. J., Hoegger, B., Kawakami, S., Ogawa, T., Fortuin, J., and Kelder, H.: Southern Hemispheric Additional Ozonesondes SHADOZ 1998-2000 tropical ozone climatology 2. Tropospheric variability and zonal wave-one, J. Geophys. Res., 8241, doi:10.1029/2002JD002241, 2003b.

Tiedtke, M.: A comprehensive mass flux scheme for parameterization in large-scale models, Mon. Wea. Rev., 117, 1779–1800, 1989.

Timmreck, C. and Schulz, M.: Significant dust simulation differences in nudged and climatological operation mode of the AGCM ECHAM, J. Geophys. Res., 109, doi:10.1029/2003JD004381, 2004.

Toyota, K., Takahashi, M., and Akimoto, H.: Modeling multi-phase halogen chemistry in the marine boundary layer with size segregated aerosol module: Implications for quasi-size-dependent approach, Geophys. Res. Lett., 28, 2899–2902, 2001.

Toyota, K., Kanaya, Y., Takahashi, M., and Akimoto, H.: A box model study on photochemical interactions between VOCs and reactive halogen species in the marine boundary layer, Atmos. Chem. Phys., 3, 1961–1987, 2004.

Troy, R. C. and Margerum, D. W.: Non-metal redox kinetics: Hypobromite and hypobromous acid reactions with iodide and with sulfite and the hydrolysis of bromosulfate, Inorg. Chem., 30, 3538 – 3543, 1991.

van Roozendael, M., Wagner, T., Richter, A., Pundt, I., Arlander, D. W., Burrows, J. P., Chipperfield, M., Fayt, C., Johnston, P. V., Lambert, J.-C., Kreher, K., Pfeilsticker, K., Platt, U., Pommereau, J.-P., Sinnhuber, B.-M., Tørnkvist, K. K., and Wittrock, F.: Intercomparison of BrO measurements from ERS-2 GOME, ground-based and balloon platforms, Adv. Space Res., 29, 1661–1666, 2002.

Vehkamäki, H., nad I. Napari, M. K., Lehtinen, K., Timmreck, C., Noppel, M., and Laaksonen, A.: An improved parameterization for sulfuric acid-water nucleation rates for tropospheric and stratospheric conditions, J. Geophys. Res., 107, 4622, doi:10.1029/2002JD002184, 2002.

Verwer, J., Spee, E., Blom, J., and Hundsdorfer, W.: A Second Order Rosenbrock Method Applied to Photochemical Dispersion Problems, Tech. rep., Centrum voor Wiskunde en Informatica, 1997.

Vignati, E., Wilson, J., and Stier, P.: M7: An efficient size-resolved aerosol microphysics module for large-scale aerosol transport, J. Geophys. Res., 109, D22 202, doi: 10.1029/2003JD004486, 2004.

Vogt, R., Crutzen, P., and Sander, R.: A mechanism for halogen release from sea salt aerosol in the remote marine boundary layer, Nature, 383, 327–330, 1996.

Vogt, R., Sander, R., von Glasow, R., and Crutzen, P.: Iodine chemistry and its role in halogen activation and ozone loss in the marine boundary layer, J. Atmos. Chem., 32, 375–395, 1999.

von Glasow, R. and Crutzen, P. J.: Model study of multiphase DMS oxidation with a focus on halogens, Atmos. Chem. Phys., 4, 589–608, 2004.

von Glasow, R., Sander, R., Bott, A., and Crutzen, P.: Modeling halogen chemistry in the marine boundary layer 1. Cloud-free MBL, J. Geophys. Res., 107, doi:10.1029/2001JD000942, 2002.

von Glasow, R., von Kuhlmann, R., Lawrence, M., Platt, U., and Crutzen, P. J.: Impact of reactive halogen chemistry in the free troposphere, Atmos. Chem. Phys., 4, 2481–2497, 2004.

von Kuhlmann, R., Lawrence, M. G., Crutzen, P. J., and Rasch, P. J.: A model for studies of tropospheric ozone and nonmethane hydrocarbons: Model description and ozone results, J. Geophys. Res., 108, doi:10.1029/2002JD002893, 2003.

Wagner, T. and Platt, U.: Satellite mapping of enhanced BrO concentrations in the troposphere, Nature, 395, 486–490, 1998.

Wagner, V., von Glasow, R., Fischer, H., and Crutzen, P.: Are CH_2O measurements in the marine boundary layer suitable for testing the current understanding of CH_4 photooxidation?: A model study, J. Geophys. Res., 4029, doi:10.1029/2001JD000722, 2002.

Wang, T. X., Kelley, M. D., Cooper, J. N., Beckwith, R. C., and Margerum, D. W.: Equilibrium, kinetic, and UV-spectral characteristics of aqueous bromine chloride, bromine, and chlorine species, Inorg. Chem., 33, 5872 – 5878, 1994.

Warneck, P.: The relative importance of various pathways for the oxidation of sulfur dioxide and nitrogen dioxide in sunlit continental fair weather clouds, Phys. Chem. Chem. Phys., 1, 5471 – 5483, 1999.

Wayne, R. P.: Chemistry of Atmospheres, Oxford University Press, 2000.

Weast, R. C., ed.: CRC Handbook of Chemistry and Physics, 61st Edition, CRC Press, Inc., Boca Raton, FL, 1980.

Weinstein-Lloyd, J. and Schwartz, S. E.: Low-intensity radiolysis study of free-radical reactions in cloudwater: H_2O_2 production and destruction, Environ. Sci. Technol., 25, 791–800, 1991.

Wennberg, P.: Bromine explosion, Nature, 397, 299–301, 1999.

Wilhelm, E., Battino, R., and Wilcock, R. J.: Low-pressure solubility of gases in liquid water, Chem. Rev., 77, 219–262, 1977.

Wilson, J., Cuvelier, C., and Raes, F.: A modeling study of global mixed aerosol fields, J. Geophys. Res., 106, 34 081–34 108, 2001.

Wimschneider, A. and Heumann, K. G.: Iodine speciation in size fractionated atmospheric particles by isotope dilution mass spectrometry, Fresenius J. Anal. Chem., 353, 191–196, 1995.

Wine, P. H., Tang, Y., Thorn, R. P., Wells, J. R., and Davis, D. D.: Kinetics of aqueous phase reactions of the SO_4^- radical with potential importance in cloud chemistry, J. Geophys. Res., 94D, 1085–1094, 1989.

Wingenter, O. W., Blake, D. R., Blake, N. J., Sive, B. C., Rowland, F. S., Atlas, E., and Flocke, F.: Tropospheric hydroxyl and atomic chlorine concentrations, and mixing timescales determined from hydrocarbon measurements made over the Southern Ocean, J. Geophys. Res., 104D, 21 819–21 828, 1999.

Winkler, P.: Observations on acidity in continental and in marine atmospheric aerosols and in precipitation, J. Geophys. Res., 85C, 4481–4486, 1980.

Winkler, P.: Relations between aerosol acidity and ion balance, in: Chemistry of Multiphase Atmospheric Systems, NATO ASI Series, Vol. G6, edited by Jaeschke, W., pp. 269–298, Springer Verlag, Berlin, 1986.

Worsnop, D. R., Zahniser, M. S., Kolb, C. E., Gardner, J. A., Watson, L. R., van Doren, J. M., Jayne, J. T., and Davidovits, P.: The temperature dependence of mass accommodation of SO_2 and H_2O_2 on aqueous surfaces, J. Phys. Chem., 93, 1159–1172, 1989.

Yin, F., Grosjean, D., and Seinfeld, J. H.: Photooxidation of dimethyl sulfide and dimethyl disulfide. I: Mechanism development, J. Atmos. Chem., 11, 309–364, 1990.

Yvon, S. A. and Butler, J. H.: An improved estimate of the oceanic lifetime of atmospheric CH_3Br, Geophys. Res. Lett., 23, 53–56, 1996.

Zafiriou, O. C.: Photochemistry of halogens in the marine atmosphere, J. Geophys. Res., 79, 2730–2732, 1974.

Acknowledgements

Many, many thanks

- to my supervisor Prof. Dr. Jos Lelieveld for including me into his working group, his always open ears, and especially for the possibility to participate in a measurement campaign.
- to my supervisor Prof. Dr. Andreas Bott for enabling me to do my PhD at the University of Bonn.
- to my 'day-to-day' adviser Dr. Rolf Sander for introducing me into the world of halogen chemistry and for his time for nearly endless discussions.
- to Dr. Patrick Jöckel for realising his idea of MESSy and providing his support in all scientific and technical aspects.
- to Holger Tost as a very helpful 'desk neighbour' and for making me the 'beta-tester' of his submodels.
- to Dr. Marian de Reus (previous MPI-C) for providing the Atlantic Ocean ozone measurements data set and her help according to the visualisation of these data.
- to those people who proofread my thesis.
- to my (previous) room mates and colleagues Sandra Bartenbach, Joachim Buchholz and Dr. Michael Traub for keeping me company and for the not only scientific communication.
- to all the other colleagues of the MPI-C.
- to Dr. Roland von Glasow, Dr. Susanne Marquart and Matthias Piot (all University of Heidelberg) and to all members of the AFO2000 subproject AFOHAL for fruitful discussions about halogen chemistry.
- to Prof. Dr. Bill Keene (University of Virginia, USA) and Prof. Dr. Alex Pszenny (University of New Hampshire and Mount Washington Observatory, USA) for inviting me to the measurement campaign on the Polarstern cruise in October 2003.
- to Prof. Dr. Otto Schrems (Alfred-Wegener-Institute, Bremerhaven) for his permission to join the above mentioned Polarstern cruise.
- to my parents and my sister for their continuous support and encouragement in every respect.
- to Bernd Maurer especially for the life beyond science.